An experimental and computational study of the effects of terminal group design in liquid crystal hosts and guest dyes

Giuseppina Barile

Doctor of Philosophy

University of York

Chemistry

February 2024

Abstract

A combination of experimental and computational methods were used to develop an understanding of the effects of bulky terminal groups on the promotion of smectic A phase formation. This work used two series of liquid crystal hosts, the 4-n-alkoxy-4′-cyanobiphenyl (nOCB) and the 4-(*t*-Bu-n-alkoxy)-4′-cyanobiphenyl (*t*-Bu-nOCB) series, which were studied separately and in guest-host mixtures containing 2,6-disubstituted anthraquinone dyes with *p*-alkoxy-phenyl and *p*-*t*-Bu-alkoxy-phenyl substituents.

From the studies of the hosts alone, it was found that the bulky terminal group promoted the formation of a smectic A phase and resulted in more ordered layers in the phase, relative to analogous molecules without the bulky group. The *t*-Bu-nOCB series also showed larger layer spacings than the nOCB series, which could be attributed to a decrease in the interdigitation of the *t*-Bu-alkoxy chains in order to accommodate the bulky terminal groups. It was found that molecular dynamics simulations provided useful insight into the trends observed for the two series, and in particular for the layer spacing measured experimentally by X-ray diffraction studies.

In the guest-host studies, TD-DFT calculations showed that there was only a small angle between the transition dipole moment and the molecular long axis for both series of dyes. The DFT calculations and molecular dynamics simulations provided insight into a wide range of guest-host mixtures, and were able to be used predictively to select which guest-host mixtures to study experimentally. Polarised UV-visible absorption measurements were used to determine the dichroic ratios of some aligned guest-host mixtures experimentally. All mixtures showed high dichroic ratios and dye orientational order, giving possible mixtures for guest-host device applications.

Contents

List of figures

List of tables

Acknowledgements

Firstly, I would like to acknowledge the support and guidance of my supervisors Dr John Moore and Dr Stephen Cowling. I am so grateful for all the opportunities and support you have provided over the last four years, and for your patience during the online years. Particular thanks also go to Dr Laurence Abbott for sharing his knowledge and being a constant friendly presence in the office. I am also grateful for the Department of Chemistry, for funding my project.

Thanks to my colleagues in Physical Chemistry, for their friendship and conversation over the years. It has been a pleasure to work alongside such so many talented people during my studies.

I would like to thank my lovely friends, both in York and further afield, for their companionship and encouragement. In particular, I want to thank my university day-one Amber, for your unwavering love and support throughout our whole university journey. Thank you for all the chaos and laughter over the last eight years.

Finally I would like to thank my family, especially my amazing parents, Annabel and Pasquale, and my wonderful brother, Giacomo, for your endless encouragement and unwavering love throughout. Thank you for never doubting me and holding my hand whenever things were tough.

To Samuel, this work is a testament to your kindness, strength and love. Thank you for everything.

Author's declaration

I declare that this thesis is a presentation of original work which was carried out between October 2019 and January 2024 and I am the sole author. This work has not previously been presented for a degree or other qualification at this University or elsewhere. All sources are acknowledged as references.

Chapter 1

Introduction

This introductory chapter will provide some background information on liquid crystals, the use of liquid crystals and dyes in guest-host systems and the important properties required for these uses, including the molecular design of each component. The final sections cover some background on the techniques used in this work and the principles behind them.

1.1 Liquid crystals

1.1.1 Background

In 1888, the observation of the "double melting" behaviour of cholesteryl benzoate, which on further study also exhibited a crystal-like double refraction effect, led the scientists Reinitzer and Lehmann to report the presence of a novel phase of matter.[1, 2] Owing to this combination of properties from both the crystal phase and the liquid phase, the first liquid crystal phase was discovered and can be referred to as a mesophase. Following this discovery, in 1922, Georges Friedel introduced a classification system for the known liquid crystal phases, namely nematic, smectic and cholesteric phases,[3] after many years of study of the liquid crystal properties with fellow researchers such as Lehmann and François Grandjean.[4] This formalisation of the classification of liquid crystals was an important step in the progress of liquid crystal research, although within this work the contributions of many different researchers are summarised and analysed. Grandjean also worked independently in the study of liquid crystal phases and developed much of the initial understanding of layered liquid crystal phases which Friedel later summarised within the classification.

1.1.2 Molecular shape and liquid crystal phases

1.1.2.1 Thermotropic liquid crystals

Liquid crystals can be classified into two main categories based on the cause of the mesophase behaviour. This first category is *thermotropic* liquid crystals, where the liquid crystal phase (mesophase) behaviour is observed within a certain temperature range. Thermotropic behaviour can occur in pure compounds or in mixtures of compounds,[3] but

they do not require a solvent for the mesophase behaviour to occur. Thermotropic liquid crystals are commonly classified by molecular shape.

Calamitic liquid crystals are composed of rod-like molecules, for example the Schiff's base shown in Figure 1.1. Calamitic liquid crystals can exhibit a broad variety of phases as a result of their anisotropic shape and the manner in which these molecules can pack. *Discotic* liquid crystals are comprised of molecules with a disc-like structure such as the examples shown in Figure 1.2, These molecules can pack to form columnar phases as a result of the discs stacking on top of one another,[5] as well as other phase structures being formed. *Bent core* liquid crystals have a particular bent molecular structure which leads to distinct packing behaviour relative to other calamitic systems and unusual chiral effects. An example structure for bent core liquid crystals is given in Figure 1.3.

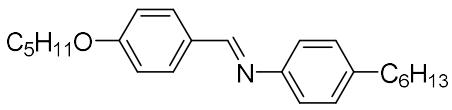

Figure 1.1: Example of a calamitic liquid crystal molecule.[3]

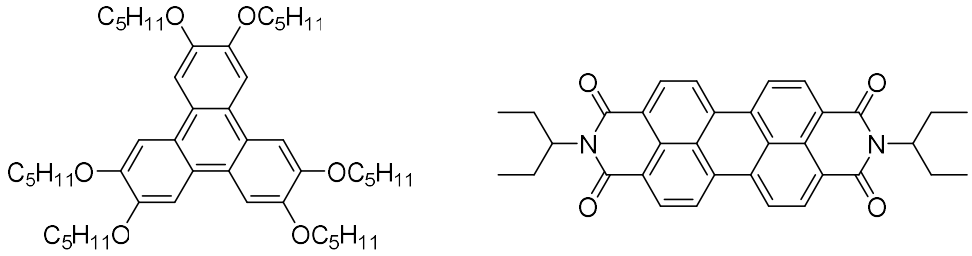

Figure 1.2: Examples of a discotic liquid crystal molecules.[3, 6]

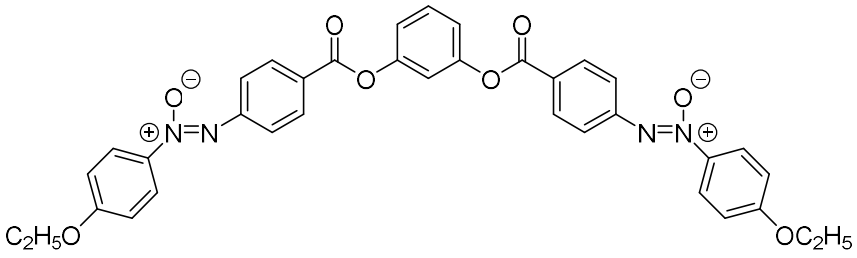

Figure 1.3: Example of a bent core liquid crystal molecule.[7]

Calamitic liquid crystals

Calamitic liquid crystals can be formed by a huge range of different molecular structures, and most commonly have a long, thin shape, as illustrated by the general structure in Figure 1.4. Calamitic molecules are composed of rigid core sections and more flexible units, and the phase behaviour is driven partly by the incompatibility of these units with respect to each other when packing together. The nature and size of these units determines the type of mesophase that may be exhibited.

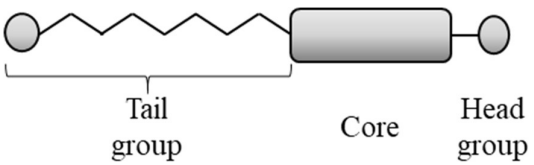

Figure 1.4: General structure of a typical calamitic liquid crystal molecule.

The molecular shape can be determined in a variety of ways, the simplest being in terms of the molecular length and width. The molecular length (l) and width (w) of an individual molecule can be used to calculate the aspect ratio (AR), as given in equation 1, which can be used to understand the shape of the molecule and assess the differences between molecules.

Equation 1.1 $$AR = \frac{l}{w}$$

Discotic liquid crystals

Discotic liquid crystal molecules have extended aromatic structures, which can pack in phases where the discs are positionally disordered, as illustrated in Figure 1.5 a), or can pack face-to-face to form columns (Col phases), as illustrated in Figure 1.5 b) and c), which can have both hexagonal and rectangular packing. Two examples of the columnar phase are the hexagonal and rectangular packing, although other packing arrangements are possible. Discotic liquid crystal phases are formed by molecules with a wide range of structures from simple discs to bowls and doughnut shapes, which all have specific structures leading to the formation of distinct phases.[3]

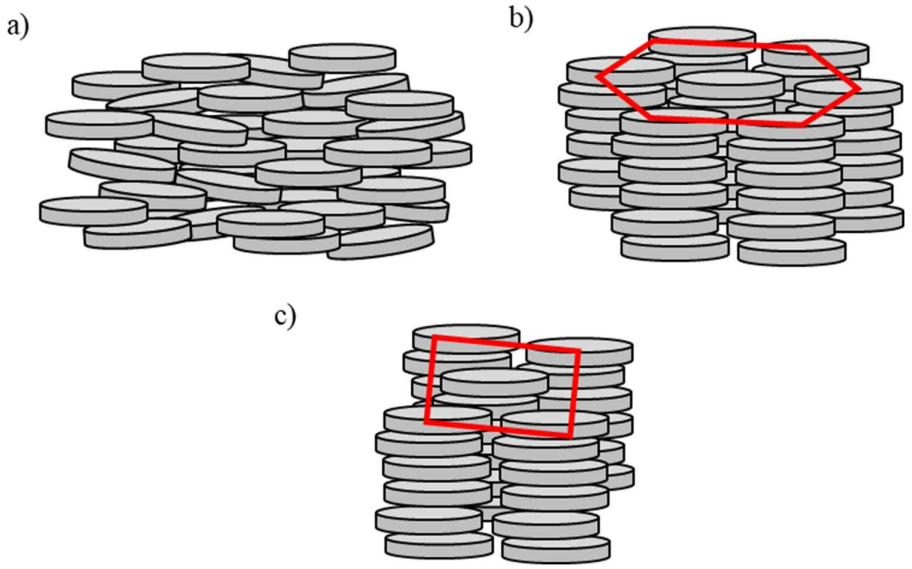

Figure 1.5: Schematic of the packing of discotic liquid crystal molecules: a) discotic nematic phase packing, b) hexagonal columnar packing, and c) rectangular columnar packing, where the red shape shows the packing structure.[3]

Bent core liquid crystals

Liquid crystal phases can also be formed by bent core molecules. The general structure of a bent core liquid crystal molecule is similar to that of a calamitic liquid crystal molecule, except the core unit has a bent molecular shape. The unusual structure of a bent core molecule leads to a variety of phases including smectic, columnar and *banana* (B) phases. These banana phases are specific to the bent core molecules.[7] Many different bent core structures have been investigated, such as structures with a rigid centre and flexible chains, illustrated in Figure 1.6 a), and hockey stick-like structures, illustrated in Figure 1.6 b).

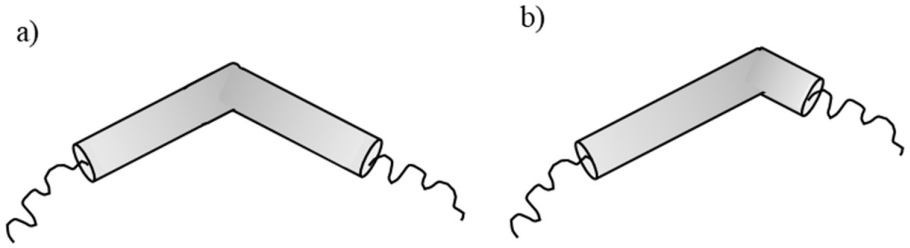

Figure 1.6: Schematic of bent core liquid crystal molecules: a) rigid centre with flexible side chains and b) hockey-stick like structure.[3]

Liquid crystal phase types

Liquid crystal phases exhibit different degrees of ordering, between the highly ordered crystalline state and the disordered isotropic liquid state, as shown in Figure 1.7. As the crystal is heated, the liquid crystal transitions through the different phases up to the isotropic liquid. The temperature at which there is a breakdown of the crystal lattice into a liquid crystal phase is called the melting point, and the temperature at which the lateral interactions breakdown and the liquid crystal phase transitions into the isotropic liquid is called the clearing point. On cooling, the order of the phase types is reversed and the transitions from the isotropic liquid to the liquid crystal phase is at a similar temperature to the clearing point. The phase sequence shown in Figure 1.7 gives an example of possible phases present, but the phases present are dependent on the molecular structures and packing of the molecules, for example the phase sequence for octylcyanobiphenyl (8CB) is:

Cr 21.5 °C **SmA** 33.5 °C **N** 40.5 °C **Iso**

In this notation, **Cr** and **Iso** represent the crystal and isotropic liquid, respectively, and the other labels represent the liquid crystal phases present with the values between showing the transition temperatures in °C. When the liquid crystal is cooled there can be supercooling, meaning that the crystallisation temperature from the liquid crystal phase to the crystal is lower than the melting point. In some cases, the liquid crystal phases may only be observed on cooling and not on heating, and where this occurs the phase is defined as monotropic as it is not present in the heating cycle. The details of these phases, and some variants of these phases containing chirality, are discussed further in this section.

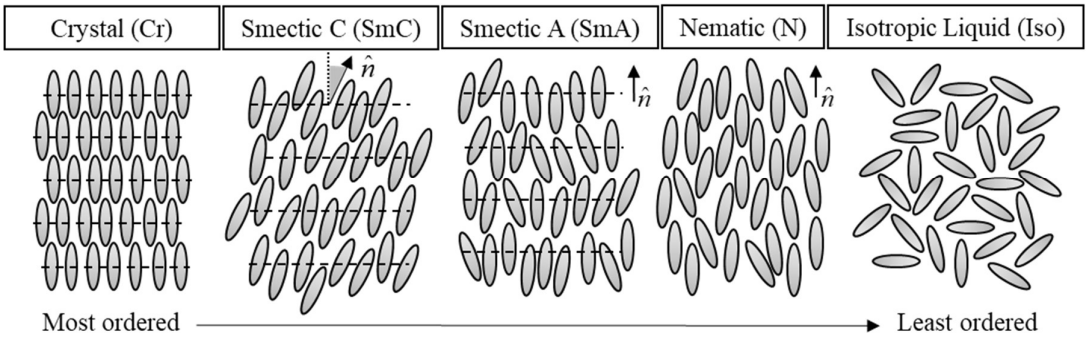

Figure 1.7: Liquid crystal phases from the crystal (most ordered) to the isotropic liquid (least ordered).

In liquid crystal phases that are not bulk aligned, the orientation of the molecules is not uniform, leading to the formations of domains. This formation of domains leads to characteristic textures for each type of liquid crystal phase, which can be observed through polarised optical microscopy. Bulk alignment can be induced with a variety of methods, such as mechanical rubbing of a glass slide with a polymer layer deposited on it,[8, 9] using ridges in the surfaces of the glass slides,[10, 11] or by binding molecules to the glass surface which induce a certain type of alignment into the bulk phase.[12, 13]

The distinct behaviour of a liquid crystal phase is observed due to the anisotropy of the molecules, where the structure of the molecule leads to the properties of the overall phase being different in different directions. This molecular structure results in the polarisability of the molecule being different in each direction, leading to a difference in the electric susceptibility parallel and perpendicular to long axes of the molecules in the phase. This difference in the parallel and perpendicular to the director leads to anisotropy in many other properties, such as dielectric permittivity (ε), refractive index (n) and other mechanical and magnetic properties as well.[3, 5]

Typically, for calamitic liquid crystal molecules the largest dielectric permittivity, which is a measure of the electric polarisability of the molecules, is parallel to the long axis of the molecules ($\varepsilon_{\parallel}$). For discotic liquid crystals typically the largest dielectric permittivity is perpendicular to the long axis of the molecules ($\varepsilon_{\perp}$), leading to the value of $n_{\perp}$ being larger than the value of $n_{\parallel}$, and so a negative birefringent phase. The dielectric permittivity difference can be considered as the dielectric anisotropy ($\Delta\varepsilon$), based on the difference of the dielectric permittivity parallel and perpendicular to the director, as shown in equation 1.2.[14] As a result of this anisotropy, if there is a positive dielectric anisotropy the director will tend to align parallel with an electric field, and if $\Delta\varepsilon$ is negative it will align perpendicular to an electric field. [3]

Equation 1.2 $$\Delta\varepsilon = (\varepsilon_{\parallel} - \varepsilon_{\perp})$$

The dielectric anisotropy also has an impact on light propagation in the liquid crystal phase, as the light parallel and perpendicular to the director of the phase propagates at different speeds. This difference in the speeds results in a bulk property known as the *birefringence* of the phase (Δn). It can be calculated using equation 1.3, based on the difference in the refractive index of the phases parallel ($n_{/\!/}$) and perpendicular ($n_{\perp}$) to the phase. The birefringence of the liquid crystal phases gives a visual indication of the type of phases present and it is a particularly critical property in the development of liquid crystal display applications.[15] As $n_{\parallel}$ is larger than $n_{\perp}$ for calamitic liquid crystals, there will be a positive value to the birefringence of the liquid crystal phase and for discotic liquid crystals the value of $n_{\perp}$ is larger than the value of $n_{\parallel}$, leading to a negative value of the birefringence.

Equation 1.3 $$\Delta n = n_{\parallel} - n_{\perp}$$

Nematic phase

The nematic (N) phase is the least ordered liquid crystal phase, and it composed of molecules that are positionally disordered but statistically the molecules are orientationally ordered with the long axes oriented along a net direction, known as the director ($\hat{n}$), as shown in Figure 1.8. This phase is uniaxial, meaning that $+\hat{n}$ and $-\hat{n}$ are indistinguishable, resulting in a disordered head-to-tail arrangement of the molecules.[15, 16] Generally, molecules have rotational symmetry about the director and there is no positional order within the phase, leading to the phase being ordered in only one dimension.[15]

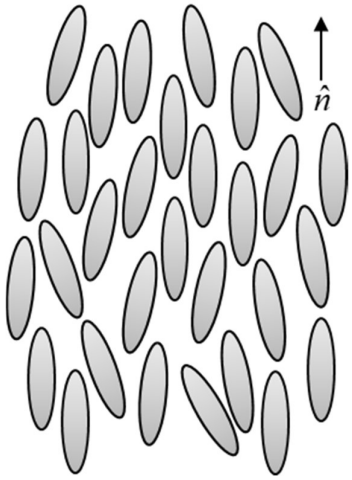

Figure 1.8: Schematic of the nematic phase, with the director ($\hat{n}$) pointing upwards.

The order of different liquid crystal phases can be quantified as an order parameter to gain a deeper insight into the phase, and it is dependent on the angle (β) the molecules make with the director of the phase (n̂). For uniaxial molecules, the full orientational distribution function, (f(β)) can be described using Legendre polynomials, given by equation 1.4, where $P_L(\cos\beta)$ is the L^{th} Legendre polynomial.[17, 18]

Equation 1.4
$$f(\beta) = \sum_{L=0}^{\infty} \frac{2L+1}{2} \langle P_L(\cos\beta) \rangle P_L(\cos\beta)$$

The orientational order parameter (S) is calculated using the second Legendre polynomial, where L = 2, but higher order polynomials can be used to improve the calculation of the order.[19, 14] The calculation of S includes an ensemble average, denoted by ⟨ ⟩, to take into account the angles of all the molecules within the system, as shown in equation 1.5. For a fully isotropic system, the orientational order parameter is 0 and for a perfectly ordered system the orientational order parameter is 1.[19] In the nematic phase the orientational order parameter typically lies between 0.4-0.7.

Equation 1.5
$$S = \langle P_2 \rangle = \left\langle \frac{1}{2}(3\cos^2\beta - 1) \right\rangle$$

The nematic phase exhibits a characteristic defect texture when viewed using a polarised optical microscope. When molecules are oriented with their long axes parallel to the glass surface of the microscope slide, known as a planar orientation, a *schlieren* texture containing 2- and 4- brush defects connected by defect lines are observed, as shown in Figure 1.9.[3, 20, 21] When the molecules are oriented with the long axis perpendicular to the glass surface of the microscope slide, known as a homeotropic orientation, the sample will appear optically extinct, as the molecules are being viewed along their optical axes. The nematic phase also has anisotropic flow properties, which can be defined by three viscosity coefficients (η_1, η_2, η_3). At higher temperatures the values of these coefficients decrease, which is observed due to the viscosity of the nematic liquid crystal phase decreasing as the temperature approaches the transition temperature into the isotropic liquid phase, known as the clearing point.[15]

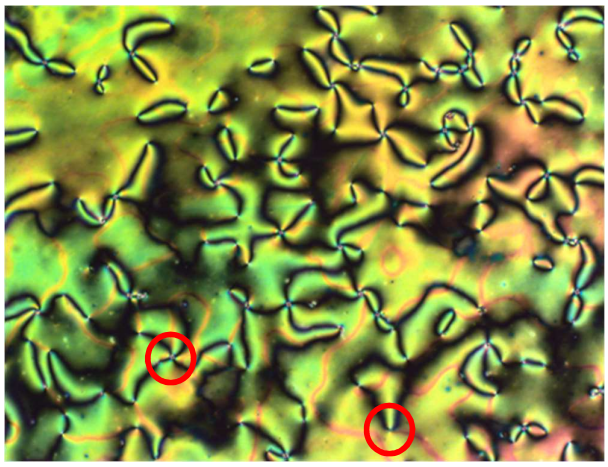

Figure 1.9: Example of a nematic (N) liquid crystal texture when viewed using a polarised optical microscope.[22] The red circles indicate the 2- and 4- brush defects present in the texture.

Chiral nematic (cholesteric) phase

A variant of the nematic phase is the chiral nematic (N*) phase, which exhibits many similar properties to the nematic phase but the important difference is that the component molecules, and resultant phase, are chiral. This phase is also known as the 'cholesteric (Ch)' phase, as it was initially observed in molecules derived from cholesterol, such as cholesteryl benzoate shown in Figure 1.10.

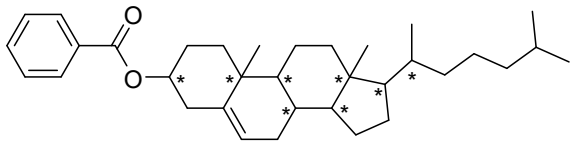

Figure 1.10: Structure of cholesteryl benzoate, * indicates a chiral centre in the molecule.

In the chiral nematic phase, locally the molecules still lack positional order and are on average oriented along the director, as in a normal nematic liquid crystal phase. However, the director rotates through the bulk to produce a helical arrangement whereby the helical axis of the phase is perpendicular to the director, as shown in Figure 1.11.[3, 23] The distance for the director to rotate through 360° is defined as the pitch and it can be left or right handed, depending on the inherent chirality of the constituent molecules. There is a temperature dependence of the pitch of the helix, whereby the pitch is short at high temperature and longer at lower temperatures.[5]

Figure 1.11: Chiral nematic phase structure. Source: User:Kebes/WikimediaCommons/CC-BY-SA-3.0[23]

When studied by polarised optical microscopy the chiral nematic phase can exhibit a variety of textures depending of the direction of the helical axis. For example, a planar or Grandjean texture is observed when the molecules are oriented parallel to the substrate, as shown on the left in Figure 1.12. A characteristic fingerprint texture is observed when the helical axis is parallel to the glass surface, as shown to the right in Figure 1.12. The chiral nematic can also exhibit a pseudo-focal conic texture, similar in appearance to that observed for smectic phases. The colour of the planar texture is related to the pitch of the phase.[3]

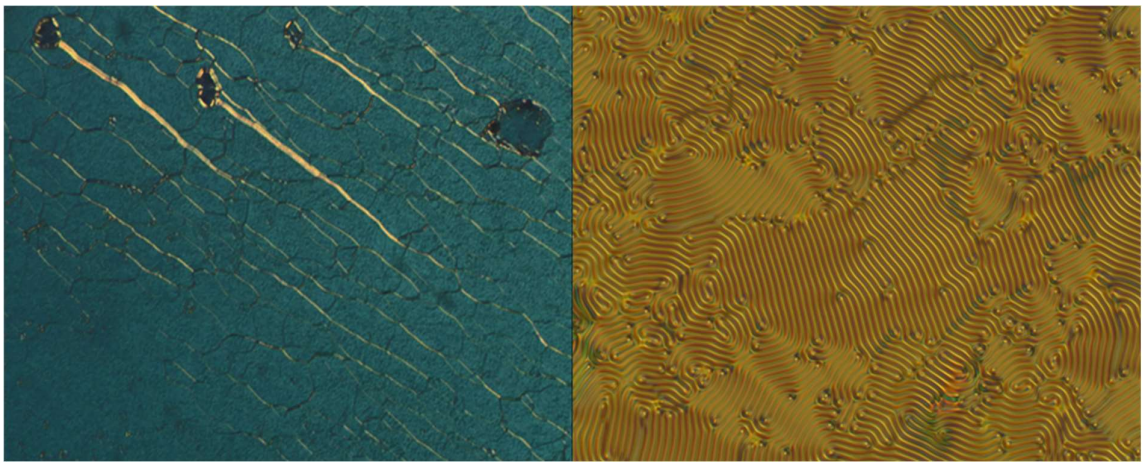

Figure 1.12: Example of chiral nematic (N*) liquid crystal textures when viewed using a polarised optical microscope, with: (L) Grandjean planar texture and (R) fingerprint texture.[22]

When synthesising chiral molecules to form chiral nematic liquid crystals, an easy synthetic route is to add the chiral unit into the terminal chain of a molecule that favours a normal nematic phase.[5] For example, Srinivasa reported a group of calamitic liquid crystalline molecules which exhibited chiral nematic phase behaviour when the structure of the molecules included a rigid core with one non-chiral chain and a chiral centre in the other chain.[24] In another example, Yoneya and Berendsen used computer simulations to model the chiral nematic phase of (+)-4-(2″-methylbutyl)-4′-cyanobiphenyl,[25] which used a chiral centre within the terminal chain of the cyanobiphenyl, as shown in Figure 1.14.

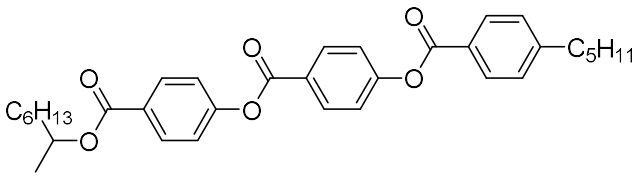

Figure 1.13: Structure of one of the chiral molecules studied by Srinivasa.[24]

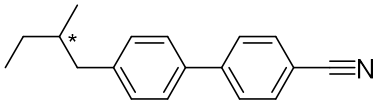

Figure 1.14: Structure of (+)-4-(2″methylbutyl)-4′-cyanobiphenyl studied through simulations by Yoneya and Berendsen,[25] * indicates a chiral centre in the molecule.

Smectic phases

Smectic liquid crystal phases are layered phases where the molecules exhibit some degree of positional order in addition to orientational order. There are many different smectic phases, which are differentiated by the extent of positional ordering of the molecules. The least ordered smectic phases are the A and C phases. In these phases, the molecules form weakly defined layers, where the layers form a one-dimensional density wave with respect to the centre of mass of each molecule.[26, 27] The molecules in these phases have no positional order within layers, and can diffuse between the layers. Many different variants of smectic phases have been discovered,[21] such as smectic F[28] and smectic I,[29, 30] phases but the most common types are the smectic A and C phases.

Smectic phases are exhibited in particular by molecular structures which are dichotomous in nature, for example with rigid, polarisable aromatic cores surrounded by more flexible, non-polar aliphatic groups and this difference drives the self-organisation into layered structures, in a process known as *nanophase segregation*.[3, 31] It has been observed that molecules containing aromatic or hetero-aromatic rings within the core of the molecule favour the formation of smectic phases. Molecules with polarisable cores often form smectic A and C phases.[32]

Smectic A phase

The molecules in the smectic A phase exhibit long range orientational ordering and form diffuse layers based on the average positioning of the centres of mass of the molecules. Within the layers the director (n̂) is parallel to the layer normal (k), meaning that the resulting phase is uniaxial, as shown in Figure 1.15. The distance between the diffuse layers is known as the smectic layer spacing (d). The value of this distance is dependent on the structure of the molecules in the phase,[16, 26] and on molecular packing between neighbouring layers.

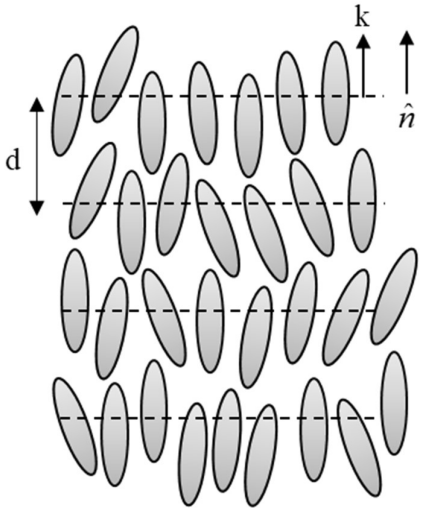

Figure 1.15: Schematic of the smectic A phase, with the director (n̂) pointing upwards. The layer spacing (d) is measured between the centres of mass of the molecules and the layer normal (k) is parallel to the director.

The molecules can be arranged in a variety of ways within the layers of the smectic A phase. The molecules can form a monolayer, known as SmA_1, where the molecules form a random head to tail arrangement within each layer and the layer spacing is defined by the molecular

length.[26, 27] If the molecules form a bilayer structure, known as SmA_2 with head and tail groups in opposite directions, with two separate layers forming, then the layer spacing will be two times the molecular length. This can occur as a result of strong head-head or tail-tail interactions. Many molecules form the smectic A phase where there is overlap of the molecules in neighbouring layers, known as *interdigitation*. These interdigitated smectic A (SmA_d) phases typically have layer spacing (d) between one and two molecular lengths.

When viewed using a polarised optical microscope, the smectic A phase exhibits a fan-like focal conic texture, accompanied by homeotropic regions, as shown in Figure 1.16. The focal conic texture is characterised by the ellipse and hyperbola defects, which appear as optically extinct lines which intersect, as shown by the red circle. The homeotropic regions appear optically extinct as the molecules are aligned with an average orientation perpendicular to the glass surfaces, so that the molecules are viewed along their optical axes.[33] The formation of smectic A phases is often favoured by a variety of molecular structures, including calamitic molecules with one terminal chain, such as in the example in Figure 1.1, and molecules with symmetrical polarisable units.[32]

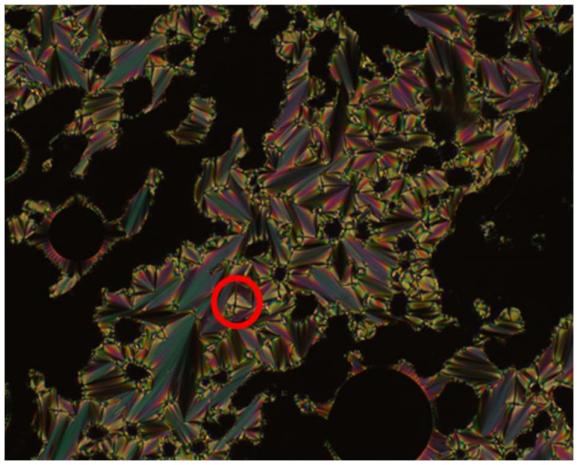

Figure 1.16: Example of the smectic A (SmA) liquid crystal textures when viewed using a polarised optical microscope.[22] The red circle indicate the optically extinct lines.

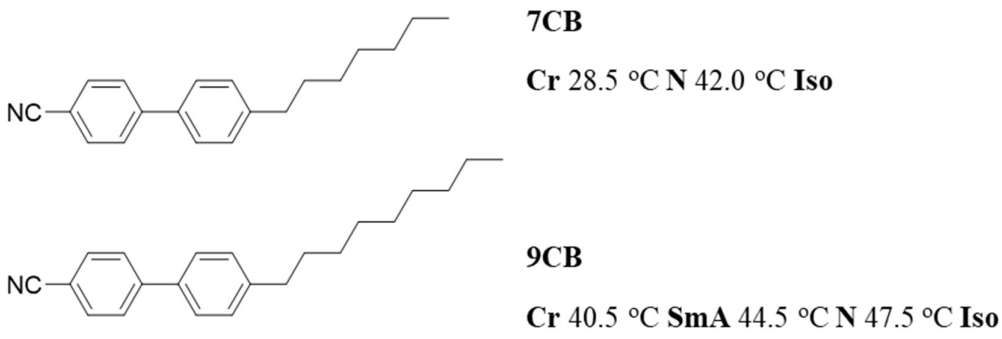

Figure 1.17: Examples of nCB molecules with increasing terminal chain length, (7CB and 9CB), with the phase transitions for each.[32]

Smectic C phase

The smectic C phase has a similar structure to the smectic A phase, but in the smectic C phase the molecular director ($\hat{n}$) makes an angle (θ) with respect to the layer normal (k) that is greater than 0°, as shown in Figure 1.18.[20, 24] The tilt in the smectic C phase is variable with temperature, with the exception of when it is formed directly from the isotropic liquid or nematic phase. As a result of the molecular tilt, the smectic C phase is biaxial.[3]

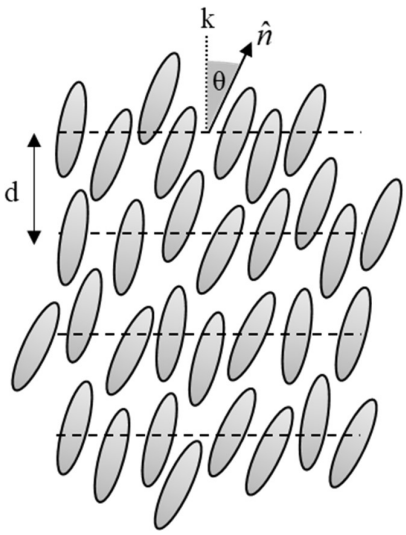

Figure 1.18: Schematic of the smectic C phase, with the layer normal (k) pointing upwards and director ($\hat{n}$) following the tilt of the phase. The layer spacing (d) is measured between the centres of mass of the molecules and is at an angle (θ) greater than 0° with respect to the layer normal.

The smectic C phase can be favoured by molecules which have asymmetry in the polar core and with molecules which have two aliphatic chains of a similar length. Also, molecules that have terminal end groups which cannot hydrogen-bond can tend to form a tilted phase.[32] The molecules within smectic C layers are locally hexagonally close-packed, but the order is extremely short range. The tilt orientational order is preserved over longer distances resulting in overall C_{2h} symmetry for the phase.[27, 32] The layer spacing (d) in the smectic C phase is related to the tilt angle (θ) of the phase, and if the tilt angle decreases to zero with increasing temperature it will result in a transition into the smectic A phase. The smectic C phase can also form a chiral variant of the structure, where the director of the phase rotates in each layer resulting in a spiral twist in the director.[5] This will occur with chiral molecules that exhibit a smectic C phase, and as with the chiral nematic phase the pitch length is temperature sensitive. Due to this sensitivity these types of phase can be used in sensing applications, and they may be used in fast switching devices.[33]

When viewed using a polarised optical microscope the smectic C phase exhibits two defect textures, a broken fan-like focal conic texture and a *schlieren* texture which only exhibits 4-brush defects, as shown in Figure 1.19. If the smectic C has formed upon cooling from a smectic A phase then the focal conic texture is preserved and becomes the broken fan texture as tilt domains form within the focal conic and *schlieren* texture appears in the homeotropic domains.

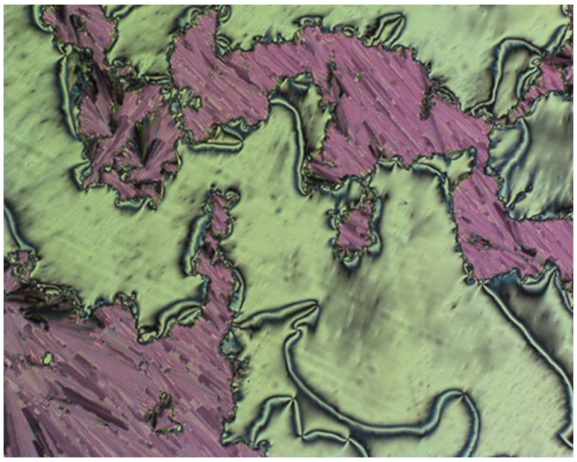

Figure 1.19: Example of smectic C (SmC) liquid crystal textures when viewed using a polarised optical microscope.[22]

1.1.2.2 Lyotropic liquid crystals

The second general category of liquid crystals is *lyotropic* liquid crystals in which the molecules form liquid crystal phases only when in a solvent, making them dependent on concentration and type of solvent. Lyotropic liquid crystals were initially observed by Virchow in 1854, in biological systems of myelin in water,[3] which predated the classification of the thermotropic liquid crystal by Reinitzer. These molecules are amphiphilic and contain a hydrophobic unit attached to a hydrophilic unit. This dichotomy drives self-organisation of the molecules within a solvent to minimise contact with the unit with the least affinity to the solvent. The behaviour of these molecules will depend on the polarity of the solvent, for example in a polar solvent the hydrophilic groups will form a boundary to reduce contact between the hydrophobic units and the solvent, and in a non-polar solvent the opposite will occur. This segregation of parts of the molecule can lead to the formation of many different phase structures such as layers (lamellar), as shown in Figure 1.20, columns (hexagonal), and spheres (cubic), which can pack into more complex bicontinuous phases.[34]

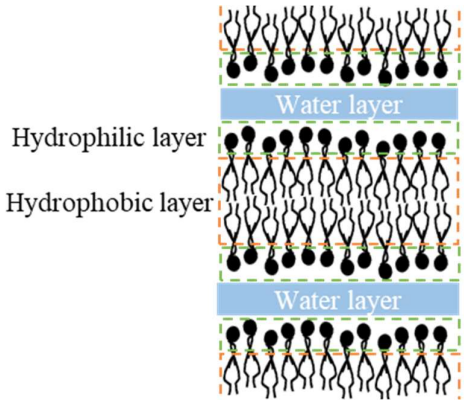

Figure 1.20: Example of lamellar lyotropic liquid phase, adapted from Collings and Goodby.[3]

Lyotropic liquid crystals are found in many biological systems, for example Steim et al. observed liquid crystalline behaviour in the membranes of bacteria which was identified through the use of calorimetric measurements of the mesophase transitions.[35] These properties can also be used to design molecules which exhibit complex liquid crystal phases such as by Schröter et al.,[36] who used the principles of lyotropic liquid crystal molecules, as shown in Figure 1.21, to form novel rigid core molecules which exhibited columnar phases when in combination with water as the solvent.

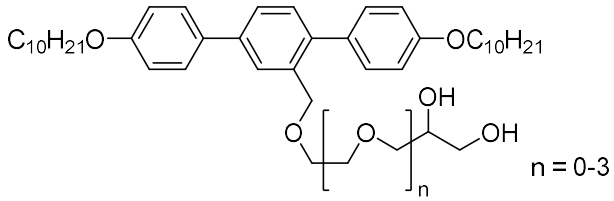

Figure 1.21: Structure of the lyotropic liquid crystal molecules studied by Schröter et al. [36]

Amphitropic molecules can exhibit thermotropic liquid crystal phases when heated in the absence of a solvent and also lyotropic liquid crystal phases when combined with a solvent.[3] For example, Hung et al. developed a derivative of cinnamic acid and cholesterol, shown in Figure 1.22, which displays a thermotropic chiral nematic liquid crystal phase and also self-assembled into helical structures upon addition of toluene, chloroform, THF or dichloromethane as a solvent. This behaviour would make this type of material useful in sensing applications.[37]

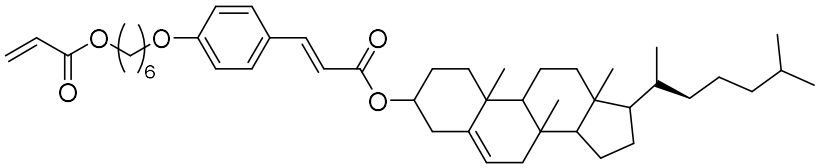

Figure 1.22: Structure of the amphitropic liquid crystal molecules studied by Hung et al. [37]

1.1.3 Applications

The main applications of liquid crystals are in displays, which can use many different liquid crystal phase types.[38, 39] Nematic liquid crystals have found use in scattering displays, where the disordered positions of the molecules scatter light and cause an opaque state,[40, 41] in guest-host displays[12, 42, 43] where a dye is added to provide colour, and in twisted/super-twisted nematic displays.[44-46] Smectic liquid crystals have also been used for scattering displays,[47] guest-host displays and also for memory devices, which can retain images or text in the absence of an electric field.[48, 49] Smectic devices have the additional benefit that they can be bistable, so do not need the constant addressing with voltage to maintain an oriented state, that nematic devices typically require. As a result, Gardiner et al. noted that smectic devices have the benefit of being a low power alternative to nematic devices.[50] Further detail on the uses of liquid crystals in displays will be discussed in section 1.2.

Due to the optical properties of nematic liquid crystals, they have found a novel application in variable focal length lenses for people with sight issues. Sato proposed the formation of lenses which contained surfaces, which were rubbed to obtain a consistent alignment of the nematic liquid crystal, such as the example given in Figure 1.23.[51] It was found that the focal length of the lens could be varied using an electric or magnetic field. The issue with these lenses is that the response time was slow as the lens had to be thicker than may normally be used for liquid cells to obtain the needed focal length.[51] Since this initial design, many other types of lens containing various types of liquid crystals have been designed to improve on the limitations of Sato's design.[52] These lenses have found use in both imaging and more varied applications, like optical trapping[53] or light concentration in photovoltatics.[54]

Figure 1.23: Example of structure of liquid crystal lens proposed by Sato.[51]

In another application, Dolgaleva et al. used a chiral nematic liquid crystal to act as a resonator for a laser, using a nematic liquid crystal with a chiral dopant to create the chiral nematic phase.[55] It was found that the dye-doped chiral nematic liquid crystal had stable output radiation and that the particular dye and liquid crystal system worked better than other more commonly used dyes.

Liquid crystal molecules have also been used in bio-sensing applications, for example Brake et al. used 4′-pentyl-4-cyanobiphenyl (5CB) aligned on coated glass to sense phospholipids.[56] The aligned liquid crystals appeared bright in the presence of water and as the phospholipids interacted with the surface of the liquid crystal, the orientation of the molecules changed resulting in the bright appearance being extinguished. Liquid crystal surfaces have also been used to probe the preferred binding orientations of ribonuclease on a surface. It was found that by starting with a liquid crystal aligned on a gold surface, when the protein binds to the surface there are different disruptions of the liquid crystal

depending on the orientation of the ribonuclease, as illustrated in Figure 1.24.[57] This results in different textures observed in the polarised optical micrographs which allowed for different orientations of the ribonuclease to be identified.

Liquid crystals have also been used in many other applications such as tuneable filters,[58] cancer tissue sensing,[59] and thermography, which indicates differences in heat signatures in tissues such as hands, knees or feet.[60]

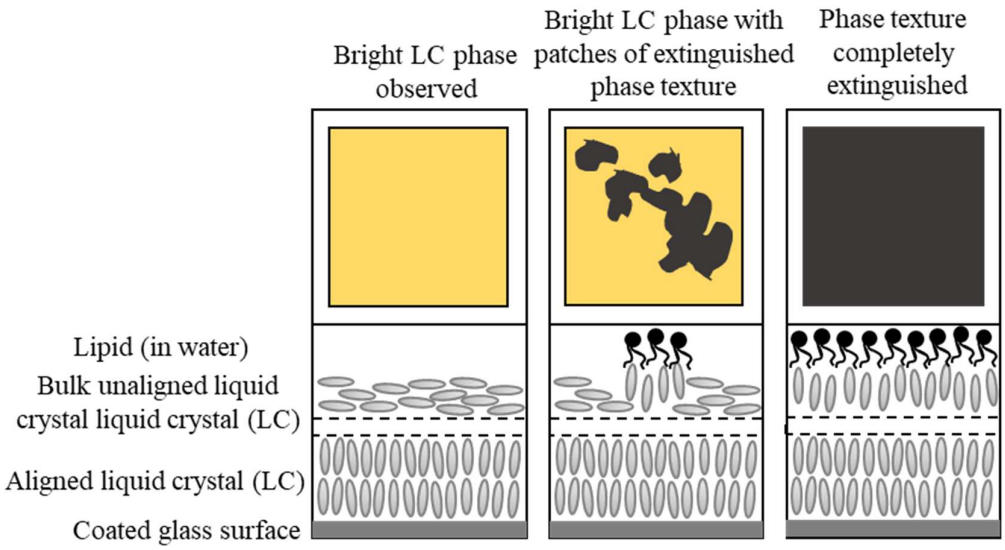

Figure 1.24: Illustration of the preferential ribonuclease bonding effect observed by Luk et al.[57] The top squares show representations of the liquid crystal textures observed, and below is the molecular arrangement at each of these states.

1.2 Guest-host devices

1.2.1 Background

In the early 1960s, it was observed that there was a drop in the light intensity transmitted through a cell containing a liquid crystal on application of an electric field to the cell. In the presence of the electric field, a nematic texture is formed which causes the light to blocked.[40, 61] This study illustrated the ability of liquid crystal phases to reorient under an electric field, which opened up the possibility for this to be used in display devices, including guest-host devices as demonstrated initially by Heilmeier and Zanoni.[42]

Heilmeier and Zanoni also studied this electro-optic effect on a guest-host mixture, which used a nematic liquid crystal as the host and Methyl Red, an azo dye with the structure given in Figure 1.25, as the dye guest.[42] In this parallel plate set-up, shown in Figure 1.26, in the 'off' state the dye is randomly oriented within the liquid crystal domains, and when the field is applied the dye molecules are reoriented with the liquid crystal host, there is a colourless appearance.[42, 62] Although this display shows interesting properties, it can have some issues with low contrast between the two states and they are not well suited to use in more complex systems. This system also included a polariser, which limited the brightness of the display.[62]

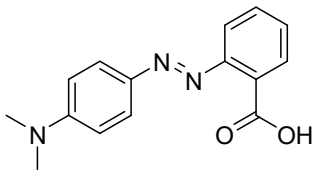

Figure 1.25: Structure of the azo dye, known as Methyl Red, used by Heilmeier and Zanoni[42].

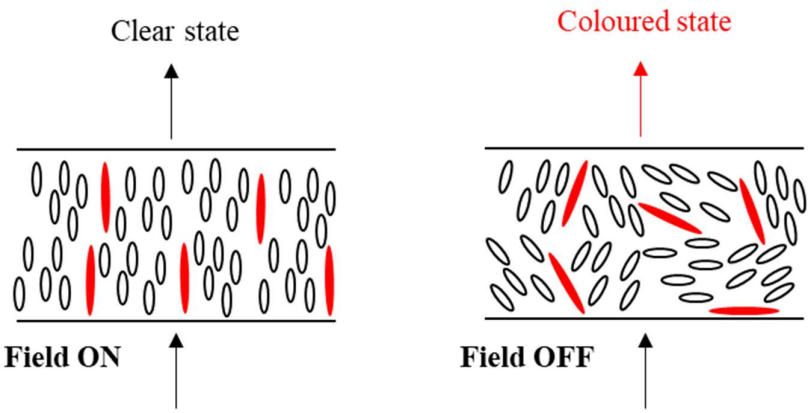

Figure 1.26: Schematic of the Heilmeier and Zanoni display where: (left) field ON, display appears colourless, (right) field OFF, display appears red.[42]

After these initial devices, many different guest-host mixtures have been studied, in particular with different liquid crystal phases. White and Taylor worked to improve on the Heilmeier and Zanoni display, by using unpolarised light and changing the dye to improve the contrast between the on and off states of the display.[12, 62] This system used the phase change between a nematic and chiral nematic liquid crystal, and required an optically active dopant for the switching to occur.[12]

Smectic A liquid crystal devices typically have two states, a disordered focal conic state which scatters light off the fine defect texture and an electrically induced reoriented state where molecules orient with the field, which is non-scattering, as shown in Figure 1.27.[48] Different types of smectic liquid crystal molecules have been used in these applications, such as siloxanes and cyanobiphenyl molecules.[63, 64] Both types of molecules have positive dielectric anisotropy, which allows the molecules to orient with the applied field at one frequency and reorient to the scattering texture at a different frequency of the applied field.[65]

These devices are notable because after the initial application of the electric field to reorient from the clear to the scattering state, it can be removed and the scattering state remains. The device is stable in both states, and so is described as *bistable* and this bistability leads to these devices being called smectic A memory (SAM) devices.[48] This bistability was also demonstrated by Fritsch et al., who found that clear and scattering states persisted on removal of the field for carbosilane terminated liquid crystals, shown in Figure 1.27.[66, 67] It was also observed that after leaving the device in the clear state for 6 months there was a less than 0.5 % decrease in the transmittance of the state.[68] These liquid crystals have been applied in flexible liquid crystal displays, which have good flexibility and stability, and also good contrast between the scattering and clear states.

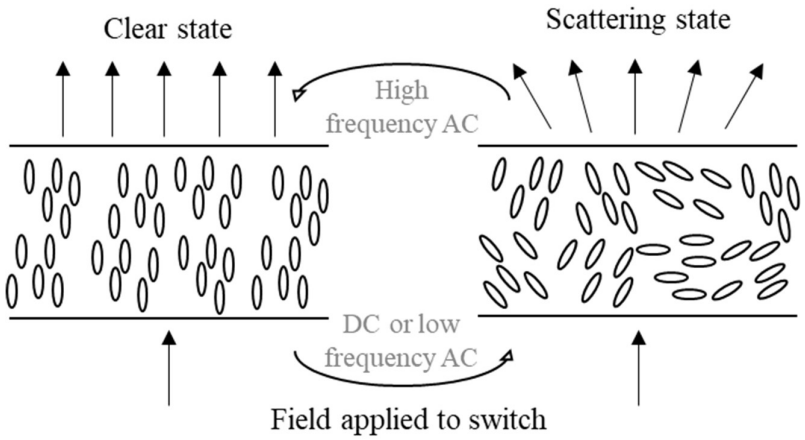

Figure 1.27: Diagram of the clear and scattering states of a smectic A device, which are switched using an electric field. Adapted from diagrams from Gardiner et al. and Bahadur.[63, 69]

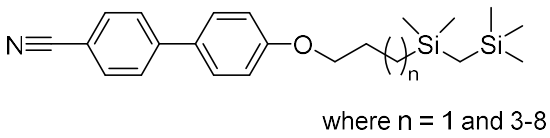

Figure 1.28: General structure of carbosilane terminated alkoxycyanobiphenyl used by Fritsch et al.[68]

Smectic scattering devices may require an ionic dopant to disrupt the smectic layers and aid in switching between the states.[48] Generally, smectic A devices use substituted ammonium salts, which disrupt the diffusely layered structure of the smectic A phase and change the conductivity of the mixtures to aid in dynamic scattering.

1.2.2 Guest dyes

A wide range of dyes have been used as the guests within guest-host mixtures, with the two main types being azo and anthraquinone dyes. These, and other dyes, have many varied properties, making them suited for different guest-host mixtures and applications.

1.2.2.1 Dye properties

The dye properties that are most relevant for guest-host applications can include the dye stability, solubility, and the molecular alignment with the liquid crystal host, as well as the absorption wavelength and the alignment of the transition dipole moment of the dye within the dye molecule. When these properties are carefully selected, it will lead to the best function for the desired applications.

Purity

In dye synthesis, it is essential to have effective purification, because symmetrically, asymmetrically, mono- and un-substituted variants of a dye will all behave differently, which would lead to a lack of clarity in the properties exhibited by the dye mixture.[70] Using a pure dye will lead to well defined properties and clearly exhibit the desired properties.

Stability

For display applications it is important that the dye has good photochemical and chemical stability, to avoid degradation by light or redox reactions, for example with ionic impurities. Some dyes, such as Schiff bases, can undergo rapid oxidation, leading to degradation of the dye.[71] In terms of photochemical stability, it has been widely observed that azo dyes can have poor stability[72] and, particularly in the case of blue and violet azo dyes, are prone to degradation over time.[73, 74] Anthraquinone dyes have been found to have better stability,[75] although they have other properties that are less favourable than those of azo dyes. Jones and Reeve found that azo type dyes experienced photo-reduction by hydrogen abstraction and that anthraquinone dyes had slower photo-degradation.[76]

Solubility

The solubility of the dye in the liquid crystal host is important, to obtain a suitable concentration of the dye within the host and achieve the desired depth of colour, to avoid faint colour in the device. The solubility is linked to the melting point temperatures of the dyes, but there are no clear trends within a series of homologous dyes. Azo and anthraquinone dyes show the best solubility out of the main dye types, and anthraquinone dyes generally show lower solubility than azo dyes.[71] The use of different substituents within the dyes has been shown to improve solubility, for example amino anthraquinones were found to have increased solubility relative to thioether anthraquinones.[71, 77]

Order parameter and dichroic ratio

It is important that the alignment of the dye molecules within the liquid crystal host is good and that the transition dipole moment of the dye is well aligned with the long axis of the dye molecules. The order of the dye molecules in a liquid crystal host can be quantified, by calculating the extent of the alignment of the molecular long axis of the dye molecules with respect to the liquid crystal director ($\hat{n}$).[14] The orientational order parameter (S_θ) of the dyes is calculated in the same way as for liquid crystal alignment, using equation 1.5, where θ is the angle between the long axis of each dye molecule and the director.[12, 78] If the dye molecules are perfectly aligned with the host director then $S_\theta = 1$, and if the orientation is random then $S_\theta = 0$.[72]

In some molecules the transition dipole moment of the dye and the molecular long axis will not align perfectly, leading to a further angle, β. This angle is illustrated in Figure 1.29, and an order parameter for the alignment of the transition dipole moment with the molecular long axis of the dye, calculated using equation 1.6.

Equation 1.6 $$S_{\beta} = \left(\frac{1}{2}\left(3\cos^2\beta - 1\right) \right)$$

Figure 1.29 shows the overall director determined by the host, and the dye order parameter that determined by the angle between the transition dipole moment of the dye molecules and the host director. This overall order parameter (S_{ϕ}) including the β angle can be calculated using equation 1.7.[79] This angle between the long axis and the transition dipole moment can lead to poorer alignment of the transition dipole moment and the director, which leads to a lower order parameter. The angle β between the transition dipole moment and the long axis of the dye molecule can be due to many factors, such as the shape of the dye used.[78]

Equation 1.7 $$S_f = S_{\theta}.S_{\beta} = \left\langle \frac{1}{2}\left(3\cos^2\theta - 1\right) \right\rangle . \left(\frac{1}{2}\left(3\cos^2\beta - 1\right) \right)$$

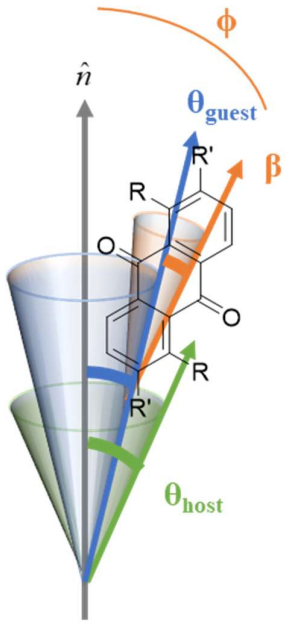

Figure 1.29: Diagram illustrating a general guest anthraquinone dye within a liquid crystal host. The long molecular axis of the guest dye and the transition dipole moment (TDM) is shown in orange, along with the two angles formed by these two axes of the molecule relative to the director of the liquid crystal (n̂).

If there is high order of the dye molecules in an aligned guest-host system, the dye is well aligned with the liquid crystal and will absorb light strongly in a device, when the bulk sample is oriented appropriately.[80] If the dye order parameter in the liquid crystal and the order parameter of the liquid crystal alone are compared it can be seen the extent to which a dye guest is impacting the packing of the host.[81]

The orientation properties of dyes can be elucidated using polarised UV-visible absorption spectroscopy. Using the absorbance data, a dichroic ratio (DR) can be obtained via equation 1.8, using measurements of the absorbance parallel ($A_{\parallel}$) and perpendicular ($A_{\perp}$) to the director of the bulk aligned sample.[80, 82] The dichroic ratio is related to the order of the dye within the liquid host and the overall properties of the device depend on the dichroic ratio.[78]A high dichroic ratio indicates good alignment of the liquid crystal host and the dye molecule.[82] The absorbance measurements also allow the calculation of the experimental order parameter of the dye in the host (S), using equation 1.9, [80, 82, 83] and where this order parameter equated to S_{ϕ} in equation 1.7.

Equation 1.8
$$DR = \frac{A_{\parallel}}{A_{\perp}}$$

Equation 1.9
$$S = \frac{\left(A_{\parallel} - A_{\perp}\right)}{\left(A_{\parallel} + 2A_{\perp}\right)} = \frac{DR - 1}{DR + 2}$$

1.2.2.2 Dye types

Azo dyes

Azo dyes are synthetic dyes that contain the R-N=N-R′ functional group, where R and R′ are substituted aryl groups, as shown in Figure 1.30. Azo dyes are commonly used dyes because they give intense colour, which arises from electron delocalisation that occurs across the azo group and the aromatic rings of the dye.[72] Azo dyes have a yellow to red colour,[84] but adaptions to the structure of the azo molecule can lead to a wide range of different colours, by alteration of the energy of the transition occurring.[72, 74] For example, by switching the end group from an alkoxy chain to a pyrrole, the colour of an azo dye can be tuned to form a purple dye with the change of one substituent, as shown in Figure 1.31.[74] In another

example, White and Taylor made alterations to the azo dyes used in a guest-host system by changing the electron-donating and -withdrawing ability of one or both of the terminal groups, and they derived an azo dye from 5-nitro-2-aminothiazole, which gave a blue dye, in a similar manner to Seki et al.[12, 74] Alteration of one or both of the terminal groups tuned the absorption wavelength of the dyes in the range 415- 620 nm, giving a range of colours in the liquid crystal host.[12]

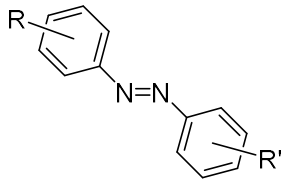

Figure 1.30: Example of basic azo dye structure, where R and R′ are substituents on the aryl rings, and R and R′ could be identical or different.

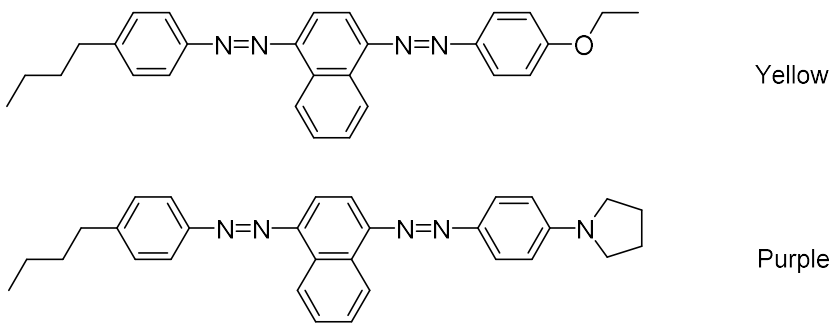

Figure 1.31: Structures of two dyes studied by Seki et al., with the change in colour as result of changing the alkoxy chain to the pyrrole group.[74]

It was also noted that addition of an electron-withdrawing group and an electron-donating group at opposite ends of the azo dye molecule led to an increase in the maximum wavelength absorbed. This also produced a dye with a blue-purple colour, but it was found that there was a lowering of the dichroic ratio and an overall decrease in the order of the particular azo dye used.[74] It has been observed that the addition of lateral groups and large terminal groups can cause steric repulsion, which may prevent an azo dye from aligning in the 8CB and 8OCB liquid crystals as reported in this work, which exhibit nematic and smectic phases.[83] The nature of the terminal groups can affect the interaction between the guest dye and the host liquid crystal, for example where the presence of a terminal $–NO_2$ group caused the order parameter of a dye within a cyanobiphenyl liquid crystal host to

decrease. It was proposed that the polar terminal group can feel a repulsive interaction from the –CN group in the liquid crystal host, resulting in poorer packing of the dye and liquid crystal molecules and a lowering of the order parameter of the guest.[83]

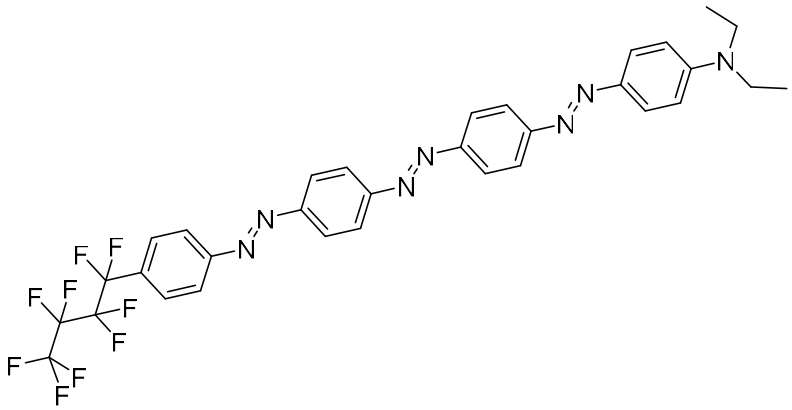

Figure 1.32: Elongated structure studied by Matsui et al. [84]

Azo dyes have been widely used in display applications, due to the previously mentioned rod-like shape. This shape often gives good alignment of the transition dipole moment with the long axis of the dye molecule,[72] and the dye molecules are also able to align well with the host molecules. The addition of substituents can widen the dye molecules and may result in a reduction in the rod-like nature of the azo dye and poorer packing.[74] Dyes with multiple azo bonds can form elongated structures, increasing the length to width ratio which can give higher order parameters. A triazo linked dye, with the three azo linkages locking the structure into an all-*trans* conformation, as shown in Figure 1.32, had an elongated structure which aligned well with the nematic liquid crystal host and had an order parameter in the range of 0.79-0.82.[84]

Anthraquinone dyes

Anthraquinone dyes contain a structure of three fused six-membered rings, with carbonyl groups on the central ring,[85] within the dye structure, as shown in Figure 1.33. They have been used as an alternative to azo dyes, particularly because they tend to be more stable in the presence of light. Like azo dyes, anthraquinone dyes can be tuned to a range of colours using different substituents, but they are less rod-like in shape, which can result in lower

dichroic order parameters when utilising these dyes within guest-host systems. The parent anthraquinone molecule absorbs principally in the UV-region and is only weakly coloured.[85] Substituted anthraquinone dyes can absorb across the visible region, dependent on the substituents, although they generally have lower absorption coefficients than azo dyes, leading to less intense colour in a display.[85] They can also have relatively low solubility, particularly in fluorinated liquid crystals.[72, 86]

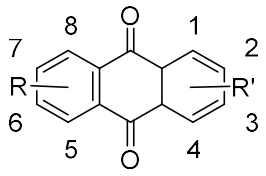

Figure 1.33: Example of basic anthraquinone dye structure, where R and R′ are substituents on the aryl rings, and R and R′ could be identical or different. The substituent position numbers are given in a clockwise direction.

In terms of symmetric dyes, Saunders et al. found that the substituent position was important, and notably found that 2,7-substitution on the aromatic ring system gave comparable solubility and order parameter to 2,6-substituted anthraquinone dyes with unsymmetrical substituents.[87]

It has been observed that asymmetrically substituted anthraquinone dyes generally have better solubility than symmetrically substituted ones, but require more complex syntheses to obtain. For example, the solubility of a series of asymmetrically substituted anthraquinone dyes was found to be higher than similar symmetrically substituted dyes, even down to temperatures of -5 ^{o}C; this solubility was similar to a comparable dye with elongated alkyl chains as substituents, which is a commonly used technique for improving solubility.[86, 87] Saunders et al. also noticed that asymmetry in anthraquinone dye molecules hindered crystallisation of the dye from the liquid crystal host in the nematic phase and gave higher order parameters in the liquid crystal host.[87]

The type of substituents can have a clear effect on the properties observed, such as a change to a substituent with a lower electron-donating character leading to a shortening of the wavelength of light absorbed by the dye.[88] Substitutions in the 1,5- position have been shown

to have clear effects on the colour exhibited by the dyes, such as the change from sulphur-based substituents to nitrogen-based substituents resulted in a change in the colour of the dye from yellow to red. It was also observed that the addition of OH groups in the 4,8-positions of a 1,5-substituted dye caused the dye to appear blue, as illustrated in Figure 1.34. The more electron-donating substituents caused a decrease in the energy of the transition, resulting in a red-shift in the absorption maximum, for example the use of an –OH substituent, which donates electron density through a mesomeric process, caused a shift of greater than 100 nm in the absorption maximum of the dye.[89] This illustrates that very simple changes to the anthraquinone structures can lead to significant changes to the dye properties.

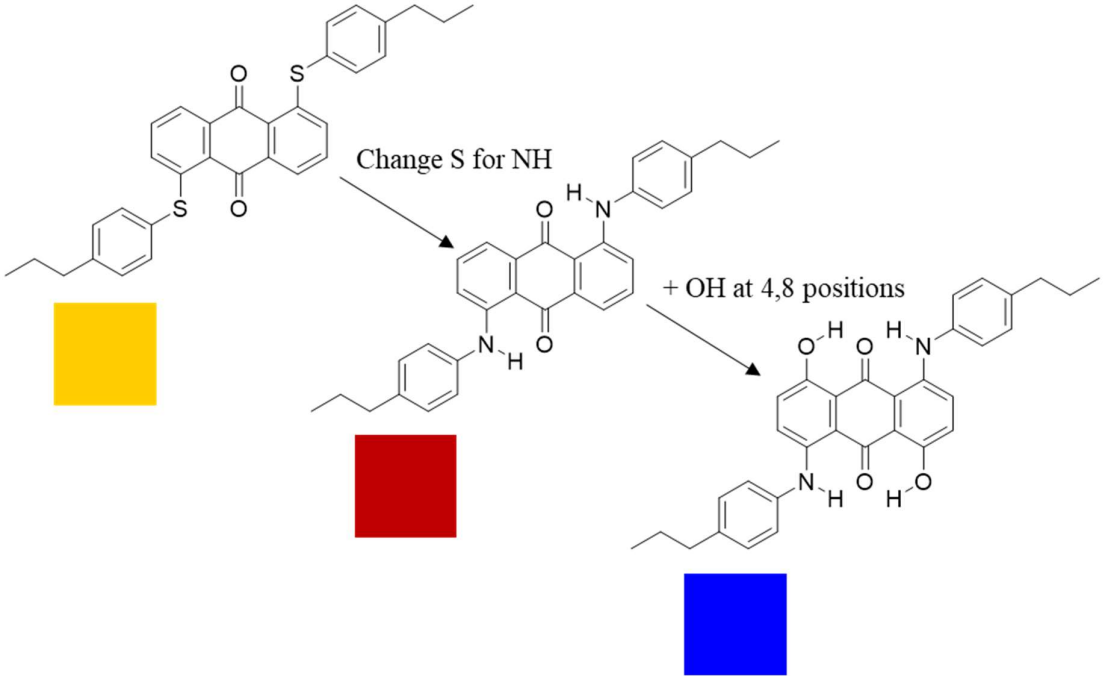

Figure 1.34: Molecules synthesised by Sims et al. shows the changes in substituents and the resulting colour of the solutions inca. 2×10^{-4} mol dm^{-3} in *p*-xylene.[89]

In addition, Iwanaga et al. observed that the type and position of the substituent could have a clear impact on the properties observed.[86] By placing a $–CF_3$ group para to a thiophenyl substituent on the anthraquinone core, as shown on the left in Figure 1.35, there was a shorter maximum absorption wavelength and a smaller molar absorption coefficient. When the $–CF_3$ group was placed in the meta position on the same ring, as shown on the right in Figure 1.35, there was no impact on the optical properties and the improvement in solubility and the high dichroic ratio of the non $–CF_3$ substituted dye was retained. The $–CF_3$ group itself

was predicted to induce a local dipole moment in the anthraquinone dye molecule due to the large electron-withdrawing ability it possesses. This effect would be expected to increase interactions between the dye molecules and lower the solubility in a liquid crystal host. This was not observed, and instead it was theorised that this dipole may provide favourable interactions with the host.[86] It has also been noted that asymmetrically 1,5-substituted anthraquinone dyes were less linear with poor packing, and hence may not be suitable as liquid crystal dyes.[70] These examples highlight the importance of molecular design and positioning of substituents and the large impact this can have on the properties of the dye.

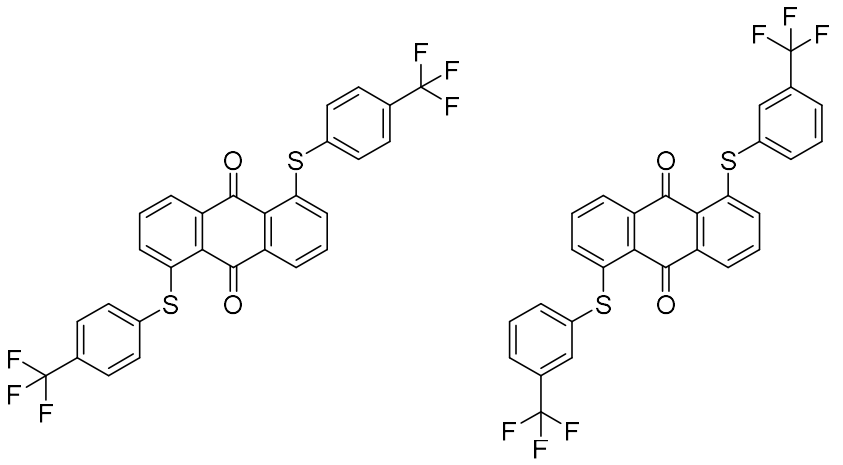

Figure 1.35: Structures of thiophenyl substituted anthraquinone studied by Iwanaga et al.,[86] with CF_3 group in the: (L) para position and (R) meta position.

As anthraquinone dyes are not as rod-like as azo dyes, there is a concern that they will not be well aligned with the host liquid crystals.[79] Similarly to the azo dyes, the aspect ratio of the dye can be important to ensure good alignment of the dye within the host system. For instance, a short dye with poor flexibility may not be able to find the correct conformation to pack efficiently within the liquid crystal and it will disrupt the local order. This has been suggested to be due to the molecules of liquid crystal and dye being more closely packed when not in the isotropic phase, meaning that dipole-dipole interactions and the molecular conformation become especially critical.[75] Although the aspect ratio can be increased to improve alignment, such molecular designs can reduce solubility and may lead to slow switching when used in a display.[72]

As mentioned previously, the alignment of the transition dipole moment with the long axis of the dye is also important to the dichroic ratio of the guest-host mixture. Sims et al. reported that 2,6- substituted anthraquinones had high aspect ratios and small angles between the long axis and the transition dipole moment.[89] These properties gave good order of the dye within the host, leading to a high dichroic ratio.[90] Alternatively, 1,5-substituted species using nitrogen based substituent had smaller aspect ratios and a larger angle between the transition dipole moment and the long axis,[89] leading to lower dichroic ratios.[90] These 1,5-substituted dyes had a larger angle between the transition dipole moment and the minimum moment of inertia axes of the dyes than the 2,6-substituted dyes, which may have resulted in the lower dichroic ratios and order parameters observed.[79]

Other dyes

Although azo and anthraquinone dyes are most widely used in guest-host systems, other dyes can also be used. Bauman and Wolarz utilised a perylene-based dye with ester side chains, as shown in Figure 1.36, as a guest with 8OCB as the host liquid crystal, which exhibits nematic and smectic A liquid crystal phases.[91] Chain lengths of 4, 5 and 7 carbon atoms were studied, and it was observed that the longer chain dyes gave the higher dye orientational order parameters, determined by absorbance measurements. This improvement was attributed to the favourable interactions of the alkyl chains of the dye with the alkyl chains of the liquid crystal host. Other studies of these dyes found that the dyes with the longest alkyl chain had the highest solubility. It was also found that a similar perylene dye with a cyclohexane group in the place of the alkyl chain had similar solubility to the longer chain lengths studied by Bauman and Wolarz, along with a higher orientational order parameter and improved stability under UV light.[92]

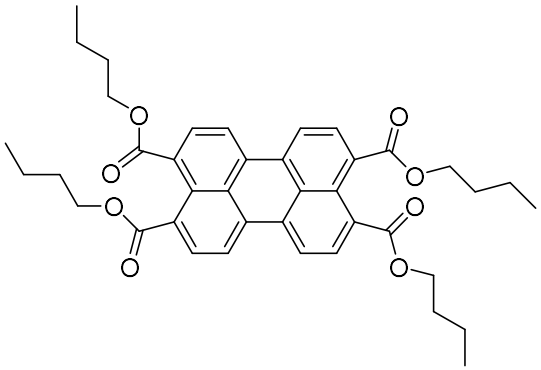

Figure 1.36: Example of the one of the perylene dyes studied by Bauman and Wolarz.[91]

Many other chromophores have been used in the production of dyes for guest-host systems, such as azulenes,[93] indigo dyes, thioindigo dyes,[94] and many other types, with example structures given in Figure 1.37.

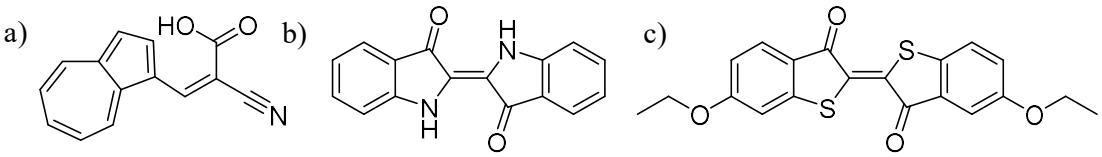

Figure 1.37: Example structures of other dye chromophores, a) azulene dye,[93] b) indigo dye molecule,[71] c) thioindigo dye molecule.[94]

1.2.3 Host liquid crystals

Many types of liquid crystal molecules have been used as hosts in guest-host systems, with some designs using nematic hosts in both non-twisted [41, 42] and twisted states.[12, 43] The design of the host is important for the type of display and also for the compatibility with the dye. While a large body of work on guest-host systems has studied nematic hosts, smectic liquid crystal hosts are much less studied but are a promising area due to the possibility of using them to create bistable devices,[63] arising from the relative stability of the layer phase structures.[48]

1.2.3.1 Smectic A hosts

Types of smectic A host – i.e. Siloxane containing molecules

In the design of host molecules to form smectic A phases, it is vital to ensure the molecules have structures which self-organise to form aligned layers. Li et al. noted that nanosegregation is important in driving self-organisation into layer structures in liquid crystals.[95] One notable approach has been the use of organosiloxane groups, which have previously been anchored to a surface to induce alignment,[13] and that can be added to liquid crystal molecules to induce layer formation for molecules moving freely in a phase. Newton et al. found that the addition of a siloxane end group on to an alkoxycyanobiphenyl molecule resulted in a low melting point and a change in the mesophase behaviour from nematic to smectic A, as shown in Figure 1.38.[96]

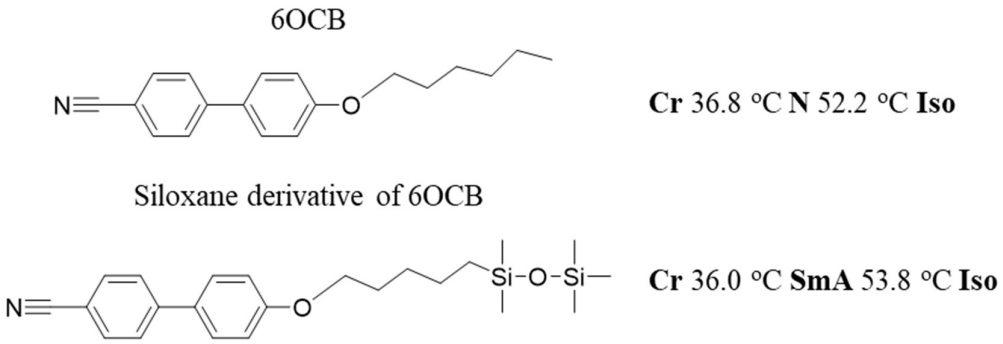

Figure 1.38: Structures and transition temperatures of 4-hexyloxy-4′-cyanobiphenyl (6OCB) and 4-(6-pentamethyldisiloxy)hexyloxy-4′-cyanobiphenyl (siloxane derivative of 6OCB), as reported by Newton et al.[96]

The ability of the siloxane moiety to promote smectic phase behaviour has been widely reported since the initial studies, and this effect has been observed also in mixtures of molecules with and without the siloxane moiety. For example, Gardiner and Coles found that although 4-pentyloxy-4′-cyanobiphenyl (5OCB) itself exhibits only a nematic phase, mixtures of up to 60% w/w of 5OCB in a mixture with 40% of an organosiloxane appended 5OCB molecule exhibited a smectic A phase instead.[47] The mixtures were found to have improved performance in smectic A devices when compared with the comparative pure material (8CB). The incorporation of polar and non-polar sections into the liquid crystal molecule was attributed as the cause of to the formation of smectic A phase,[97] and one benefit

of these smectic A phases was that they required a lower switching voltages than other liquid crystal systems.[47, 98, 99]

The packing of a liquid crystal with a siloxane end group was reported to lead to siloxane-rich regions, which have been termed a siloxane backbone, as shown in Figure 1.39. This was proposed to stabilise the smectic A phase, by forming strongly coupled siloxane regions.[100] Siloxanes exhibited a reduction in crystallinity compared to straight hydrocarbon analogues,[96, 99] a wider temperature range for the smectic A phase,[98] and a preference for the formation of a smectic A phase over the nematic phase. The alkyl chain length between the core and the siloxane group affected the phase range and performance of the material in a device; increasing the chain length resulted in a higher clearing point and a decrease in the melting point, as well as lowering the threshold voltage for changing a smectic A device from a clear state to a scattering state.[47]

The presence of a "siloxane backbone" was probed by Ibn-Ekhaj et al., who observed that the smectic A phase of siloxane terminated cyanobiphenyls has an interdigitated packing arrangement (SmA_d).[101] The X-ray diffraction pattern exhibited a sharp small angle Bragg reflection attributed to the smectic layer, with a calculated layer spacing of 1.7 times the molecular length, due to interdigitation of the molecules.[47] It was also observed that the bulky nature of the siloxane moiety resulted in lateral expansion of the alkyl chains within the layers.[101]

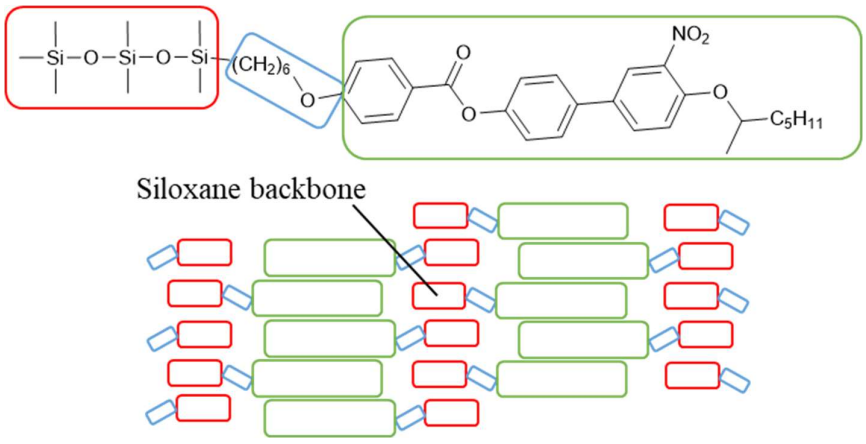

Figure 1.39: Example of siloxane containing molecule used by Carboni et al and a schematic of siloxane backbone structure proposed.[100]

Other host molecules

Although siloxanes were thought to be particularly exceptional in their ability to self-organise to form smectic phases, more recent works on non-siloxane containing molecules suggest that they may not be exceptional.[102] It has been observed that smectic phases form with molecules with all aromatic cores, such as the wide variety of structures reported by Dabrowski and Żytyński,[103] and in some cases molecules with fully alicyclic cores also formed smectic phases, such as the examples shown in Figure 1.40.[104] In the case of a mixture of alicyclic and aromatic rings in the core, layering was disfavoured leading to the formation of nematic phases. Hird also noted that other important features were a rod-like shape to favour packing in layers, and a suitable linking group between the aromatic sections to enhance the interactions between molecules.[105]

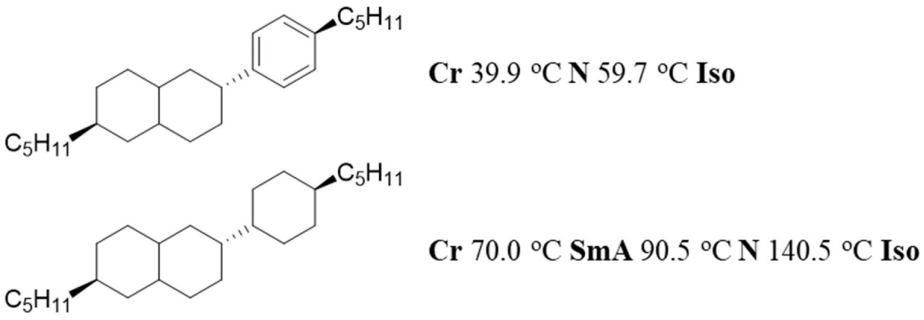

Figure 1.40: Examples of two liquid crystal phase forming molecules, one containing a phenyl ring and one completely alicyclic compound, and the liquid crystal phase transition temperatures associated with them.[104]

For these liquid crystal molecules, the layer formation has been suggested to occur as a consequence of the overall shape of the molecule,[106, 107] and the segregation of the aliphatic and aromatic parts of the molecules.[108] It has been observed that increasing the terminal chain length can cause the type of phase observed to change, for example the 4-alkyl-4′-cyanobiphenyl (nCB) and 4-alkoxy-4′-cyanobiphenyl (nOCB) molecules have nematic phases at shorter chain lengths but there are also smectic phases present for n = 8-12.[105, 109]

Other adaptions to the molecules, such as the addition of lateral groups, can lead to a decrease in the clearing point,[102] due to the disruption of the packing of the molecules. It was observed that lateral methyl groups on an ethyleneoxy tail group resulted in suppression of the smectic phase, due to steric repulsion disfavouring the packing arrangement of the smectic phase. This was surprising in this system because it was thought that the polarity of the ethyleneoxy group would dominate the interactions and stabilise the smectic phase, but the steric interactions were more dominant.[97]

Fluorine atoms can also be utilised as lateral groups on aromatic cores; fluorine atoms are a similar size to hydrogen so do not alter the shape of the molecule overall but this alters the polarity of the core of the molecule. The modification of polarity in this context can lead to the formation of nematic and tilted smectic phases, but the addition of multiple fluorine atoms can result in a smectic A phase.[97]

The effect of smectic phase promotion that is observed with the siloxane terminal groups has been found for many terminal groups apart from siloxanes, such as glucose derivatives[110] and cyclic end groups.[111] The addition of the terminal group induced nanophase segregation, leading to the formation of a smectic liquid crystal phase when previously there was only a nematic phase.[47] Queneau et al. observed that the glucose terminal groups promoted smectic layer formation, which was suggested to occur as a result of hydrogen-bonding between the glucose units.[102, 110] Mandle et al. studied apolar cyclic rings, which ranged in size from 3-membered to 7-membered rings, and observed that the smectic A phase was induced for larger rings due to the steric bulk of the group and that the smaller chain lengths, such as the 3-membered ring, formed only nematic phases.

Sims et al. observed that addition of a bulky tertiary butyl (*t*-Bu) group to an alkoxycyanobiphenyl (nOCB) molecule resulted in smectic phase behaviour and a less interdigitated phase structure. There was greater sensitivity of the layer spacing with temperature compared to the regular alkoxycyanobiphenyl, shown by a larger change in the layer spacing with decreasing temperature.[106] The *t*-Bu group has also been compared to trimethylsilyl, which was of a comparable size and compounds containing them exhibited

near identical melting and clearing points.[108] The introduction of such bulky terminal groups was suggested to a cause a decrease in melting point and clearing points.[102, 108, 112]

Halogens, such as chlorine and bromine, can also be used as bulky terminal groups. These atoms were found to suppress the formation of a smectic phase, with respect to the same liquid crystal molecule without a halogen, which was attributed to electrostatic repulsion.[102] Iodine in the terminal position was found to be non-mesogenic and did not form any liquid crystal phase.[108] It has also been observed that overly bulky groups can also cause a breakdown of a smectic phase, due to difficulty packing the large groups in the inter-layer region.[102, 108]

1.2.3.2 Odd-even effect

The odd-even effect is commonly observed in the transition temperatures of liquid crystal series with changing terminal chain length (n).[3] It is a subtle shape effect, and it has been confirmed for the nematic and smectic phases of many liquid crystal molecules, including alkylcyanobiphenyls (nCB), alkoxycyanobiphenyls (nOCB) and siloxane terminated species.[96, 109] Generally the effect is due to the shape of the terminal chain changing with increasing n, but it can also be considered in entropic terms.[113] This effect becomes progressively smaller with increasing chain length, as the chain becomes increasingly flexible, and the importance of the non-elongated conformations becomes greater.[113, 114]

The odd-even effect results in the change, such as the increase or decrease, in the transition temperature on going from one chain length to the next being smaller than the previous change and then becoming larger on the next increase in chain length. This can be more clearly illustrated through looking at the clearing point trends for the alkylcyanobiphenyl series,[105] where the chain length contains 1-9 carbon atoms, as shown in Figure 1.41 and the transition temperatures are plotted in Figure 1.42. As the chain length (n) goes from odd to even, for example a chain length of 3 to 4, then there is a change in the clearing point of -9.0 ^{o}C and as the chain length goes from even to odd, for example a chain length of 4 to 5, there is change in the clearing point of 18.5 ^{o}C. It is clear in this example that all the even to odd chain length changes have a larger magnitude than those of the odd to even chain lengths.

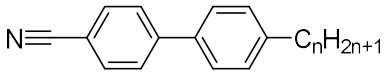

Figure 1.41: Structure of the alkylcyanobiphenyl molecules, where n = 1-9.

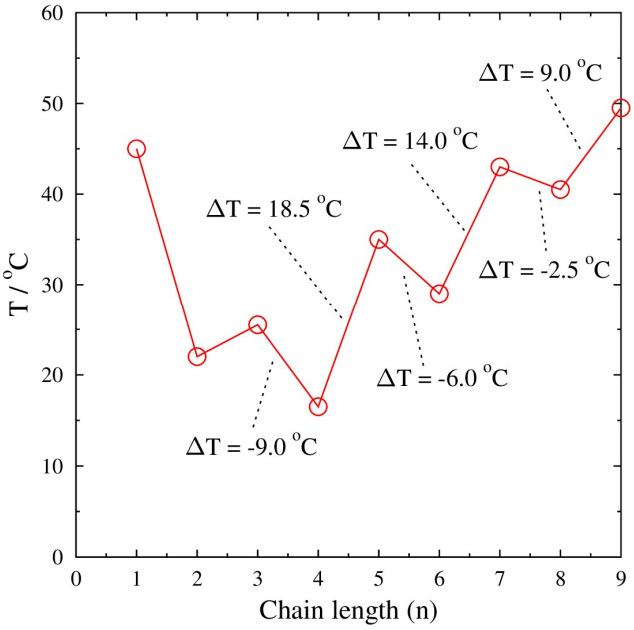

Figure 1.42: Plot of clearing point for the alkylcyanobiphenyl series (nCB), where n=1-9, and the ΔT labels indicate the change occur at each change in n. Transition temperatures are taken from Hird in Physical Properties of liquid crystals: Nematics.[105]

A simple shape-based model relies on the assumption that the chain is in the all *trans* conformation, and it is suggested that the addition of an alkyl unit from odd to even results in a decrease in order in the nCB series, due to the end group no longer being aligned with the molecular long axis. This results in a broadening of the molecule, not lengthening, on addition of a CH_2 group to the alkyl chain. The opposite trend is observed for the alkoxycyanobiphenyl series due to the addition of the O atom, which causes an inversion of the trend shown in Figure 1.42.[115, 116]

The odd-even effect has been observed in many different properties, such as through conductivities, dielectric anisotropies,[47] transition temperatures and entropies.[113, 117] Gardiner and Coles found that there was a variation between odd and even siloxane smectic

liquid crystals for dielectric anisotropy and conductivity ratio.[47] Molecules with even chain lengths in the series showed higher dielectic permittivity parallel to the director, due to an increased length to breadth ratio and molecules with odd chain lengths showed higher conductivity ratio than the even chain length molecules, which could be due to the formation of less diffuse smectic layers for the odd chain length molecules, which lowered the conductivity perpendicular to the layers.[47] The odd-even effect has also been observed using computer simulations, with many groups seeing the same trends for nCB and nOCB series as seen in experiment.[114, 118] Berardi et al. concluded that the effect originated from two main features of the molecules; the length to breadth ratio and the alignment of the terminal group with molecular long axis of the molecule and of the overall liquid crystal director ($\hat{n}$).[114]

1.2.4 Ionic Dopants

For scattering states to form with smectic A phases a layer disrupting dopant can either be added or it can form from electrochemical degradation. [119] The most commonly used dopants are substituted ammonium salts, and salts such as cetrimonium bromide (CTAB), shown in Figure 1.43. This dopant was found to disrupt the layering of a siloxane derivative of a cyanobiphenyl molecule on the application of a low frequency field, forming the dynamic scattering texture.[119]

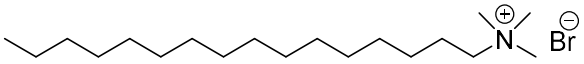

Figure 1.43: Structure of cetrimonium bromide dopant used by Gardiner and Coles.[119]

Dopants do not need to be liquid crystalline in nature themselves, but should not disrupt the normal phases of the liquid crystal, unless specifically required, and should be soluble in the host at low concentrations.[16] It is important that ionic dopants used in smectic A devices are inert and not degrade the liquid crystal host, as the dopant could be depleted through oxidation or reduction, which in turn could deplete the host molecules via subsequent reactions. This depletion would be a problem in display applications as it would lead to the production of ions that may carry current but would not form domains that scatter. One example of a previously reported ion is the bromide ion, which can be used as an ionic dopant; it is stable with respect to redox process on short time-scales, but over longer times scales it can become oxidised to bromine resulting in the display becoming stained brown.

An alternative to the bromide ion would be the perchlorate anion.[48] The size of the cation will affect the amount of scattering produced, so smaller cations only produce small amounts of scattering. It has been observed that small dopants destabilised the liquid crystal phase, but longer chain dopants did not disrupt the phase.[48] Longer chain dopants can also help the alignment of the liquid crystal molecules in the clear state.[65]

Smectic dopants can also serve additional functions in the device, such as to lower switching voltages or to introduce chirality into the liquid crystal phase.[112] Dierking et al. found that that increasing the concentration of dopant decreased the switching time, due to the ionic convection amplifying the natural switch and also caused a change in the direction of the director.[120]

1.2.5 Devices and applications

1.2.5.1 Properties

When designing a guest-host system there are many properties that need to be carefully tuned to ensure the most effective features for the desired applications, such as high contrast, fast switching time or suitable operating temperature range.

Alignment

In the absence of external factors, a liquid crystal phase has order over small length scales called domains, in a bulk sample. At the boundaries of the domains, light is scattered, leading to an opaque appearance. This is generally not ideal for display applications, as the phase needs to be consistent across the whole display when using a transmission device or for the clear state of a scattering display, so an external source of alignment is required to give the display consistent switching and colour.[9] Hence, various methods have been employed to induce bulk alignment of liquid crystals in devices, generally doing so via a coating on the surface of the device.

The alignment of a liquid crystal in a display device can be either *planar* or *homeotropic*, depending on the direction that the molecules are organised by the alignment layer on the surface of the device. In the homeotropic alignment the molecules in the liquid crystal phase

(n̂) are perpendicular to the glass substrates, as shown in Figure 1.44 a), and in the planar alignment the molecules align so that the director of the liquid crystal phase (n̂) is parallel to the plates, as shown in Figure 1.44 b).

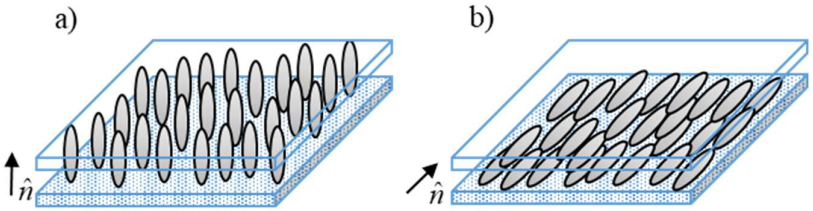

Figure 1.44: Schematic of a) the homeotropic alignment and b) the planar alignment.

Alignment of the liquid crystal phase can be obtained by coating the glass surfaces of a cell with a polymer layer and rubbing the layer with a cloth or using a roller with a fine-fibered cloth.[121] The cloth is rubbed in one consistent direction forming channels, which causes the liquid crystal phase to align; the cloth pile depth and the rotation speed have been shown to have an effect on the alignment angle and on the strength of the alignment layer produced, but the actual mechanism is not fully understood.[9] It has also been suggested that the rubbing motion can cause the formation of microgrooves, which the liquid crystal molecules can align with to attain the lowest energy position on the surface,[122] or that when the surface is a polymer, the rubbing action causes mechanical alignment of the polymer chains or bonds at the surface, leading to alignment of the liquid crystal molecules.[8, 9]

Slow cooling from the isotropic liquid can be used to align the liquid crystal samples with an alignment coated surface, with the best results occurring at slow cooling rates with a magnetic field applied to the sample. This method can allow the smectic A phase to form in a single aligned domain with the field, with limited defect texture forming.[123] Slow cooling of the sample has also been studied with the use of lateral spacers in the cells, which nucleate the alignment of the phase. This method was found to give an aligned liquid crystal sample in both the smectic A and the chiral smectic C phases, but one limitation was that this could only be used over small cell areas.[124]

Alignment can also be induced by using ridges attached to the surface of the alignment layer, which cause the molecules to align in the region between two protrusions and this method has been referred to as automatic domain formation (ADF).[10, 11] This technique can lead to light leakage and slow switching,[9] due the presence of the protrusions, but methods using UV-curable monomers have been developed. A curable monomer is added into the liquid crystal, then cured using UV light to form polymer layers on the plate surface, which induces alignment in the liquid crystal. This is reported to reduce light leakage as there are no gaps in the polymer layer and can lead to faster switching times.[11]

Liquid crystals can also be aligned by the groups on the surface of the plates, either by the use of surfactant or by species bonded to the surface. Organosiloxanes can be bonded to the surface to induce either homeotropic or planar alignment of liquid crystals, based on the structure used.[12] For example, for the same liquid crystal, planar alignment could be attained using N-methyl-3-aminopropyltrimethoxysilane (MAP) as it forms surface channels, whereas N-N-dimethyl-N-octadecyl-3-aminopropyltrimethyoxysilyl (DMOAP) chloride has a bulky $C_{18}H_{37}$ group which sits perpendicular to the plate surface, causing perpendicular alignment of the liquid crystal molecules.[13] Surface bonded siloxane groups can also be used to induce switching in the liquid crystal which can be done by using the *cis* and *trans* isomers of azobenzene units attached to the siloxane group. When bonded to the surface the *trans* isomer induces the liquid crystal molecules to align perpendicular to the surface, and after a photo-isomerisation switching step the *cis* isomer induces the liquid crystal to align parallel to the surface.[9, 125] This combination of switching and alignment gives scope for simplifying display functions in guest-host displays and providing strong alignment of the liquid crystals in both the on and off positions.

Contrast and dichroic ratio

The difference in brightness between the on and off states of a display is generally expressed as the contrast (C), which can be calculated using equation 1.10.[26] This would be very important for display applications, but would also be relevant for any application that needs a clear difference between on and off states. Often when discussing displays it is more relevant to discuss the contrast ratio (CR), which is the ratio of the most absorbing (darkest) state (A_{OFF}), and the least absorbing (brightest) state of the display (A_{ON}), as given by

equation 1.11, where A is the measured absorbance in each state.[12, 126] Contrast and contrast ratio can also be expressed in terms of transmittance.[12]

Equation 1.10 $$C = \frac{A_{OFF} - A_{ON}}{A_{OFF}}$$

Equation 1.11 $$CR = A_{OFF} / A_{ON}$$

For guest-host displays, high contrast can be achieved by ensuring low absorbance of the dye in the on state and high absorbance of the dye in the off state, [127] as illustrated in Figure 1.26 for the Heilmeier and Zanoni display.[49] The high absorbance in the off state can be achieved by using a dye with a high absorption coefficient and by ensuring that there is good alignment between the dye transition dipole moment and the long axis of the dye, and between the dye long axis and the host director. In scattering displays, as shown in Figure 1.27, the scattering state has high absorbance and aligned state has low absorbance, so the contrast ratio can be calculated between the two different states.

Contrast can also be improved through the addition of contrast improving dopants (CIDs), which are most commonly used in the field of scattering displays. Dopants can act as nucleation points for smectic phases and help ensure greater order in such systems,[128] which could be applied to guest-host displays. If a dopant induces greater order, it may lead to better alignment of the dye within the host liquid crystal, improving the contrast between the on and off states, and hence contrast ratio. The contrast ratio between the off and on state of a guest-host device is theoretically proportional to the dichroic ratio between the parallel and perpendicular absorbance of a static sample in a cell, but the dichroic ratio is more related to the dye within a static liquid crystal system whereas the contrast ratio is focussed on the device properties and switching. Often the contrast ratio will be comparable to but less than the dichroic ratio of the guest-host system. This difference can be as a result of switching of the dye molecules not occurring for every molecule, which will reduce the change in absorbance and so affect the contrast ratio. For example, incomplete switching may happen because dye molecules are being adsorbed to the alignment layer or anchored in a liquid crystal area close to the alignment area.[129] As a result it can be more practical to discuss the contrast ratio, rather than dichroic ratio, when considering a device as a whole.[126]

1.2.5.2 Applications

Guest-host systems can be applied in display applications, as illustrated by Heilmeier and Zanoni, and also by White and Taylor.[12, 42] Iwanaga noted that guest-host mixtures were useful for display applications, as they can have high brightness, low power consumption and clear colour, but that there were problems with dye solubility to be addressed particularly in the case of fluorinated hosts.[86] Cole and Kashnow also illustrated the use of guest dyes in a twisted nematic display, which had greater brightness due to the lack of external polarisers and required a low voltage to switch it.[130] These examples show the variety of ways that guest-host devices can be used in display applications, and highlight the huge variety of possible guest-host mixtures that can be created. Wolarz et al. created a nematic-based liquid crystal guest-host display, which used a variety of fluorescent dyes as the guest. It was observed that the dye did not disrupt the packing of the host significantly and showed good stability in sunlight and high fluorescence efficiency.[78]

Aside from the dye applications, guest-host mixtures have found applications in the design of smart window technology.[131] Wu et al. created a guest-host mixture which showed a good contrast between on and off states, over a range of dye concentrations. These mixtures were found to switch in under 200 ms using low voltages, meaning they could be used as low-power dimming windows in vehicles and buildings.[132] This dimming technology has also been used in dimmable eye glasses, as shown by Baburaj et al.[133] This technology has also been used for self-shading windows, where sunlight causes the switching between the on and off states.[134] An et al. proposed a cell which would go on a car windscreen, to be tinted from the outside but clear from the inside. This design utilised a pre-tilt angle to block the incident light, using a low driving voltage to change the transmittance for the person in the car without affecting the blocking effect for the external light.[135] This example shows the complex ways that guest-host displays can be adapted to specific functions.

There have been many other applications of guest-host displays such as in the production of thin film polarisers, colour changing textiles and thermal sensors.[136] The thin film polarisers use dye doped diacrylates that are polymerised in light to create smectic B phases, which form the polarisation direction due to the highly ordered liquid crystal phase.[137] The colour

changing textiles use the guest-host mixtures encapsulated in micelles which changed from coloured to colourless under an applied voltage.[138]

1.3 Experimental methods background

This section will gives a brief summary of commonly used characterisation techniques used for liquid crystal phases, such as polarised optical microscopy, differential scanning calorimetry and X-ray diffraction, and the electronic spectroscopy techniques used for guest-host mixtures containing dyes.

1.3.1 Liquid crystal characterisation

1.3.1.1 Polarised optical microscopy (POM)

Liquid crystal phases can be characterised and the transition temperatures can be determined using a polarising transmission light microscope.[3] In this method, the liquid crystal samples are sandwiched between a glass microscope slide and cover slip, with the sample heated into the isotropic liquid to create a thin layer on the slide. The microscope consists of a light source providing a beam of light that passes through a polariser to reach the sample, which is placed within a holder inside a temperature controlled furnace, on top of a rotatable sample stage, as shown in Figure 1.45. The light then passes through the objective and a second polariser (analyser), which is rotated at 90^{o} with respect to the other polariser, before reaching the viewer or a camera.[3]

The samples are heated and then cooled to observe the defect texture associated with the liquid crystal phases, and the camera is used to document the textures exhibited. When the liquid crystal is heated to the isotropic liquid phase, it appears optically extinct (black) between the crossed polarisers due to the isotropic nature of the phase. As the isotropic liquid is cooled into the liquid crystal phase, the phase has optical anisotropy, and as a result exhibits birefringence. This birefringence leads to the parallel and perpendicular components of the polarised light becoming out of phase when travelling through the sample. This results in the change in the polarisation of the light and these bright textures being observed through the microscope.[3] The types of textures present are characteristic of the different liquid crystal

phases, and are caused by the different packing of the molecules around defects, as mentioned previously in section 1.1 for the different liquid crystal phases.

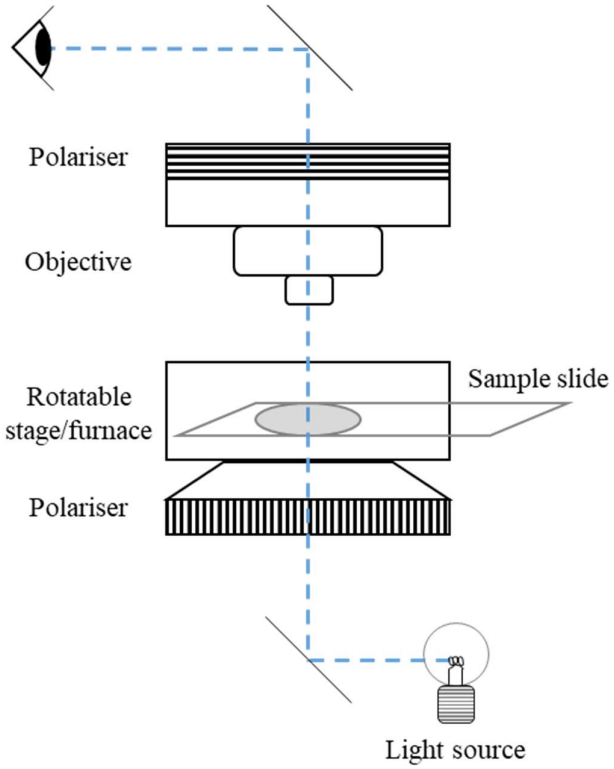

Figure 1.45: Schematic of the polarised optical microscope set up.[3]

1.3.1.2 Differential scanning calorimetry (DSC)

The phase transitions of materials, including liquid crystals, can be studied using differential scanning calorimetry (DSC), which measures the heat capacity of the material as a function of the temperature with reference to an empty sample pan, and calibrated to a known sample, which is usually indium. The calorimeter determines the input or output of energy with reference to an empty cell, which experiences no change, and using a set-up as shown in . The DSC measurements are carried out on heating and cooling cycles, with peaks present for first order transitions and changes in the baseline for second order transitions.[139] Transition temperatures are taken from the peak value, or an average of peak values over repeat cycles, and the areas under the peaks in the DSC trace give the latent heats of

transition. These values can be converted into the transition enthalpies and entropies to gain further insight into the thermodynamics of the phase transitions.[3]

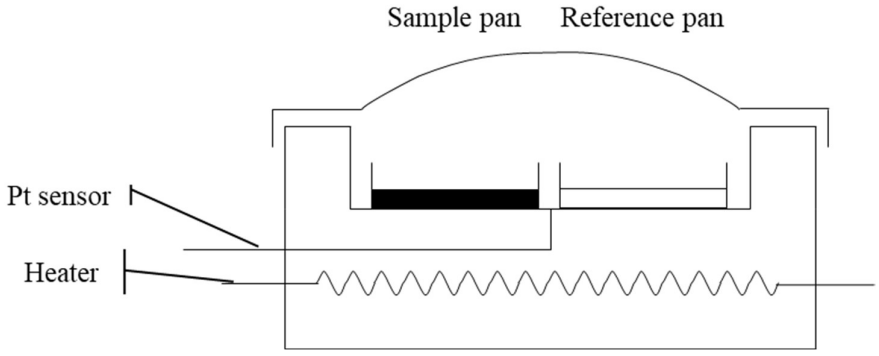

Figure 1.46: Schematic of DSC furnace, with sample and reference pans in the same chamber.

An example of a DSC trace is given in Figure 1.47, and the labels in red and blue show the phases present on heating and cooling, respectively. On this plot, peak **A** shows the transition from the liquid crystal phase to the crystal on the cooling cycle and peak **B** shows the transition from the crystal to the liquid crystal phase, which in this case is smectic A (SmA), on the heating cycle. The pair of peaks at **C** shows the transition between the liquid crystal phases (smectic A and nematic) on heating and cooling. The pair of peaks at **D** shows the transition from the liquid crystal phase, in this case nematic (N) to the isotropic liquid phase (Iso) on both the heating and cooling cycle. The two transitions **C** and **D** occur at similar temperatures on both cycles. Usually a liquid crystal transition occurs at a similar temperature on heating and cooling, showing reversibility of this transition, but the melting and crystallisation points, labelled as peaks **A** and **B**, are generally not at the same temperature, due to the kinetic factors that result in an extended temperature range of the liquid crystal phase on cooling, termed supercooling.[3]

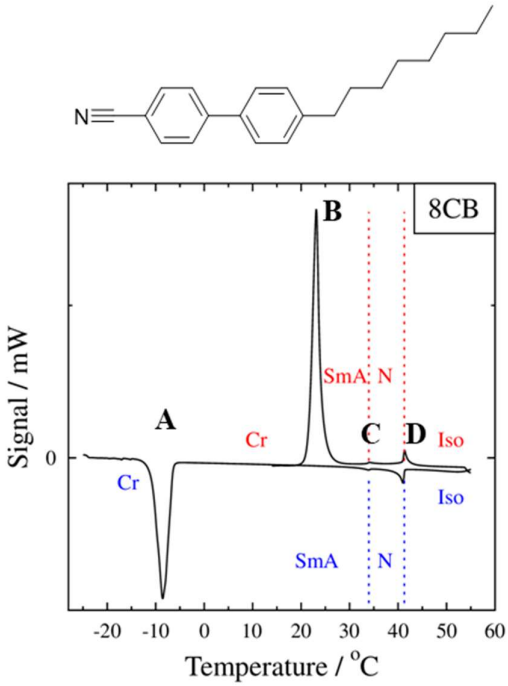

Figure 1.47: Example DSC trace for 8CB, with the molecular structure and the trace labelled. Peak **A** shows the crystallisation point on the heating and peak **B** shows the melting point on heating. The pair of peaks at **C** shows the transitions between liquid crystal phases on heating and cooling, and the pair of peaks at **D** shows the clearing point on heating and cooling.

1.3.1.3 X-ray diffraction (XRD)

X-ray diffraction can be used to gain an understanding of the local structure of a liquid crystal phase. In this experiment, a source provides X-rays that are collimated and directed at the sample, and the resulting diffracted rays are captured by an area detector, as shown schematically in Figure 1.48.[3] For these measurements, electromagnetic radiation with a wavelength similar to the spacing between the distances to be measured is needed.[3] In particular for measuring the distances between layers in smectic phases the X-rays have to be detected at small angles,[26] due to the typical X-ray wavelengths used experimentally and Bragg's Law, as given in equation 1.12.[3, 26] As shown in Figure 1.49, the distance between layers (d) can be calculated using the angle of incidence (θ) and the wavelength of the X-rays used (λ).

Equation 1.12 $$2d.\sin\theta = n\lambda$$

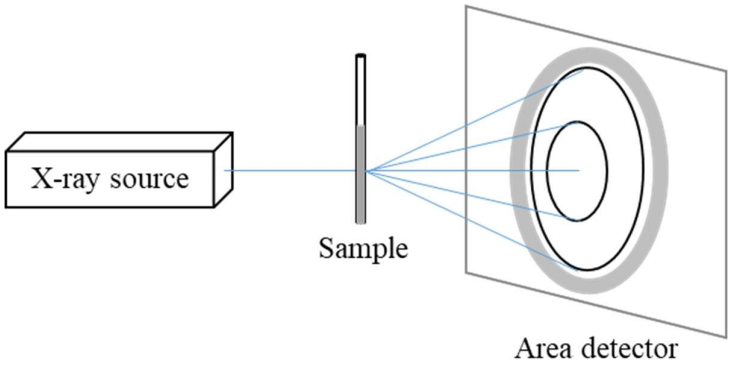

Figure 1.48: Simplified schematic of X-ray diffraction experiments, modified from Agra-Kooijman and Kumar.[140]

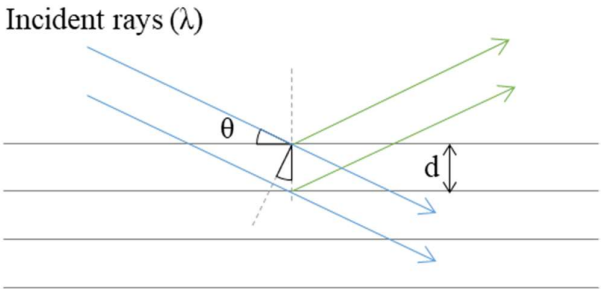

Figure 1.49: Diagram illustrating the method of determining the layer spacing (d) in an example crystal structure from the angle (θ), using X-ray incident rays of wavelength λ.

In the isotropic liquid crystal phase there is very weak, diffuse scattering, so it may appear that there are no peaks in the diffraction pattern.[3] With unaligned liquid crystal samples where a liquid crystal phase is present as domains, the diffraction patterns are similar to powder samples but the liquid crystal phases can be distinguished by the diffraction angles and the widths of the rings. Nematic phases can be observed using X-ray diffraction,[140] and can be used to determine the average distance between the centres of mass and molecular lengths through the diffraction patterns, as shown in Figure 1.50.

When the sample is unaligned, the smectic A and smectic C phases are not distinguishable. However, they give a sharp diffraction in the small-angle region that is indicative of the layer spacing, due to the smectic density wave, and a broad diffraction in the wide-angle region that represents a lateral distances between the centres of mass within the molecules in the

diffuse layers, due to the liquid-like order within the smectic phase.[140] A liquid crystal phase can sometimes be bulk aligned using a magnetic field, which would allow the smectic A and smectic C phase to be distinguished from one another. In the diffraction pattern for an aligned sample in the smectic A phase the wide angle peaks appear at 90° to the small angle peaks, and for the smectic C phase the wide angle peaks are at an angle of <90°, which is related to the tilt angle of the phase.[140] In the crystal, there are many peaks due to the many layer planes in the crystal structure.

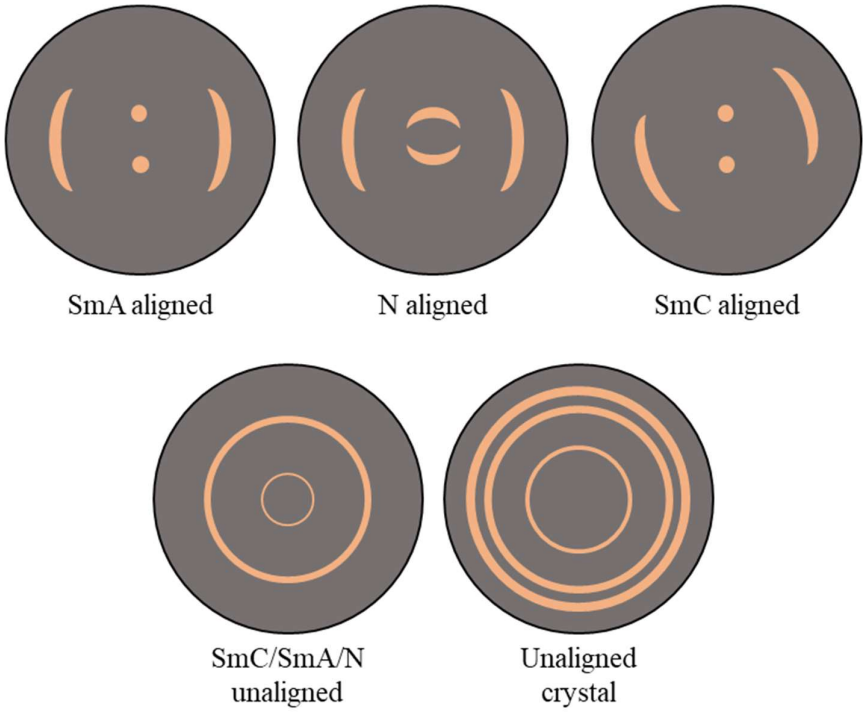

Figure 1.50: Diagrams showing the typical diffraction patterns formed for different types of liquid crystal phase and the pattern for the crystal.

1.3.2 Dye characterisation

1.3.2.1 Electronic spectroscopy

Electronic absorption spectroscopy can be used to probe the electronic states of molecules. The spectrometer for this technique uses a tuneable light source which is in the UV-visible region.[141] When the sample is irradiated, there is an absorption of energy which promotes the molecule from a low energy state to a higher energy state, which can be called a ground

to excited state transition. When this transition occurs, there is an absorption of the light and the intensity of the light transmitted (I) can be measured. This transmitted intensity is related to the initial light intensity (I_o) via the Beer-Lambert law. This relationship also depends on the molar absorption coefficient of the sample (ε), the concentration of the solution (c), and the path length of the cell or cuvette containing the sample (l). The Beer-Lambert law is commonly given in terms of the absorbance (A) which can be expressed as shown in equation 1.13.[85]

Equation 1.13

$$A = -\log\left(\frac{I}{I_o}\right) = \varepsilon cl$$

In some spectrometers, a double-beam arrangement uses a split beam of incident light which passes through a sample of solution containing the dye and a sample of pure solvent, in optically matched sample cuvettes.[141] Some spectrometers only use single beam, so measurements of the pure solvent and samples have to be undertaken separately and subtracted to determine the sample absorbance.

In the case of dyes in solution, electronic absorption spectroscopy can be used to ch aracterise the dyes, which can provide insight into the relationship between the colour of a dye and the molecular structure. The light interacts with the dye via a transition dipole moment and selective absorption occurs at certain wavelengths. The remaining wavelengths of light are transmitted, thus giving rise to the observed colour of the dye. The Beer-Lambert law is obeyed by most dyes in solution at low concentrations, but if there is dye aggregation then there is an apparent deviation from the law due to a change in the sample composition.[85]

1.4 Computational methods background

Computational modelling is a great tool for the studies of the properties of molecules, either in isolation or as many molecules in a bulk phase. Although there are many different types of studies that can be done computationally, this section will give a brief summary on the use of single molecule studies using density functional theory (DFT) studies and molecular dynamics (MD) simulations using more than one molecule, in order to simulate liquid crystal phases.

1.4.1 Electronic structure calculations

Calculations of isolated gas phase molecules have been widely used to understand the properties observed experimentally. There are many different methods that can be used for computing the energy of particular molecular structures, such as Hartree-Fock (HF) and Density Functional Theory (DFT). Hartree-Fock theory uses the assumption that each electron in the molecule observes all the other electrons as an average field.[142] This theory does not take all the interactions of the individual electrons into account, and as a result a different model was proposed, to incorporate more detail into the model. The first DFT models were based on theorems by Hohenberg and Kohn.[143-145] These models state that the ground state properties of the system are determined by the electron density distribution of the molecule and the calculations include electron correlation effects to take in account interactions between electrons.[144, 146] DFT can also be used to predict properties that are linked to the energy of the structure expected for a certain molecule. The energy and the associated properties are obtained by solving the Schrödinger equation, as given in equation 1.14, and DFT uses a function of the electron density, which is calculated from the coordinates of the molecule, in the calculation to simplify the equation.[146, 147]

Equation 1.14 $$\hat{H}\Psi = E\Psi$$

For these DFT calculations a method and a basis set must be selected, which select the amount of functions used in the calculations. For example the B3LYP functional is the particular functional developed by Becke which uses a 3 parameter exchange functional (B3) and the Lee-Yang-Parr (LYP) correlation function. The basis set determines the gaussian functions that are used for the calculations, and gives a mathematical representation of the atomic orbitals within each molecule. For example a 6-31G basis set would have six gaussian functions for the core orbitals, and two basis functions comprising three and one functions for the valence orbitals, respectively.[147]

DFT and TD-DFT calculations can be used to improve understanding of molecular properties and also to aid in the design of molecules. Chen et al. used DFT and time-dependent DFT calculations to understand the effects of different lateral substituents on the reported photo-stability of liquid crystal molecules, thus removing the need to synthesise a

larger number of molecules to test them.[148] For liquid crystals these calculations can also provide insight into the molecular geometry, such as terminal alkoxy chain conformations or the angle between aromatic ring systems.[149] DFT can also be used to understand the molecular orbitals of dyes, and time-dependent DFT (TD-DFT) to gain an understanding of the electronic transitions occurring that result in the dye colour and the orientation of the transition dipole moment of the dye within a host.[88, 150] Alignment of the transition dipole moment and the long axis is also important, and this can be modelled using DFT simulations of the structure.[79] If there is poor alignment of these two factors, then a simple calculation of the resultant order parameter can be inaccurate so the angle between them must be factored in to the calculation.[89] Aspect ratios and angles between the transition dipole moment and molecular axis have been modelled computationally, and this method showed a good model of the trends and further comparison also showed the order parameter of the dye can be higher in simulations than in experiment, due to the highly ordered host environment modelled by the simulation.[79]

1.4.2 Molecular dynamics simulations

Molecular dynamics (MD) simulations can be used to simulate the motions and energies of assemblies of molecules using a force field that gives parameters to estimate the forces between molecules and between atoms within the molecules. This can be done using a course-grain model, with a shape representing the whole or part of a molecule, or using atomic models, where each of the atoms of the molecules is represented explicitly in the model. In the fully atomistic method, the location, velocity and sometimes orientation of the molecules are determined at the start, before Newton's laws are integrated to obtain these quantities again after a small time-step. It is important to have as many molecules as possible to get a good model for the system overall.[3] Overall, this method can be very computationally expensive, and requires many calculations at every step to determine all the interactions taking place during each time step.

MD simulations can be a vital tool for understanding liquid crystal systems and to aid in the design of hosts and guests for guest-host devices. To use simulations within the design process of liquid crystal host molecules requires a strong understanding of the structure-property relationship. It has been noted that small changes in molecular structure can have a

significant effect on transition temperatures and the types of phases formed,[151] so modelling of novel liquid crystal molecules can provide a powerful tool to allow property predictions of phase behaviour to be made to inform and direct synthesis.[109] Simulations can be used to calculate theoretical phase transitions and layers spacings where applicable, and also to predict the type of phases expected from a molecule.

1.4.2.1 Force field optimisation

Conventional force fields such as AMBER, Gromos and OPLS-UA have all been used previously to model liquid crystal systems, but in some cases the simulated transition temperatures and densities are not closely matched to the experimental values.[152] Despite this, general force fields can be used to show a good match to experimental trends, even if absolute values are not closely matched.

There has been a significant body of work focused on force field optimisation to attain transition temperatures which match experimental values.[152, 153] It is important to have a good parameter set, which is complete and self-consistent to enable good modelling of the experimental values of a system,[154] and subsequently the force field, TraPPE-UA, was found to gives values consistent with the experimental values for 5CB and 8CB reported in the literature, by adjustment of the torsional parameters for this series.[152] This consistency was also found to be independent of the sample size used in the model. Making an accurate force field can be achieved by parametrising the force field from *ab initio*, electronic structure calculations.[151] This is done by setting parameters for different atom types, atom charges, Lennard-Jones potentials, bond parameters, angles and torsional angles from literature values,[154] but the effectiveness of this technique is highly dependent on the quality of the data used.[151, 155] Done well, this can allow good modelling of the conformation changes and the non-covalent interactions occurring, but these empirical values can also lead to overestimation in the properties observed,[156] for example a much higher density in the simulation than in reality.[118] Using this technique of force field optimisation is very time consuming and results in a force field which is highly accurate for one series of liquid crystal molecules, but is not necessarily useful for any other liquid crystal molecule or for the same liquid crystal upon addition of another component such as a dye or a dopant.[155]

1.4.2.2 Use of general force fields

Although there has been much work on optimising force fields for liquid crystal modelling, it can be more desirable to use a more general purpose force field which will describe more liquid crystals, rather than the highly specialised ones described above.[154] An AMBER-OPLS force field has been utilised to model the isotropic-nematic transition temperature of n-alkyl cyanobiphenyl molecules, which was able to reproduce the experimental trends for transition temperature and density.[153] These models can also be used to model odd-even effects observed experimentally for a series of liquid crystal molecules, but these simulations can be computationally expensive.[106, 118]

Smectic liquid crystal systems have been less widely studied by molecular dynamics[153] and the formation of the layers can be dependent on the simulation size used. It was observed that at larger simulation size there was increased stability of the smectic phase resulting in a greater layer spacing, which reflected the experimental value more accurately.[152, 156] As well as simulation size, the relative dimensions of the simulation box can impact the layer formation in the smectic phase. Restrictive boundary conditions that fix the shape of the box can disfavour layer formation, whereas less restricting conditions where the box can vary in shape can allow molecules to position more easily in the layers.[156] Layer spacing was also modelled using a general AMBER force field (GAFF) for 11OCB and *t*-Bu 11OCB , which resulted in similar values to X-ray diffraction measurements undertaken.[106] Smectic phases were also found to be sensitive to the point charges in a way that nematic phases were not. De Gaetani *et al.* observed that omitting the point charges led to a normal smectic A phase being formed for 8OCB, whereas if the point charges were included the phase was an interdigited smectic A (SmA_d). The interdigitated phase matched the observed phase from experiment, so the phase seen was very responsive to the point charges present.[156] Overall, general force fields can be applied to liquid crystals without a huge amount of adaption, to approximate experimental results and to allow a deeper understanding of the phases of the liquid crystal being studied.

1.5 Aims

The overall aim of this work was to make a systematic study of the use of a bulky terminal group design to promote the formation of smectic phases in host and guest-host systems. The host molecules studied here consisted of two series; the 4-n-alkoxy-4′-cyanobiphenyl (nOCB) series and 4-(*t*-Bu-n-alkoxy)-4′-cyanobiphenyl (*t*-Bu-nOCB) series, shown in Figure 1.51 and Figure 1.52, respectively. These hosts were selected due to the relative synthetic ease of making the novel *t*-butyl hosts by synthetic researchers within the Department, and the work done previously at York on one of the molecules from each series, 11OCB and *t*-Bu-11OCB, by Sims et al.[106] The two different ranges of the chain lengths (n) were selected to give two series of equal chain length with the only difference being the two additional methyl groups on the terminal carbon of the chain.

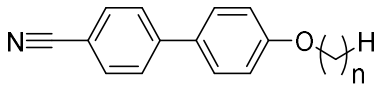

Figure 1.51: General structure of 4-n-alkoxy-4′-cyanobiphenyl (nOCB) series, where n = 8-13.

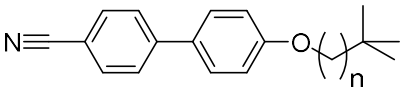

Figure 1.52: General structure of 4-(*t*-Bu-n-alkoxy)-4′-cyanobiphenyl (*t*-Bu-nOCB) series, where n = 6-11.

The guest dyes selected were 2,6-substituted anthraquinone dyes, related to one of the 2,6-substituted dyes studied by Sims et al.[89, 90, 157, 158] These studies identified this type of dye as one with good colour and the best alignment within a nematic liquid crystal host for the range of dyes studied. The dye studied by Sims et al. contained propyl chains, rather than the alkoxy chains used in the dyes studied in this work.

Two series of dyes were studied; the 26B(**m**O)OH anthraquinone dyes, where the 2,6-substitution is a para-alkoxy-phenyl, and the 26B(*t*-Bu-**m**O)OH anthraquinone dyes, where the 2,6- substitution is a para-*t*-Bu-alkoxy-phenyl. These are shown in Figure 1.53 and Figure 1.54, respectively, and were selected for the comparison between the straight chains and bulky terminal group chains.

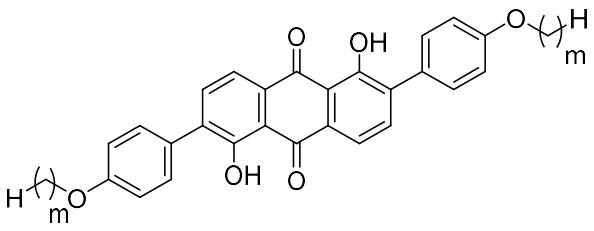

Figure 1.53: General structure of the 2,6-disubstituted anthraquinones, with *p*-alkoxy-phenyl substituents where **m** = 4-13.

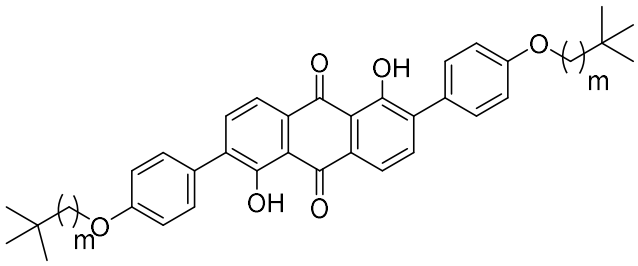

Figure 1.54: General structure of the 2,6-disubstituted anthraquinones, *p*-*t*-Bu-alkoxy-phenyl substituents, where **m** = 2-11.

The initial aim of this work was to study the effect of molecular design on the phases of the liquid crystal hosts using a combination of experimental methods, including polarised optical microscopy, differential scanning calorimetry, and X-ray diffraction, and computational methods, including DFT studies and molecular dynamics simulations. The secondary aim of this work was to gain an insight into the effects of guest dyes in guest-host mixtures using these hosts, applying the above methods and the additional technique of polarised UV-visible absorption spectroscopy. These studies were undertaken with the aim of developing an understanding of underlying principles that might then allow this work to be used for designing guest-host mixtures, with potential applications in guest-host devices.

Chapter 2

Experimental

2.1 Materials

The 4-n-alkoxy-4′-cyanobiphenyl (nOCB) series was used as received from BDH, where n = 8-13. The 4-(*t*-Bu-n-alkoxy)-4′-cyanobiphenyl (*t*-Bu-nOCB) series, where n = 6-11, were synthesised by M.Holmes as part of a final year undergraduate project in the Department supervised by S.J.Cowling, using a previously reported method, as reported in appendix 6.1.[108]

The guest dye molecules were 2,6-disubstituted anthraquinone dyes, where the 2,6-substitution is para-substituted *t*-Bu-**m**-alkoxy-phenyl, where **m** = 7, 9 and 11. These dyes have a similar structure to the 2,6-disubstituted anthraquinone abbreviated as 26B3OH, studied by Sims et al., although the dyes studied here have *t*-Bu-alkoxy chains rather than alkyl chains.[79, 89] These dyes were synthesised by C.Biddlecombe as part of a final year undergraduate project in the Department supervised by S.J.Cowling, using previously reported methods, as reported in appendix 6.1.[70]

For the home-built cells, nylon-6,6 (Sigma Aldrich, Merck Life Science Ltd.) was dissolved in *m*-cresol (Alfa Aesar) and methanol (Fisher) or in methanoic acid (Acros Organics). The cells were glued with optical adhesive (Norland Optical adhesive 68, Thorlabs Ltd.)

2.2 Experimental methods

2.2.1 Polarised optical microscopy (POM)

Polarised optical microscopy (POM) measurements were performed using a Zeiss Axioskop 40 Pol microscope, with a Mettler FP82HT furnace in conjunction with a FP90 temperature controller. The temperature of the furnace was accurate to ± 0.1 ^{o}C. The microscope was used in transmission mode with crossed polarisers, at a total magnification of x100, with x10 magnification on the objective and x10 magnification on either the eyepiece or the camera. Initially, samples were heated at a hot stage ramp rate of 5 ^{o}C min^{-1} from room temperature

to the temperature at which they became isotropic, to determine the approximate transition temperatures. Accurate transition temperatures were then determined by heating/cooling at a rate of 1 °C min^{-1} in the region of the transition. All transition temperatures were recorded on cooling, except for the melting points (crystal to smectic A or isotropic liquid) which were recorded on heating. Photographs were taken using a 21M pixel Infinity-X camera, which was mounted on top of the microscope, to observe the characteristic textures exhibited by the liquid crystal phases on cooling from the isotropic liquid.

For producing the images of the phases, the sample slides of both the host alone samples and guest-host samples were prepared by heating a solid sample to the isotropic liquid (approximately 100 °C), before allowing it to flow under the cover slip by capillary action. This procedure ensured that the sample was suitably thin to obtain a clear image of the phases present.

2.2.2 Differential scanning calorimetry (DSC)

Differential scanning calorimetry (DSC) measurements were performed using a Mettler DSC 822^e instrument, which was calibrated using an indium standard. This standard has a peak onset temperature of 156.55 ± 0.20 °C and a transition enthalpy (ΔH) of 28.45 ± 0.40 J g^{-1}. Accurately measured samples of 1.0 – 2.0 mg were loaded into 20 µl aluminium pans. The DSC experiment involved heating the sample from room temperature to above the temperature at which it became isotropic, as determined by the polarised optical microscopy results (heating to 110 °C for the nOCB compounds and 100 °C for the *t*-Bu-nOCB compounds). The sample was then cooled to -30 °C to allow the sample to crystallise. The heating and cooling cycle was repeated twice more to determine the reproducibility of the phase transitions. Unless otherwise stated, the heating/cooling rate used was 10 °C min^{-1}. Data was collected at 10 data points per second.

The DSC traces were analysed using Mettler $Star^e$ software to determine transition temperatures and transition enthalpies. The transition temperatures were taken from the peak values. The normalised transition enthalpies (ΔH) were obtained using the Mettler software from the integrated DSC peaks, in units of J g^{-1} and then converted into units of kJ mol^{-1}

using the molar mass of each compound. The transition enthalpies were all recorded from the heating cycle, unless stated otherwise. The transition entropy (ΔS) values were calculated from the transition enthalpies determined from the DSC traces, using the assumption the transition has a Gibbs free energy change (ΔG) of 0, which allows the enthalpy values from DSC to be converted to entropy values via equation 2.1, where the transition temperature (T) is in kelvin.

Equation 2.1: $$\Delta S = \frac{\Delta H}{T}$$

2.2.3 X-ray diffraction (XRD)

2D X-ray diffraction (XRD) experiments were performed using a Bruker D8 Discovery X-ray diffractometer with a CuKα microfocus X-ray generator (λ = 1.5406 Å) and a Bruker Vantec 500 area detector, and with a magnetic field which can interact with the samples. Samples were loaded into a borosilicate capillary (80 mm length, 0.9 mm outer diameter, glass wall thickness 0.01 mm; Capillary Tube Supplies Ltd.). The capillary was mounted in a home-built heated graphite furnace and the furnace temperature was controlled by a Eurotherm controller and held constant to within ± 0.1 ºC. The measurements were taken every 3.6 ºC for the nOCB series and every 2.4 ºC for the *t*-Bu-nOCB series and the guest-host mixtures. Samples were held at each temperature for 30 s to allow the sample temperature to equilibrate and then were irradiated for 120 s. The samples were cooled at a rate of 10 ºC min^{-1} over a range of temperatures, which was 95.5-29.7 ºC for the nOCB series, 95.1-30.9 ºC for the *t*-Bu-nOCB series and 100.0-29.0 ºC for the guest-host mixtures. Temperatures were calibrated using data taken from a thermocouple placed in a sample of 8CB, from which a calibration graph with an accuracy of ± 0.5 ºC was obtained. Integrated scattering intensities were obtained using the Bruker software and the layer spacing calculated using equation 2.2, and with the angle of incidence (2θ) taken from the diffraction pattern from the XRD experiment.[159]

Equation 2.2: $$d = \frac{\lambda}{2\sin\theta}$$

2.2.4 Guest-host studies

2.2.4.1 Samples

Guest-host samples were prepared by accurately measuring the liquid crystal host and guest dye into a vial and heating the sample to a temperature higher than the clearing point of the liquid crystal host. A dye concentration of 1 wt% was used to ensure that the peak absorbance of the samples was within the instrumental range for the cells used. The accurate weight percent and concentration used in each guest-host sample is summarised in Table 2.1 and Table 2.2. The guest-host samples were made in small quantities, approximately 40 mg of host to 0.4 mg of guest dye, and were used for the guest-host studies using POM, DSC, XRD and the UV-visible absorption spectroscopy.

Table 2.1: Summary of dye weight percent in different guest-host samples, for the nOCB liquid crystal hosts.

Guest-host mixture	Dye wt%	Concentration / $x10^{-3}$ mol ratio
12OCB_*t*-Bu-**7** dye	0.98	4.85
12OCB_ *t*-Bu-**11** dye	1.01	4.62
13OCB_*t*-Bu-**9** dye	0.99	4.75
13OCB_ *t*-Bu-**11** dye	1.04	4.66

Table 2.2: Summary of dye weight percent in different guest-host samples, for the *t*-Bu-nOCB liquid crystal hosts.

Guest-host mixture	Dye wt%	Concentration / $x10^{-3}$ mol ratio
t-Bu-10OCB_ *t*-Bu-**7** dye	0.97	5.96
t-Bu-10OCB_ *t*-Bu-**11** dye	1.01	5.25
t-Bu-11OCB_ *t*-Bu-**9** dye	0.97	5.73
t-Bu-11OCB_ *t*-Bu-**11** dye	1.02	5.62

2.2.4.2 Commercial cells for UV-visible spectroscopy

Commercial cells of a variety of path lengths were initially used to study the guest-host mixtures. All the commercial cells used had rubbed, polyimide alignment layers that were aligned parallel to each other on facing cell walls, known as homogenous alignment layers, and were coated with an indium tin oxide (ITO) layer.

The initial tests were undertaken using 20 μm path length commercial cells (Instec, 2.5 cm x 2.0 cm) and two guest-host mixtures, 8OCB with 1,5-thio substituted anthraquinone (15SB3) dye (1.37 wt%), which has the structure shown in Figure 2.1, and t-Bu-11OCB with t-Bu-9 dye (1.64 wt%) were added into these cells. The thio substituted dye was previously studied by Sims et al.[89] The next set of commercial cells had path lengths of 5 μm (Instec, 1.7 cm x 1.2 cm), 4 μm (Planar System Inc., 1.5 cm x 2.0 cm) and 3.2 μm (Instec, 2.5 cm x 2.0 cm), which were filled with 11OCB liquid crystal host. The uniformity of the sample alignments in the filled commercial cells was checked using POM (Zeiss Axioskop 40 Pol microscope), after heating above the clearing point and cooling into the respective smectic A phase.

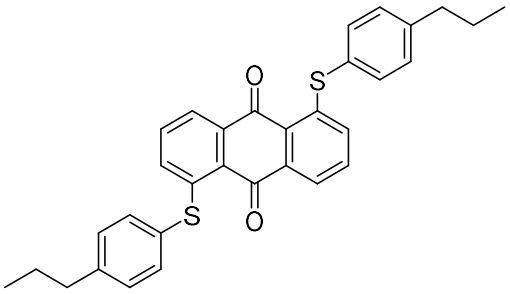

Figure 2.1: Structure of the 1,5-thio substituted anthraquinone dye (15SB3)

The samples within these commercial cells were also studied through slow temperature cycling, by heating to the isotropic liquid and cooling the samples at 0.1 ^{o}C min^{-1} into the smectic A phase. The slow cooling was also repeated with a variety of voltages in the range 1-5 V applied to the cell, at varying frequencies in the range of 1-15 MHz, using a HP 33120A waveform generator and home-built linear amplifier. The aim was to induce alignment of the liquid crystal host within the cell, using a square waveform.

2.2.4.3 Home-built cells for UV-visible spectroscopy

Home-built cells were prepared by cleaning 2.5 cm x 2.5 cm glass squares thoroughly with soap and water, before dipping them into acetone and then isopropanol. The glass was allowed to air dry between each of the cleaning steps. Cells were assembled using the methodology below. For the first batch of cells, a solution of nylon-6,6 in a mixture of *m*-cresol and methanol at 60:40 v/v (0.5 g in 100 mL) was used to prepare the alignment surface and for the second batch of cells, a solution of nylon-6,6 in methanoic acid (0.4 g in 80 mL) was used to prepare the alignment surface.

The clean squares of glass were spin-coated with a nylon solution (1000 rpm for 3 s, then 4000 rpm for 60 s). The coated squares of glass were then dried in an oven for 1 hour at 100 ^{o}C, to ensure the removal of the solvent and to anneal the nylon-6,6 onto the glass surface. A glass square with the nylon-6,6 layer on it was rubbed unidirectionally against a lint-free cloth, to orient the nylon-6,6 alignment surface, and a 15 μm Mylar spacer was glued, using Norland optical adhesive (NOA68), on two opposing edges of the glass square. A second glass square with a rubbed nylon layer was placed on top of the first slide, with the alignment layer facing inward and with identical rubbing directions. The cells were placed together and glued, then clamped in place, before irradiating using a UV lamp (15 W, UVA/UVB (300-400 nm)) for 1 hour, to cure the optical glue.

The path length of the empty cells was measured accurately using the interference pattern obtained from a UV-visible spectrum of an empty cell. The first batch of cells were only used for preliminary measurements and the second batch of cells were used for the detailed studies in this work, which are summarised in Table 2.3 and Table 2.4.

Table 2.3: Summary of cell widths used for the nOCB liquid crystal hosts alone and for the guest-host mixtures.

Host alone	Host alone cell path length /μm	Guest-host mixture	Guest-host cell path length /μm
12OCB	17.3	12OCB_ *t*-Bu-**7** dye	17.6
		12OCB_*t*-Bu-**11** dye	17.8
13OCB	17.0	13OCB_ *t*-Bu-**9** dye	16.7
		13OCB_*t*-Bu-**11** dye	15.9

Table 2.4: Summary of cell widths for the *t*-Bu-nOCB liquid crystal hosts alone and for the guest-host mixtures.

Host alone	Host alone cell path length /μm	Guest-host mixture	Guest-host cell path length /μm
t-Bu-10OCB	14.9	*t*-Bu-10OCB _ *t*-Bu-**7** dye	15.1
		t-Bu-10OCB _ *t*-Bu-**11** dye	14.3
t-Bu-11OCB	15.8	*t*-Bu-11OCB _ *t*-Bu-**9** dye	15.8
		t-Bu-11OCB _ *t*-Bu-**11** dye	15.5

2.2.4.4 Spectroscopic measurements

Polarised UV-visible absorption experiments were performed using an Agilent Technologies Cary 8454 UV-vis spectrometer, with a rotatable polariser and an in-house built heated slide holder. The filled cells were placed within the heated slide holder and the measurements were taken at 5 ^{o}C intervals on cooling, in the range of 25-95 ^{o}C starting from above the clearing point of the liquid crystal host. At each temperature the polariser was turned parallel to the alignment direction to record the resulting absorption spectrum ($A_{\parallel}$), then the polariser was rotated 90 ^{o} and the perpendicular measurement ($A_{\perp}$) recorded.

Polarised spectra of an aligned sample of each of the hosts alone was recorded using the same method. The appropriate resulting spectra from the hosts were subtracted from the respective guest-host spectra to give the final results presented in these studies.

2.3 Computational methods

2.3.1 Density functional theory (DFT) calculations

Density functional theory (DFT) calculations were performed using the Gaussian 16A.03 software package,[160] using the B3LYP functional[161] and the 6-31G(d) basis set. The structures were optimised for molecules in the gas phase.

Molecular lengths and widths were measured from the DFT optimised structures using a script made by L.C.Abbott. The molecular length of the host molecules was defined as the distance between the centres of the atoms at the opposite ends of the molecule parallel to the minimum MOI axis, plus the van der Waals radii of the atoms at each extreme, as illustrated as **a** in Figure 2.2. The molecular width was defined as twice the atom furthest distance perpendicular to the minimum MOI axis plus the van der Waals radii of the atoms at each extreme, as illustrated as **b** in Figure 2.2. For the host molecules, the structures were optimised with the alkoxy chains in the all-*trans* conformation and for the dye molecules the two chains were optimised with the alkoxy chains in the all-*trans* conformation.

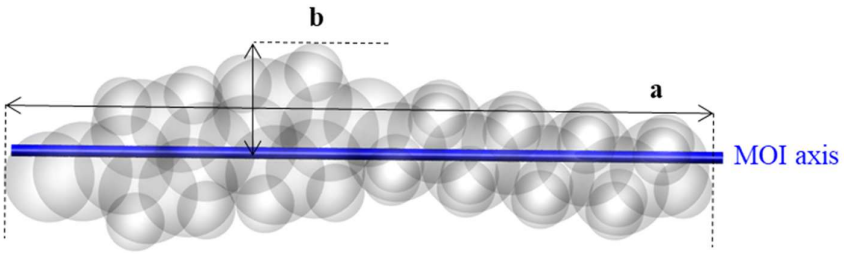

Figure 2.2: Schematic of 8OCB to show distances being measured for the molecular length and width, relative to the minimum moment of inertia (MOI) axis.

The molecular length for the dye molecules are defined in the same way as for the hosts, with the length coming from the van der Waals radii of the of the furthest atoms and the width coming from twice the furthest distance perpendicular to the minimum MOI axis. The TD-DFT calculations for the dyes were carried out at the same level of theory as the DFT calculations. These calculations determined the transition dipole moments and energies for 20 transitions to excited singlet states.

2.3.2 Molecular dynamics (MD) simulations

Fully atomistic molecular dynamics (MD) simulations were performed using GROMACS 2019.3 employing the General Amber Force Field (GAFF v. 1.81),[162-168] with modifications utilised for the simulation of liquid crystal molecules, as outlined below. Initial topologies were produced using AmberTools 19, and converted into GROMACS compatible formats using Acpype, using a script which was made by M.T.Sims/L.C.Abbott.

Modifications were made to the van der Waals parameter for aromatic carbon atoms and the torsional force constants of the C-C-C-C groups within the alkoxy chains, which were replaced with values reported by Boyd and Wilson.[169] The values are summarised in Table 2.5.

Table 2.5: Summary table of constants for Ryckaert-Bellemans potential.

	Constants / kJ mol^{-1}					
	C0	C1	C2	C3	C4	C5
Original GAFF C-C-C-C values	3.68192	3.09616	-2.09200	-3.01248	0.00000	0.00000
Adjusted C-C-C-C values[169]	0.518587	-0.230192	0.896807	-1.491340	0.000000	0.000000

Atomic charges were determined using the RESP method for structures optimised at the B3LYP/6-31G (d) level using the Gaussian 16A.03 software package.[160] An initial gas-phase density lattice was constructed with random head–tail molecular orientations and an initial isotropic gas phase randomisation was undertaken for 20 ps, at 298 K with no pressure coupling. The initial simulation set up resulted in an essentially isotropic phase at the start of the simulation, which was determined by an orientational order parameter (S) of <0.1. The system was then compressed at 50,000 bar over ca. 7 ps at 298 K, with v-rescale temperature coupling and Berendsen pressure coupling, to give an isotropic liquid density.[168] Next, the energy of the system was minimised and then a short run of ca. 10 ps at 298 K was carried out with an isotropic Berendsen pressure coupling at 1 bar, using v-rescale temperature coupling.[170-172]

The simulation was then equilibrated at a chosen temperature by a short MD run for 200 ps, with v-rescale temperature coupling and Berendsen pressure coupling, and then the final MD simulation was run at the equilibrated temperature. These two steps were done with a long range dispersion correction applied to the energy and pressure (DispCorr = EnerPres). Simulations were run using 2 fs steps, with periodic boundary conditions and with all bonds constrained at their equilibrium lengths using the LINCS algorithm.[173] The temperature of the final simulations was controlled using a Nosé–Hoover thermostat (tau_t = 1.0 ps) and a pressure of 1 bar was maintained using Parrinello-Rahman pressure coupling (tau_p = 4.0 ps).[174] A van der Waals cut-off of 1.2 nm was employed, and long-range electrostatic interactions were calculated by using the Particle Mesh Ewald method also with a cut-off of 1.2 nm.[175]

MD trajectory frames were recorded every 50 ps and were visualised using VMD v. 1.9.3 software. The simulations were analysed using Gromacs analysis tools or prewritten analysis tools made by M.T.Sims and L.C.Abbott.

The director at each frame was calculated using the eigenvector from the largest eigenvalue from the ordering tensor, as defined by Sims et al.[106] The orientational order parameter (S) was calculated for each frame using a vector chosen for the rigid part of each molecule, and using the ordering tensor as defined by Boyd and Wilson.[169] The vector chosen here for the host molecules was from the nitrogen of the –CN to the aromatic C attached to the oxygen atoms for the liquid crystal host molecules and between the phenyl carbon atoms which are attached to the alkoxy chain of each of the phenyl groups in the guest dye molecules. The angle (θ) between this vector and the overall director of the nematic or SmA phase was used to calculate S for each molecule, which was then averaged over the whole ensemble to give an overall order parameter for the phase as a whole, as shown in equation 2.3.

Equation 2.3: $$S = \left\langle \frac{1}{2}\left(3\cos^2\theta - 1\right) \right\rangle$$

The translational order parameter, τ, was calculated using equation 2.4 and was determined based on the translated order of the molecules in the layers, with a layer spacing (d) in a simulated box of length (L);[176] the translational order parameter was determined along the layer normal vector.[106] In order to determine the layer normal and translational order parameter the position of the molecule, z, can be assigned by selected an atom to represent it.[106] For the liquid crystal host molecules it was selected as the C_4' biphenyl carbon atom attached to the CN group and for the dye guest molecules it was selected as the centre of the molecule for the analysis.

Equation 2.4: $$\tau = \sqrt{\left[\left\langle \cos\left(\frac{2\pi z}{d}\right)\right\rangle - \frac{d}{2\pi L}\sin\left(\frac{2\pi L}{d}\right)\right]^2 + \left\langle \sin\left(\frac{2\pi z}{d}\right)\right\rangle^2}$$

For the initial set of liquid crystal host simulations the lattice was 6 x 6 x 6 molecules (216 molecules). These simulations were done using isotropic pressure coupling, allowing the dimensions of the box to vary but maintaining the relative box dimensions. For the second, full set of liquid crystal host simulations the lattice was 10 x 10 x 10 molecules (1000

molecules). These full simulations were done using anisotropic pressing coupling, allowing the dimensions of the box to change by different amounts in any dimension. The GAFF modifications were also employed in these simulations with the exception of the parameter for the O-C-C-C dihedral, for the original GAFF values were used.[177]

The guest-host simulations were done using 1000 molecules of the host with 9 molecules (~1-1.5 wt%) of the chosen dye, which were added into the initial lattice by adding the dye molecules in random positions in the starting box. A larger range of dyes were used in the simulations than the experimental studies, using m = 4-13 for the **m** dyes and m = 2-11 for the *t*-Bu-**m** dyes. These simulations were run at the same temperatures as the respective host only simulation. For the orientational order parameters of the dyes, a vector between the terminal carbon atom of the phenyl rings was used, as the long axis of the molecules for the analysis. The orientational order parameter of the dyes was calculated with respect to the director of the host liquid crystal phase. For the translational order parameter a point in the centre of the middle aromatic ring of the anthraquinone unit was selected as a proxy for the centre of mass (COM) The translational order parameters were calculated using the respective layer spacings from the host alone simulations.

Chapter 3

Liquid crystal host molecules

3.1 Introduction

This chapter will detail the experimental and computational work undertaken on the nOCB and *t*-Bu-nOCB liquid crystal host materials, using the methods outlined in chapter 1 and described in chapter 2. Section 3.2 reports the experimental results and initial analysis and section 3.3 reports the computational results and initial analysis. In section 3.4 there is further analysis along with a combined discussion of the experimental and computational results, with conclusions to this chapter given in section 3.5.

3.2 Experimental studies

3.2.1 Polarised optical microscopy and differential scanning calorimetry studies

3.2.1.1 Phase identification

The host materials studied in this work exhibited liquid crystalline behaviour which was characterised initially using polarised optical microscopy (POM). The POM samples were heated into the isotropic liquid phase and the defect textures were observed upon slow cooling, as shown in Figure 3.1, Figure 3.2 and Figure 3.3, until the sample crystallised. On cooling, 8OCB and 9OCB first exhibited a schlieren texture with both two- and four- brush disclinations, as illustrated by the red circles in Figure 3.1, indicating the presence of a nematic (N) phase. The nematic phase has a characteristic "threaded" texture under crossed polarisers,[21] and the brush-like texture corresponds to optical extinction due to the orientations of the molecules, with either two or four of these brushes meeting at point defects in the structure to form the characteristic texture observed.[20] At lower temperatures, 8OCB and 9OCB exhibit a fan-like focal conic texture accompanied by homeotropic regions, indicating the presence of the smectic A (SmA) phase. The homeotropic regions appear optically extinct as the molecules are aligned with an average orientation perpendicular to the glass surfaces.[33] The focal conic texture is characterised by the ellipse and hyperbola defects, as illustrated by the blue squares in Figure 3.1. The ellipse and hyperbola appear as optically extinct intersecting lines, representing the local changes in the direction of the optical axis. The fan-like shapes are due to the surface of the focal conic domains which are flattened against the glass surfaces.[33] The other compounds studied in this series, 10-13OCB,

exhibit only a smectic A phase, given by the combination of focal conic and homeotropic defect textures as shown in Figure 3.2.

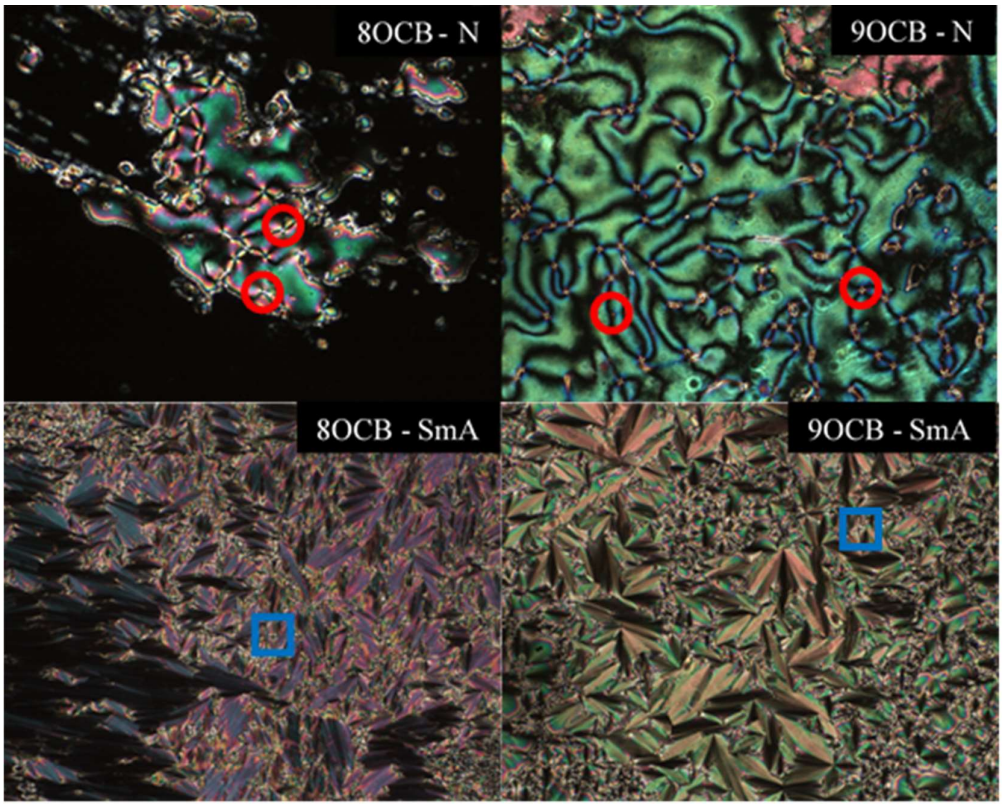

Figure 3.1: Photomicrographs showing the nematic (N) and smectic A (SmA) phases of 8OCB and 9OCB as observed between crossed polarisers. Images were taken on cooling from the isotropic liquid, captured at: (top L to R) 70.0 ºC, 79.0 ºC, (bottom L to R) 66.6 ºC and 77.8 ºC. The red circles show characteristic features for the nematic phase and blue squares show characteristic features of the smectic A phase.

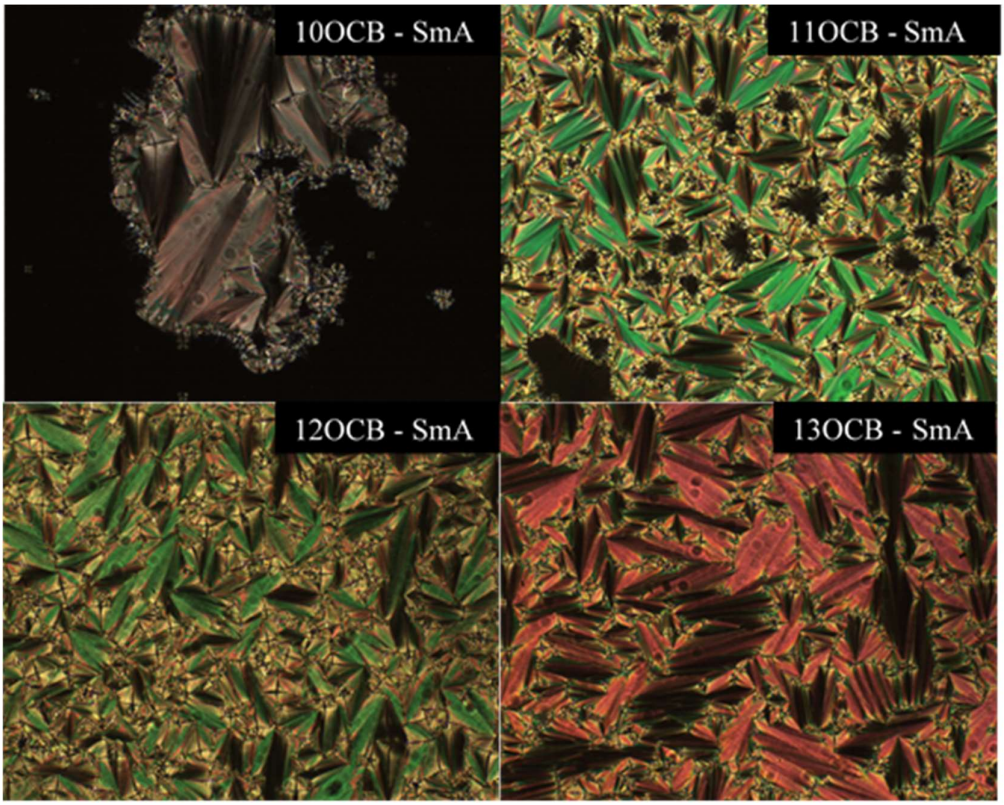

Figure 3.2: Photomicrographs showing the smectic A (SmA) phase of the nOCB series, where n = 10-13, as observed between crossed polarisers. Images were taken on cooling from the isotropic liquid, captured at: (top L to R) 84.1 ^{o}C, 86.9 ^{o}C, (bottom L to R) 86.4 ^{o}C and 89.7 ^{o}C.

For the *t*-Bu-nOCB series, all the members of the series exhibited only a focal conic texture accompanied by regions of homeotropic orientation, as illustrated by the example photomicrographs shown in Figure 3.3. This observation confirms that all members of this series only exhibit the smectic A liquid crystalline phase and no nematic phases were evident.

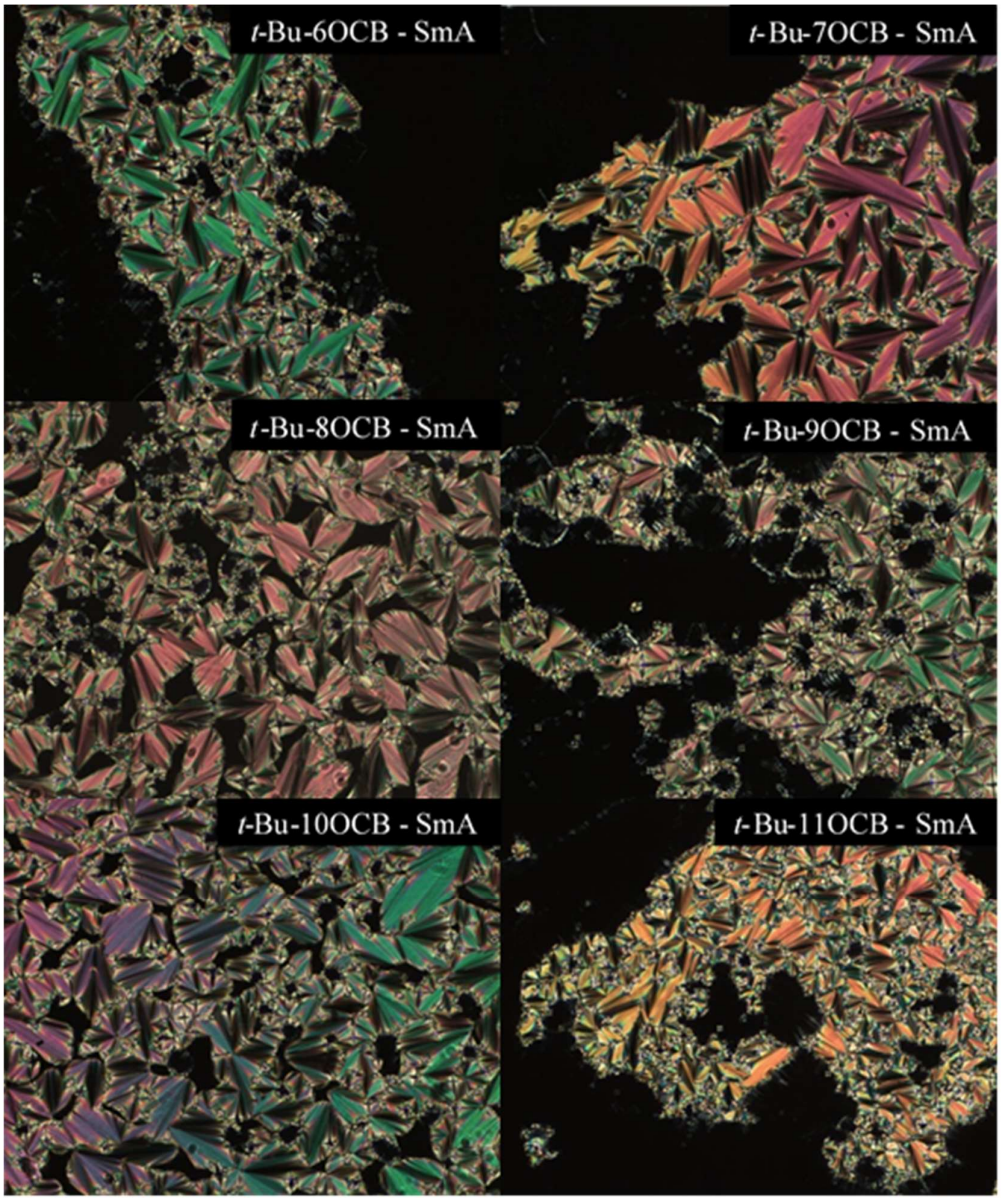

Figure 3.3: Photomicrographs showing the smectic A (SmA) phase of the *t*-Bu-nOCB series, where n = 6-11, between crossed polarisers. Images were taken on cooling from the isotropic liquid, captured at: (top L to R) 59.2 °C, 77.5 °C, (middle L to R) 76.0 °C, 79.8 °C, (bottom L to R) 82.2 °C and 84.0 °C.

3.2.1.2 Transition temperatures and enthalpies

Transition temperatures were determined using a combination of POM and differential scanning calorimetry (DSC). The transition from the crystal (Cr) to either the liquid crystal (N or SmA) phase or the isotropic (Iso) liquid phase, known as the melting point, was recorded on the first heating cycle of the DSC experiment. The transition temperature between the isotropic liquid and a mesophase, known as the clearing point, and the transition temperatures between different mesophases were recorded on cooling during POM studies. The transition temperatures and transition enthalpies for the nOCB series are given in Table 3.1, with the related DSC traces given in Figure 3.4.

On each DSC heating cycle, the largest peak shows the melting point of the crystal to form the smectic A phase, which was identified by microscopy. For some of the materials additional peaks are observed in the region of the melting point, and may be attributed to transitions occurring between different crystal forms. In the synthesis of the liquid crystal samples, the samples were crystallised from ethanol and additional peaks in the first heating cycle of some of the samples may be attributed to different crystal forms present from the synthesis. In each DSC cooling cycle, the largest peak arises from crystallisation and it occurs at a lower temperature than the respective melting point observed on heating. This observation may be attributed to supercooling of the molten samples,[3] which may also produce crystals with subtly different forms and structural defects. Due to this process, the different crystal forms may melt at different temperatures in the following heating cycles, resulting in different melting points on the three cycles. The melting point from the first cycle is reported here as the measurement from the initial crystal form. The largest peaks in each cooling cycle may also appear different on each cooling cycle due to different crystal forms occurring.

In each DSC heating cycle, the smaller peak in the region of 80-90 ^{o}C shows the clearing point transition from the mesophase into the isotropic liquid. For 8OCB and 9OCB, there is another small peak at 70-80 ^{o}C which can be assigned to the smectic A to nematic phase transition, which was also identified from the microscopy experiments; these peaks are small, with this peak for 8OCB being particularly weak, as shown in the magnified regions in Figure 3.4. In each DSC cooling cycle, there is a smaller peak in the region of 80-90 ^{o}C

corresponding to the clearing point, and it is similar to that in the heating cycle. For 8OCB and 9OCB, there is also a corresponding nematic to smectic A peak which also is similar to that in the heating cycle.

Across the three DSC cycles there is good reproducibility observed for the clearing points and the transition temperatures between the mesophases, indicating the compounds were thermally stable, and there is also good reproducibility when the heating and cooling cycles are compared for these transitions. The presence of DSC peaks at all these phase transitions indicates that they are all first order transitions that involve a distinct energy intake and or release at the transition temperature. The phase transition temperatures measured by DSC and POM for the nOCB series show a good match with literature values for n = 8-12.[105] As the chain length increases from 8OCB to 13OCB the melting point and clearing point transition temperatures generally increase as summarised in Table 3.1. The transition enthalpies, given in square brackets in Table 3.1, also show a general increase with chain length. The transition enthalpy values for the melting point are approximately 10 times larger than the other transition enthalpies, reflecting the relative changes in the phase structure at the transitions. The transition enthalpies for the clearing points of 8OCB and 9OCB are approximately 1 kJ mol^{-1}, whereas those for the rest of the series are ~3-5 kJ mol^{-1}, reflecting that these two sets of clearing points are in relation to two different mesophases, namely nematic and smectic A, respectively.

Table 3.1: Transition temperatures, in ^{o}C, for the nOCB series. Transition enthalpies, in kJ mol^{-1}, for each transition are given in square brackets.

Molecule	Cr	T [ΔH]	SmA	T [ΔH]	N	T [ΔH]	Iso
8OCB	●	52.1 [32.65]	●	67.2 [0.05]	●	80.1 [0.83]	●
9OCB	●	64.5 [38.65]	●	78.3 [0.71]	●	80.3 [1.37]	●
10OCB	●	60.9 [37.31]	●	-	-	84.7 [2.87]	●
11OCB	●	69.9 [37.37]	●	-	-	87.1 [3.70]	●
12OCB	●	69.1 [42.07]	●	-	-	89.1 [4.35]	●
13OCB	●	76.0 [42.20]	●	-	-	92.3 [4.69]	●

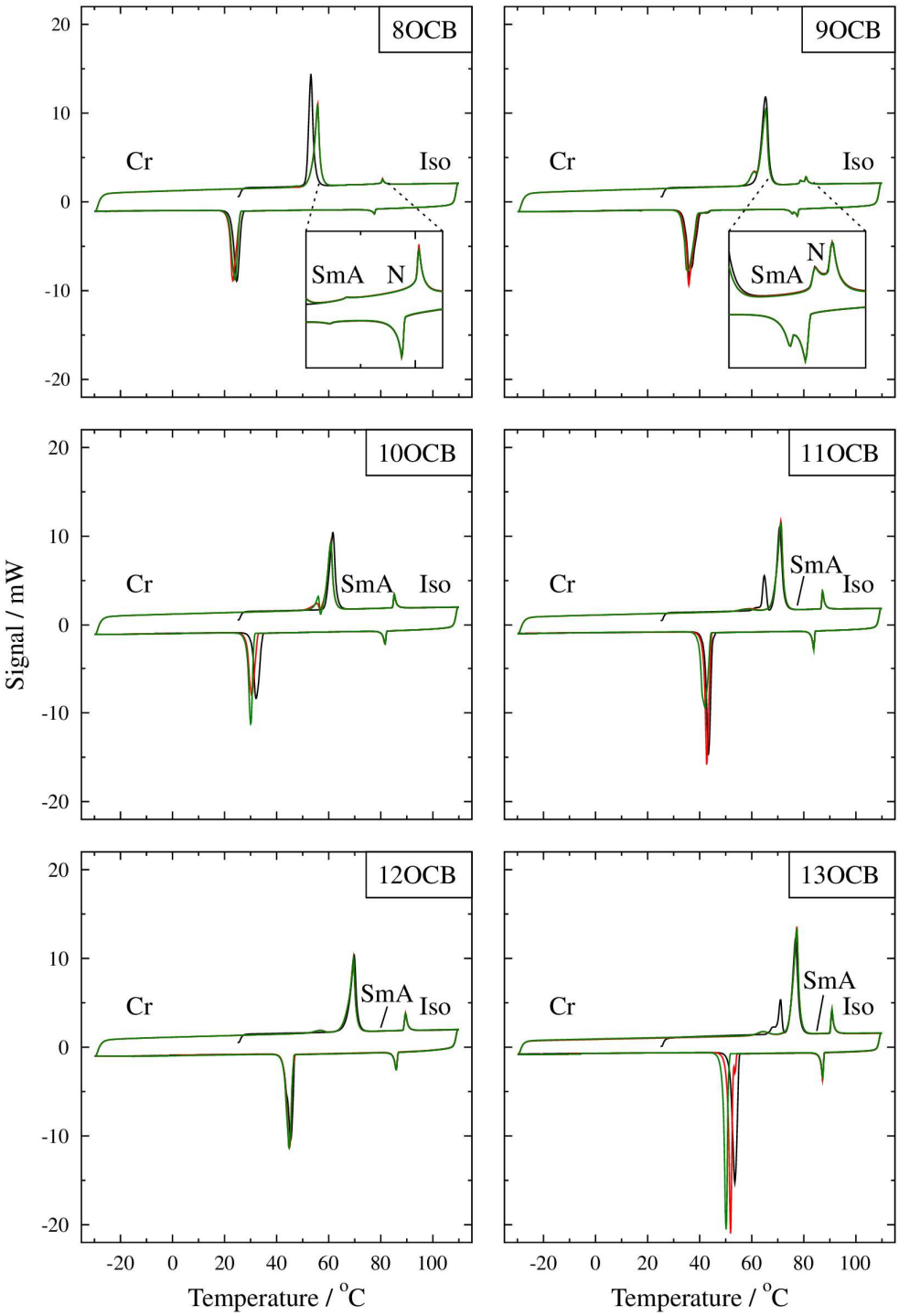

Figure 3.4: Differential scanning calorimetry traces for the nOCB series. The three cycles are coloured black, red and green for the first, second and third cycles, respectively.

The transition temperatures and transition enthalpies for the *t*-Bu-nOCB series are given in Table 3.2, with the related DSC traces given in Figure 3.5. In each DSC heating cycle for *t*-Bu-8OCB to *t*-Bu-11OCB, the largest peak shows the melting point of the crystal to form the smectic A phase, which was identified by microscopy. For some of the materials additional peaks are observed in the region of the melting point, and may be attributed to transitions occurring between different crystal forms, as discussed above for the nOCB series. The smaller peak in the region of 70-90 °C for n = 8-11 shows the clearing point transition from the smectic A phase into the isotropic liquid. For *t*-Bu-6OCB and *t*-Bu-7OCB, only the melting point is observed on heating with no peak observed for the clearing point transition. A small peak in the range 60-80 °C in the cooling cycle for these compounds is attributed to the isotropic to smectic A transition. This transition is observed at a temperature below the melting point, indicating that for these materials there is a monotropic smectic A phase which was identified by microscopy.

For all these samples, the temperature at which crystallisation occurs on cooling is lower than the melting point and may be attributed to supercooling of the sample.[3] There is a smaller peak in the region of 70-90 °C on cooling for *t*-Bu-8OCB to *t*-Bu-11OCB, corresponding to the clearing point, which has a similar value to that in the heating cycle. There is good reproducibility of the transition temperatures and clearing points across the three DSC cycles. There is also good reproducibility of these transitions when the heating and cooling cycles are compared, indicating that the compounds were thermally stable. The presence of DSC peaks at all these phase transitions indicates that they were all first order transitions.

For the *t*-Bu-nOCB series, only the smectic A phase was observed. As the chain length increases from *t*-Bu-8OCB to *t*-Bu-11OCB, there is a general increase in the clearing point temperature, as summarised in Table 3.2, as observed for the nOCB series. The transition enthalpies for the clearing point of the *t*-Bu-nOCB series also show an increase with chain length, which is similar to the nOCB series. For the melting point transition temperatures, the general trend is a decrease with chain length for the *t*-Bu-nOCB series, which is opposite to the trend seen for the nOCB series. The transition enthalpy values for the melting point

are approximately 10 times larger than the other transition enthalpies for the *t*-Bu-nOCB series, reflecting the change in structure at the transitions, as seen also for the nOCB series.

Table 3.2: Transition temperatures, in °C, for the *t*-Bu-nOCB series. Transition enthalpies, in kJ mol^{-1}, for each transition are given in square brackets. Values in round brackets denote a monotropic phase transition.

Molecule	Cr	T [ΔH]	SmA	T [ΔH]	Iso
t-Bu-6OCB	●	75.5 [35.96]	(●	60.4 [3.18])	●
t-Bu-7OCB	●	80.0 [33.26]	(●	79.3 [3.99])	●
t-Bu-8OCB	●	73.7 [30.89]	●	76.4 [4.09]	●
t-Bu-9OCB	●	55.4 [24.65]	●	82.1 [4.93]	●
t-Bu-10OCB	●	61.7 [34.11]	●	82.8 [5.65]	●
t-Bu-11OCB	●	62.7 [27.52]	●	87.2 [6.66]	●

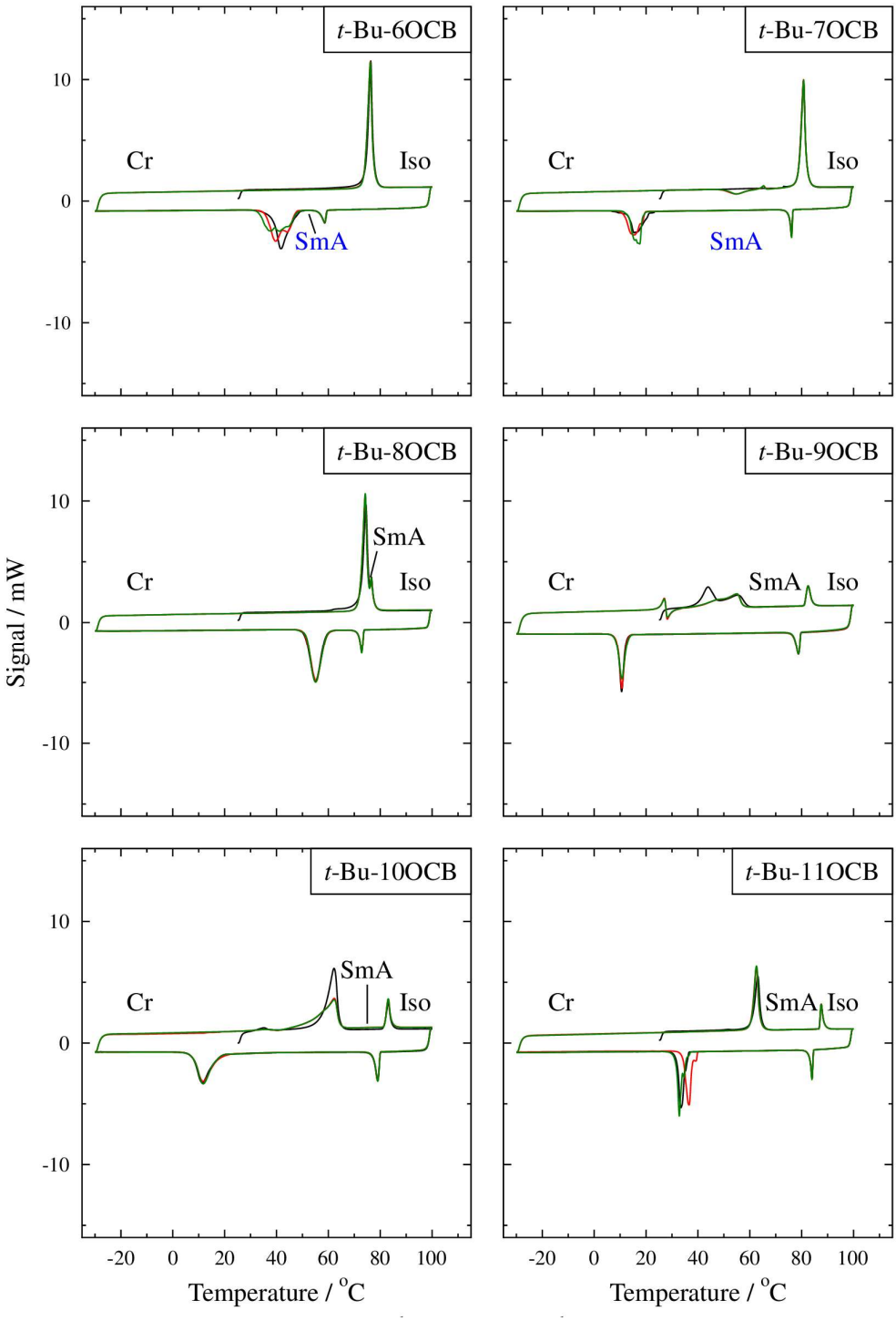

Figure 3.5: Differential scanning calorimetry traces for the t-Bu-nOCB series. The three cycles are coloured black, red and green for the first, second and third cycles, respectively. The SmA labels below the trace (blue) show the presence of a monotropic liquid crystal phase.

3.2.1.3 Transition entropies

Transition entropy values were calculated using the transition temperatures and transition enthalpies from the DSC experiments. The calculated transition entropies in J K^{-1} mol^{-1} are given in Table 3.3 for the nOCB series and Table 3.4 for the *t*-Bu-nOCB series. The transition entropy values are also given as ΔS/R, which are normalised unitless values obtained on division by the universal gas constant (R).

For the nOCB series, the melting point and clearing point transition entropies show a general increase with increasing chain length. For 8OCB and 9OCB the clearing point transition entropies are in the range 2-4 J K^{-1} mol^{-1}, whereas for 10OCB to 13OCB the clearing point transition entropies are in the range 8-13 J K^{-1} mol^{-1}. The values for this transition may reflect the difference in the phases at the clearing point transition, as for 8OCB and 9OCB this is a transition between the nematic phase and the isotropic liquid and for the rest of the series it is between the smectic A phase and the isotropic liquid. For 8OCB and 9OCB the transition entropies for the smectic A to nematic phase transition are in the range 0.1-2 J K^{-1} mol^{-1}, which is lower than those for the other transitions occurring.

For the *t*-Bu-nOCB series, the clearing point transition entropies increase with chain length, which was also observed for the nOCB series. The melting point transition entropies show a general decrease with increasing chain length, which is in contrast to the nOCB series.

Table 3.3: Transition entropies, given in J K^{-1} mol^{-1} and ΔS/R values, for the nOCB series.

Molecule	Cr	ΔS	$\frac{\Delta S}{R}$	SmA	ΔS	$\frac{\Delta S}{R}$	N	ΔS	$\frac{\Delta S}{R}$	Iso
8OCB	●	100.3	12.07	●	0.1	0.02	●	2.4	0.28	●
9OCB	●	114.4	13.76	●	2.0	0.24	●	3.9	0.47	●
10OCB	●	111.7	13.43	●	-	-	-	8.0	0.97	●
11OCB	●	108.9	13.10	●	-	-	-	10.3	1.24	●
12OCB	●	122.9	14.78	●	-	-	-	12.0	1.44	●
13OCB	●	120.9	14.54	●	-	-	-	12.9	1.55	●

Table 3.4: Transition entropies, given in J K^{-1} mol^{-1} and ΔS/R values, for the *t*-Bu-nOCB series. Values in brackets denote a monotropic phase transition.

Molecule	Cr	ΔS	$\frac{\Delta S}{R}$	SmA	ΔS	$\frac{\Delta S}{R}$	Iso
t-Bu-6OCB	●	103.1	12.40	(●	9.6)	1.15	●
t-Bu-7OCB	●	94.2	11.33	(●	11.4)	1.37	●
t-Bu-8OCB	●	89.0	10.71	●	11.8	1.42	●
t-Bu-9OCB	●	75.0	9.02	●	13.9	1.67	●
t-Bu-10OCB	●	101.8	12.25	●	15.9	1.91	●
t-Bu-11OCB	●	81.9	9.85	●	18.4	2.22	●

3.2.2 X-ray diffraction studies

3.2.2.1 Diffraction patterns

To assess the structure of the liquid crystal phase within the hosts, X-ray diffraction (XRD) experiments were undertaken for each sample. At selected temperature intervals starting from the isotropic liquid the sample was irradiated and diffraction images collected. Figure 3.6 shows examples of the diffraction images for the shortest comparable chain lengths in the nOCB series (8OCB) and *t*-Bu-nOCB series (*t*-Bu-6OCB), with the temperature going from lower to higher from left to right.

At the highest temperatures for all samples, the diffraction pattern shows a feature-less texture, which corresponds to the isotropic liquid (Iso) phase and results from the lack of structure within this phase. As the temperature decreases, 8OCB and 9OCB exhibit two broad arcs in the small angle region, at 2θ = 2-3 °, which is close to the centre of the 2D diffraction pattern, and two broad arcs in the wide angle region, at 2θ = 15-22 °, at the edge of the diffraction pattern and at 90 ° to the arcs in the small angle region. The arcs in the small angle region indicate the distance between the centres of neighbouring molecules along the long axis of the molecules, giving an average molecular length.[140] The arcs in the wide angle region indicate the distance between the centres of masses of neighbouring molecules, perpendicular to the molecular long axis, giving an approximation of the average molecular width. The presence of the small angle peaks suggests that there is some diffuse structure in the phase, but as both pairs of arcs are broad it can be suggested that the phase

is more liquid-like, consistent with it being a nematic (N) phase. At lower temperatures for 8OCB and 9OCB, the small angle peak becomes sharper and the wide angle peak remains broad. The sharper small angle peak suggests a more defined diffraction plane, suggesting that there is a more defined structure in the phase, arising from a layer spacing and indicating the presence of a smectic A (SmA) phase. At the lowest temperatures the samples showed multiple diffractions, which correspond to the layer planes in the crystal (Cr).

For 10OCB to 13OCB in the nOCB series and all the *t*-Bu-nOCB series, there is no nematic phase present and only the sharper small angle peaks and broader wide angle peaks arising from the smectic A (SmA) phase are observed. The small angle peaks for these materials appear as a ring rather than the two arcs observed for 8OCB and 9OCB. The sample holder in the SAXS instrument has magnets applying a field across the sample. The presence of diffraction spots or narrow arcs are a direct result of alignment of the nematic phase and retention of the alignment upon transition to the smectic A phase in these particular samples.[140]

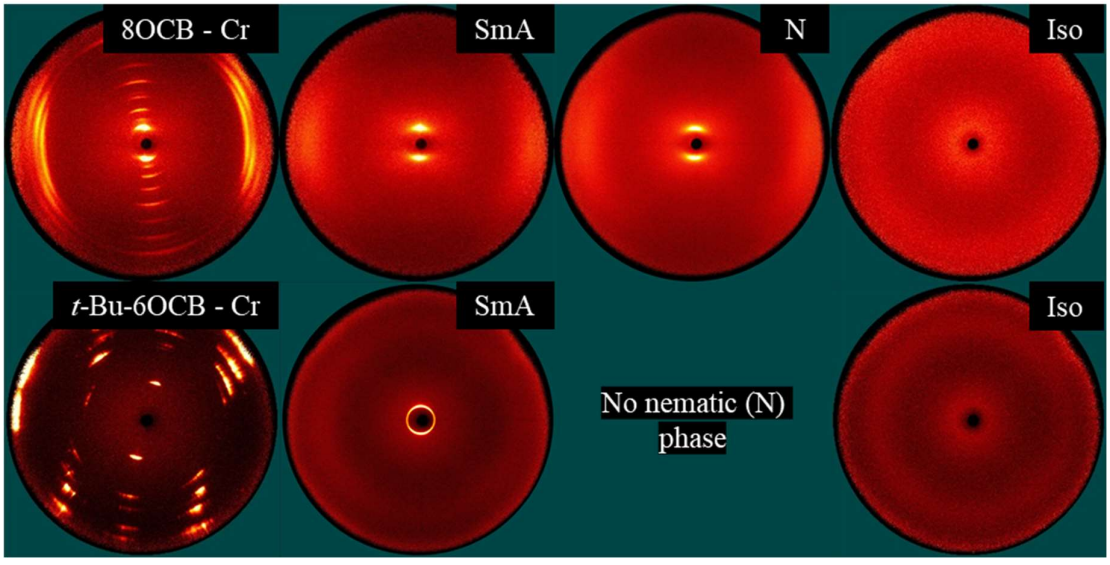

Figure 3.6: Example diffraction patterns for the two shortest alkoxy chain lengths of the nOCB series and *t*-Bu-nOCB series (8OCB and *t*-Bu-6OCB). The temperatures are (Top left to right) 33.3, 66.2, 77.1, 95.3 ºC, (Bottom left to right) 30.9, 57.7, 94.1 ºC.

The 2D diffraction pattern was integrated at each temperature interval to produce a 1D plot of signal intensity against diffraction angle (2θ), as shown in Figure 3.7 for the nOCB series and Figure 3.8 for the *t*-Bu-nOCB series. The figures show the full 2θ range of 0-25 °, and two expanded figures in the small and wide angle regions show the peaks in greater detail. For the nOCB series the intensity of the peaks from 8OCB and 9OCB was 2 to 4 times higher than the intensity of the peaks from the rest of the nOCB series. This may be due to the presence the nematic phase occurring before the smectic A phase on cooling, resulting in bulk alignment of the phase giving a higher intensity. Generally the smectic A phase peak showed an increase in intensity with decreasing temperature, with slight shifts to lower 2θ values being observed. The *t*-Bu-nOCB series only showed the presence of one liquid crystal phase for all values of n in the series, and where n = 7, 9, 10 and 11 it can be observed that the peak shows an increase in intensity with and a shift to lower 2θ values as the temperature decreases.

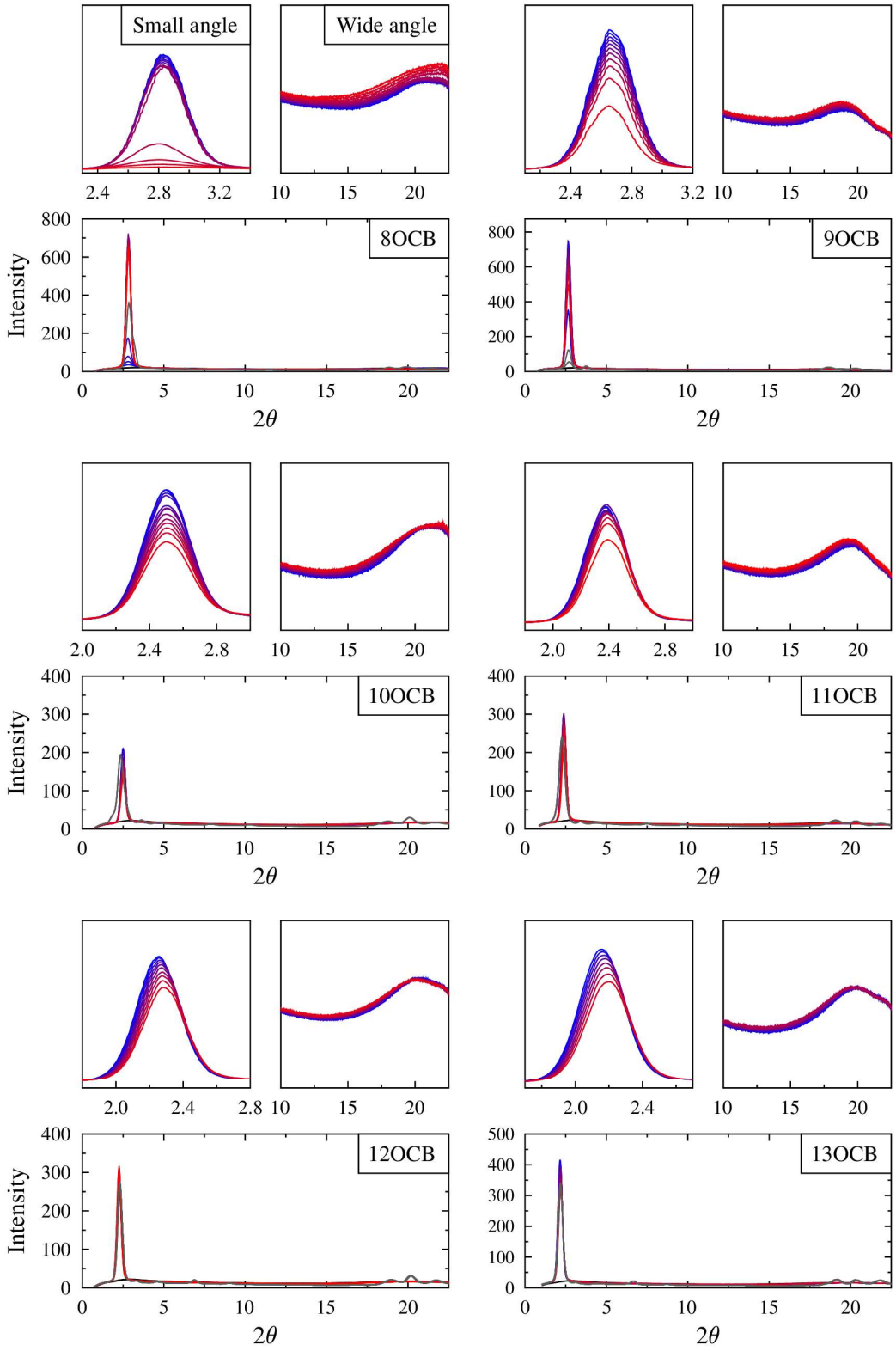

Figure 3.7: X-ray diffraction traces for the nOCB series. The isotropic liquid and crystal phases are coloured grey and the red to blue colouring of the liquid crystal peaks illustrates the change with decreasing temperature in the range 95.3 to 29.7 ºC.

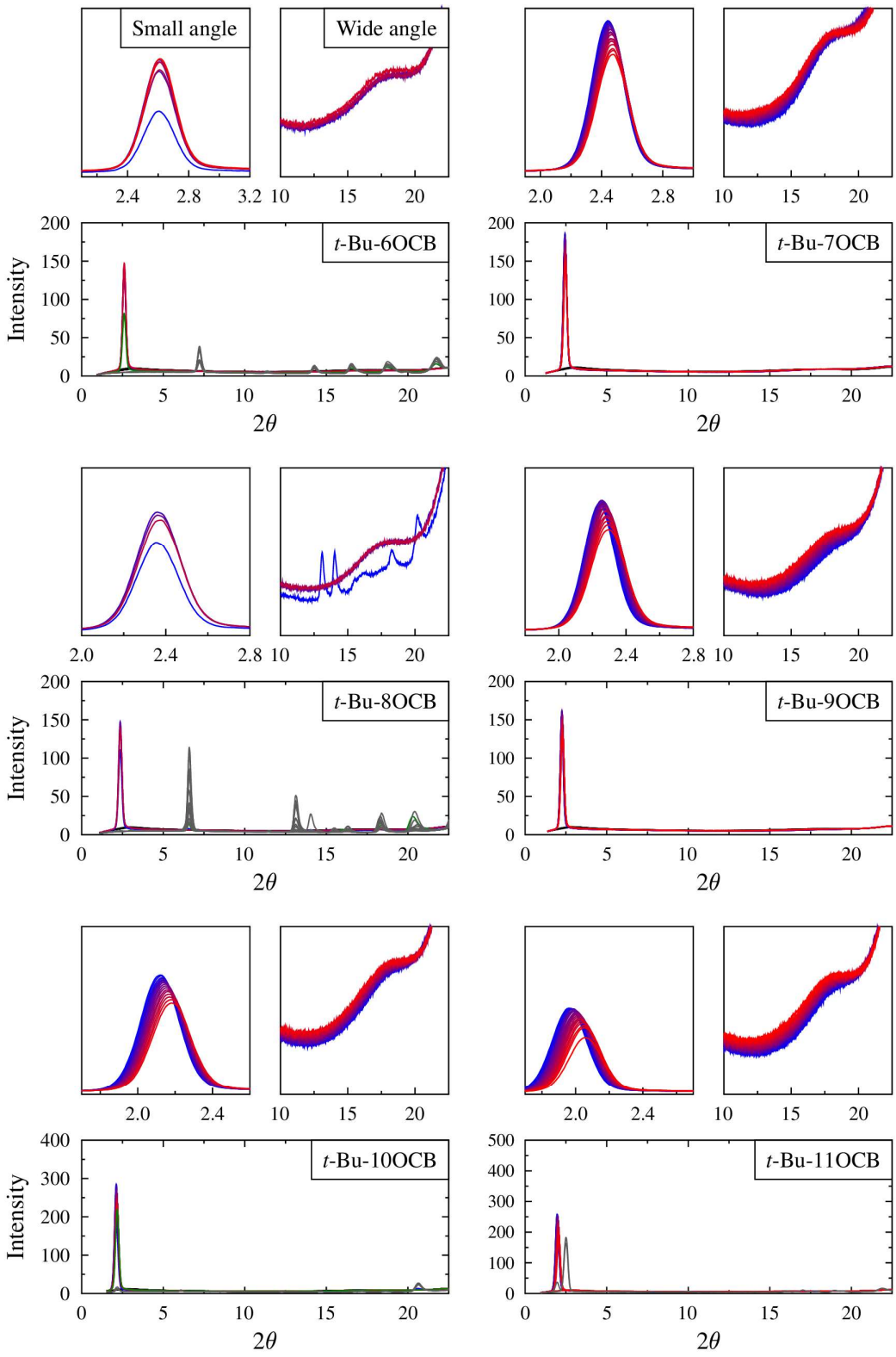

Figure 3.8: X-ray diffraction traces for the *t*-Bu-nOCB series. The isotropic liquid and crystal phases are coloured grey, co-existing phases are coloured green and the red to blue colouring of the SmA peak illustrates the change with decreasing temperature in the range 94.1 to 30.9 °C.

3.2.2.2 Layer spacing

In order to gain an insight into the structure of the liquid crystal phases the diffraction angle peaks were converted into layer spacing values, d. For the nOCB series, the small angle layer spacing at each temperature interval is given in Table 3.5. 8OCB and 9OCB show a slightly larger layer spacing at higher temperatures, which may be attributed to the nematic phase being present, followed by a decrease in the layer spacing at the nematic to smectic A phase transition. For the layer spacing in the smectic A phase, there is a small increase in the layer spacing as the temperature decreases for n =11-13, but any increase in layer spacing as the temperature decreases is small for the shorter chain lengths.

Table 3.5: Layer spacing values determined from small angle XRD peaks for the nOCB series, * denotes the nematic phase for 8OCB and 9OCB.

nOCB, where n =	8	9	10	11	12	13
T / °C	d /nm					
29.7						
33.3	3.12					
37.0	3.12					
40.6	3.12		3.53			
44.3	3.12	3.31	3.53			
47.9	3.12	3.30	3.52			
51.6	3.12	3.30	3.52	3.72		
55.2	3.12	3.30	3.52	3.71	3.92	
58.9	3.12	3.30	3.52	3.71	3.91	
62.5	3.13	3.30	3.52	3.70	3.91	
66.2	3.10	3.30	3.52	3.70	3.90	4.09
69.8	3.16*	3.31	3.52	3.70	3.89	4.08
73.5	3.15*	3.31	3.52	3.69	3.88	4.07
77.1	3.14*	3.32	3.52	3.69	3.88	4.06
80.7	3.12*	3.33*	3.52	3.68	3.87	4.05
84.4			3.52	3.68	3.86	4.04
88.0				3.68	3.86	4.03
91.7						4.02
95.3						

For the *t*-Bu-nOCB series, the small angle layer spacing at each temperature interval is given in Table 3.6. Generally, it is observed that as the temperature decreases the layer spacing increases, but the effect is very small for the shortest chain length (n = 6). For *t*-Bu-10OCB and *t*-Bu-11OCB the change across the relevant temperature range is 0.12 nm and 0.21 nm, respectively, which clearly shows an increase in the layer spacing with the decreasing temperature.

Table 3.6: Layer spacing values determined from small angle XRD peaks for the *t*-Bu-nOCB series. † denotes the co-existence of the smectic A phase and crystal phase.

t-Bu-nOCB, where n =	6	7	8	9	10	11
T / °C	d /nm					
30.9		3.62		3.94		
33.3		3.62		3.93		
35.8		3.61		3.93		4.50
38.2		3.61		3.92		4.49
40.6		3.61		3.92		4.48
43.1		3.60		3.91	4.17†	4.47
45.5		3.60		3.91	4.17	4.46
47.9	3.39†	3.60		3.90	4.16	4.45
50.4	3.39	3.60		3.90	4.15	4.44
52.8	3.38	3.59		3.89	4.14	4.43
55.2	3.38	3.59		3.89	4.14	4.42
57.7	3.38	3.59		3.89	4.13	4.41
60.1	3.38	3.59		3.88	4.12	4.40
62.5	3.38	3.58		3.88	4.11	4.39
64.9		3.58		3.87	4.10	4.38
67.4		3.58	3.75†	3.87	4.10	4.37
69.8		3.58	3.74	3.87	4.09	4.36
72.2		3.58	3.73	3.86	4.08	4.35
74.7		3.58	3.73	3.86	4.07	4.34
77.1		3.57	3.72	3.85	4.06	4.33
79.5		3.57		3.85	4.06	4.32
82.0				3.85	4.05	4.31
84.4						4.30
86.8						4.29
89.2						
91.7						
94.1						

The wide angle peaks for both series are observed to be broad, as shown in the inset plots in Figure 3.7 and Figure 3.8. The peak positions were approximated by using a Gaussian fit to the relevant region in the plots, using 2θ = 17-22 ° for the nOCB series and 2θ = 15-20 ° for the *t*-Bu-nOCB series. This approach gives a 2θ value for the diffraction peak correlating to adjacent molecules within the layers, which was converted into a distance as given in Table 3.7 and Table 3.8 for the respective series. The wide angle distances were only calculated for the start and end of the phase ranges to give the overall changes occurring in each case.

For both series there is no significant change in the distance between adjacent molecules with changing temperature or for the different phases for 8OCB and 9OCB, where a nematic phase is present. It can be observed that the distance between the adjacent cyanobiphenyl cores is in the range 0.44-0.46 nm for the nOCB series and 0.50-0.52 nm for the *t*-Bu-nOCB series.

Table 3.7: Distance between adjacent molecules determined from wide angle XRD peaks for the nOCB series. * denotes the nematic phase for 8OCB and 9OCB.

nOCB, where n =	8	9	10	11	12	13
T / °C	Distance between adjacent centres of mass /nm					
29.7						
33.3	0.437					
37.0						
40.6			0.435			
44.3		0.461				
47.9						
51.6				0.453		
55.2					0.442	
58.9						
62.5						
66.2	0.440					0.450
69.8	*					
73.5	*					
77.1	*	0.463				
80.7	0.442*	0.462*				
84.4			0.445			
88.0				0.455	0.450	
91.7						0.455
95.3						

Table 3.8: Distance between adjacent molecules determined from wide angle XRD peaks for the *t*-Bu-nOCB series. † denotes the co-existence of the smectic A phase and the crystal phase.

t-Bu-nOCB, where n =	6	7	8	9	10	11
T / ºC	Distance between adjacent centres of mass /nm					
30.9		0.504		0.501		
33.3						
35.8						0.500
38.2						
40.6						
43.1					†	
45.5					0.499	
47.9	†					
50.4	0.510					
52.8						
55.2						
57.7						
60.1						
62.5	0.507					
64.9						
67.4			†			
69.8			0.515			
72.2						
74.7						
77.1			0.514			
79.5		0.507				
82.0				0.505	0.506	
84.4						
86.8						0.503
89.2						
91.7						
94.1						

3.3 Computational studies

3.3.1 Density functional theory studies

Density function theory (DFT) studies were undertaken on the two series, to determine the molecular dimensions by optimising the structures with the alkoxy chain in the all-*trans* conformation. The optimised structures for the nOCB series are given in Figure 3.9 and the optimised structures for the t-Bu-nOCB series are given in Figure 3.10. These figures show the all-*trans* conformation for each single-molecule calculation, and using these structures the molecular length (l) and width (w) was calculated. These distances were then used to calculate the aspect ratio (AR), using equation 3.1, and the values are summarised in Table 3.9, Table 3.10 and Figure 3.11.

Equation 3.1: $$AR = \frac{l}{w}$$

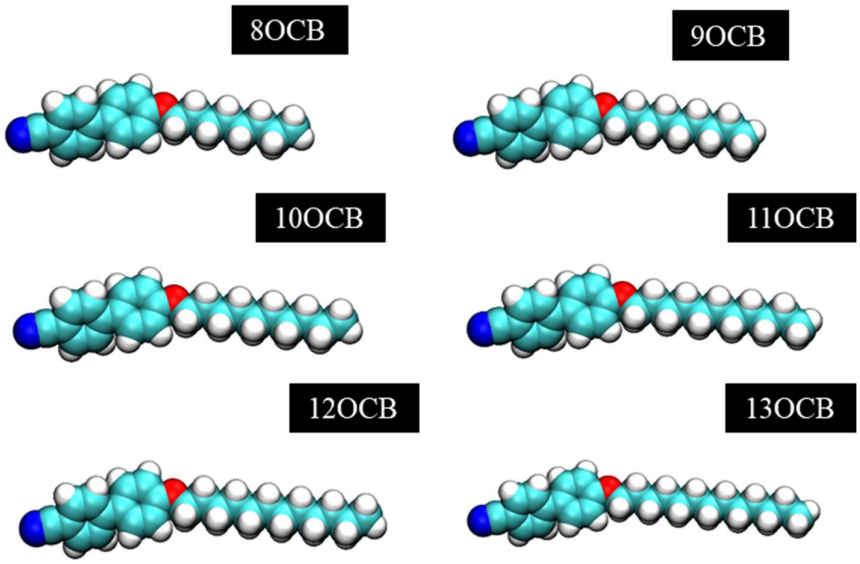

Figure 3.9: Optimised structures of the nOCB series, where the alkoxy chain is in the all-*trans* conformation. The biphenyl core is scaled to the same size.

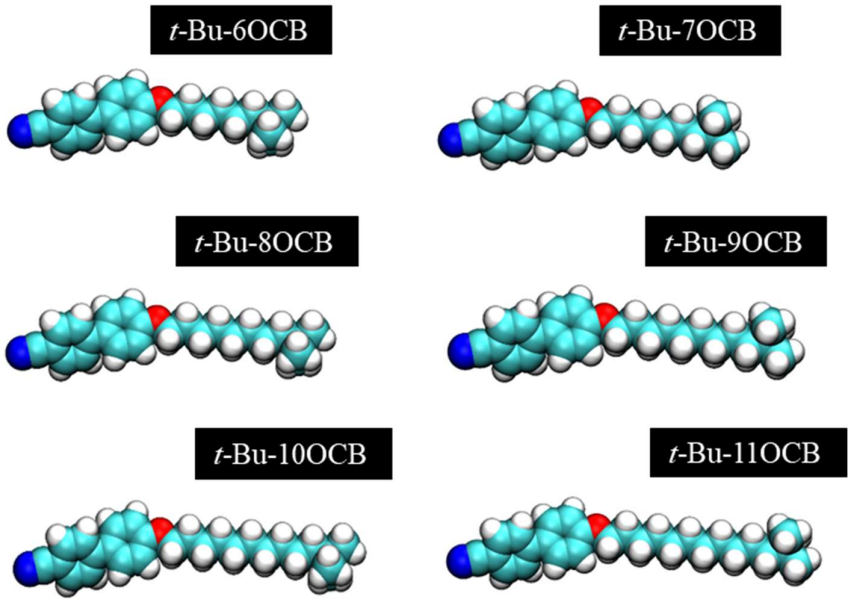

Figure 3.10: Optimised structures of the *t*-Bu-nOCB series, where the alkoxy chain is in the all-*trans* conformation. The biphenyl core is scaled to the same size.

Table 3.9: Summary of molecular lengths, widths and aspect ratios for the nOCB series.

Molecule	l /nm	w /nm	AR
8OCB	2.433	0.790	3.08
9OCB	2.565	0.799	3.21
10OCB	2.688	0.801	3.36
11OCB	2.819	0.805	3.50
12OCB	2.943	0.806	3.65
13OCB	3.074	0.808	3.81

Table 3.10: Summary of molecular lengths, widths and aspect ratios for the *t*-Bu-nOCB series.

Molecule	l /nm	w /nm	AR
t-Bu-6OCB	2.448	0.802	3.05
t-Bu-7OCB	2.570	0.788	3.26
t-Bu-8OCB	2.703	0.805	3.36
t-Bu-9OCB	2.827	0.795	3.55
t-Bu-10OCB	2.958	0.805	3.68
t-Bu-11OCB	3.083	0.799	3.86

Figure 3.11 shows plots of the molecular lengths, widths and aspect ratios against n for both series. It can be observed that the molecular length of the all-*trans* conformer is similar for comparable chain lengths in the two series. For both series the length increases

approximately linearly with the number of carbon atoms in the alkoxy chain. In the case of the widths, the nOCB series shows a general increase in width with increasing chain length, but there is also a small odd-even variation observed; as the chain length increases from odd to even values there is a smaller increase in the width than observed for the increase seen from even to odd. For the *t*-Bu-nOCB series, the is no clear general trend over the increasing chain length, but a pronounced odd-even effect is seen, with a smaller width being observed at odd chain lengths with respect to the even chain lengths.

For the nOCB series the slight odd-even trend in the widths is not clearly evident in the aspect ratios, which appear to show an approximately linear increase with increasing chain length. For the *t*-Bu-nOCB series, the odd-even trend in the widths is large enough to appear in the aspect ratio and there is also a general trend of increasing aspect ratio with increasing chain length.

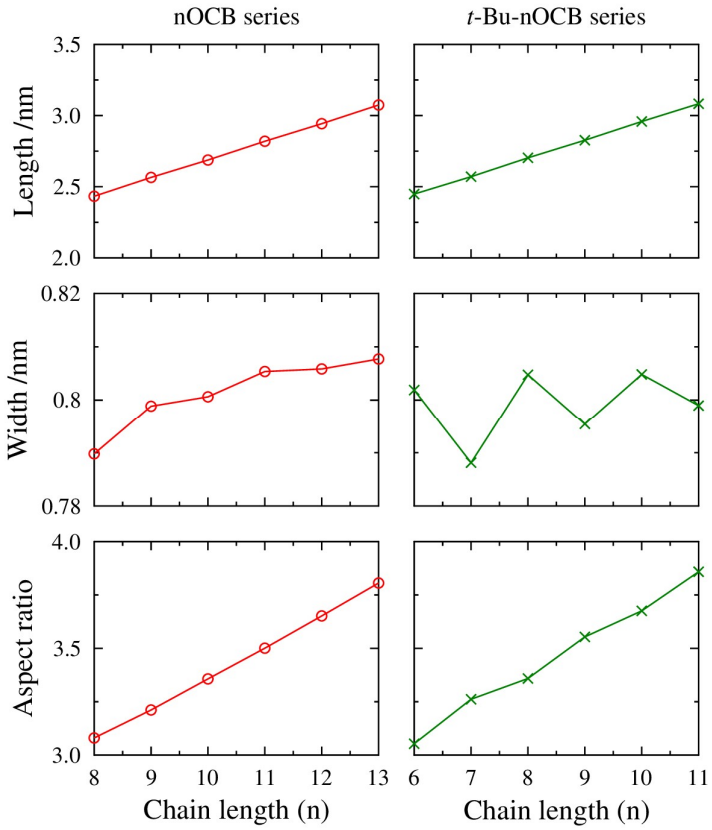

Figure 3.11: Summary of the lengths (l), widths (w) and aspect ratios (AR) across the two series with increasing alkoxy chain length.

3.3.2 Molecular dynamics studies

3.3.2.1 Clearing point determination

The first step in the MD simulation work was to observe the formation of a liquid crystal phase, smectic A in particular, for the two series. The initial simulations used the optimised structure from the DFT calculations and placed 216 molecules in a 6 x 6 x 6 lattice as the starting point for the simulations, as shown in Figure 3.12 a). From this point an isotropic gas phase randomisation was done and two energy minimisations were undertaken, with an illustrative result shown in Figure 3.12 b). The box was then compressed to give a liquid density and then equilibrated at the given simulation temperature, with an illustrative result shown in Figure 3.12 c). From this point the simulations were run for 500 ns, with an illustrative result shown in Figure 3.12 d). Each figure, a-d is scaled for illustration and the box dimensions differ in each case.

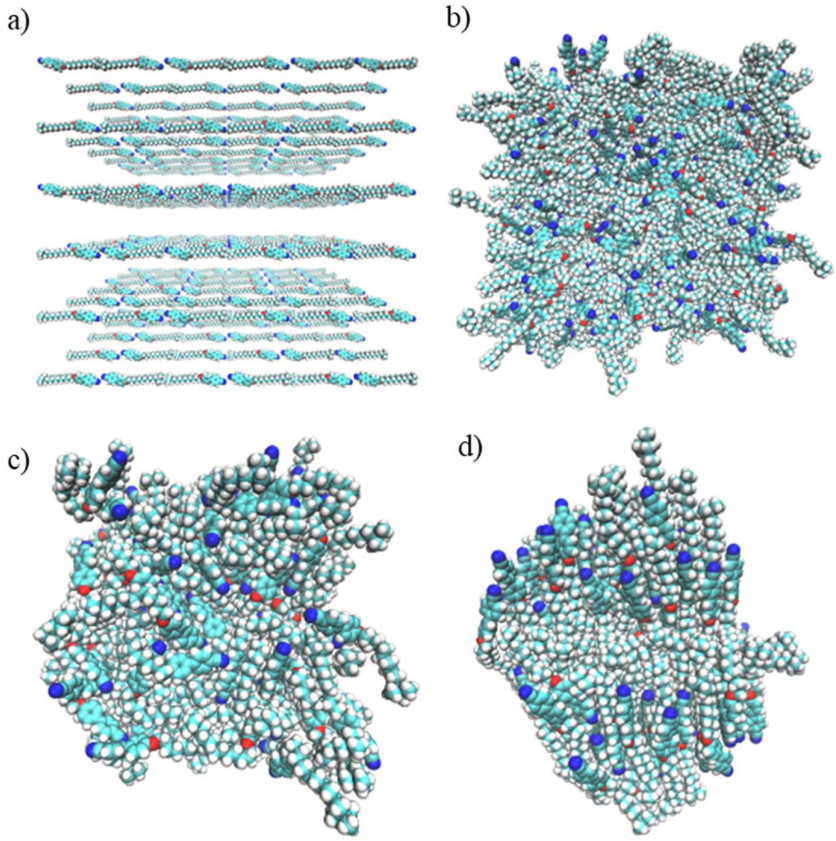

Figure 3.12: Examples of the simulation steps for t-Bu-11OCB, with each scaled appropriately for illustration. a) Initial lattice. b) After isotropic gas phase randomisation and energy minimisations steps. c) After compression and equilibration. d) After 500 ns run at 353 K.

These steps were repeated across a range of temperatures for each of the materials and simulation runs were done at temperatures of 353, 363 and 373 K. The initial run of 353 K was used to match the simulations run on 11OCB and *t*-Bu-11OCB by Sims et al.[106] The orientational order (S) and translational order (τ) at each temperature were calculated from the simulation runs and the results are shown in Figure 3.13 for the nOCB series and Figure 3.14 for the *t*-Bu-nOCB series.

It is worth noting that the order parameter values do not start at zero, as would be expected for a completely disordered isotropic liquid system, due to the small number of molecules used in the system. For the nOCB series, it can be observed that the orientational order parameter increased with time in the simulation and reached a plateau at 0.7-0.8, suggesting that the molecules aligned with one another and formed an organised phase. The translational order parameter also increased to a plateau at 0.2-0.4, for n = 10-13, suggesting that there was a diffusely layered structure being formed, such as a smectic phase.

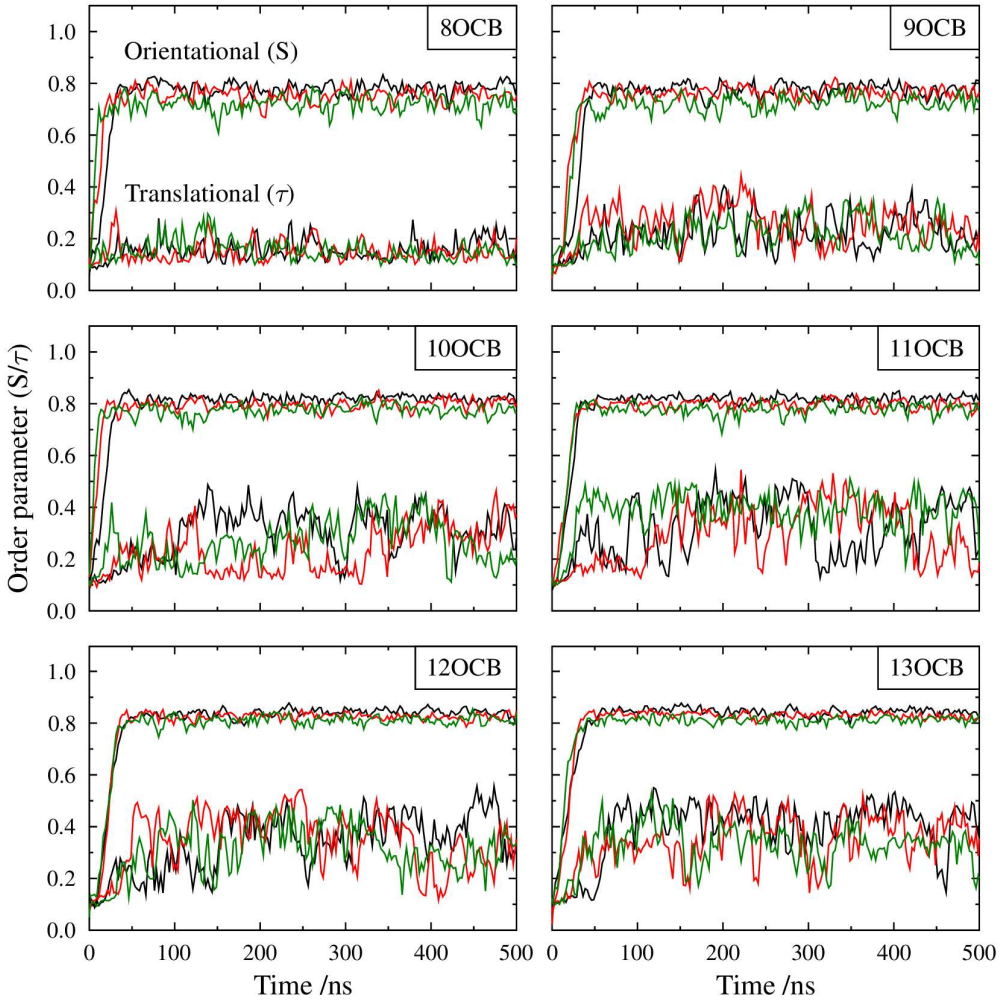

Figure 3.13: Summary plots of the orientational (S, top lines) and translational (τ, bottom lines) order parameters for the nOCB series, at 353, 363 and 373 K (black, red and green lines respectively). The values have been averaged over 50 frames in these plots.

For the *t*-Bu-nOCB series, the orientational order parameters increase to 0.6-0.8, which are similar to the values seen for the nOCB series, and the translational order parameters increase to 0.4-0.6, and are slightly higher than the values for the nOCB series. These order parameters suggest that the smectic phase has also formed for this series, at these simulated temperatures. For some of the simulations there is some breakdown in the order parameters, suggesting that these simulation temperatures are not as well suited for forming the smectic phase for this series as they were for the nOCB series. The rise time of the orientational and translational order parameters of the *t*-Bu-nOCB series was also longer than those of the nOCB series.

Overall, these small simulations showed that it was possible to simulate the smectic phase for both the nOCB series and the *t*-Bu-nOCB series. From these simulations it can also be observed that the phase is not stable at all the simulation temperatures, indicating that it is particularly important to select the simulation temperature carefully to allow the phase to reach a stable plateau.

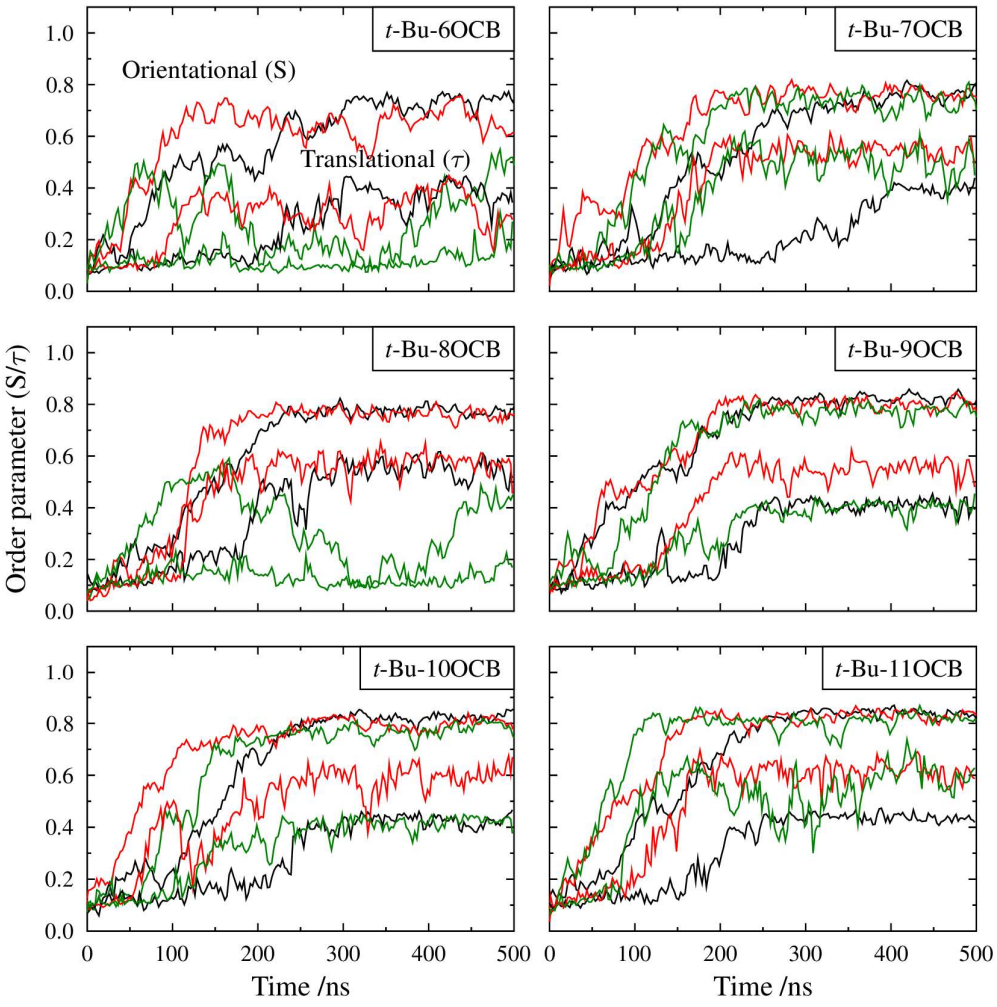

Figure 3.14: Summary plots of the orientational (S, top lines) and translational (τ, bottom lines) order parameters for the *t*-Bu-nOCB series, at 353, 363 and 373 K (black, red and green lines respectively). The values have been averaged over 50 frames in these plots.

Following these initial 216 molecule simulations, it was necessary to determine the temperature at which the smectic phase of each compound transitioned into the isotropic liquid, known as the simulated clearing point. As the simulations are run using a general force field for liquid crystals that has not been parameterised for these particular molecules, as discussed in the chapter 1 and 2, the simulated clearing point may not match the experimental clearing point.

To begin with, the final coordinates of the 353 K simulations with 216 molecules were used as the starting point of simulations to determine the simulated clearing point. The temperature of each simulation was varied and the impact on the liquid crystal phase was observed. From this starting point with the molecules in the liquid crystal phase, 100 ns simulations were undertaken at a range of temperatures. For both series increments of 10 K were selected for the simulation temperatures, starting at 363-383 K and going to 413-423 K for the nOCB series, and starting at 363-383 K and going to 423 K for the *t*-Bu-nOCB series. A smaller window of 2 K increments was also selected around the region that the clearing point was observed to be occurring. As shown in Figure 3.15 and Figure 3.16, for the nOCB and *t*-Bu-nOCB series, respectively, the orientational order of the phase was preserved throughout the 100 ns simulation at the lower temperature in these series, but as the temperature was increased there was a breakdown in the order of the phase and the orientational order parameter decreased to a value of ~0.1 at the highest temperatures.

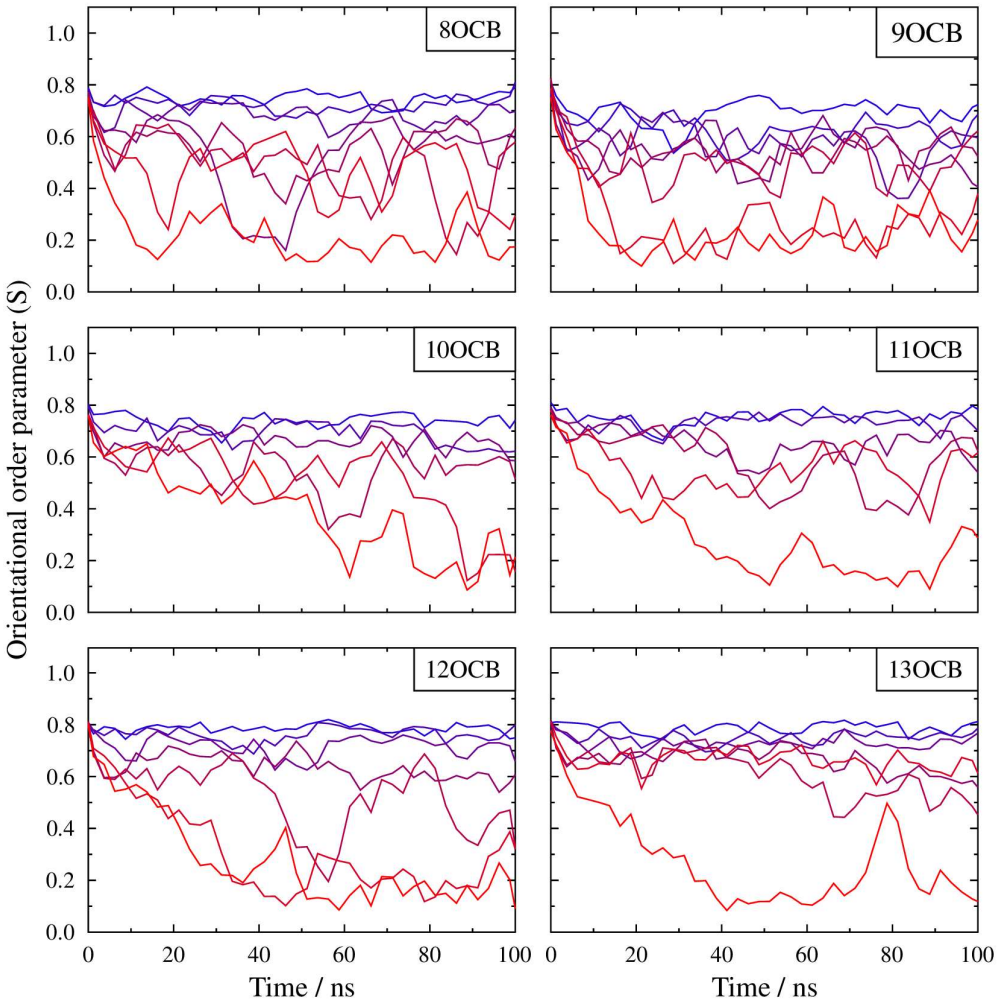

Figure 3.15: Orientational order parameter (S) of the nOCB series across a range of temperatures of 363-413 K for n = 8, 383-413 K for n = 9-11 and 383-423 K for n = 12-13. Colour gradient blue to red from lowest temperature simulation to highest temperature simulation. The values have been averaged over 50 frames in these plots.

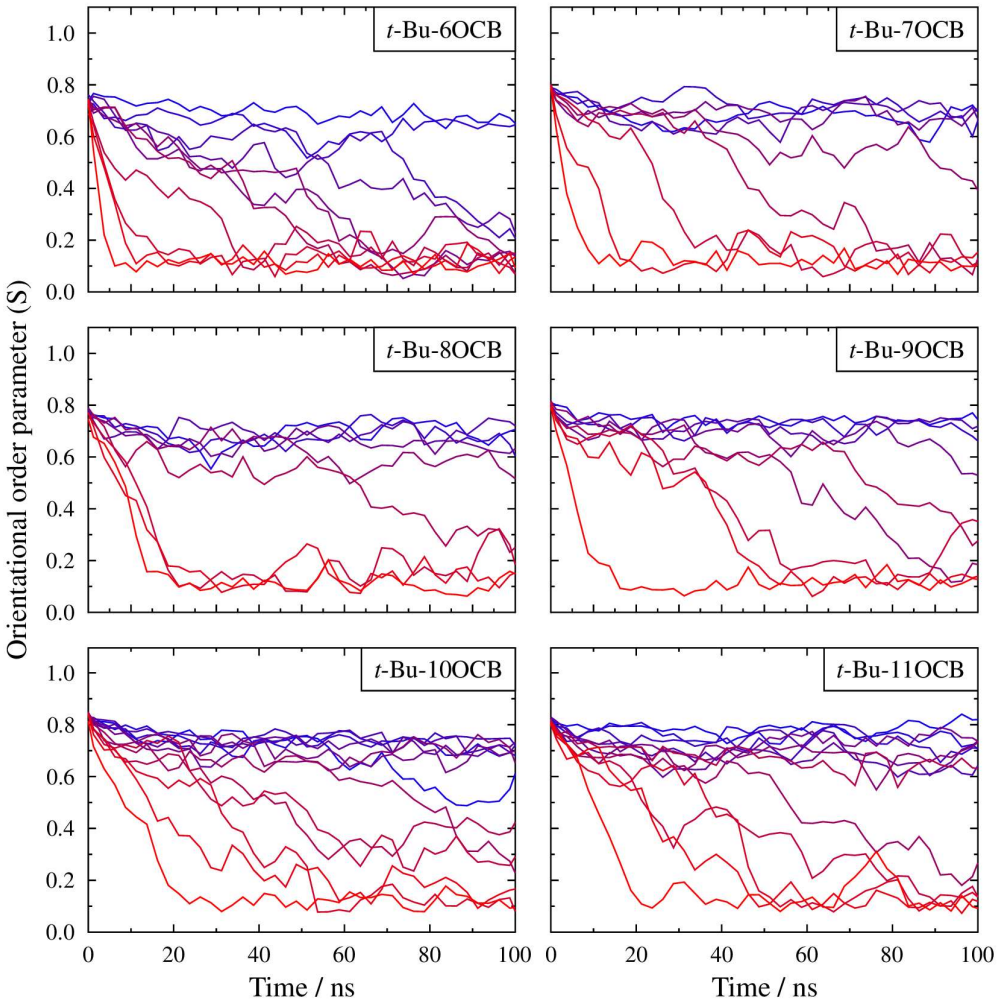

Figure 3.16: Orientational order parameter (S) of the *t*-Bu-nOCB series across a range of temperatures of 363-423 K for n = 6, and 383-423 K for all others. Colour gradient blue to red from lowest temperature simulation to highest temperature simulation. The values have been averaged over 50 frames in these plots.

The average orientational order parameter (S) in the final 20 ns of each simulations was plotted against the temperature (T) of the simulation, shown in Figure 3.17. The data shows the orientational order parameter remains higher at the lower temperatures, and as the temperature increases there is a point at which the orientational order parameter drops to less than 0.25, showing a breakdown in the orientational order. A modified Haller equation,[178, 179] given in equation 3.2, was used to fit the data where S was greater than 0.25. These fits are shown as the red lines in Figure 3.17.

The fits were used primarily to determine the approximate simulated clearing point (T_c) for each of the compounds in these simulations, and this also gave the respective order parameter exponent (β) values

Equation 3.2:
$$S = \left(1 - \left(\frac{T_c}{T}\right)\right)^{\beta}$$

The results of the fits are given in Table 3.11 and Table 3.12. Given that these are small simulations over a limited time, there is a reasonably good fit to the orientational order parameters for both the nOCB series and the *t*-Bu-nOCB series. The nOCB series has higher simulated clearing point values than the *t*-Bu-nOCB series and the simulated clearing point values generally increase with chain length for each series. Both of these trends match the observations from the experimental work on these materials. The order parameter exponent (β) determined for 8OCB showed a similar magnitude to the value for 8OCB determined from the XRD measurements of Kapernaum and Giesselmann,[178] and the respective values of β for 11OCB and *t*-Bu-11OCB also show a similar magnitude to those reported by Sims et al. from simulations and application of a modified Haller equation.[106]

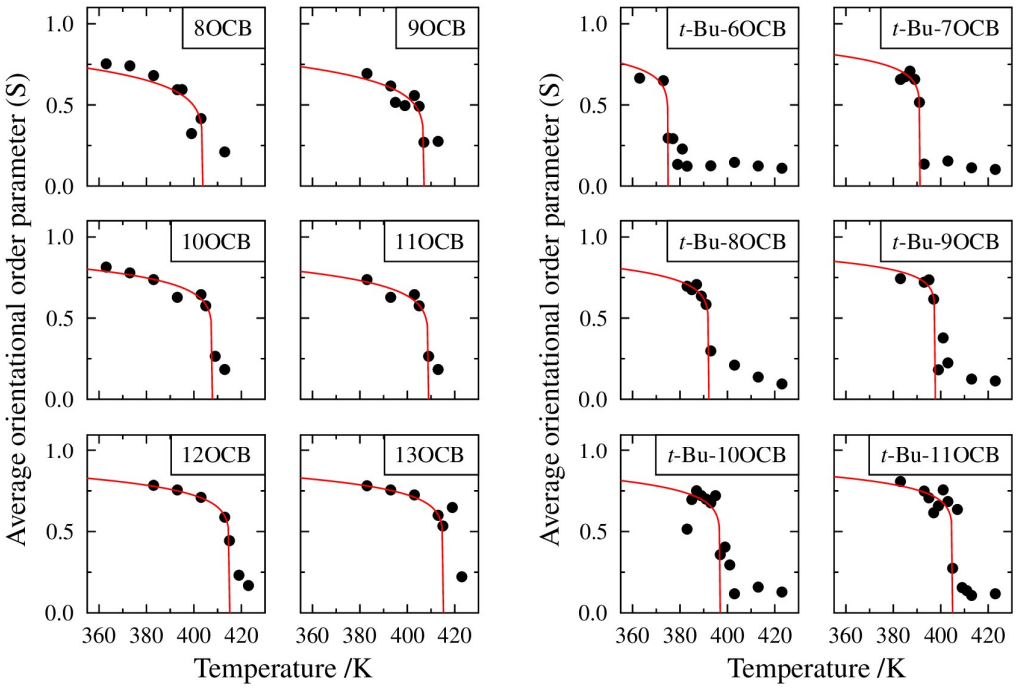

Figure 3.17: Orientational order parameters (S) averaged over the last 20 ns of each different temperature simulation for both series, given as dots. The red line gives a fit to the modified Haller equation obtained by non-linear fitting of the data.

Table 3.11: Summary of clearing point (T_c) and order parameter exponent (β) values obtained using the modified Haller fit with errors of 2σ, and the R^2 of the fit in each case, for the nOCB series.

Molecule	T_c / K	β	R^2
8OCB	403.8 ± 2.8	0.15 ± 0.04	0.715
9OCB	407.1 ± 0.2	0.15 ± 0.02	0.853
10OCB	407.8 ± 4.0	0.11 ± 0.02	0.880
11OCB	409.0 ± 7.5	0.12 ± 0.03	0.965
12OCB	415.1 ± 0.3	0.10 ± 0.02	0.998
13OCB	415.6 ± 0.3	0.10 ± 0.04	0.993

Table 3.12: Summary of clearing point (T_c) and order parameter exponent (β) values obtained using the modified Haller fit with errors of 2σ, and the R^2 of the fit in each case, for the *t*-Bu-nOCB series.

Molecule	T_c / K	β	R^2
t-Bu-6OCB	375.0 ± 3.5	0.10 ± 0.03	0.945
t-Bu-7OCB	391.3 ± 0.4	0.09 ± 0.01	0.755
t-Bu-8OCB	392.2 ± 1.1	0.09 ±0.08	0.829
t-Bu-9OCB	397.7 ± 1.1	0.07 ± 0.01	0.649
t-Bu-10OCB	397.0 ± 8.6	0.09 ±0.04	0.507
t-Bu-11OCB	405.0 ± 5.3	0.09 ± 0.02	0.886

3.3.2.2 1000 molecule simulations

For the larger simulations with 1000 molecules, the clearing point temperatures determined from the 216 molecule simulations were used to calculate reduced temperatures (T_{red}) within the simulations, as given by equation 3.3, where T is the temperature and T_c is the clearing point temperature.

Equation 3.3: $$T_{red} = \frac{T}{T_c}$$

Using this information, a single reduced temperature of 0.95 was selected for all the simulations, to try to ensure that the simulations all ran at approximately the same point in the phase across both series. 8OCB and 9OCB are in the nematic phase at the experimental reduced temperature of 0.95 and so the relevant reduced temperature was calculated relative to the transition temperature of the smectic A phase into the N phase ($T_{SmA \rightarrow N}$) rather than the clearing point (T_c) to ensure that the smectic A phase was present. From the experimental data, a reduced temperature of 0.95 relative to the nematic to smectic A transition temperature corresponds to 0.91 and 0.92 for 8OCB and 9OCB, respectively, and hence these reduced temperatures were used relative to the clearing point temperatures in the 1000

molecule simulations. The simulation temperatures used are summarised in Table 3.13 for the nOCB series and Table 3.14 for the *t*-Bu-nOCB series.

Table 3.13: Summary of temperatures used in the 1000 molecule simulations for the nOCB series.

Molecule	Simulation T / K
8OCB	369.5
9OCB	375.3
10OCB	387.4
11OCB	388.6
12OCB	394.3
13OCB	394.8

Table 3.14: Summary of temperatures used in the 1000 molecule simulations for the *t*-Bu-nOCB series.

Molecule	Simulation T / K
t-Bu-6OCB	356.3
t-Bu-7OCB	371.7
t-Bu-8OCB	372.6
t-Bu-9OCB	377.9
t-Bu-10OCB	377.2
t-Bu-11OCB	384.8

The 216 molecule simulations had used isotropic pressure coupling, such that the box dimensions were limited to varying by the same amount in all directions. The 1000 molecule simulations were run with anisotropic pressure coupling which allowed the box to vary by different amounts in all directions and allowed the layers to form without any constraints as a result of the box shape. As a result of this anisotropic pressure coupling, the box shape extended a large amount in one dimension for some of the simulations, resulting in a breakdown in the liquid crystal phase. In these cases the simulation was stopped at a point where the liquid crystal phase had formed and before the box had extended, then the simulation was restarted from that point, which generally gave a relatively stable simulation after the restart. The simulations were analysed to determine the orientational order parameter (S), translational order parameter (τ) and layer spacing (d), which can be compared within and between the two series of materials because all the simulations were run at the same reduced temperature.

The orientational order parameter (S), translational order parameter (τ) and layer spacing (d) against time for the MD simulations of the nOCB series and the *t*-Bu-nOCB series are shown in Figure 3.18. All the simulations were run over a time range which was suitable to obtain a stable liquid crystal phase which was found to 500 ns for the nOCB series and 1500 ns for the *t*-Bu-nOCB series. An analysis was undertaken over the same time range within each series where the simulations had reached a stable plateau in both order parameters. Values for the nOCB series were averaged over the final 200 ns of the 500 ns simulations and values for the *t*-Bu-nOCB series were averaged over the final 600 ns of the 1500 ns simulations. The averaged values for each of the hosts in the series is given in Table 3.15 and Table 3.16 for the nOCB and *t*-Bu-nOCB series respectively

For the nOCB series, the orientational order parameter (S) rises to a plateau in 25-50 ns and remains relatively stable through the rest of the simulation, with the value showing less fluctuation for the longer chains in the series. In terms of the translational order parameter (τ), for the nOCB series where n = 11-13 the value rises over a longer time of 60-80 ns and reaches a stable plateau which remains relatively stable for the rest of the simulation. In the case of 13OCB, there is a small decrease in the translational order parameter after 450 ns. For the nOCB series where n = 8-10 the translational order parameter rises over a similar time range to that for n = 11-13, but the plateau reached has a lower value. For the layer spacing (d), there is plateau reached in all cases but the value is less stable for the shorter chain lengths than the longer chain lengths in the series. Overall, the longer chain lengths of n = 11-13 show a relatively stable, layered structure, whereas the shorter chain lengths of n = 8-10 show a more diffuse structure within the layers. The nOCB series has an average layer spacing range of 3.1-4.3 nm across the series.

For the *t*-Bu-nOCB series, the orientational order parameter (S) rises to a plateau over a longer timescale than the nOCB series, rising in approximately 200-400 ns, where n = 9-11, and 600-900 ns where n = 6-8. The orientational order parameter shows less fluctuation at the plateau for the longer chains in the series than the shorter chains in the series. In particular *t*-Bu-6OCB shows the greatest variation in orientational order parameter. The translation order parameter and layer spacing also show similar trends, and for *t*-Bu-6OCB the translational order parameter is of a similar magnitude to the shorter chain nOCB series

results. The layer spacing for *t*-Bu-6OCB also shows greater variability after it has reached a plateau. This suggests that the *t*-Bu-nOCB series has a relatively stable layered systems when n = 7-11 and that *t*-Bu-6OCB has a more diffusely layered structure. The *t*-Bu-nOCB series has an average layer spacing range of 3.4-4.7 nm, which is slightly higher than the range for the nOCB series.

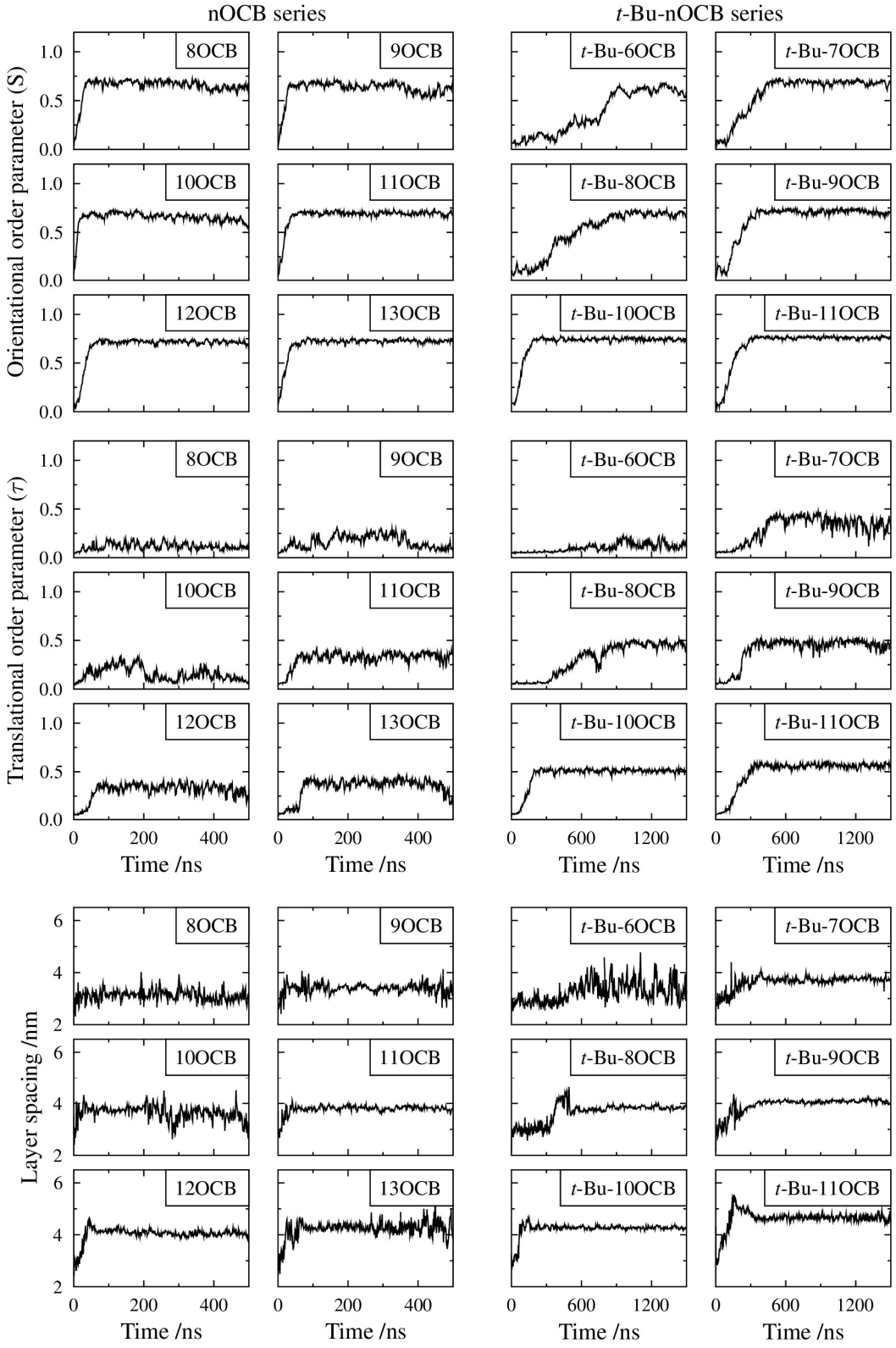

Figure 3.18: Orientational order parameter (S), translational order parameter (τ) and layer spacing (d), throughout the simulations at a reduced temperature of 0.95.

Table 3.15: Average orientational order parameter (S), translational order parameter (τ) and layer spacing (d), averaged over the final 200 ns of the 1000 molecule simulations of the nOCB series.

Molecule	S	τ	d /nm
8OCB	0.64	0.11	3.08
9OCB	0.62	0.15	3.38
10OCB	0.64	0.13	3.56
11OCB	0.70	0.34	3.81
12OCB	0.71	0.32	4.04
13OCB	0.73	0.37	4.28

Table 3.16: Average orientational order parameter (S), translational order parameter (τ) and layer spacing (d), averaged over the final 600 ns of the 1000 molecule of the *t*-Bu-nOCB series.

Molecule	S	τ	d /nm
t-Bu-6OCB	0.61	0.14	3.41
t-Bu-7OCB	0.68	0.34	3.74
t-Bu-8OCB	0.69	0.46	3.85
t-Bu-9OCB	0.71	0.47	4.08
t-Bu-10OCB	0.74	0.51	4.27
t-Bu-11OCB	0.76	0.56	4.65

The simulated phases were visualised, in accordance with Figure 3.19, from the frames with the highest translational order parameter in the simulations. The different shapes of the boxes, shown in Figure 3.20 and Figure 3.21, reflect the anisotropic pressure coupling used in the simulations, resulting in the phase developing differently within the simulation boxes for the different host molecules. The boxes are scaled to give a simple visualisation of the phases and are not all similar dimensions. These visualisations do not show every atom of each molecule. In each molecule, the biphenyl aromatic rings are drawn in orange and the corresponding carbon atom of the terminal group of each of the two series is labelled in blue, shown in Figure 3.19.

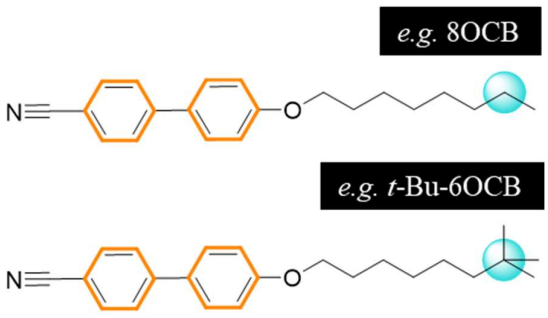

Figure 3.19: Examples of the colour labelling in the phase visualisations for 8OCB and *t*-Bu-6OCB.

A visual inspection of the boxes during the simulations showed the orientational order developing with the alignment of the molecular axes, and the translational order developing, with the molecular layering, in accordance with the plots given in Figure 3.18. The layering of the phase indicates the presence of a smectic liquid crystal phase. For 8OCB it can be seen that the layers are particularly diffuse, and for all the other hosts in both the nOCB and *t*-Bu-nOCB series there are more well defined layers.

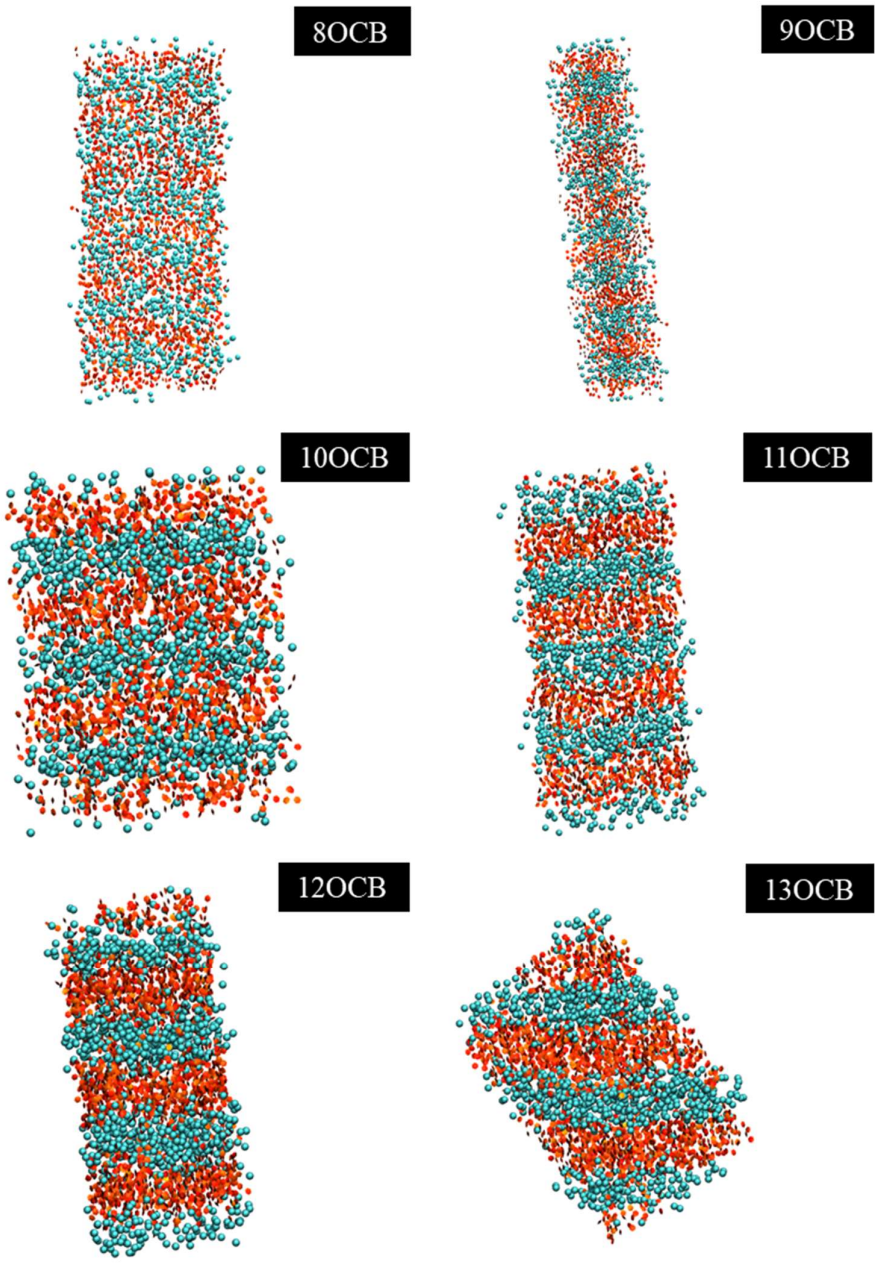

Figure 3.20: Visualisations of the 1000 molecule simulations for the nOCB series using the frame with the highest translational order parameter for each simulation, at t = (Top L to R) 169.95 ns, 168.60 ns, (Middle L to R) 182.50 ns, 164.30 ns, (Bottom L to R) 192.75 ns and 92.80 ns. The visualisations are scaled for illustration and are at different scales.

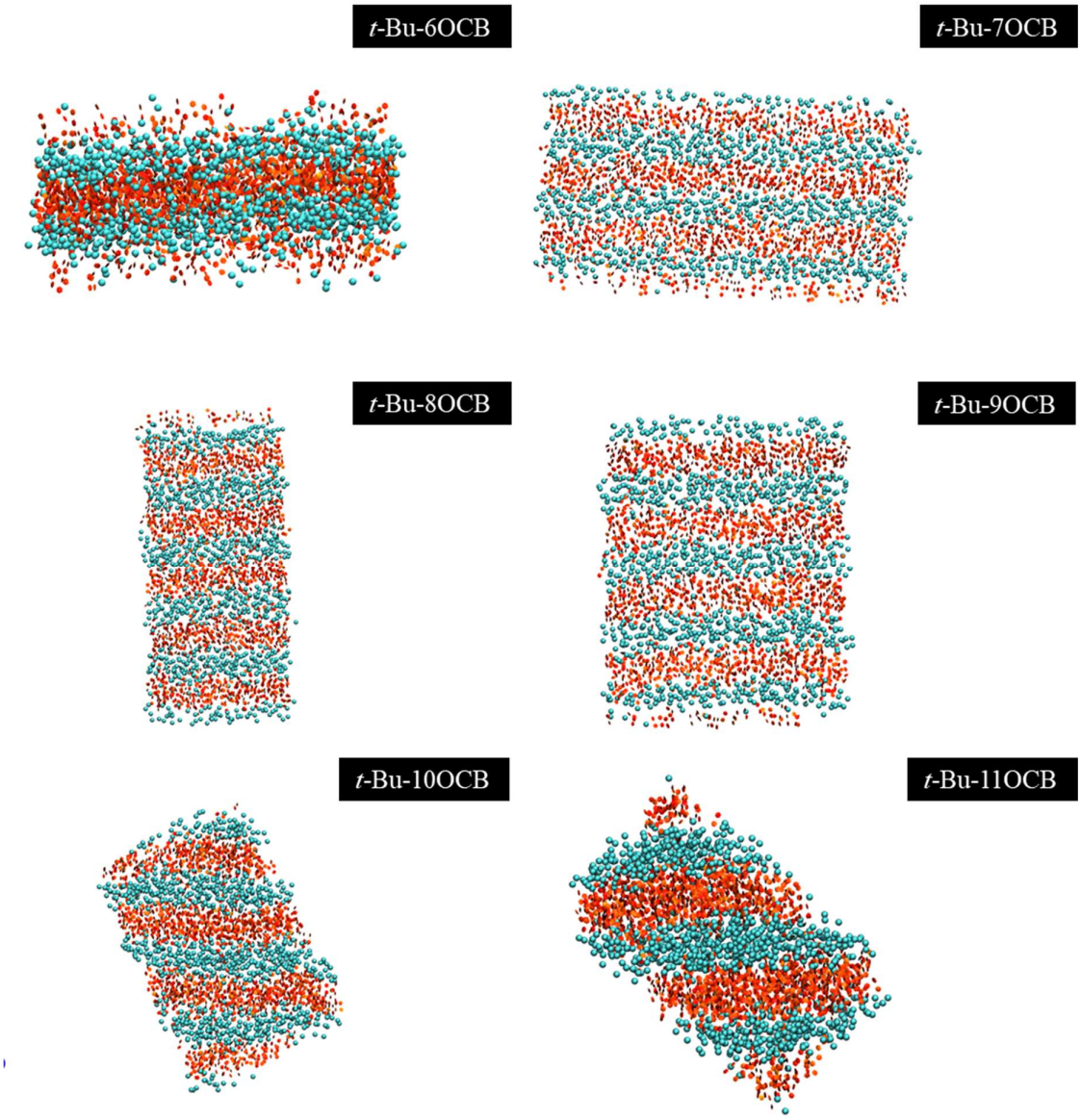

Figure 3.21: Visualisations of the 1000 molecule simulations for the *t*-Bu-nOCB series at the highest translational order parameter for each simulation, at t = (Top L to R) 1028.55 ns, 1215.00 ns, (Middle L to R) 1026.10 ns, 1224.85 ns, (Bottom L to R) 258.85 ns and 1010.55 ns. The visualisations are scaled for illustration and are at different scales.

For each frame of the simulations, the population of the C_4' biphenyl carbon atom connected to the cyano moiety was determined with respect with the layer normal (z-direction) of the phase, which was approximately equivalent to the director ($\hat{n}$) in these liquid crystal phases. The population density was calculated by dividing the population by the cross sectional area of the simulation box and then plotted against the z-direction in Figure 3.22 for the nOCB series and Figure 3.23 for the *t*-Bu-nOCB series.

In these plots, the development of the liquid crystal phase for the nOCB series can be clearly seen to develop much faster than that for the *t*-Bu-nOCB series, as previously observed from the plots of translational order parameter in Figure 3.18. For the nOCB series, the colour map shows that where n = 8-10 the layers form in 25-50 ns and for n = 11-13 there is a longer time to form a layered system. The colour maps also more clearly show the difference between the more stable, defined layers for n = 11-13 and the more diffuse layering for n = 8-10. For the *t*-Bu-nOCB series, the stable layers are clearly seen for n = 7-11 and for *t*-Bu-6OCB the layers take the longest amount of time to form and are the most diffuse. These observations reflect what was seen from the translational order parameter plots shown previously.

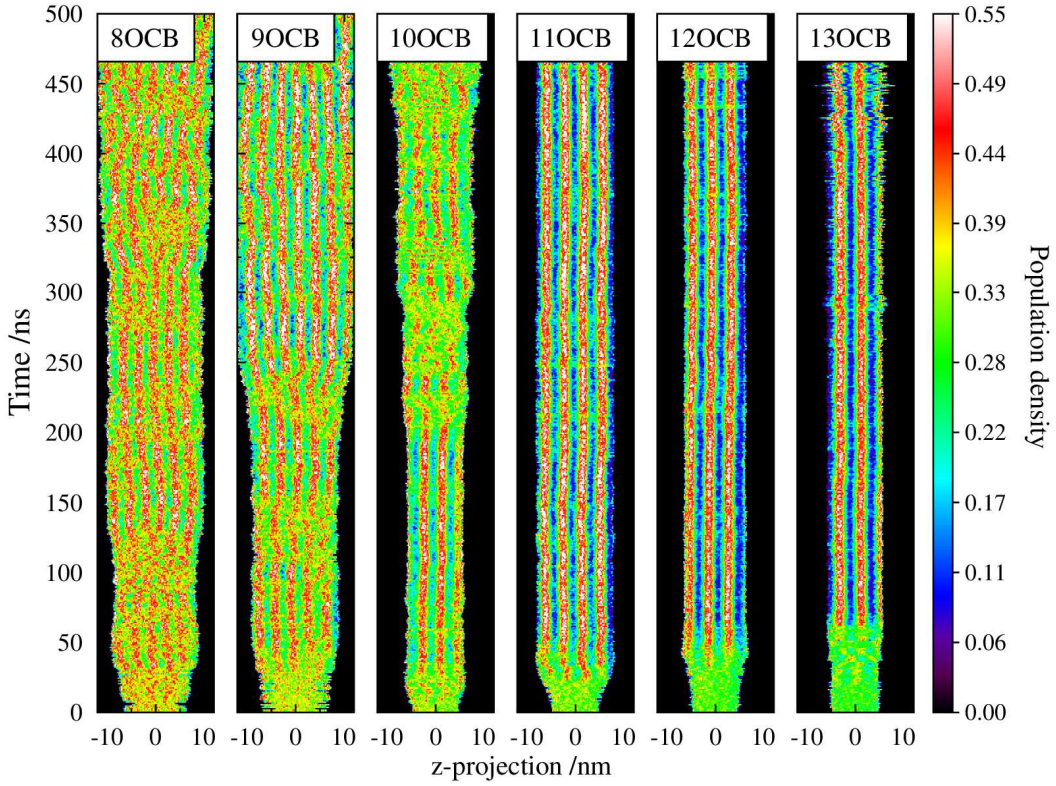

Figure 3.22: Population density of the C_4' biphenyl carbon atom along the z-direction for the nOCB series, for the 500 ns simulations.

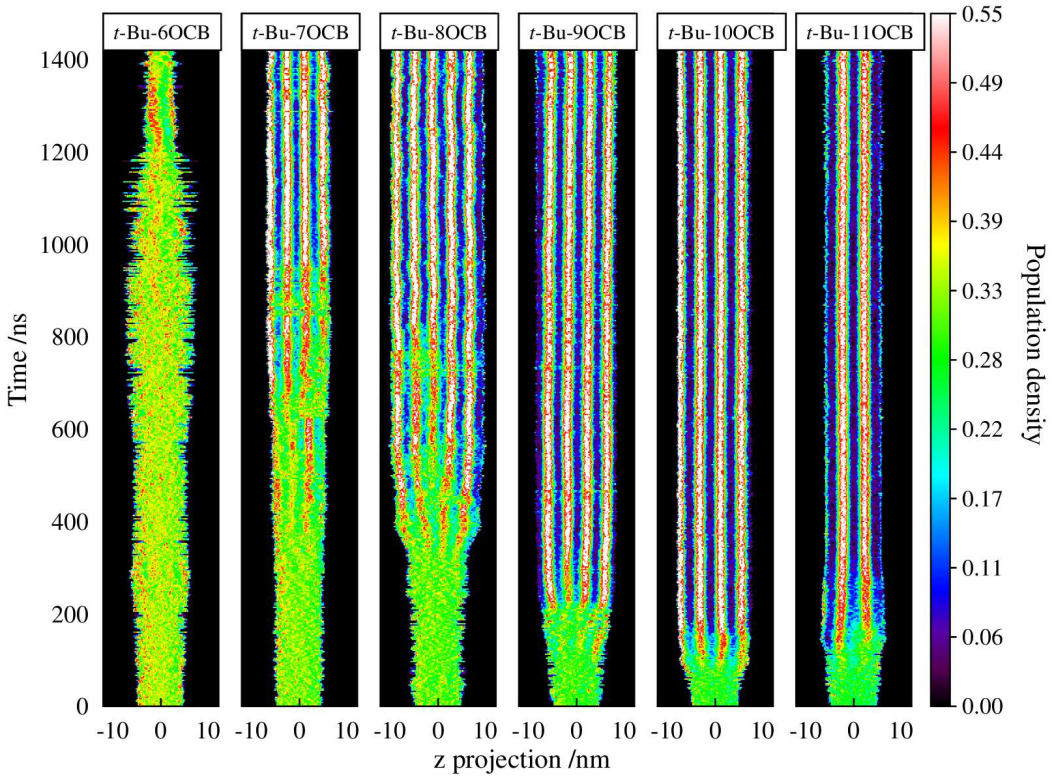

Figure 3.23: Population density of the C_4' biphenyl carbon atom along the z-direction for the *t*-Bu-nOCB series, for the 1500 ns simulations.

Using this type of population density analysis, a 100 ns section was selected from each run and analysed to gain an insight into the level of overlap between different groups in the molecules. This analysis can be used to assess the degree of interdigitation between molecules, which quantifies the proportion of molecules which show an overlap of the groups being studied. For the analysis here, two atoms in each molecule were selected to represent the 'head' and 'tail' of the molecule. The 'head' group atom was the C_4' biphenyl carbon atom connected to the cyano moiety and the 'tail' group atom was the carbon at the centre of the *t*-Bu group and the equivalent atom in the nOCB series, as labelled in Figure 3.24. Molecules were defined as 'up' molecules where the vector from the biphenyl carbon attached to the alkoxy chain to the cyano nitrogen was pointing up with respect to the z-direction, and 'down' when pointing the opposite to this, as shown in Figure 3.25. The resulting plots of the relative populations are shown in Figure 3.26and Figure 3.27, where the red line is the atoms in the 'up' molecules, the blue line is the atoms in the 'down' molecules and the black line gives the population for all the atoms in both the 'up' and

'down' molecules. These plots show data from the entire simulation boxes, meaning that the upper and lower regions of the z-projections show some features that are as a result of the general structure of the layering in the box.

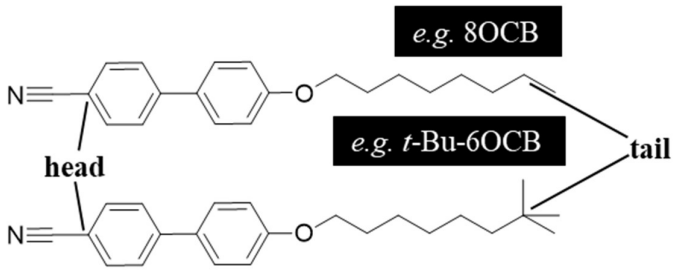

Figure 3.24: Examples of the head and tail group atoms used for interdigitation analysis for 8OCB and *t*-Bu-6OCB.

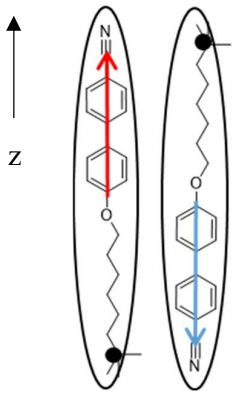

Figure 3.25: Illustration of the labelling of: (L) 'up' molecules and (R) 'down' molecules using *t*-Bu-6OCB as an example. The arrow label shows the z-direction defined this analysis.

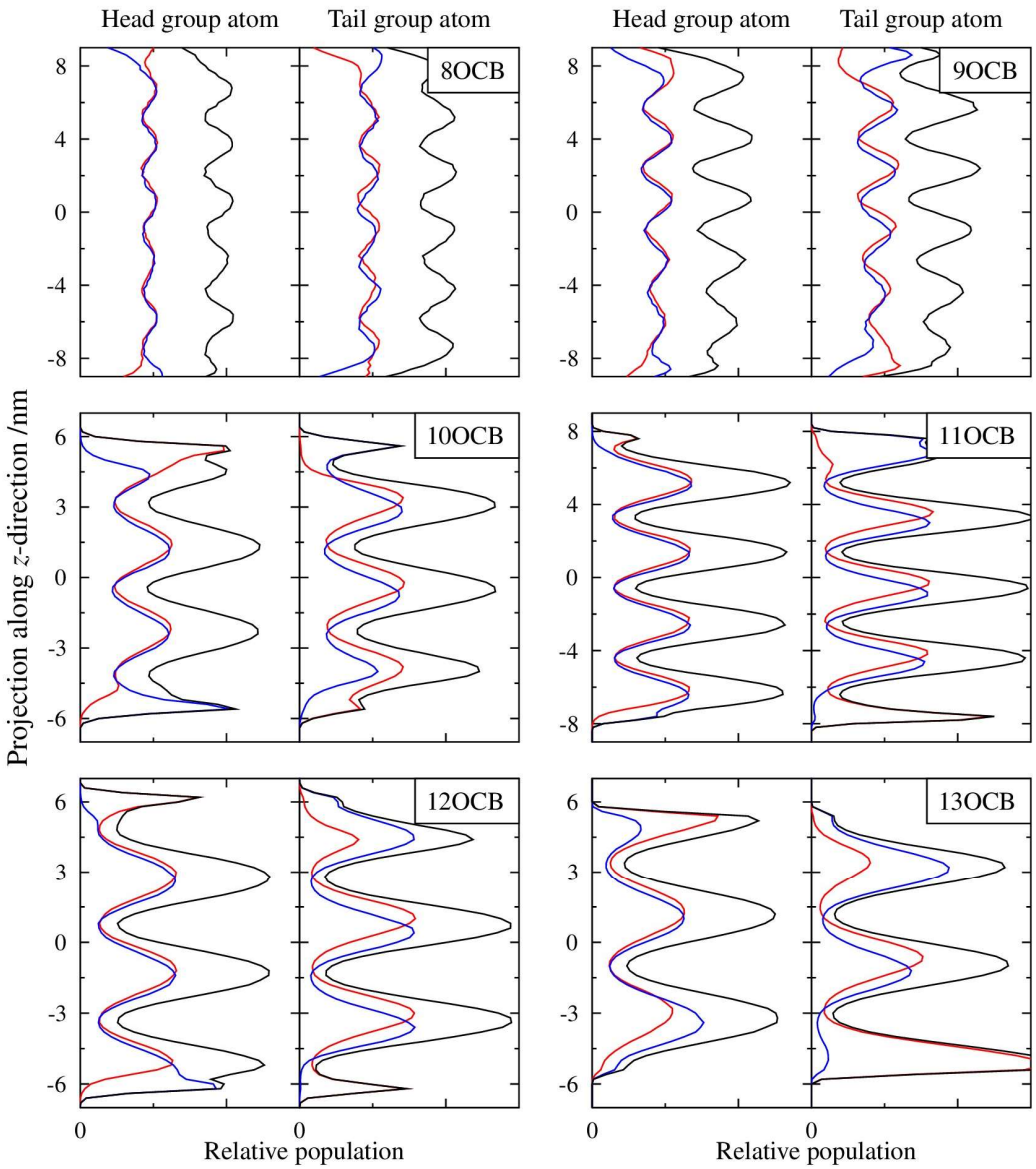

Figure 3.26: Relative population of head and tail group atoms along the z-direction for nOCB series, averaged over 75 to 175 ns in the simulations.

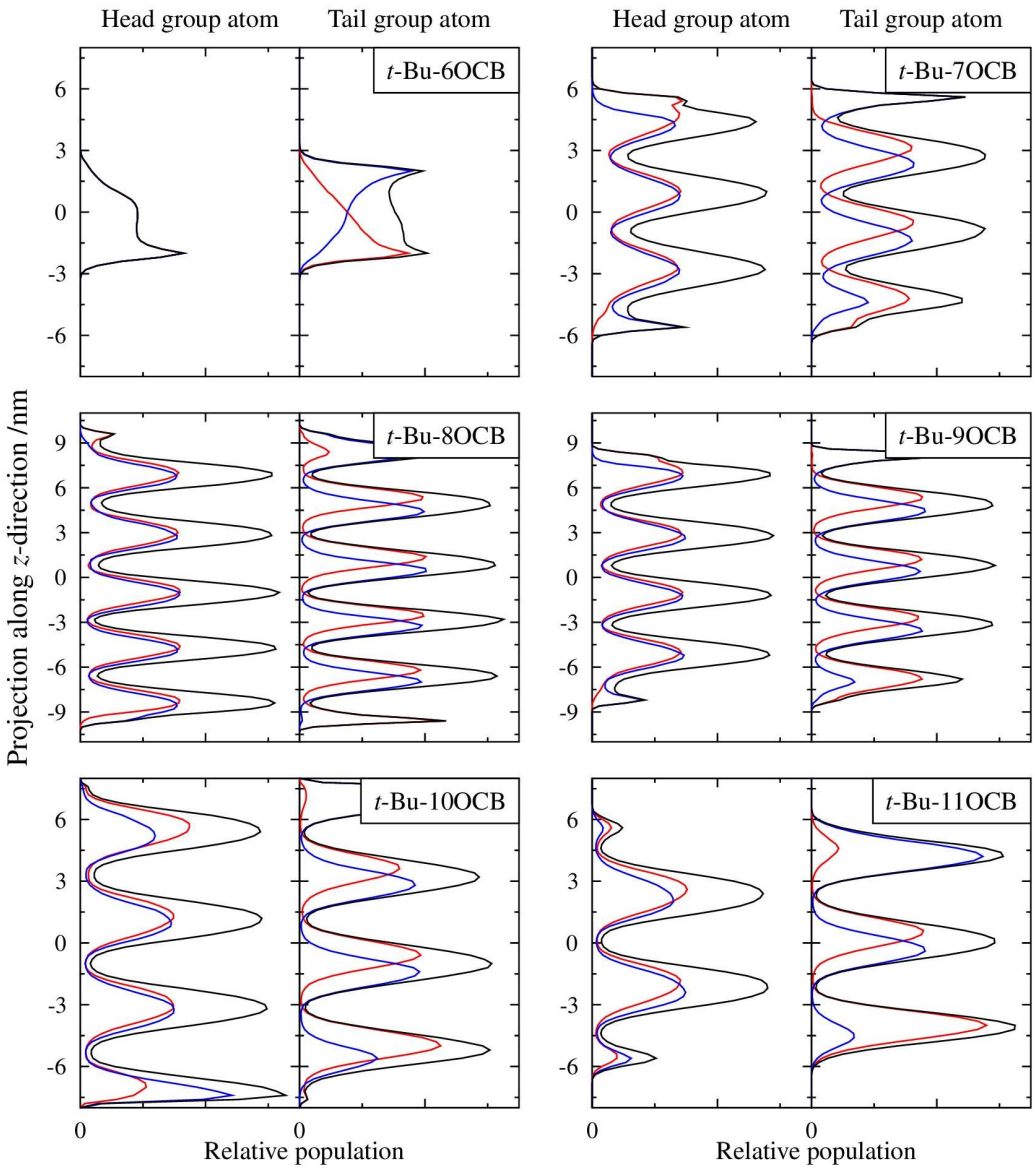

Figure 3.27: Relative population of head and tail group atoms along the z-direction for *t*-Bu-nOCB series, averaged over 1400 to 1500 ns in the simulations.

The z-direction was defined as zero at the centre of the simulation box and population scales are consistent between plots.[106] It is observed that the populations of the head and tail groups are out of phase with one another, which is most clearly illustrated by the black line in the plots. This indicates that the two groups are in regions that are distinct from one another, consistent with layer formation. For both series, the minima can be observed to get closer to zero as the chain length increases. It can also be noted that for the nOCB series the minima in both the head and tail group atom plots do not reach zero, whereas for all the *t*-Bu-nOCB series, excluding *t*-Bu-6OCB and *t*-Bu-7OCB, which not did form consistent layers, the minima reach or approach zero. This may suggest that the layers formed are better defined and would be consistent with the generally higher translational order parameters and larger layer spacings observed in the simulations for the *t*-Bu-nOCB series.

For the head layer atoms in both series there is little difference in the populations or the positioning for the up and down molecules, as shown by the red and blue lines in Figure 3.26 and Figure 3.27. For the nOCB series, the tail group atoms have a small offset in the z-direction of the peaks for the up and down molecules, suggesting the level of interaction between the tail groups in the up and down molecules is not the same as that between the head groups. For the *t*-Bu-nOCB series, the tail group atoms also have an offset in the positioning in the z-direction and it is more distinct than that from the nOCB series.

These analyses can be used to calculate the degree of interdigitation for the head and tail atoms for both series, as given in Table 3.17 and Table 3.18. The degree of interdigitation is quantified as the percentage of molecules which overlap a central layer position, where the molecule is defined by a chosen reference atom, as shown schematically in Figure 3.28. The tail interdigitation percentage could not be calculated for *t*-Bu-6OCB as there was no peak present to be analysed. It can be observed that for both series the tail group shows a lower percentage interdigitation than the head group, and that the head group percentage is similar between the two series, with a value of ~50 %. This suggests that the interdigitation of the head groups is similar between the two series. The lower tail group percentage suggests that the tail groups are less closely associated than the head groups even through there are different end groups. The *t*-Bu-nOCB series has the lowest percentage interdigitation of ~30 %, suggesting that there is more definition in the interlayer boundary when the bulky terminal group is present.

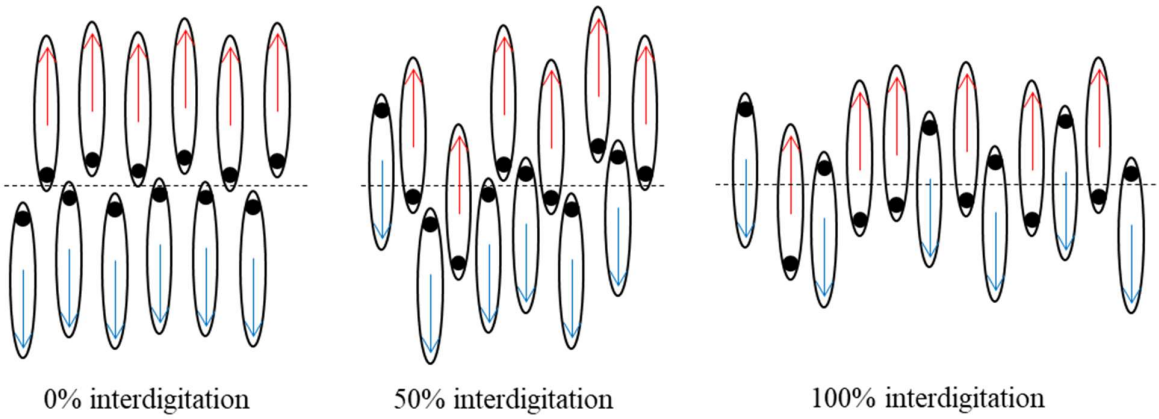

Figure 3.28: Schematic of different percentages of tail group interdigitation, where red arrows denote up molecules, blue arrows denote down molecules and the black dot represents the tail reference atom. The dashed line shows the layer position.

Table 3.17: Summary of degree of interdigitation for the head and tail group atoms of the nOCB series.

	Degree of interdigitation /%	
Molecule	Head group	Tail group
8OCB	50.5	48.5
9OCB	51.0	47.7
10OCB	52.3	45.4
11OCB	53.3	39.2
12OCB	53.1	38.8
13OCB	54.2	39.9

Table 3.18: Summary of degree of interdigitation for the head and tail group atoms of the *t*-Bu-nOCB series.

	Degree of interdigitation /%	
Molecule	Head group	Tail group
t-Bu-6OCB	42.6	
t-Bu-7OCB	53.3	32.7
t-Bu-8OCB	54.3	26.9
t-Bu-9OCB	54.1	28.6
t-Bu-10OCB	54.7	27.3
t-Bu-11OCB	56.4	27.3

The interdigitation can also be visualised, as shown in Figure 3.29 with 11OCB and *t*-Bu-9OCB as examples for the two series, using spheres for the head and tail group atoms, as defined in Figure 3.24. In this visualisation, the 'up' molecule atoms are labelled in red and the 'down' molecule atoms are labelled in blue. From these visualisations, it can be observed that for the head atoms the up and down molecules are found in the same regions and seem to be well mixed together within this region. For the tail atom groups, for *t*-Bu-9OCB it can be seen that the red and blue atoms are in the same region but seem to be segregated into two distinct regions of the up and down atoms. This is illustrating the interdigitation of ~30% as shown in Table 3.18. For 11OCB, the segregation is less evident but there is still some separation between the regions of up and down atoms, which illustrates the percentage of interdigitation seen for the nOCB series tail group atoms, shown in Table 3.17.

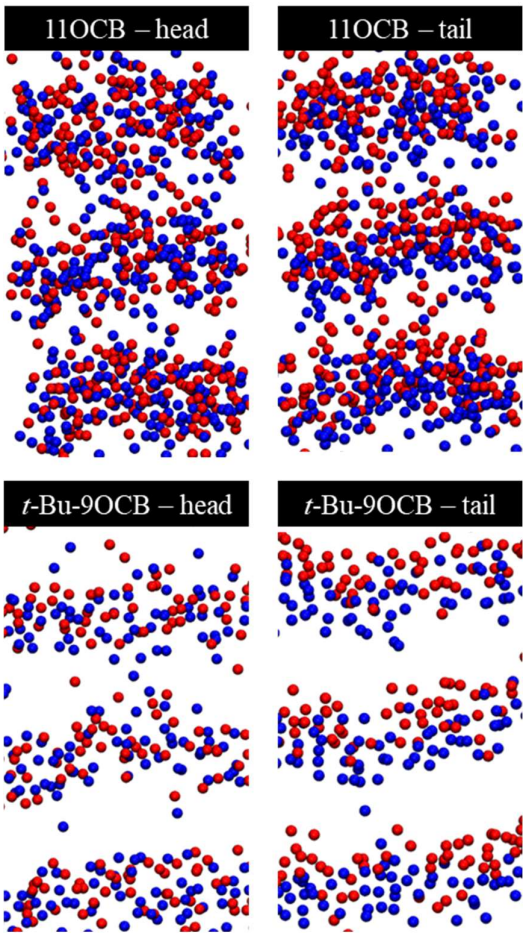

Figure 3.29: Example visualisations of the 1000 molecule simulations for 11OCB and *t*-Bu-9OCB where red atoms represent the up molecules and blue atoms represent the down molecules for either the head or tail reference atoms, at the end of the 500 ns and 1500 ns simulations respectively. These images are just part of the whole boxes to show three layers for comparison.

The tilt angle of a phase (θ_{nk}) is the angle between the director of the phase ($\hat{n}$) and the layer normal (k). This is important for the determination of the type of smectic phase present, as for the smectic A phase this angle will be close to 0°, because the director of the phase is parallel to the layer normal, but in the case of the smectic C phase there is a tilt angle of greater than 0° due to a tilt in the director of the phase relative to the layer normal. In Figure 3.30, the population versus the tilt angle is given as a proportion of the total population using a histogram with angle bin widths of 2°. The probability of the angles versus the tilt angle was calculated by dividing these populations by the sines of the angle, to account for the angular degeneracy, as is shown as a black line on the plots.[16] For both series this analysis shows that the most probable tilt angle in all the simulations is 0°, showing that the director is parallel to the layer normal and indicating the presence of a smectic A phase. This observation was also confirmed through visualisations of the phases, such as the example given in Figure 3.31, which showed no tilt in the phase relative to the layer normal of the phase.

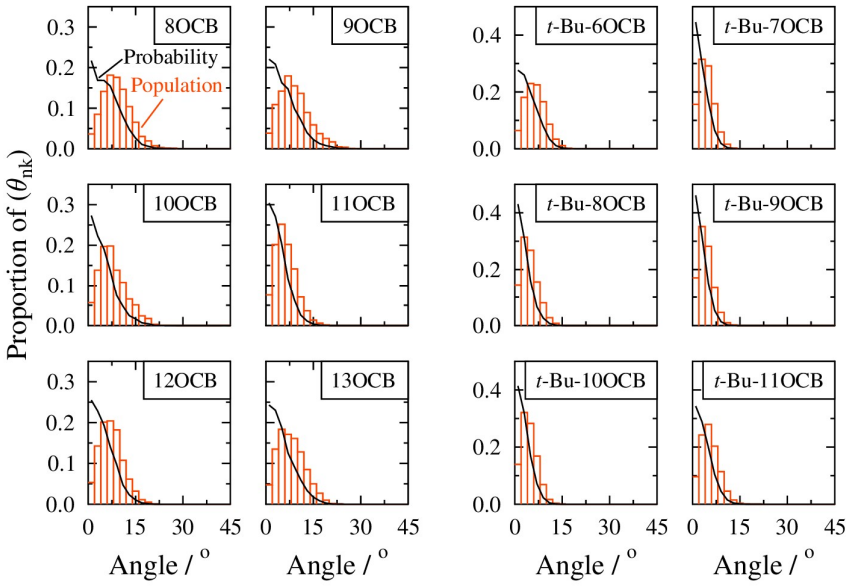

Figure 3.30: Populations and probabilities of the tilt angle for the nOCB series, averaged over the last 100 ns of the simulations, and for the *t*-Bu-nOCB series, averaged over the last 400 ns of the simulations.

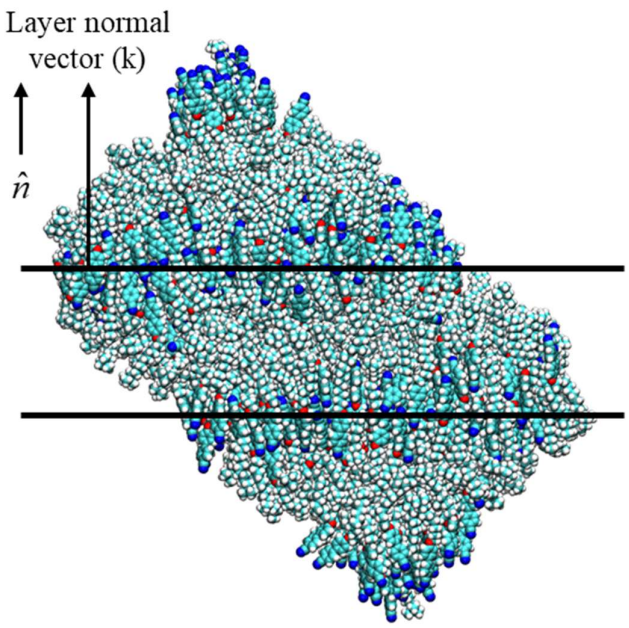

Figure 3.31: Visualisation of *t*-Bu-11OCB 1000 molecules simulation, with the black lines giving approximate layer position, and the director ($\hat{n}$) and layer normal vector (k) which

3.4 Discussion

3.4.1 Transition temperatures and thermodynamic results

The transition temperatures as reported from POM and DSC can be compared across the different chain lengths, as illustrated in Figure 3.32. Both series show a general increase in the temperature of the clearing point with n, with the nOCB series having generally higher values at each comparable chain length than the *t*-Bu-nOCB series. This could suggest that the *t*-Bu terminal group is reducing the clearing point temperature. For the shorter comparable chain lengths, the melting points of the nOCB series (n = 8-10) are lower than those of the *t*-Bu-nOCB series (n = 6-8), but at longer comparable chain lengths the melting points of the nOCB series are higher. The transition temperatures for the nOCB series, determined by POM and DSC, showed a good match with values reported by Hird for 8OCB to 12OCB[105] and Mandle et al. for 8OCB to 11OCB.[112]

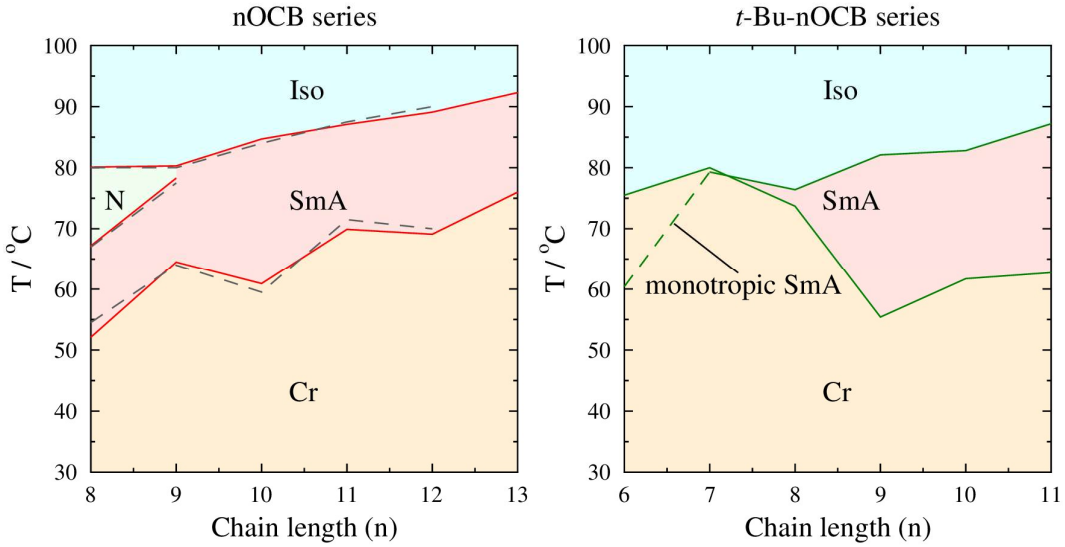

Figure 3.32: Phase transition temperatures for the nOCB and *t*-Bu-nOCB series. The grey dashed lines gives the literature values for the nOCB series.[105]

In the case of the nOCB series, 8OCB and 9OCB exhibit both a smectic A and nematic liquid crystal phase, while the rest of the series (10OCB-13OCB) exhibit only a smectic A phase. This observation may be attributed to the rigid cores of the molecules forming π-π interactions that dominate the interactions between molecules at shorter chain lengths, leading to the presence of a nematic phase. As the alkoxy chain length increases the aliphatic region has greater flexibility, and different dominating interactions lead to the stabilisation

of the smectic A phase through the segregation of the more rigid and flexible parts of the molecule.[97] For the *t*-Bu-nOCB series, *t*-Bu-6OCB and *t*-Bu-7OCB do not exhibit a nematic phase, suggesting that the presence of the bulky *t*-Bu group has suppressed the nematic phase. This suppression of the nematic phase may occur as a result of nanophase segregation, based on the presence of the bulky terminal group,[34, 97] which may disfavour the formation of the nematic phase for the shorter chains. However, the smectic A phase is observed only on cooling from the isotropic phase, with the temperature range of this phase narrowing as the chain length increases from *t*-Bu-6OCB to *t*-Bu-7OCB. This change may be attributed to the increase in the melting point upon the addition of the *t*-Bu group for these shorter chain lengths. This increased melting point may be due to the lower flexibility of the alkoxy chain, which could lead to more favourable crystal packing and a more stabilised crystal structure. The monotropic phase transition indicates that the *t*-Bu-6OCB and *t*-Bu-7OCB molecules self-organise into a smectic A phase more readily from the isotropic phase than from the crystal.

Interestingly, both series exhibit an odd-even effect in the clearing point transition temperatures. For the nOCB series, although there is the general increase across the series, there is a larger increase in the clearing point for the even chain lengths than is observed for the odd chain lengths. The *t*-Bu-nOCB series shows this as an inverted effect with a larger increase in the clearing point for the odd chain lengths than for then even chain lengths. It is important to note that the odd-even effect is very slight for the nOCB series and more pronounced for the *t*-Bu-nOCB series, suggesting that the *t*-Bu terminal group is the cause of the more pronounced behaviour. Figure 3.33 shows possible schematic molecular structures for the nOCB series and *t*-Bu-nOCB series to illustrate the origin of the odd-even behaviour seen for these materials, as discussed below. The model uses the assumption that the alkoxy terminal chain adopts an all-*trans* conformation.

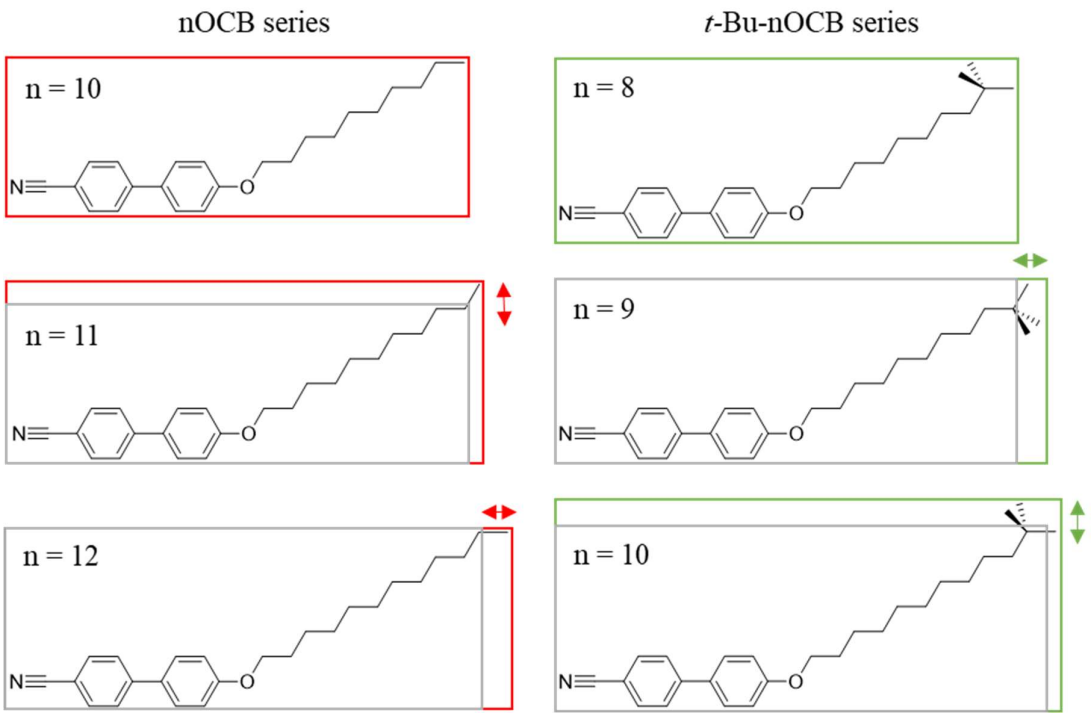

Figure 3.33: Diagram of the odd-even effect for the nOCB and *t*-Bu-nOCB series, showing the alternating effect of increasing chain length. The grey boxes illustrate the previous molecular dimensions and the coloured boxes illustrate the new dimensions.

The odd-even effect has been observed in many different properties such as through conductivities, dielectric anisotropy,[47] transition temperatures and entropies.[113, 117] Berardi et al. also illustrated that the odd-even effect on transition temperatures could be modelled using molecular dynamics simulations.[114] The odd-even effect can be considered with respect to the molecular aspect ratio of each of the molecules, which takes into account the length and width in each case,[114] and has been determined here using DFT studies for both series as given in Table 3.9 and Table 3.10 and as plotted in Figure 3.11. For example, in the case of the nOCB series, as the chain length goes from 10 to 11 it can be seen that the molecule has become 0.1 nm longer and has an increase in width of 0.004 nm, due to the off-axis terminal group, resulting in an increase of 0.14 in the aspect ratio. This can be related to an increase in the clearing point of 2.4 °C, from 84.7 to 87.1 °C. Conversely, as the chain length goes from 11 to 12, it can be observed that the molecule has become 0.1 nm longer but only has a small increase in the width of 0.001 nm. This results in an increase of 0.15 in the aspect ratio and can be related to as an increase in the clearing point of 2.0 °C, from 87.1 to 89.1 °C. It is also observed here that the odd-even effect gets less pronounced at longer

chain length, as reported in the literature,[113] which could be attributed to the increased conformational flexibility of the chains. This property of the longer chains may result in the all-*trans* conformation being less dominant due to the large number of other conformations available to achieve an entropically favourable packing arrangement.[112] For the nOCB series in particular, the literature clearing point temperatures for chain lengths of shorter than 8 show a more pronounced odd-even effect than those for the longer chains,[105] suggesting that at the chain lengths studied in this work the flexibility of the alkoxy chain has already reduced how clearly the odd-even effect can be observed. In the case of the *t*-Bu-nOCB series, as the chain goes from 8 to 9 it can be seen that the molecule has become 0.1 nm longer and has slight decrease in the width of 0.01 nm, due to the inline positioning of the bulky *t*-Bu terminal group, resulting in an increase of 0.19 nm in the aspect ratio. This can be related to an increase in the clearing point of 5.7 ºC, from 76.4 to 82.1 ºC. Conversely, as the chain length goes from 9 to 10, it can be observed that the molecule has become 0.1 nm longer with a slight increase in the width of 0.01 nm, due to the off axis positioning of the bulky *t*-Bu terminal group. This results in an increase of 0.13 in the aspect ratio, which can be related to the smaller increase in the clearing point of 0.7 ºC, from 82.1 to 82.8 ºC. These results may suggest that the addition of the sterically bulky *t*-Bu group is causing the more pronounced odd-even effect seen in the clearing point values, due to a molecular shape effect. In the case of the bromine terminated nOCB series studied by Gibb et al., the change of terminal group did not seem to change how large the odd-even effect was for the series where n = 5-9, but this may be justified by the similarity in the van der Waals volume of the bromine and the methyl terminal groups.[117]

When comparing between the two series it can be observed that for the longer comparable chain lengths the *t*-Bu-nOCB series has lower melting and clearing points. The decrease in the melting point may suggest that the presence of the *t*-Bu terminal group is affecting the packing of the crystal, resulting in a lower transition temperature to go into the smectic A phase. The decrease in the clearing point transition is smaller, but would also suggest that the transition temperature is reduced by the presence of the bulky terminal group. Gibb et al. highlighted that the addition of the bromine atom as a terminal group lowered the clearing point temperature relative to the nOCB series, due to the addition of the steric bulk.[117] This was also observed by Mandle et al. for several siloxanes and for the *t*-Bu group when added as a terminal group to 11OCB.[108] In the system studied here the change to a terminal *t*-Bu

group results in a small increase in the temperature range of the smectic A phase from 16.3-20.0 °C for the nOCB series to 21.1-26.7 °C for the *t*-Bu-nOCB series. This increased temperature range could be relevant for potential applications of these liquid crystals, as it may be beneficial to have the smectic A phase stable over a larger temperature range.

The transition enthalpies and entropies for the different chain lengths for both series are illustrated in Figure 3.34. The transition enthalpies obtained for the melting points of nOCB series shows a general increase with chain length. The *t*-Bu-nOCB series generally exhibits lower values at this transition than the nOCB series and a general decrease in the transition enthalpies with increasing chain length. This may suggest that the addition of a *t*-Bu terminal group is changing the packing in the crystal phase and reducing the transition enthalpy required for this transition to occur. The transition entropies are proportional to the transition enthalpies determined and it can be observed that the transition entropies at the melting point are generally larger for the nOCB series than for the *t*-Bu-nOCB series, suggesting that the change in entropy occurring for the nOCB series is larger due to the order of the two phases being less alike. For *t*-Bu-10OCB, the transition enthalpy for the melting point seems to deviate from the trend of the other transition enthalpies. This may be due to over-estimation of the transition enthalpy as a result the broad DSC peak being analysed at this transition, as seen in Figure 3.5, which will also carry forward into the transition enthalpy and entropy.

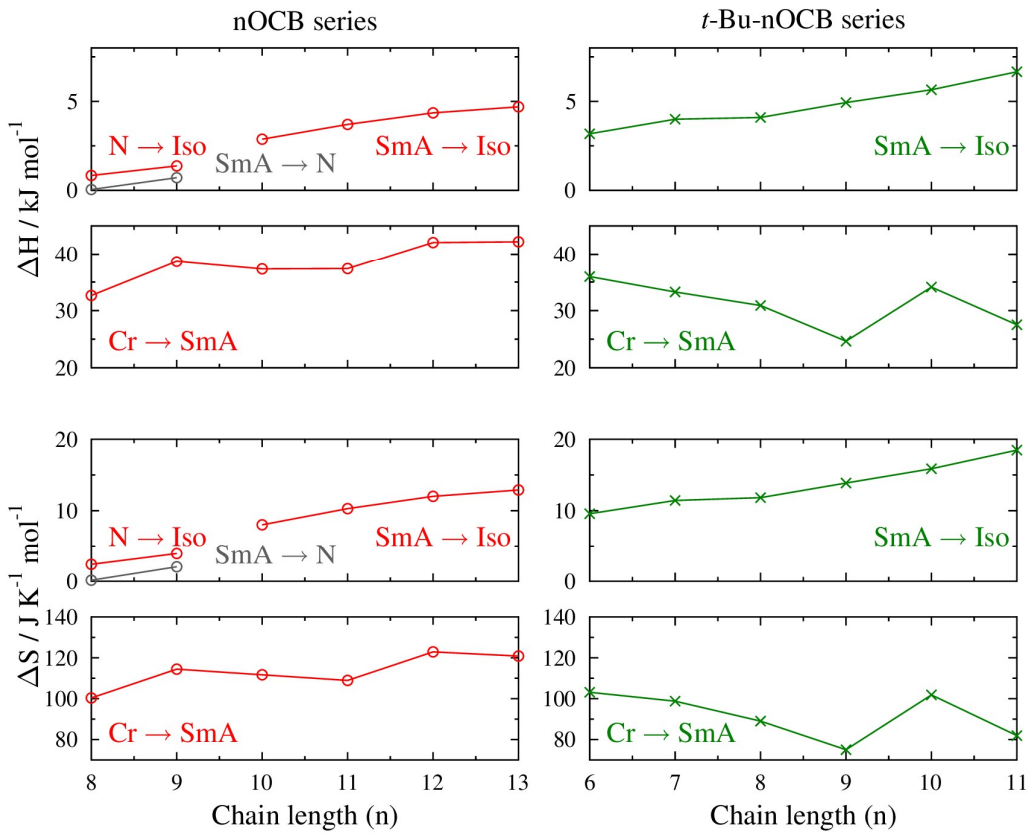

Figure 3.34: Comparison plots for the transition enthalpy and entropy values for the two series. The grey data shows the transitions from the nematic to smectic A phase (N → SmA) which only occurs for the nOCB phase where n = 8 and 9.

The transition enthalpies obtained for the clearing point of both series show a general increase with increasing chain length, suggesting that the longer chain lengths may require more energy to reorganise into the isotropic liquid phase due to the greater flexibility of the chain. The *t*-Bu-nOCB series shows higher transition enthalpies than the nOCB series at each comparable chain length, which suggests that the energy required for change from the liquid crystal phase to the isotropic liquid is greater for the *t*-Bu-nOCB series. This may indicate the smectic A phase is stabilised by the bulky *t*-Bu-nOCB series, resulting in a greater transition enthalpy required for this transition to occur. In terms of transition entropies at the clearing point, the larger transition entropy for the *t*-Bu-nOCB series may indicate that the order of the smectic A phase is less liquid-like than that of the smectic A phase for the nOCB series and so results in a greater change in the entropy of the system at this transition. For both series the transition entropies show an increase with chain length for

the clearing point, indicating that the smectic A phase becomes less like the isotropic liquid as the anisotropy of the molecules increase.

The nOCB series also exhibits the smectic A to nematic transition for 8OCB and 9OCB, which has a transition enthalpy and entropy of a very small magnitude, suggesting that the energy required for the change and the change in the order between the phases is very small. This could be attributed to the similarity between the phase structures of the smectic A and nematic phases. The nematic phase is a relatively disordered liquid crystal phase as it only has orientational order of the molecules, but no long range translational order. The smectic A phase is relatively more ordered than the nematic but it only has some degree of translational order in the form of diffuse layers.[16] This transition entropy has a small magnitude as the phase maintains orientational order and loses the additional diffuse translational order of the smectic A phase as it occurs.[180]

The transition enthalpies for the clearing point are a magnitude of 10 lower than those for the melting point for both series, which may be attributed to the different nature of the molecular reorganisation taking place at each transition. The reorganisation from the solid to the liquid-like liquid crystal phase has a larger enthalpy as more energy input is required to break down the crystal lattice, whereas from the liquid crystal phase to the isotropic liquid less energy input is required as less reorganisation of the molecules is occurring. The transition enthalpies of the nOCB series show good agreement with reported values for all transitions,[181] including the very small transition enthalpies observed for the nematic to smectic A transition. For 11OCB and *t*-Bu-11OCB, the transition enthalpies are similar to the values reported by Mandle et al.,[108] with very good agreement for the clearing point transitions in particular. Cowling et al. suggest that for a standard material incorporating n-alkyl terminated chains the normalised transition entropy value for the smectic A to isotropic transition would be $\Delta S/R = 1$.[182] The normalised transition entropy values observed for the nOCB series are close to this value (Table 3.3), with values of 0.97-1.44 when n = 10-13, which suggests they are similar to this n-alkyl terminated chain model, whereas the comparable *t*-Bu-nOCB series all show larger values of 1.42-2.22 where n = 8-11 (Figure 3.4). These larger values suggest that a more strongly associated smectic A phase is being formed, which correlates with the overall stabilisation of the smectic A phase upon addition of the terminal *t*-Bu group.

3.4.2 XRD results

The XRD measurements can provide insight into the structure of the phases observed by POM and DSC. The first observation for the nOCB series and the *t*-Bu-nOCB series was the difference in the 2D diffraction patterns for 8OCB and 9OCB in comparison with the rest of the diffraction patterns, such as the example given in Figure 3.6. These two samples have a nematic phase, which has anisotropic flow properties,[15] allowing it to align to the magnetic field in the XRD experiments. The samples which only have a smectic A phase, which is more viscous as a result of the greater order in the system, do not align in this way.[3] It is also worth noting that for 8OCB and 9OCB, the presence of the nematic phase can be distinguished through the sharpening of the small angle peak (2θ = 2-3 °) at the transition to the smectic A phase.

The temperature dependent layer spacing for both series is given in Figure 3.35, which was determined from the small angle peak in the XRD patterns. For 8OCB and 9OCB the small angle peak had a low intensity and a broad peak shape in the nematic phase, but in the smectic A phase the small angle peak was of higher intensity with a sharper peak shape. These peak shapes are indicative of the types of phase present, as the nematic exhibits broad peaks due to the lack of positional order in the phase and the smectic A has a diffusely layered structure leading to sharper small angle diffraction peaks.[140] For these samples it can be seen from Figure 3.35 that the layer spacing in both phases is similar, although slightly larger in the nematic phase. This might suggest that for the shortest chain lengths there is not a large change in the structure of the phase occurring at the nematic to smectic transition, which is consistent with the small transition enthalpies and entropies seen for this transition from DSC. Considering the nOCB series as a whole, there is a small increase in the layer spacing with decreasing temperature for n = 11-13 and no clear change where n = 8-10. For the *t*-Bu-nOCB series the layer spacing increases as the temperature decreases for all the samples, particularly for the longer chains where there is a 0.1-0.2 nm change in the layer spacing across the full temperature range. This may be attributed to a change in the conformation of the alkoxy chains, as at higher temperatures a wider range of possible conformations of the chains may be occupied. As the temperature decreases, fewer conformations may be occupied leading to the conformations becoming more like the all-*trans* conformation. This will make the molecules more elongated on average and move the layers apart, leading to

the swelling seen in the XRD results as the temperature is decreased. Although the effect seems to be present for both series, the swelling seems more prominent for the *t*-Bu-nOCB series, which could be attributed to the bulky *t*-Bu terminal group pushing the layers further apart to maintain the preferential packing of these bulky groups.

The layer spacing for 8OCB and 10OCB show a good match with the values reported by Leadbetter et al., but the value for 12OCB is slightly lower than reported.[183] The layer spacing for 11OCB and *t*-Bu-11OCB show a good match with layer spacing measured by Sims et al.[106] These similarities suggest that the experimental results are consistent with literature reports, with some deviation in values likely due to differences in samples and techniques used.

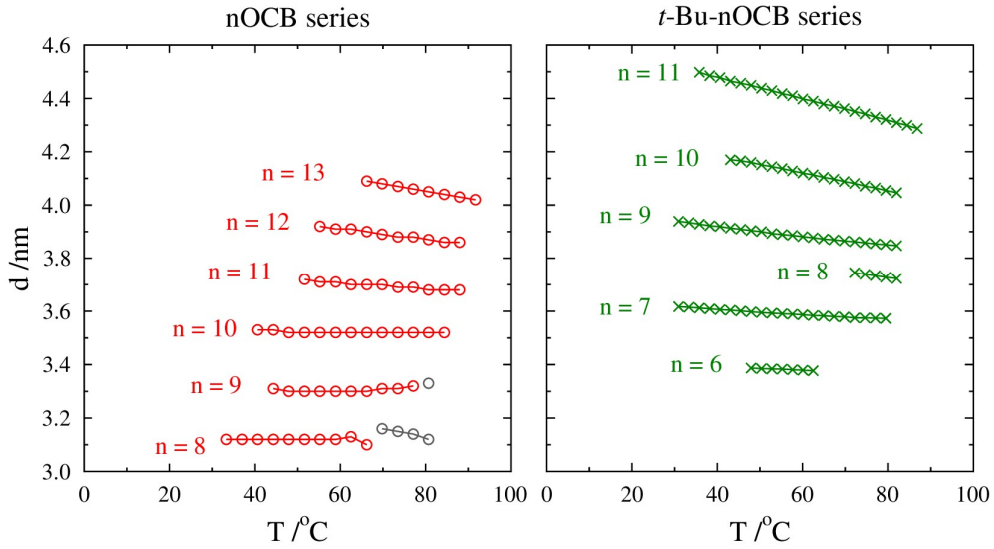

Figure 3.35: Comparison plots for the layer spacing values with temperature for the two series. The values in grey represent the nematic phase for 8OCB and 9OCB.

Using the DFT length measurements, an assessment of the structure of the phase can be made based on how the layer spacings related to the all-*trans* molecular length. The result of this calculation is plotted against reduced temperature in Figure 3.36, and shows that the layer spacings for the nOCB series has a lower value of 1.27-1.34 times the molecular length whereas the layer spacings for the *t*-Bu-nOCB series shows a higher value of 1.36-1.46 times the molecular length. For both series, these values suggest that the molecules are overlapping with other molecules, forming a structure similar to a partially interdigitated bilayer, which

can be given the label SmA_d.[27] The nOCB series has lower values than the *t*-Bu-nOCB series indicating that that there is greater overlap of the molecule in the nOCB series than the *t*-Bu-nOCB series, which is supported by observations from the MD simulations, which show that there is greater interdigitation of the tail groups of the nOCB series than the *t*-Bu-nOCB series. The values for the nOCB series are slightly lower than the value of 1.4 reported by Leadbetter et al. (8OCB, 10OCB and 12OCB)[183] and the value of 1.47 reported by Mandle et al. (10OCB and 11OCB)[108] but this difference may be due to the difference in the method of molecular length measurement as the method used in this studied calculated the length based on the moment of inertia axis of the molecules.

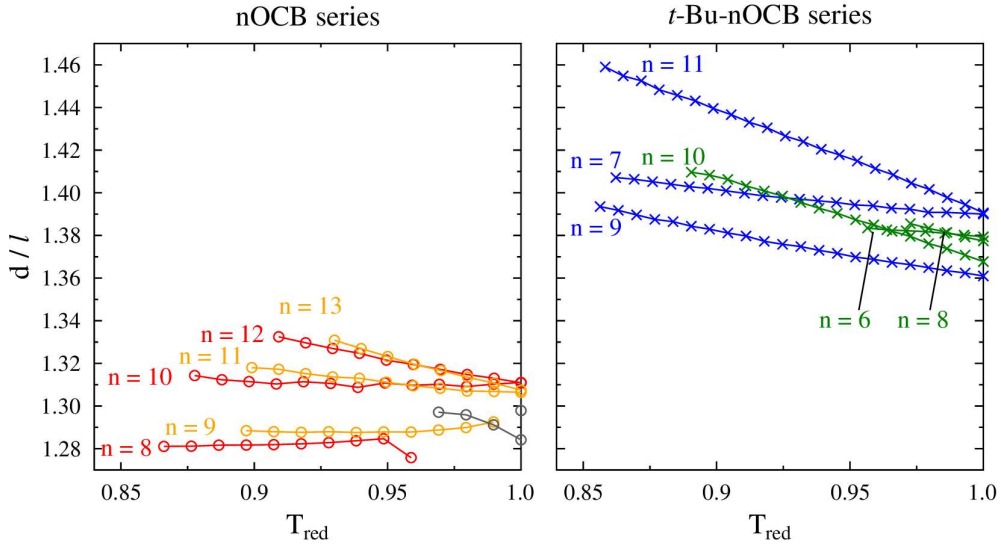

Figure 3.36: Comparison plots for the layer spacing to all-*trans* molecular length ratio with reduced temperature for the two series. The values in grey represent the nematic phase for 8OCB and 9OCB.

For the nOCB series it can be observed that there is a trend of increasing d/l value with increasing chain length. It can also be seen that there seems to be an odd-even effect, with three pairs of sequential molecules, for example with 8OCB and 9OCB, which behave similarly across the temperature ranges. For the two shortest chain lengths, the nematic phase shows higher d/l values than the smectic A phase, indicating that upon the formation of the diffuse layers in the smectic A phase result in the overlap between molecules increasing and resulting in a smaller layer spacing. These molecules also show the smallest change in the d/l value with decreasing temperature, whereas molecules like 12OCB and 13OCB show a

more significant swelling with decreasing temperature. This may indicate that these longer chains are undergoing a larger change in average length as the temperature decreases as the d/l ratio is increasing the most. For the *t*-Bu-nOCB series, there does not seem to be an obvious sequential trend as for the nOCB series but it can be seen that the comparable longest chain lengths of *t*-Bu-10OCB and *t*-Bu-11OCB also have the greatest change in d/l value with decreasing temperature. This increase is larger than for 12OCB and 13OCB, and it shows that the effect is occurring no matter the terminal group, and that the bulky *t*-Bu group is amplifying the effect.

The wide angle values from XRD can give some information about the lateral distance between the molecules in the smectic A and nematic phases, which will relate to the distances between the cyanobiphenyl groups of the molecules. The distances for both of the series are shown in Figure 3.37, with the values for the lowest and highest smectic A temperatures recorded and the nematic phase plotted against the temperature and the adjacent distances versus the chain length for both series are plotted in Figure 3.38. For the nOCB series, it can be observed that the odd and even chain lengths show slightly different distances between adjacent molecules that decreases with decreasing chain length, which may be due to the odd-even effect that dampens at longer chain length as previously observed. From the DFT molecular widths, the odd chain lengths are observed to have a larger widths than the preceding even chain lengths in the series, which may provide some insight into the slight increase in the distance between the adjacent molecules. Also for the odd chain lengths it can be seen that 9OCB has the largest distance, which may be a combination of the relatively wider molecule and also a reduced flexibility due to the short chain length that may result in the cyanobiphenyl groups of the molecules being pushed further apart to accommodate the more rod-like alkoxy chain of 9OCB. For the *t*-Bu-nOCB series, the odd and even chain lengths show little difference in the lateral distances, but the overall variation amongst the series is smaller than for the nOCB series. All the even chain lengths are wider than the odd chain lengths from DFT in this case, and it can be observed that *t*-Bu-6OCB and *t*-Bu-8OCB have larger distances between the adjacent molecules in this series. This could be explained by the widening of the molecules, resulting in the cyanobiphenyl groups being pushed further apart to pack the *t*-Bu terminal groups efficiently. It can be seen *t*-Bu-10OCB does not fit the trend of the even numbered chains, but this may be due to the longer chain length

showing greater flexibility resulting in less packing disruption and allowing the cyanobiphenyl groups to sit closer together like the odd numbered chains do.

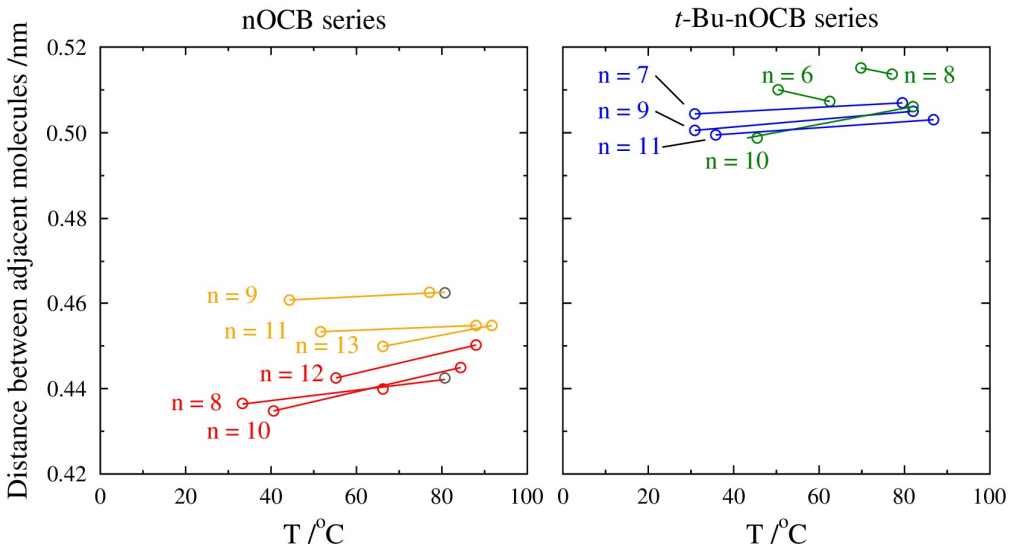

Figure 3.37: Comparison plots for the distance between adjacent molecules with temperature for the two series. The values in grey represent the nematic phase for 8OCB and 9OCB.

When comparing between the two series, as shown in Figure 3.38, it can be observed that the distance between the cyanobiphenyl groups of adjacent molecules is larger for the *t*-Bu-nOCB series than for the nOCB series, with ranges of 0.50-0.52 nm and 0.43-0.46 nm, respectively. The larger values for the *t*-Bu-nOCB series suggests that the terminal *t*-Bu groups are impacting the packing of the phase resulting in the molecules being pushed further apart.[140] When these values are compared to the molecular widths the lateral distances from XRD are smaller than those obtained by DFT. For the nOCB series the molecular width by DFT was 0.790-0.808 nm and for the *t*-Bu-nOCB series the molecular width from DFT was 0.788-0.805 nm, which is based on the optimised structure of the molecule with the all-*trans* conformation of the alkoxy chain. These DFT molecular widths were determined as maximum width, effectively representing cylinders around each molecule, which leads to an overestimation in the width when the packing of the actual molecules is considered. The molecules are able to pack closer than the cylinder model would suggest allowing the molecules to pack closer together.

A further DFT calculation for the cyanobiphenyl core with an alkoxy chain where n=1 gave a molecular width of 0.689 nm. This value was larger than that observed for either series of molecules, but may show that the maximum cylindrical widths from DFT are not showing a realistic value in terms of the liquid crystal phase. For a phenyl pyridine system, a value of 0.44 nm (4.4 Å) was reported by Thompson et al., from wide angle XRD measurements of the smectic A phase.[184] This value is similar to that seen for the nOCB series, which may suggest that the behaviour seen here is similar to the packing of the cores in other molecules which have a smectic A phase.[106, 111]

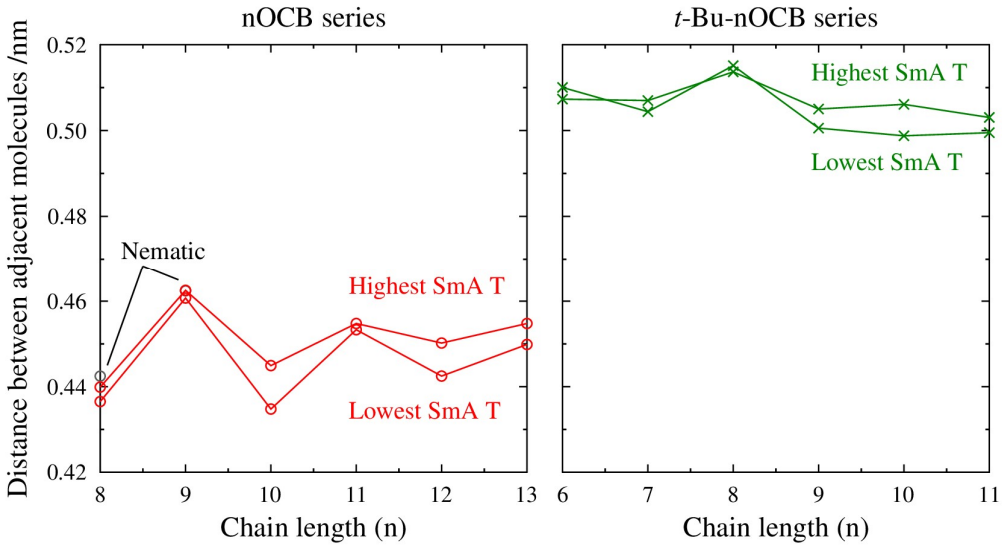

Figure 3.38: Comparison plots for the distance between adjacent molecules with chain length for the two series, from the wide angle XRD. The values in grey represent the nematic phase for 8OCB and 9OCB.

3.4.3 MD simulation results

The molecular dynamics simulations gave clearing point temperatures (T_c), via the modified Haller fits of the short 100 ns, 216 molecule simulations. These simulated clearing points are plotted against chain length for both series along with the experimental values in Figure 3.39. For both series there is large difference observed between the simulated value and experimental values, in the range of 49-54 K for the nOCB series and 38-45 K for the *t*-Bu-nOCB series, which may be attributed to the general force field which has not been parametrised for this particular system. Despite this difference, the general trend of increasing clearing point with increasing chain length can be observed from the simulations, as seen in the microscopy results. For the nOCB series, the simulated values do not show the

exact, weak odd-even trend observed from the POM experimental results, but for the *t*-Bu-nOCB series the stronger odd-even pattern can be seen also in the simulated results. This result may indicate that the simulations are acting as a good model for the trends in the *t*-Bu-nOCB series in particular. Overall, the results indicate that the simulations may be a good model for both series and that using reduced temperatures in relation to the clearing points in the simulations provides a valid approach for carrying out larger simulations with comparable conditions.

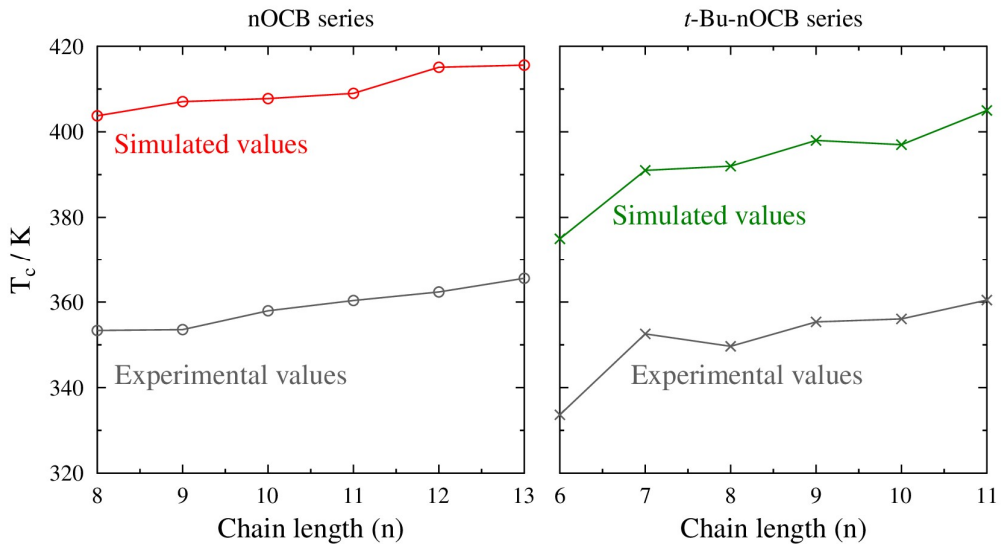

Figure 3.39: Comparison of the simulated clearing points for both series, including the experimental values determined by POM.

From the longer, 1000 molecule MD simulations, a comparison can be made of the orientational and translational order parameters at each chain length, which is given in Figure 3.40. For these simulations, an average was taken over the last 600 ns of the simulation for the *t*-Bu-nOCB series and over the last 200 ns of the simulations for the nOCB series. These sections of the simulations were selected as most of the simulations had reached a relatively stable plateau in the order parameters at this point.

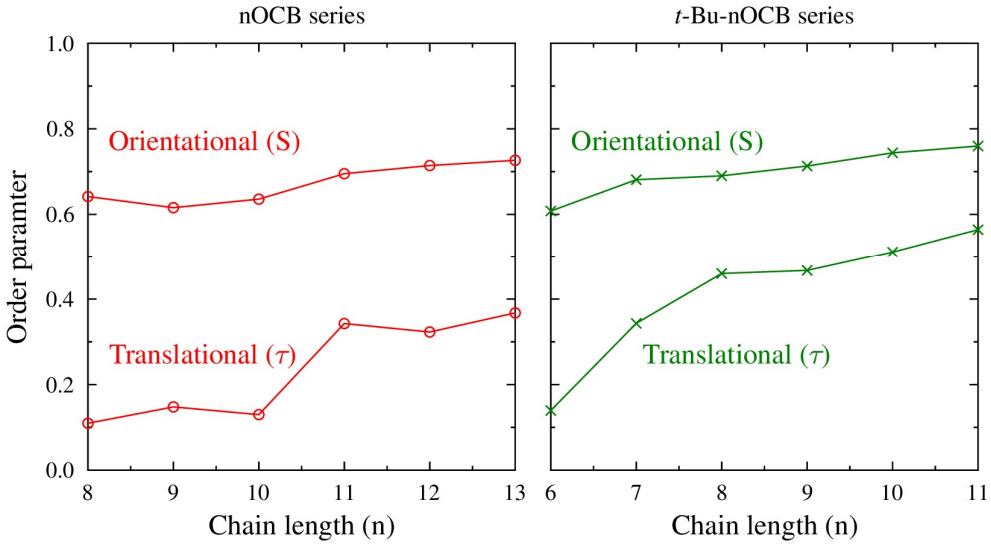

Figure 3.40: Orientational and translational order parameters with chain length, averaged over the final 200 ns of the simulations for the nOCB series and the final 600 ns of the simulations for the *t*-Bu-nOCB series.

It can be seen from this comparison that the orientational order parameter of the biphenyl vector is similar for comparable chain lengths within the two series, with the values being slightly higher for the *t*-Bu-nOCB series than the nOCB series apart from the shortest comparable chain lengths. This may suggest that the molecular orientation of the biphenyl groups in the two series is similar for similar chain lengths. In the case of the translational order parameter using the C_4' biphenyl carbon atom, it can be seen that the *t*-Bu-nOCB series has a higher translational order parameter than the *t*-Bu-nOCB series at all comparable chain lengths, suggesting the presence of a more ordered layer structure to the smectic A phase. Both series show lower values of the translational order parameter at lower comparable chain lengths, particularly for the nOCB series. This may be an indication that the simulations may not be fully stable, which is also observed in the z-direction projections seen in Figure 3.18

Figure 3.18: for 8OCB-10OCB and *t*-Bu-6OCB.

In comparison to the simulations presented by Sims et al.,[106] the order parameters reported here for *t*-Bu-11OCB are similar, but for 11OCB the orientational order parameter is slightly lower and the translational order is higher. This could be due to Sims et al. using slightly

different simulation conditions and particularly a lower reduced temperature of 0.87, which places the simulations at a different point in the phase temperature range.

The layer spacings from the MD simulations can also be compared to the layer spacings determined from the small angle measurements from XRD, as summarised in Table 3.19 and Table 3.20 and plotted in Figure 3.41. To ensure that the experimental results can be compared to the simulations, an interpolation of the XRD layer spacings was undertaken to determine the layer spacing at the same reduced temperature as the simulations. It is important to select a reduced temperature as the simulated clearing point does not match the clearing point transition temperature from experiment. As a result, a comparison can be made at the same reduced temperature but not the same temperature in kelvin, although in some cases it places the XRD experimental data in the super cooled region, below the melting point.

For the experimental results at this reduced temperature, the difference between the shortest and longest comparable chain lengths is similar for the two series at 0.95 nm for the nOCB series and 0.97 nm for the *t*-Bu-nOCB series. This suggests that the general trend is a result of the increase in molecular length across the series and independent of the terminal group effect. The simulation layer spacing shows a larger range, of 1.20 nm for the nOCB series and 1.24 nm for the *t*-Bu-nOCB series, but the same general trend is shown by the simulations.

Table 3.19: Summary of experimental and computational layer spacing for the nOCB series, at the same reduced temperature (T_{red}) of 0.95.

	d /nm	
Molecule	Experimental	Simulation
8OCB	3.12	3.08
9OCB	3.31	3.38
10OCB	3.52	3.56
11OCB	3.70	3.81
12OCB	3.89	4.04
13OCB	4.07	4.28

Table 3.20: Summary of experimental and computational layer spacing for the *t*-Bu-nOCB series, at the same reduced temperature (T_{red}) of 0.95.

	d at T_{red} = 0.95 /nm	
Molecule	Experimental	Simulation
t-Bu-6OCB	3.39	3.41
t-Bu-7OCB	3.59	3.74
t-Bu-8OCB	3.77	3.85
t-Bu-9OCB	3.87	4.08
t-Bu-10OCB	4.11	4.27
t-Bu-11OCB	4.36	4.65

In both the experimental and computational results, given in Figure 3.41, the *t*-Bu-nOCB series shows generally wider layer spacing than the nOCB series at each comparable chain length, suggesting that for the bulky *t*-Bu terminal group to incorporate into the packing the layers must push apart. From this plot it can be seen that there is a good match between the experimental and computational layer spacing for all the molecules in both series, as the values determined from the MD simulations are close to the XRD measurements. This is indicating that the simulations are a good model for these systems as they are behaving in a similar way to the real samples. These simulation results also match the values observed by Sims et al., which had simulated layer spacing values of 3.76 nm and 4.58 nm for 11OCB and *t*-Bu-11OCB respectively at a lower reduced temperature of 0.87.[106]

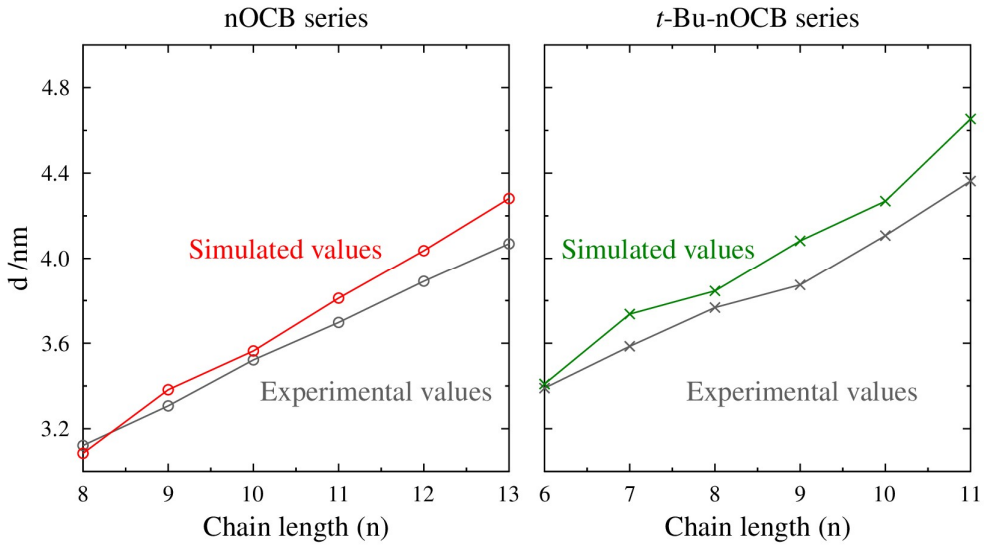

Figure 3.41: Comparison of the simulated layer spacing and the experimental values determined by XRD for both series, at the same reduced temperature (T_{red}) of 0.95.

The layer spacing may also be interpreted in terms of the degree of interdigitation of the head and tail groups of the molecules. As seen in Figure 3.42, the head groups of both series show very similar degrees of interdigitation, which are very similar to the comparable values determined by Sims et al.[106] This shows a large degree of interdigitation is occurring for the cyano head groups. For the tail groups the value is different between the two series, as the nOCB series has a value of 40-50% whereas the *t*-Bu-nOCB series has a value of 27-33%, which is roughly illustrated in Figure 3.43. The nOCB series has a high degree of tail group interdigitation, suggesting that the alkoxy chains are able to overlap to pack within the phase. The *t*-Bu-nOCB series shows much less tail group interdigitation, indicating that the bulky terminal groups are not as able to overlap as the other parts of the molecule. This observation lines up with the larger experimental layer spacing observed as the terminal groups could be pushing the layers further apart to pack efficiently and with less overlap in the phase. The tail group interdigitation values for and *t*-Bu-11OCB shows a good match to the 28% reported by Sims et al.,[106] but the value of 39.1% for 11OCB is much lower than the 47% observed in the previous report.

The difference between the interdigitation of the bulky *t*-Bu terminal groups and the end group of the nOCB series may also explain the increased swelling effect seen with decreasing temperature from the XRD. As the interdigitation of the *t*-Bu-nOCB tail group atoms is lower. the bulky terminal groups are packing together is a more segregated manner. This may result in the swelling effect observed in XRD to be more exaggerated as a result of the lower interdigitation of the bulky *t*-Bu groups. From the XRD data, the *t*-Bu-nOCB series has a higher d/l values at all temperatures, which links to the lower percentage interdigitation of the tail groups observed here as the lower percentage interdigitation means that the molecules have less overlap leading to higher d/l values.

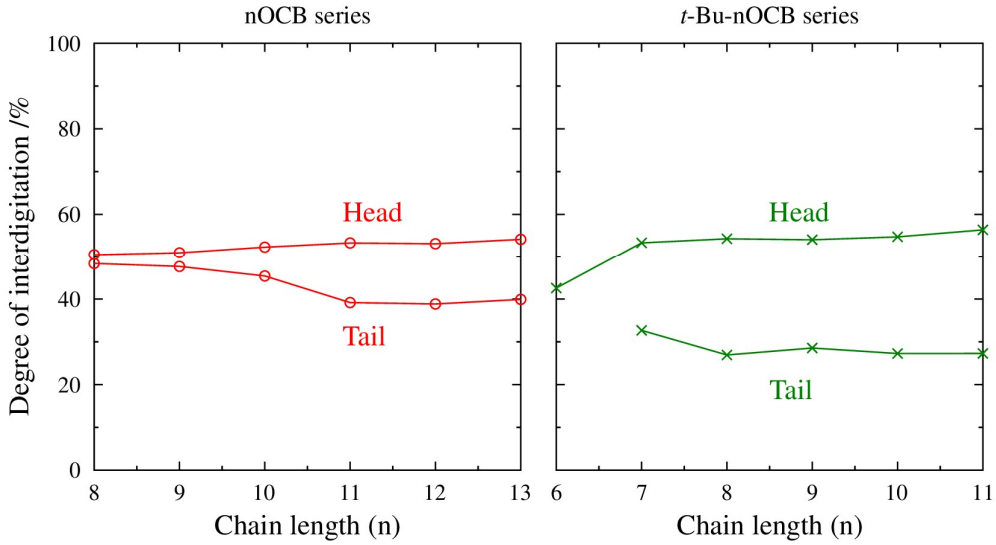

Figure 3.42: Comparison of the degree of interdigitation for both series. The labels 'Head' and 'Tail' refer to reference atoms at the C_4' biphenyl carbon atom, and at the carbon atom at the centre of the *t*-Bu group and the equivalent atom in the nOCB series respectively, for all molecules in both series.

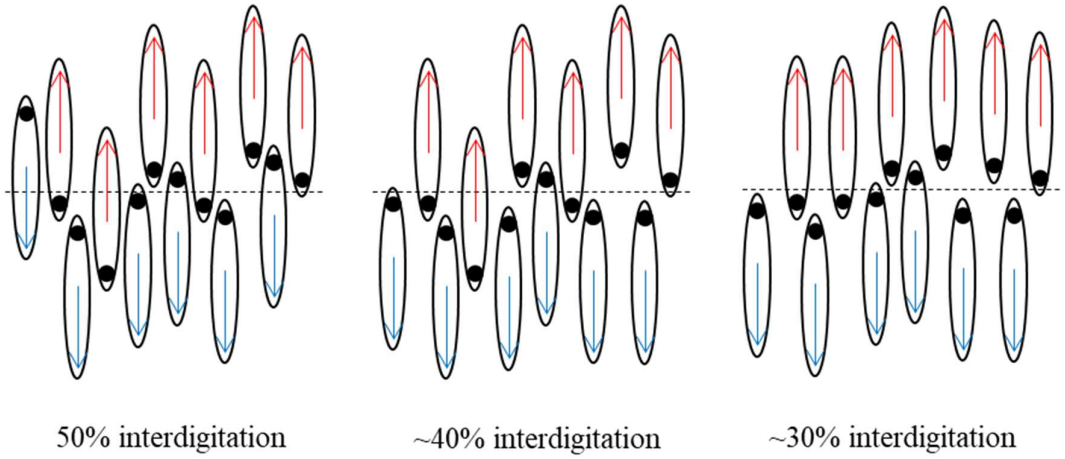

Figure 3.43: Illustration of the interdigitation observed for the head and tail groups of the nOCB and *t*-Bu-nOCB series.

3.5 Conclusions

The experimental studies of the host alone samples have shown that there are some clear differences in the behaviour of the nOCB series and the *t*-Bu-nOCB series, which include different phase behaviour at the shorter comparable chain lengths, and larger layer spacings and more pronouced odd-even trends for the *t*-Bu-nOCB series than for the nOCB series. These differences in the experimental studies have also been evident in the simulation work, which showed higher orientational and translational order parameters at longer comparable chain lengths and lower interdigitation of the tail groups for the *t*-Bu-nOCB series, compared to the nOCB series. Together, these studies show that the *t*-Bu-nOCB series are hosts which form more ordered smectic A phases and with a more defined layered structure, as a result of the inclusion of the bulky *t*-Bu terminal group to the chain. It was also found that this effect was particularly evident at chain lengths of $n \geq 8$ in the *t*-Bu-nOCB series.

The simulations were shown to provide a good model for the trends observed for the two series, and in particular the layer spacing determined from simulations matched closely with the layer spacing from XRD. These results provide insight into the liquid crystal phases of the nOCB and *t*-Bu-nOCB series, with the simulations giving complementary results which can enhance the understanding of the phases being studied. In a wider context, the use of such simulations could be used in a predicitive manner, to gain an insight into the properties of the liquid crystal phases formed and aid in the molecular design of smectic A hosts.

Chapter 4

Guest-host mixtures

4.1 Introduction

This chapter will detail the experimental and computational work on guest-host mixtures using the nOCB and *t*-Bu-nOCB liquid crystal host materials and the 26B(**m**O)OH dyes and 26B(*t*-Bu-**m**O)OH dyes , which are abbreviated to '**m** dye**'** and '*t*-Bu-**m** dye**'** from this chapter onwards, as the guests, using the methods described in chapter 2. Section 4.2 reports the computational results and analysis and section 4.3 reports the experimental results and analysis, with justification for the samples studied based on the computational section. In section 4.4 there is a combined discussion of the computational and experimental results, with conclusions to this chapter given in section 4.5.

4.2 Computational studies

This section will detail the initial isolated molecule optimisations of a range of dyes and will cover the DFT and TD-DFT studies, the guest-host dye selection process for the MD simulations, and the resulting MD simulations undertaken.

4.2.1 Density functional theory studies

Density functional theory (DFT) studies were undertaken on the **m** dye series and *t*-Bu-**m** dye series, to determine the molecular dimensions by optimising the structures of isolated molecules in the gas phase, with the alkoxy chains in the all-*trans* conformation. The phenyl rings were oriented parallel to one another, as optimised by Sims et al. for comparable alkyl dyes,[89] with the alkoxy chains in the plane of the phenyl rings. The optimised structures are given in Figure 4.1, for the **m** dye series, and in Figure 4.2, for the *t*-Bu-**m** dye series, and show the all-*trans* conformation from each of the single molecule calculations which were used to calculate the molecular length (l), width (w) and aspect ratio (AR). The grey cylinder is illustrated to show dimensions relative to the molecule. These values are summarised in Table 4.1 for the **m** dye series, where **m** = 4-15, and Table 4.2 for the *t*-Bu-**m** dye series, where **m** = 2-13. The values of the parameters are plotted in Figure 4.3.

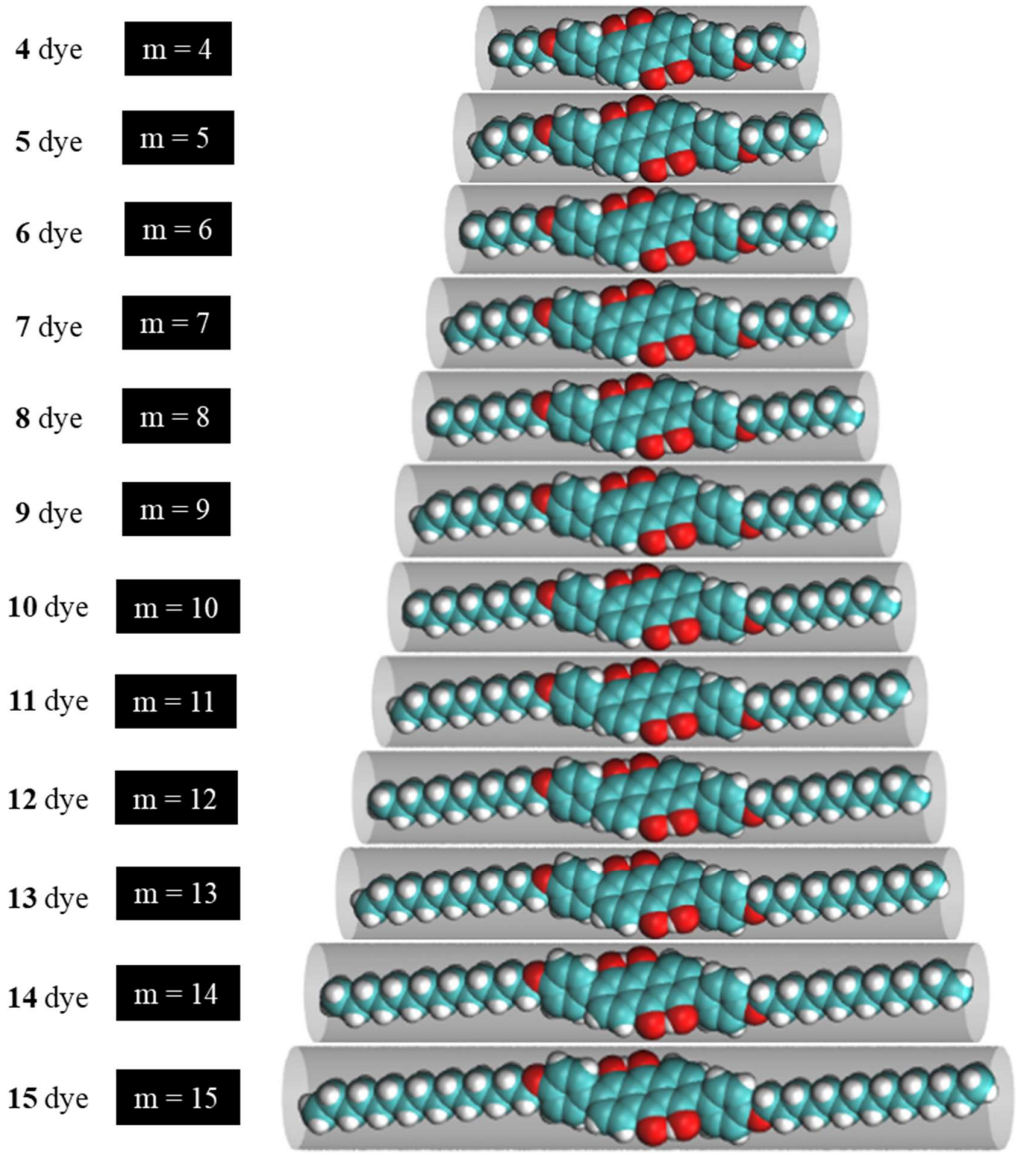

Figure 4.1: Optimised structures of the **m** dye series, where **m** = 4-15, with the alkoxy chain in the all-*trans* conformation. The anthraquinone core is scaled to the same size for each structure.

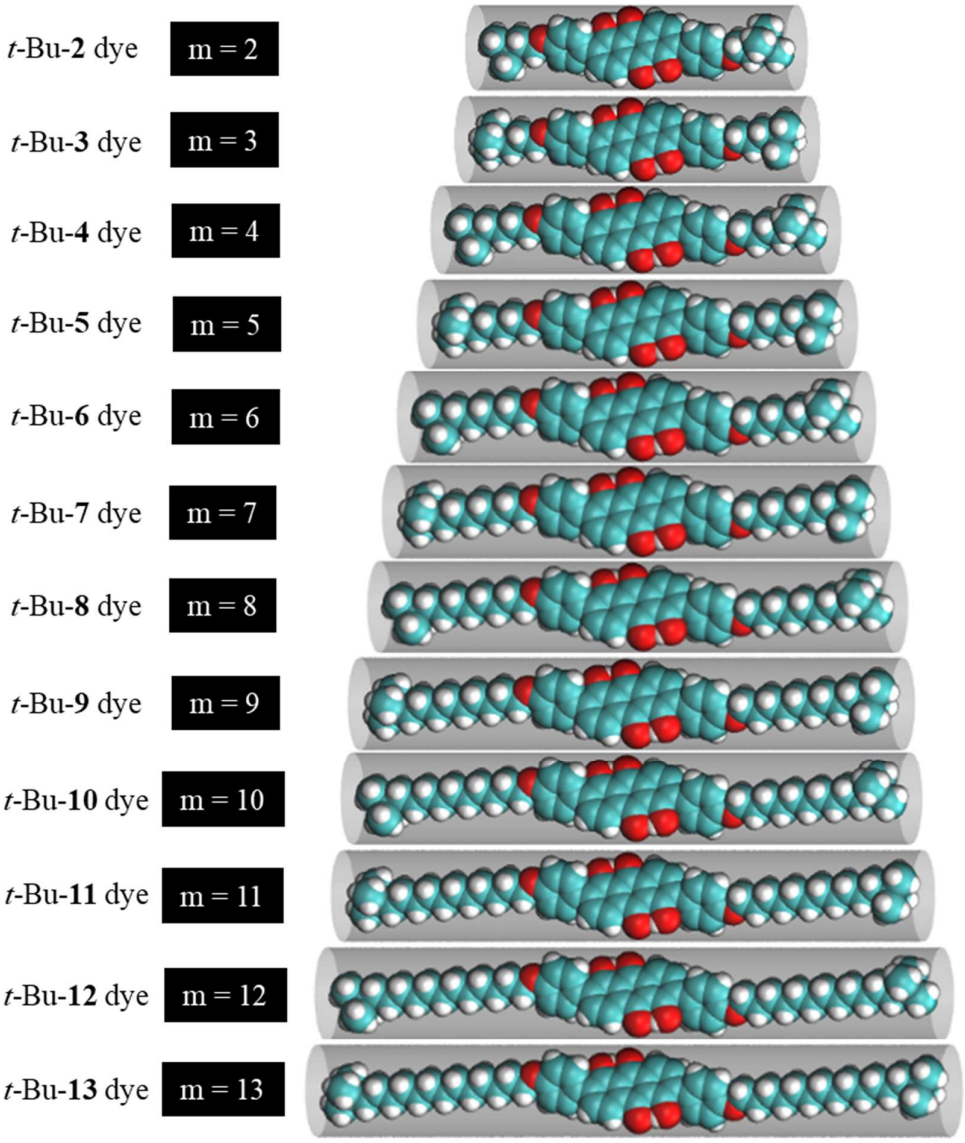

Figure 4.2: Optimised structures of the *t*-Bu-**m** dye series, where **m** = 2-13, with the alkoxy chain in the all-*trans* conformation. The anthraquinone core is scaled to the same size for each structure.

Table 4.1: Summary of molecular lengths, widths and aspect ratios for the **m** dye series.

Molecule	l /nm	w /nm	AR
4 dye	3.21	0.841	3.82
5 dye	3.48	0.838	4.16
6 dye	3.72	0.838	4.45
7 dye	3.99	0.835	4.78
8 dye	4.24	0.835	5.07
9 dye	4.50	0.832	5.41
10 dye	4.75	0.832	5.71
11 dye	5.01	0.831	6.04
12 dye	5.26	0.830	6.33
13 dye	5.53	0.835	6.62
14 dye	5.78	0.839	6.88
15 dye	6.04	0.849	7.12

Table 4.2: Summary of molecular lengths, widths and aspect ratios for the *t*-Bu-**m** dye series.

Molecule	l /nm	w /nm	AR
t-Bu-**2** dye	3.23	0.835	3.87
t-Bu-**3** dye	3.47	0.841	4.12
t-Bu-**4** dye	3.74	0.832	4.50
t-Bu-**5** dye	3.98	0.837	4.75
t-Bu-**6** dye	4.25	0.831	5.12
t-Bu-**7** dye	4.49	0.834	5.38
t-Bu-**8** dye	4.76	0.831	5.73
t-Bu-**9** dye	5.00	0.832	6.02
t-Bu-**10** dye	5.28	0.845	6.24
t-Bu-**11** dye	5.52	0.835	6.60
t-Bu-**12** dye	5.79	0.857	6.75
t-Bu-**13** dye	6.03	0.849	7.11

The molecular length of all the all-*trans* conformer, as shown in Figure 4.3, is similar for dyes of comparable chain length within each series, being within 0.1-0.2 nm of one another. For both series, there is a general increase in chain length with **m** and an odd-even variation, with this variation being slightly larger for the *t*-Bu-**m** dyes. However, in the case of the widths, the **m** dyes show a general decrease in the width with increasing chain length, with a small odd-even variation, until **m** = 12; as the chain length increases from odd to even there is a smaller decrease in the width than the decrease seen for even to odd. For **m** = 12 to **m** = 15, there is an inversion in the trend and an increase in the width. For the *t*-Bu-**m** dyes, there is also a general decrease in the width with increasing chain length, with a more pronounced odd-even variation, until **m** = 9. For **m** = 9 to **m** = 13, there is an inversion in the trend and an increase in the width. A smaller width is observed at even chain lengths compared to the

odd chain lengths. The odd-even trend for the *t*-Bu-**m** dyes is observed to be the opposite of the trend for the **m** dyes, as was also observed for the trend between the nOCB series and *t*-Bu-nOCB series previously in Chapter 3.

For both series, there is a general increase in aspect ratio with increasing chain length dye due to the dominant effect of the increasing chain length. As a direct result of the odd-even effects seen in the widths of the two series of dyes, the **m** dyes show a slight odd-even trend in the aspect ratios and the *t*-Bu-**m** dyes show a more clear odd-even trend in the aspect ratios, with the aspect ratio showing a smaller increase in going from even to odd, than going from odd to even.

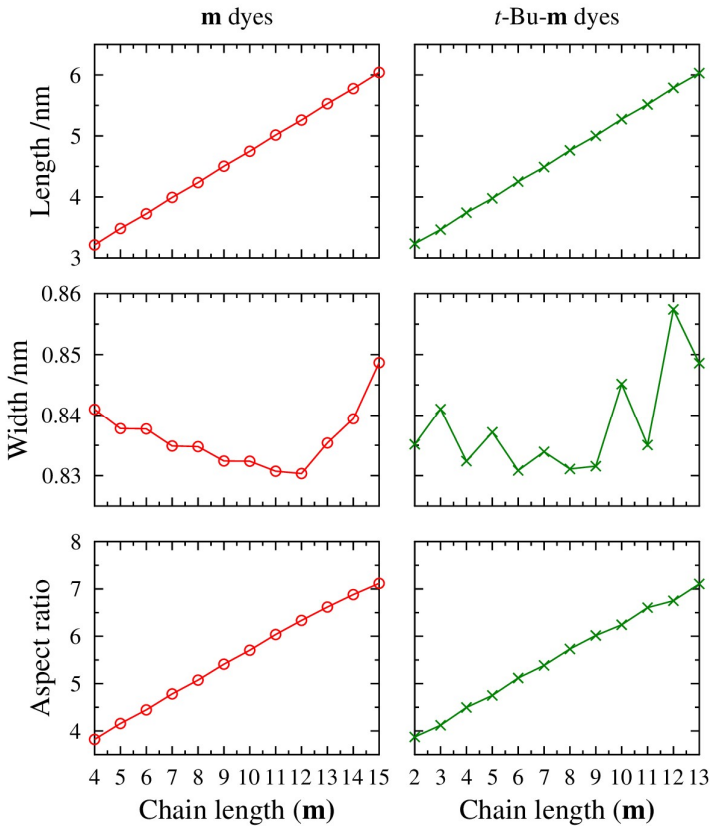

Figure 4.3: Summary of the lengths (l), widths (w) and aspect ratios (AR) across the two series of dyes with increasing alkoxy chain length (**m**).

4.2.2 Time-dependant density functional theory studies

Time-dependent DFT calculations were undertaken to determine the transition dipole moments (TDMs) which are associated with visible transitions of the dyes. From these calculations, the visible absorption transition wavelength (λ) and the oscillator strength (f) for this transition is summarised in Table 4.3 for the **m** dyes and Table 4.4 for the *t*-Bu-**m** dyes. It was observed that for all chain lengths in both series, the visible absorption transition wavelength was similar for all the dyes and the oscillator strength shows a small increase with increasing chain length. The orbitals involved in the transitions were found to be similar between the two series, and example dyes (**9** dye and *t*-Bu-**7** dye) are given in Figure 4.4.

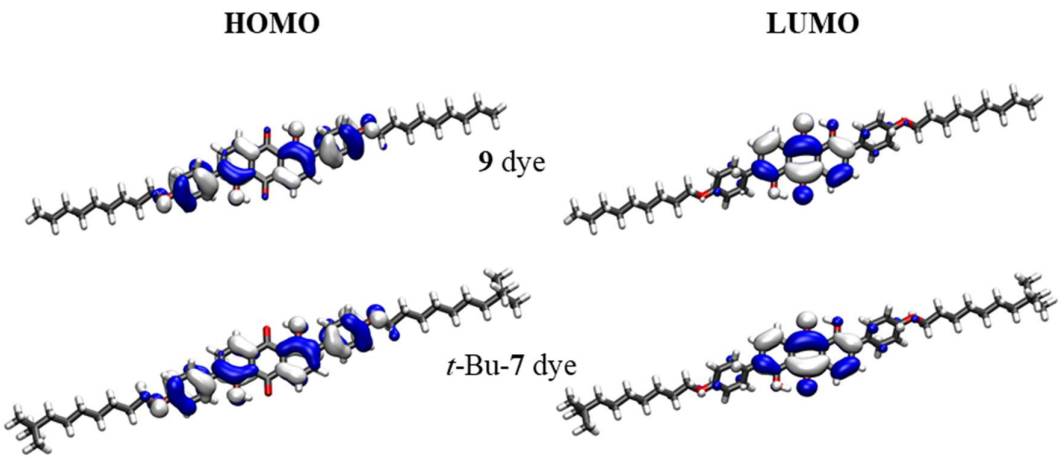

Figure 4.4: Optimised structures of the example dyes from each of the series and orbitals involved in the visible transitions.

Table 4.3: Summary of calculated visible absorption transition wavelength (λ) and oscillator strength (f) for the **m** dyes.

Molecule	λ /nm	f
4 dye	547	0.56
5 dye	548	0.56
6 dye	548	0.57
7 dye	548	0.57
8 dye	547	0.58
9 dye	547	0.58
10 dye	547	0.58
11 dye	547	0.58
12 dye	547	0.58
13 dye	547	0.58
14 dye	547	0.58
15 dye	547	0.58

Table 4.4: Summary of calculated visible absorption transition wavelength (λ) and oscillator strength (f) for the *t*-Bu-**m** dyes.

Molecule	λ /nm	f
t-Bu-**2** dye	548	0.57
t-Bu-**3** dye	548	0.58
t-Bu-**4** dye	548	0.58
t-Bu-**5** dye	548	0.58
t-Bu-**6** dye	547	0.58
t-Bu-**7** dye	547	0.58
t-Bu-**8** dye	547	0.58
t-Bu-**9** dye	547	0.59
t-Bu-**10** dye	547	0.59
t-Bu-**11** dye	547	0.59
t-Bu-**12** dye	547	0.59
t-Bu-**13** dye	547	0.59

Another important parameter to determine for the dyes is the angle (β) between the transition dipole moment (TDM) and the long axis of the 'core' of the dye molecule.[185] For these dyes the 'core' selected was a vector from the carbon where the alkoxy chain connects to the phenyl substituent to the same atom on the other phenyl substituent, as shown by the red line in Figure 4.5. Using the angles determined, the order parameter (S_β) of the dyes can be calculated, using equation 4.1, and these angles and order parameters are summarised in Table 4.5 for the **m** dyes and Table 4.6 for the *t*-Bu-**m** dyes.

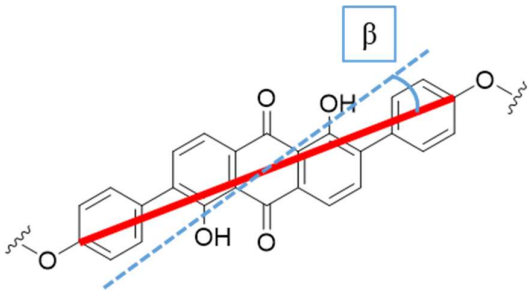

Figure 4.5: Diagram showing the long axis vector in the 'core' of both series of dyes (red), and an example transition dipole moment showing the origin of the angle β.

Equation 4.1 $$S_\beta = \frac{1}{2}\left(3\cos^2\beta - 1\right)$$

The angles in Table 4.5 and Table 4.6 show that difference between the vector and the TDM is small for these dyes, with a similar magnitude of angle across both series. As this angle is small across all the dyes, then the order parameter is close to 1 for all the different dyes. This potentially makes them good dyes for guest-host applications as the TDM will be well aligned with the long axis of the dye. The small angles between the long axis of the dye and the transition dipole moment match those determined by Sims et al. for the comparable 2,6 substituted anthraquinone with propyl chains.[158]

Table 4.5: Summary of calculated angle (β) between the visible TDM and the vector between the two Ph groups of the dye and the associated order parameter (S_β) for the **m** dyes.

Molecule	β /°	S_β
4 dye	1.03	0.9995
5 dye	1.15	0.9994
6 dye	1.16	0.9994
7 dye	1.23	0.9993
8 dye	1.22	0.9993
9 dye	1.26	0.9993
10 dye	1.26	0.9993
11 dye	1.28	0.9992
12 dye	1.30	0.9992
13 dye	1.31	0.9992
14 dye	1.32	0.9992
15 dye	1.33	0.9992

Table 4.6: Summary of calculated angle (β) between the visible TDM and the vector between the two Ph groups of the dye and the associated order parameter (S_β) for the *t*-Bu-**m** dyes.

Molecule	β /°	S_β
t-Bu-**2** dye	1.32	0.9992
t-Bu-**3** dye	1.11	0.9994
t-Bu-**4** dye	1.31	0.9992
t-Bu-**5** dye	1.21	0.9993
t-Bu-**6** dye	1.29	0.9992
t-Bu-**7** dye	1.28	0.9993
t-Bu-**8** dye	1.31	0.9992
t-Bu-**9** dye	1.31	0.9992
t-Bu-**10** dye	1.33	0.9992
t-Bu-**11** dye	1.33	0.9992
t-Bu-**12** dye	1.33	0.9992
t-Bu-**13** dye	1.33	0.9992

4.2.3 Dye and guest-host mixture selection

For the polarised UV-visible studies of the guest-host mixtures, the dye materials available were limited to three dyes, the *t*-Bu-**7**, *t*-Bu-**9**, and *t*-Bu-**11** dye. As a result, the selection of the guest-host mixtures for the molecular dynamics (MD) studies was based on which hosts could be predicted to be compatible with the dyes available. Figure 4.6 shows the layer spacing of the host from the nOCB series (left) and *t*-Bu-nOCB series (right), with the experimental values, given in grey, and values from the host alone MD simulations, given in red (nOCB) and green (*t*-Bu-nOCB). To take into account the interdigitation of the layers, reported in Chapter 3 and by Sims et al,[106] the lengths of the dyes were taken as the distances between the carbons at the centre of the *t*-Bu groups or terminal Me groups. These lengths are shown as horizontal dashed lines in Figure 4.6, with **m** chain length labels on the right-hand axis for the *t*-Bu-**m** dyes (bottom) and **m** dyes (top), respectively.

The studies of the host alone reported in chapter 3 showed that the *t*-Bu-nOCB series gave a more defined layer structure than the nOCB series, due to the presence of the bulky *t*-Bu terminal group in the chain. For a *t*-Bu dye to have good compatibility within a given host, it seems reasonable to suggest that the length of the dye should match the layer spacing of the host in order that the terminal *t*-Bu groups of the dyes can be accommodated into the layered structure of the host. Moreover, it might be suggested that *t*-Bu-**m** dyes might have better compatibility with *t*-Bu-nOCB hosts, than with the nOCB hosts.

From the bottom two plots in Figure 4.6, it can be seen that the *t*-Bu-**9** dye shows the best length compatibility with *t*-Bu-10OCB or the *t*-Bu-11OCB based on the experimental and simulated layers spacings from the host-alone studies. Also, these longer chain hosts have the advantage that the smectic A phase is formed quickly in the MD studies of the host-alone and have more stable phases than the shorter chain lengths in both the series, as reported in Chapter 3. Hence, the *t*-Bu-10OCB and *t*-Bu-11OCB hosts were selected for MD studies alongside 12OCB and 13OCB hosts of comparable chain length. For the guest selection, the experimentally available *t*-Bu-**7**, *t*-Bu-**9**, and *t*-Bu-**11** dyes were selected for the MD simulations alongside the comparable chain length **m** dyes, **9**, **11**, and **13** dye. For the *t*-Bu-nOCB hosts, additional *t*-Bu-**m** dyes where **m** = 4, 8 and 10 were studied along with the comparable **m** dyes where **m** = 2, 6 and 8 to evaluate a broader range of dye lengths with the

t-Bu-nOCB hosts. For the experimental studies, Figure 4.6 suggests that *t*-Bu-**9** dye might have good compatibility with the *t*-Bu-10OCB or *t*-Bu-11OCB hosts and the *t*-Bu-**7** dyes might have good compatibility with the 12OCB or 13OCB hosts. The *t*-Bu-**11** dye does not show a clear length match with any of the selected hosts, but acts as a possible mismatch in length. This may provide insight into the impact of using a dye with longer chains than the measured layer spacing of the host.

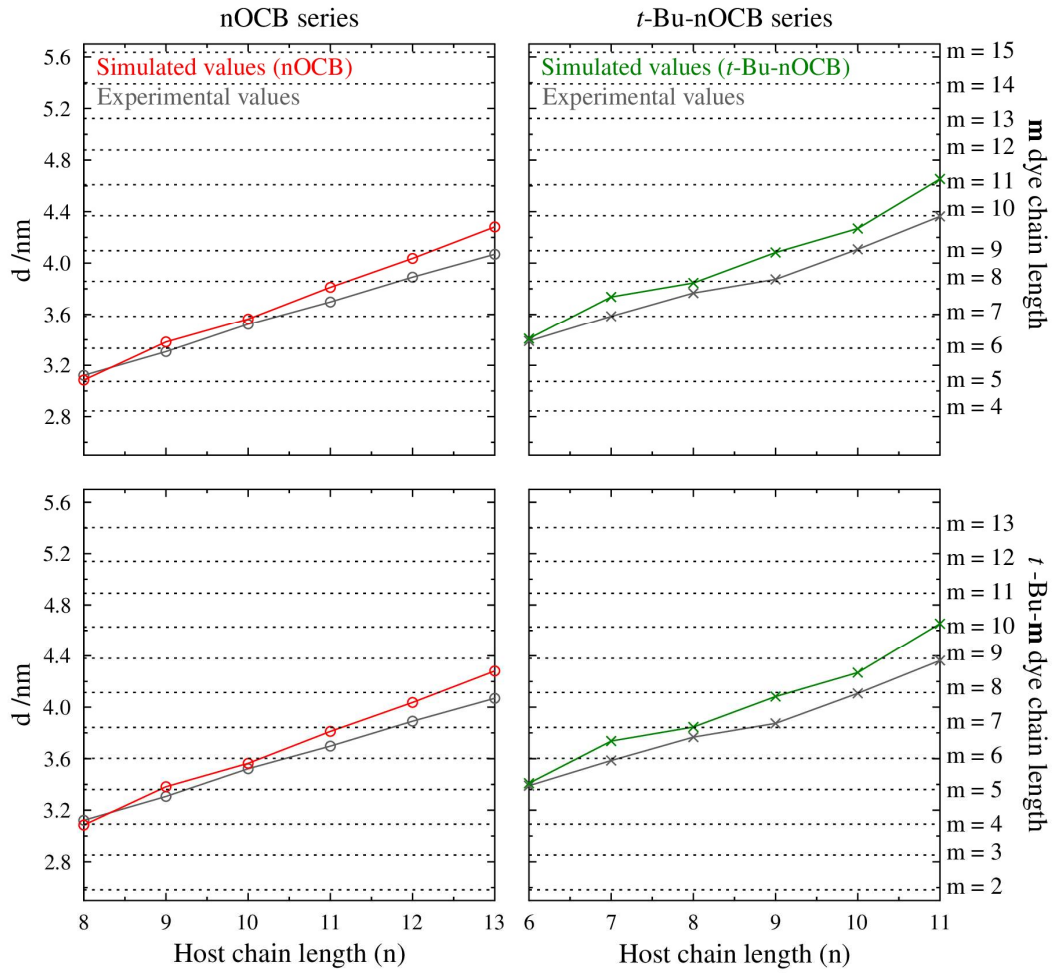

Figure 4.6: Comparison of the layer spacing from the host MD simulations (red for the nOCB series, green for the *t*-Bu-nOCB series) and the experimental values determined by XRD for both of the host series (grey), at the same reduced temperature (T_{red} = 0.95) on the left axis, with the DFT lengths of the **m** dyes (top plots) and *t*-Bu-**m** dyes (bottom plots) shown as dotted lines and identified on the right axis.

4.2.4 Molecular dynamics studies

The guest-host simulations were run from isotropic starting conditions, with the use of anisotropic pressure coupling at the same temperature as used in the respective host alone simulations, which was a reduced temperature of 0.95 relative to the simulated clearing point of the respective host-alone simulations. These conditions were used to match the conditions of the host alone simulations, and the simulations were run over 500 ns as this was found to be an adequate run to allow the orientational and translational order to reach a plateau. The simulations were analysed to determine the orientational order parameter (S), translational order parameter (τ) and layer spacing (d) of the host molecules. These values could then be compared with those from host alone simulations in order to determine the how the dye affected the host. Analysis of the orientational and translational order parameters of the dye molecules within the host were also undertaken. For the dye orientational parameter a vector between the phenyl rings was used, as shown in Figure 4.5, and the translational order a point in the centre of middle ring in the anthraquinone core was used, to give insight into dye ordering within the liquid crystal host.

Plots of the host orientational order parameter (S), translational order parameter (τ) and layer spacing (d) for the MD simulations of the guest-host mixtures with 12OCB and 13OCB as the host are given in Figure 4.7and for the guest-host mixtures with *t*-Bu-10OCB and *t*-Bu-11OCB are given in Figure 4.8, Figure 4.9 and Figure 4.10. All simulations were analysed over the plateau regions of the plots, and are summarised in Table 4.7 and Table 4.8.

For all the guest-host mixtures, the phases observed in the simulations are the same types of phases present for the host alone simulations and the rise times observed are also similar to the host alone systems. For both sets of guest-host mixtures with nOCB hosts, the orientational order parameter (S) of the host, shown at the top of Figure 4.7 has a rise time of <50 ns before reaching a plateau at a value of 0.63-0.72, with the orientational order forming very quickly as observed for the host alone simulations. The translational order parameter (τ) of the host, shown in the middle of Figure 4.7, rises in 50-100 ns to a plateau of 0.27-0.36 for most of the guest-host mixtures, with the exceptions of 12OCB with *t*-Bu-**7** dye and 13OCB with **9** dye which show some breakdown in the translational order at ≥ 300 ns. For 13OCB with **9** dye the breakdown is short-lived and the order parameter re-

establishes the plateau but for 12OCB with *t*-Bu-**7** dye the translational order does not reach the same plateau over the following ~200 ns. The layer spacing (d), shown at the bottom of Figure 4.7, shows similar trends in stability to the respective translational order parameter. The layer spacing of 3.94-4.12 nm, for the guest-host mixtures with 12OCB, is lower than the layer spacing of 4.19-4.35 nm, for the guest-host mixtures with 13OCB. This observation matches the trend observed for the respective host alone samples.

For both sets of guest-host mixtures with *t*-Bu-nOCB hosts, the orientational order parameter (S) of the hosts, shown in Figure 4.8, has a rise time of 200-400 ns before reaching a plateau at 0.86-0.77 for all except *t*-Bu-11OCB with *t*-Bu-**11** dye, with the orientational order forming over similar to longer time scales than for the hosts alone. The translational order parameter (τ) of the host, shown in Figure 4.9, rises in 200-400 ns to a plateau of 0.43-0.56 for most of the guest-host mixtures, with the exception of *t*-Bu-11OCB with *t*-Bu-**11** dye which does not reach the same plateau of approximately 0.5 in the 500 ns run. The layer spacing (d) of the host, shown in Figure 4.10, shows similar trends in stability to the respective translational order parameter. The layer spacing of 4.13-4.33 nm, for the guest-host mixtures with *t*-Bu-10OCB, is lower than the layer spacing of 4.14-4.71 nm, for the guest-host mixtures with *t*-Bu-11OCB. This observation matches the trend observed for the respective host alone samples.

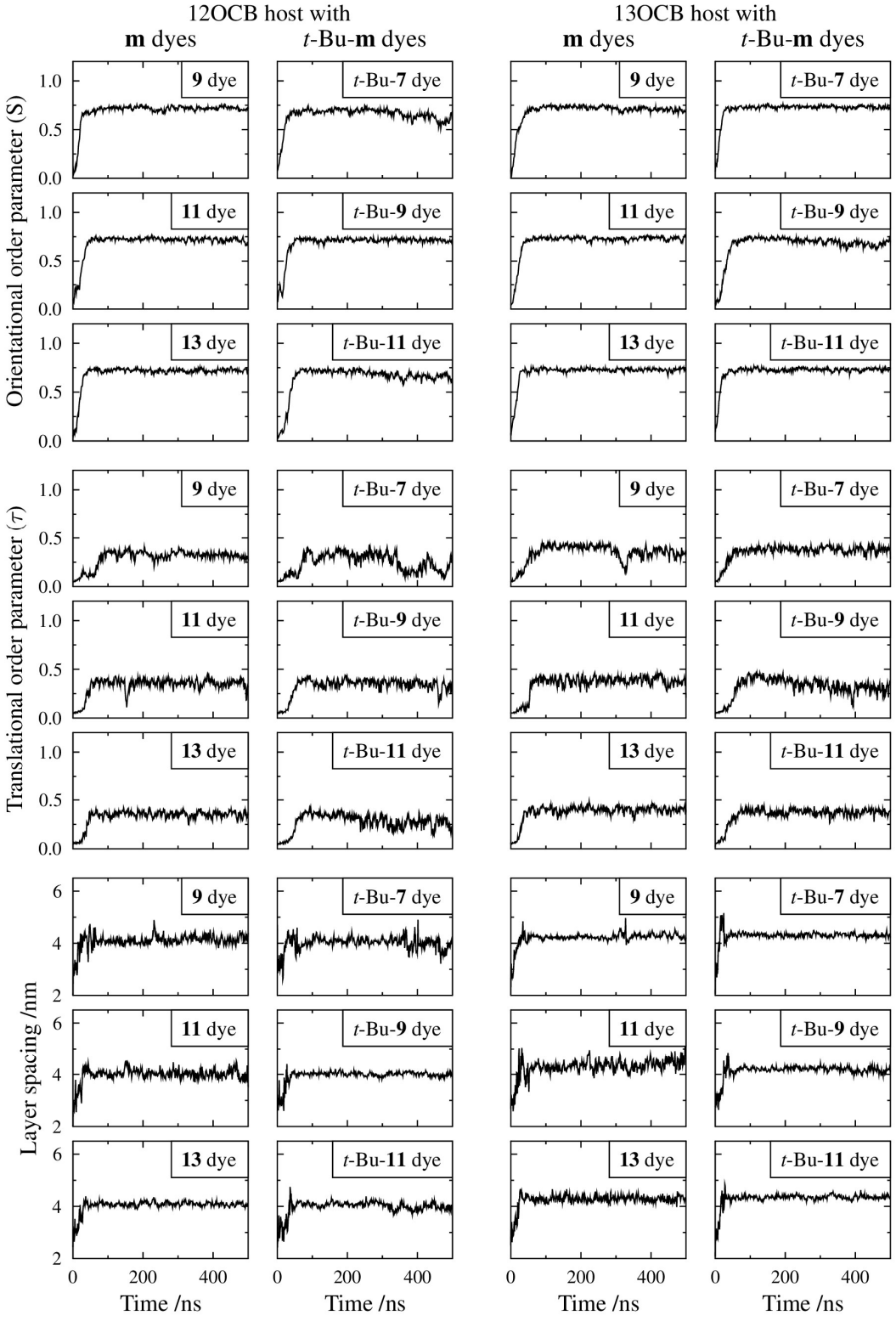

Figure 4.7: Orientational order parameter (S), translational order parameter (τ) and layer spacing (d) of the host molecules as a function of time through the guest-host simulations with 12OCB and 13OCB as the host, at a reduced temperature of 0.95.

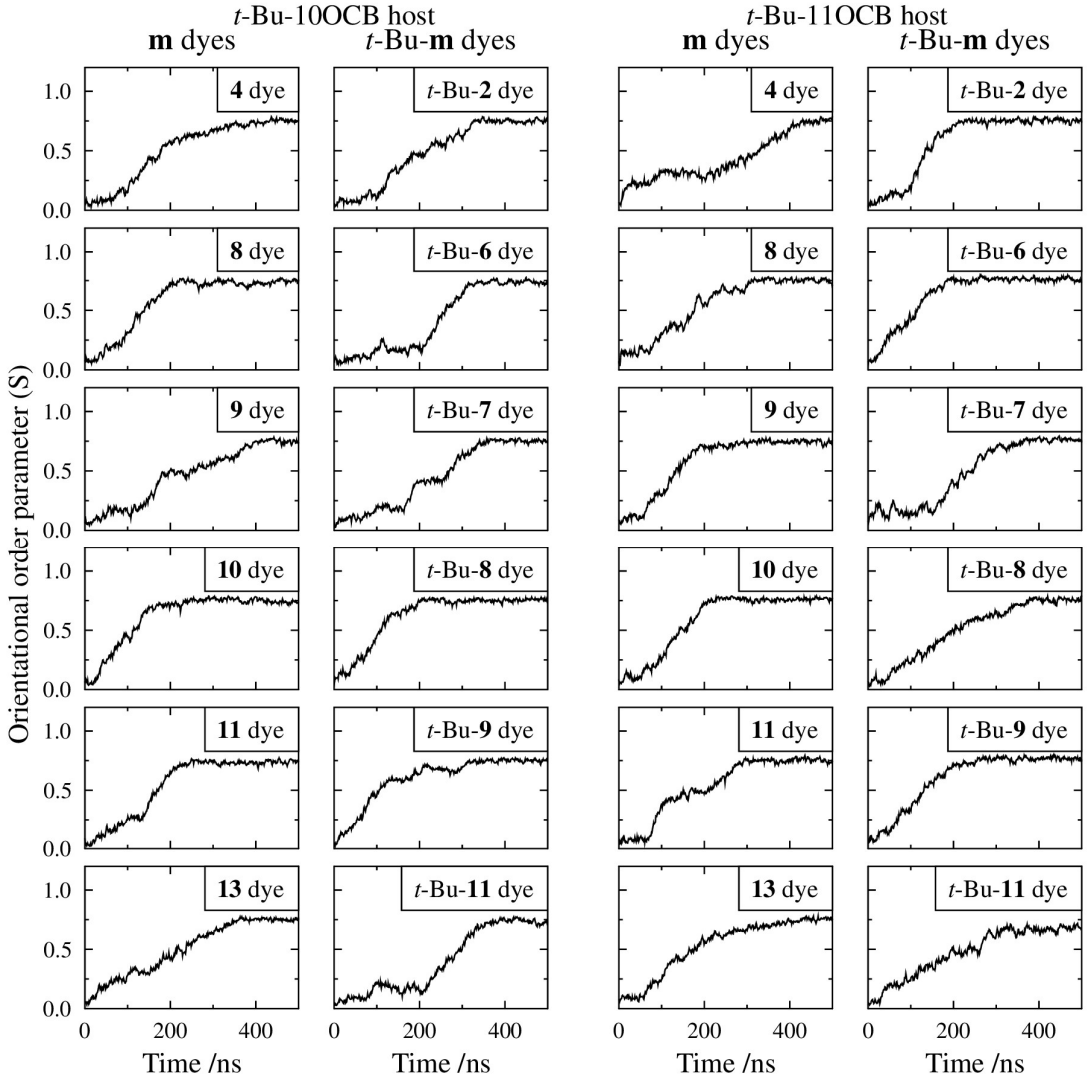

Figure 4.8: Orientational order parameter (S) as a function of time though the guest-host simulations with *t*-Bu-10OCB and *t*-Bu-11OCB as the host, at a reduced temperature of 0.95.

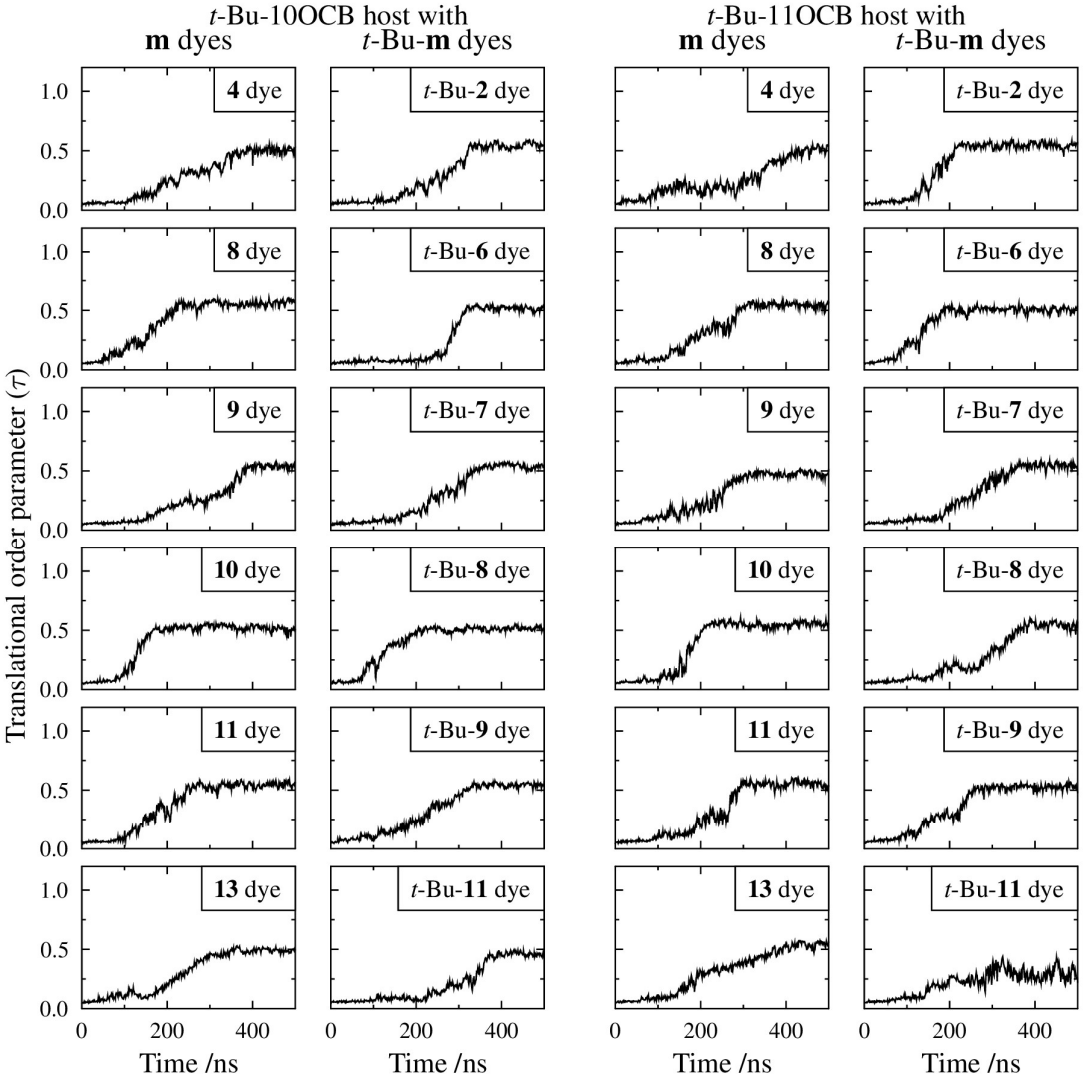

Figure 4.9: Translational order parameter (τ) as a function of time through the guest-host simulations with *t*-Bu-10OCB and *t*-Bu-11OCB as the host, at a reduced temperature of 0.95.

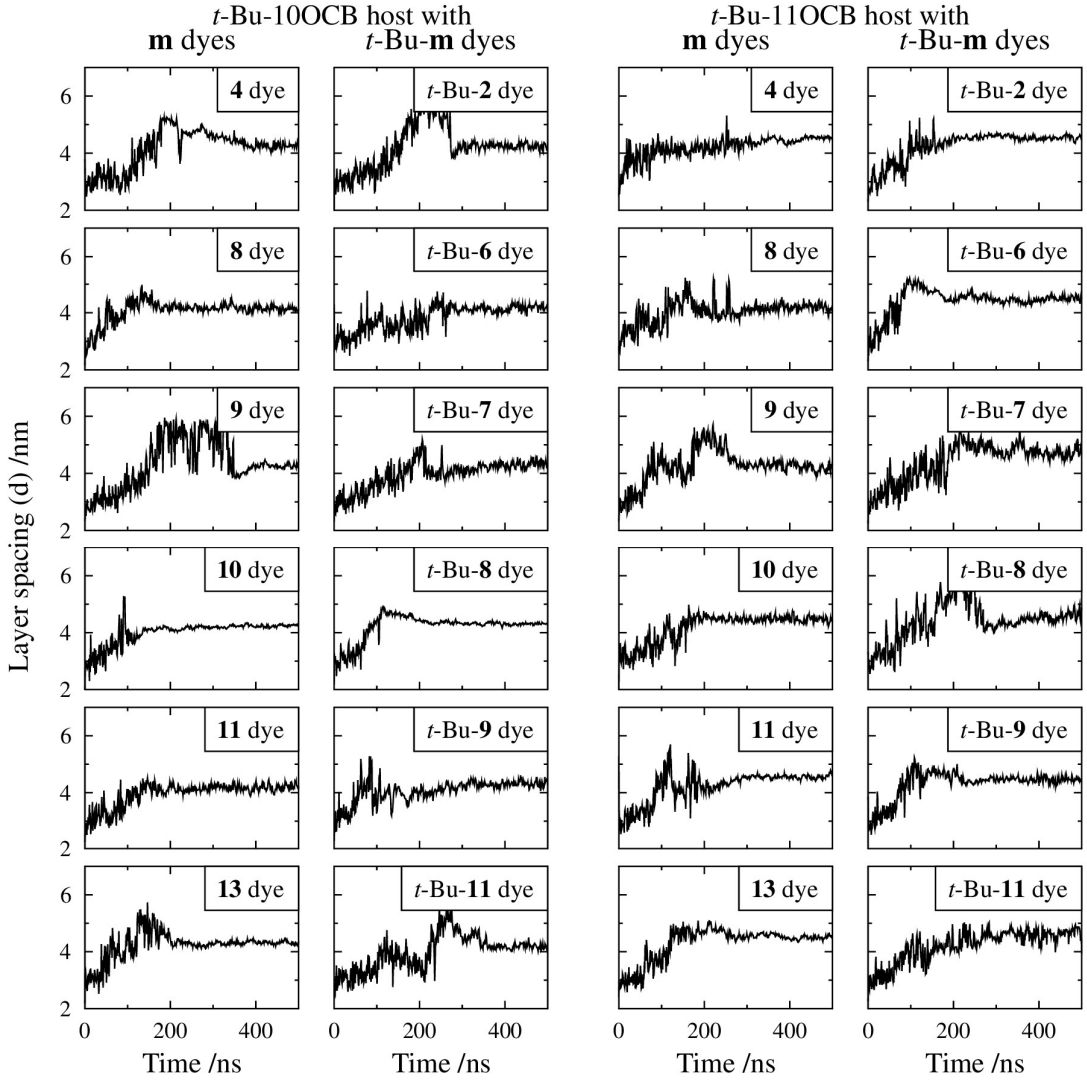

Figure 4.10: Layer spacing (d) of the host molecules as a function of time through the guest-host simulations with *t*-Bu-10OCB and *t*-Bu-11OCB as the host, at a reduced temperature of 0.95.

Table 4.7: Average orientational order parameter (S), translational order parameter (τ) and layer spacing (d) of the host molecules averaged over the plateau region for the guest-host mixtures with 12OCB and 13OCB as the hosts. * denotes averages taken before drop in parameter values.

Host	Guest	S	τ	d /nm	Guest	S	τ	d /nm
12OCB	**9** dye	0.72	0.36	4.12	*t*-Bu-**7** dye	0.63	0.31*	4.10*
	11 dye	0.72	0.36	4.02	*t*-Bu-**9** dye	0.72	0.35	4.00
	13 dye	0.72	0.33	4.09	*t*-Bu-**11** dye	0.66	0.27	3.94
13OCB	**9** dye	0.71	0.41*	4.22*	*t*-Bu-**7** dye	0.73	0.38	4.31
	11 dye	0.73	0.39	4.33	*t*-Bu-**9** dye	0.67	0.31	4.19
	13 dye	0.73	0.40	4.29	*t*-Bu-**11** dye	0.73	0.38	4.35

Table 4.8: Average orientational order parameter (S), translational order parameter (τ) and layer spacing (d) of the host molecules averaged over the plateau region for the guest-host mixtures with *t*-Bu-10OCB and *t*-Bu-11OCB as the hosts.

Host	Guest	S	τ	d /nm	Guest	S	τ	d /nm
t-Bu-10OCB	**4** dye	0.76	0.50	4.26	*t*-Bu-**2** dye	0.75	0.54	4.25
	8 dye	0.73	0.56	4.16	*t*-Bu-**6** dye	0.74	0.52	4.15
	9 dye	0.74	0.54	4.23	*t*-Bu-**7** dye	0.75	0.54	4.29
	10 dye	0.74	0.51	4.15	*t*-Bu-**8** dye	0.76	0.52	4.31
	11 dye	0.73	0.54	4.13	*t*-Bu-**9** dye	0.75	0.54	4.31
	13 dye	0.75	0.49	4.33	*t*-Bu-**11** dye	0.73	0.45	4.19
t-Bu-11OCB	**4** dye	0.75	0.51	4.54	*t*-Bu-**2** dye	0.75	0.54	4.49
	8 dye	0.75	0.55	4.14	*t*-Bu-**6** dye	0.76	0.51	4.50
	9 dye	0.75	0.48	4.25	*t*-Bu-**7** dye	0.76	0.55	4.71
	10 dye	0.76	0.56	4.47	*t*-Bu-**8** dye	0.76	0.54	4.57
	11 dye	0.75	0.55	4.43	*t*-Bu-**9** dye	0.77	0.53	4.46
	13 dye	0.76	0.54	4.57	*t*-Bu-**11** dye	0.67	0.29	4.61

The simulated phases were visualised, as shown in Figure 4.11 and Figure 4.12 for the guest-host simulations with 12OCB and 13OCB as the hosts, and Figure 4.13 and Figure 4.14 for the guest-host simulations with *t*-Bu-10OCB and *t*-Bu-11OCB as the hosts, respectively. As seen with the hosts alone the different shapes of the boxes reflect the anisotropic pressure coupling used in the simulation, resulting in the phase developing differently for the different guest-host simulations. The boxes are scaled to give a simple visualisation of the phases and are not all similar dimensions. As with the host alone simulations, every atom of each molecule is not shown but the molecules are labelled with the orange areas representing the biphenyl aromatic rings and the blue sphere representing the corresponding terminal group of the host molecules, as shown in Figure 3.19. All the atoms of the dyes are shown and are labelled in green. For all these simulations, there are diffuse layers formed in the phase, reflecting the presence of a smectic liquid crystal phase consistent with observations for the host alone simulations. It can be observed in most cases that the long axes of the dye molecules are aligned with the layer normal of the smectic layers and that the dye molecules are generally situated within a layer with the terminal chains sitting within the terminal chains of the host molecules.

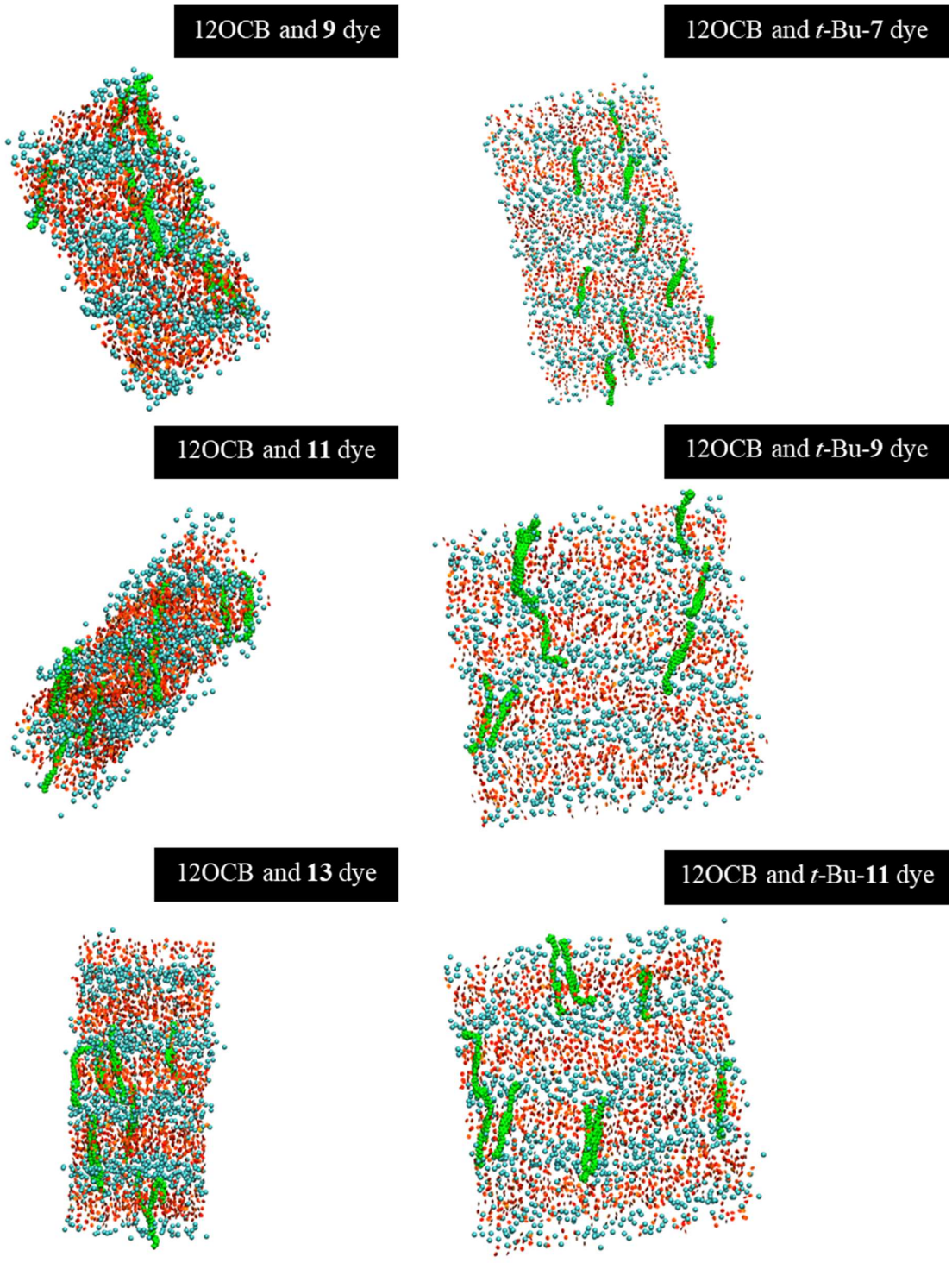

Figure 4.11: Visualisations of the guest-host simulations with 12OCB as the host, at the end of the 500 ns simulation.

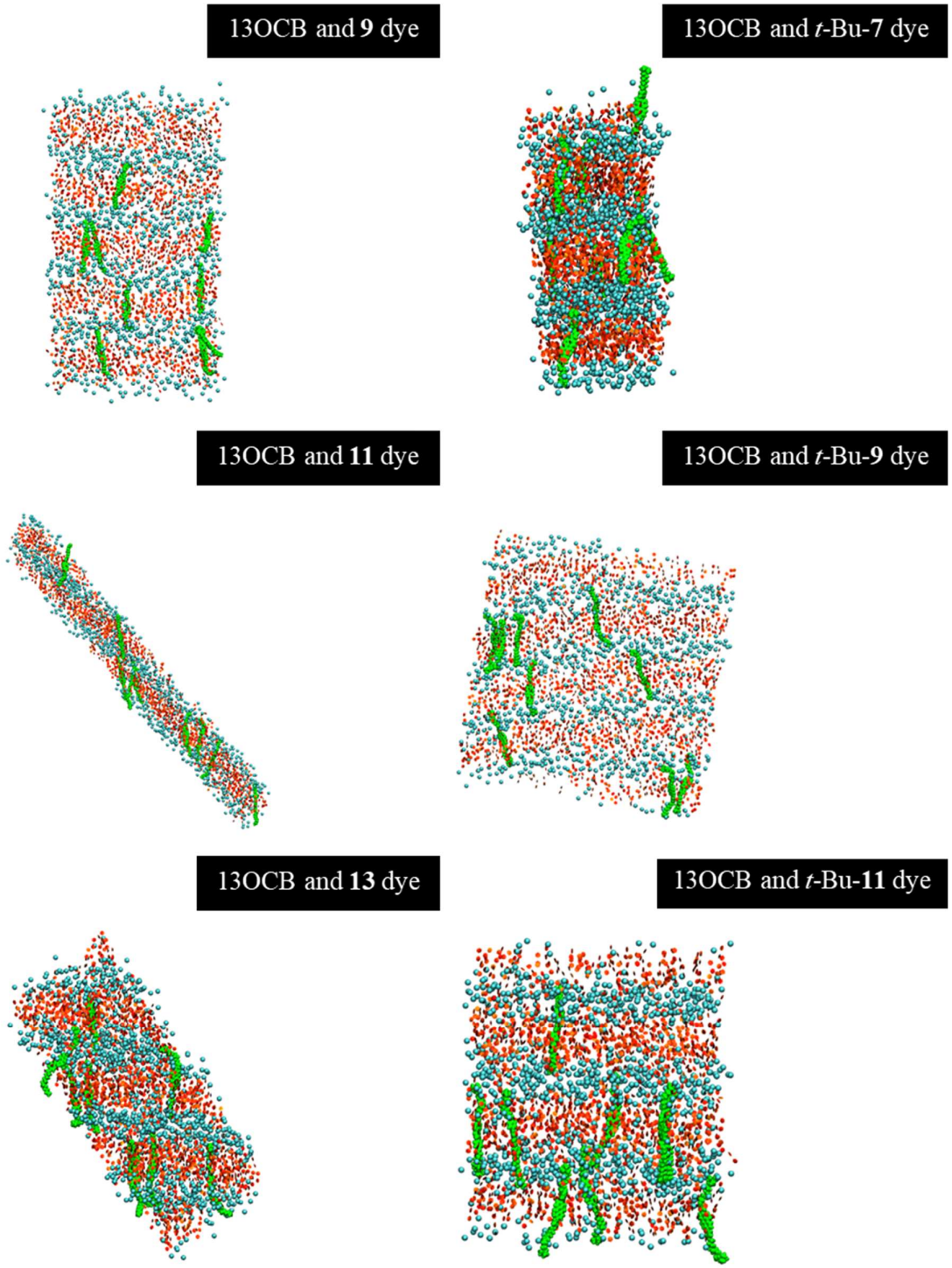

Figure 4.12: Visualisations of the guest-host simulations with 13OCB as the host, at the end of the 500 ns simulation.

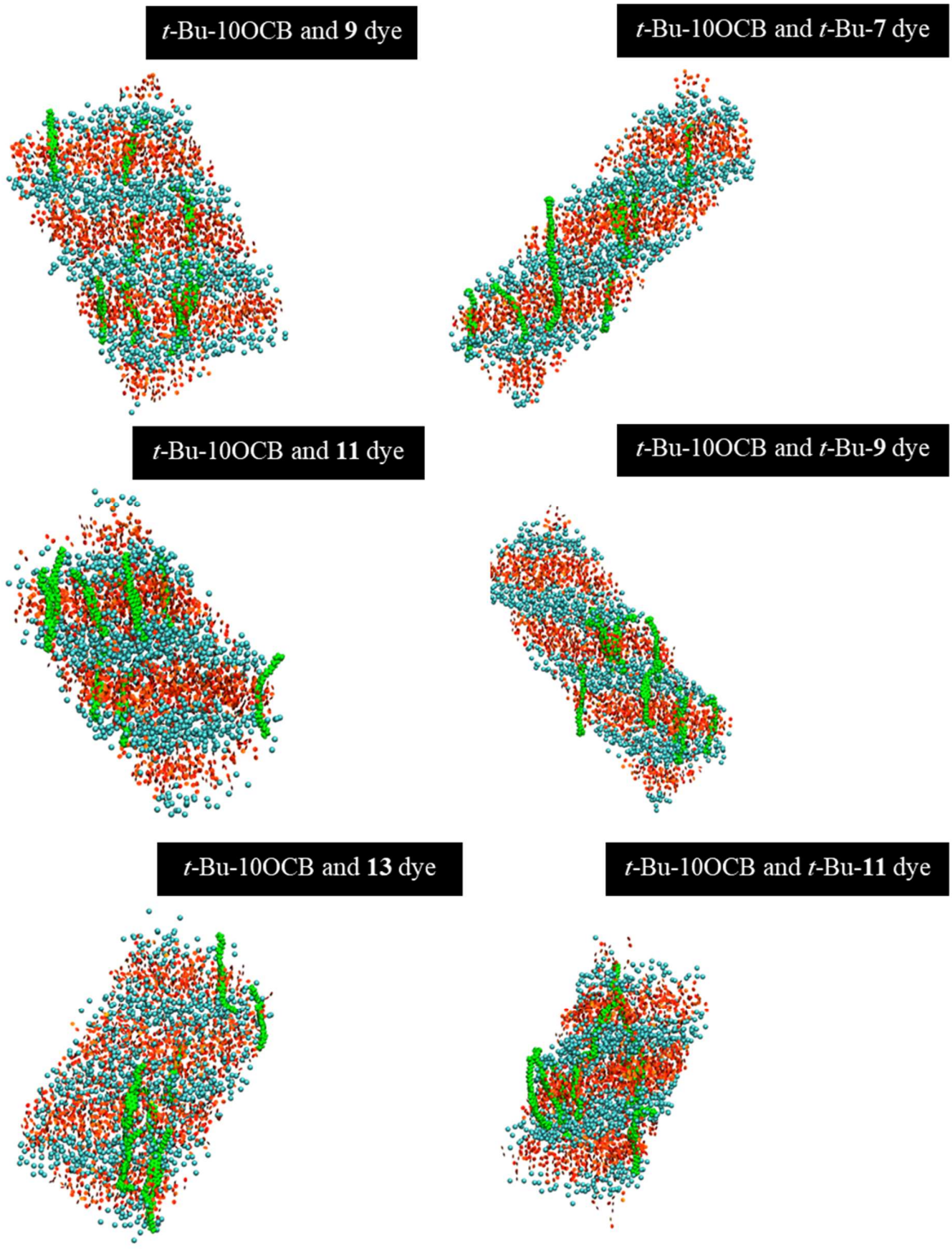

Figure 4.13: Example visualisations of the guest-host simulations with *t*-Bu-10OCB as the host, at the end of the 500 ns simulation.

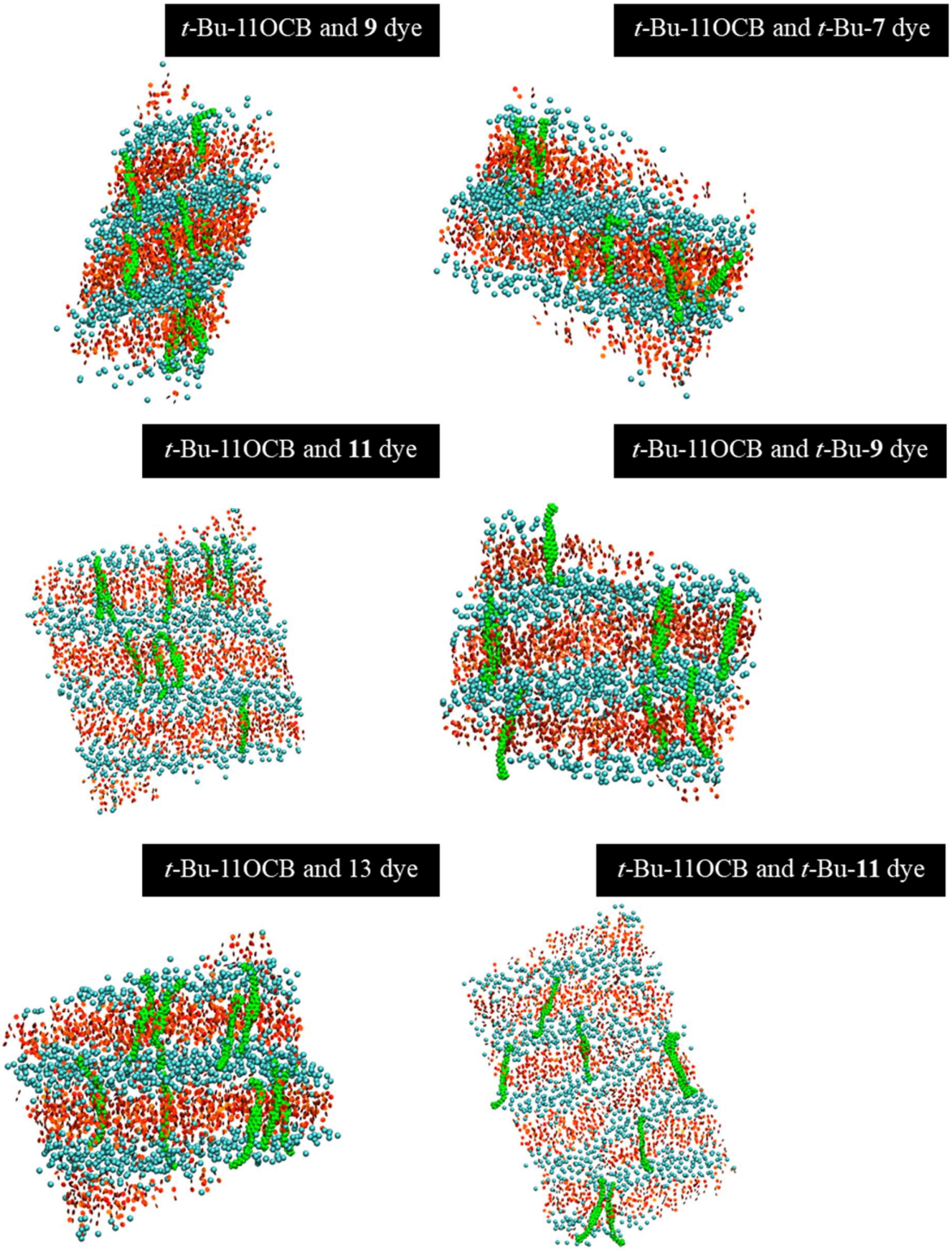

Figure 4.14: Example visualisations of the guest-host simulations with *t*-Bu-11OCB as the host, at the end of the 500 ns simulation.

As the dye molecules are oriented within the host, the orientational order parameter of the dye can be determined with respect to the host director and also the translational order parameter of the dyes, relative to the layer spacing of the host. In order to calculate the orientational order parameter a vector between the terminal carbon atoms of the phenyl rings, shown as a red line in Figure 4.15, was used as the long axis for the analysis. A proxy was selected because the orientation of the core is the most important part for determining the alignment of the dyes within the host, and also using a proxy simplifies the calculation. The orientational order parameter was calculated with respect to the director of the host liquid crystal phase. For the translational order parameter a point in the centre of the middle aromatic ring of the anthraquinone unit was selected as a proxy for the centre of mass (COM), shown as a blue dot in Figure 4.15. The translational order parameters were calculated using the respective layer spacings from the host as a reference.

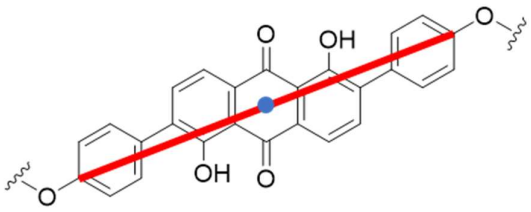

Figure 4.15: Example dye to show the proxy minimum MOI axis, red line, and the proxy COM, blue dot.

These values are plotted in Figure 4.16 for the guest-host mixtures with 12OCB and 13OCB as the hosts, and in Figure 4.17 and Figure 4.18 for the guest-host mixtures with *t*-Bu-10OCB and *t*-Bu-11OCB as the hosts. These dye parameters follow the rise times and general trends seen for the equivalent host parameters, and as a result these simulations were also averaged over the same regions as the host parameters, to give the average parameters shown in Table 4.9 for the guest-host mixtures with 12OCB and 13OCB as the hosts, and Table 4.10 for the guest-host mixtures with *t*-Bu-10OCB and *t*-Bu-11OCB as the hosts.

The order parameters of the dyes show greater noise due to the smaller number of vectors or centres of mass being averaged over as there are only 9 dye molecules relative to the 1000 host liquid crystal molecules. For the dyes within the nOCB hosts, the orientational order parameter of the dyes closely follows the rise time of the host orientational order parameter but the dye orientational order parameter of ca. 0.8 than those forth is larger than these for the host. The dye translational order parameter of 0.5-0.7 is also higher than these for the host.

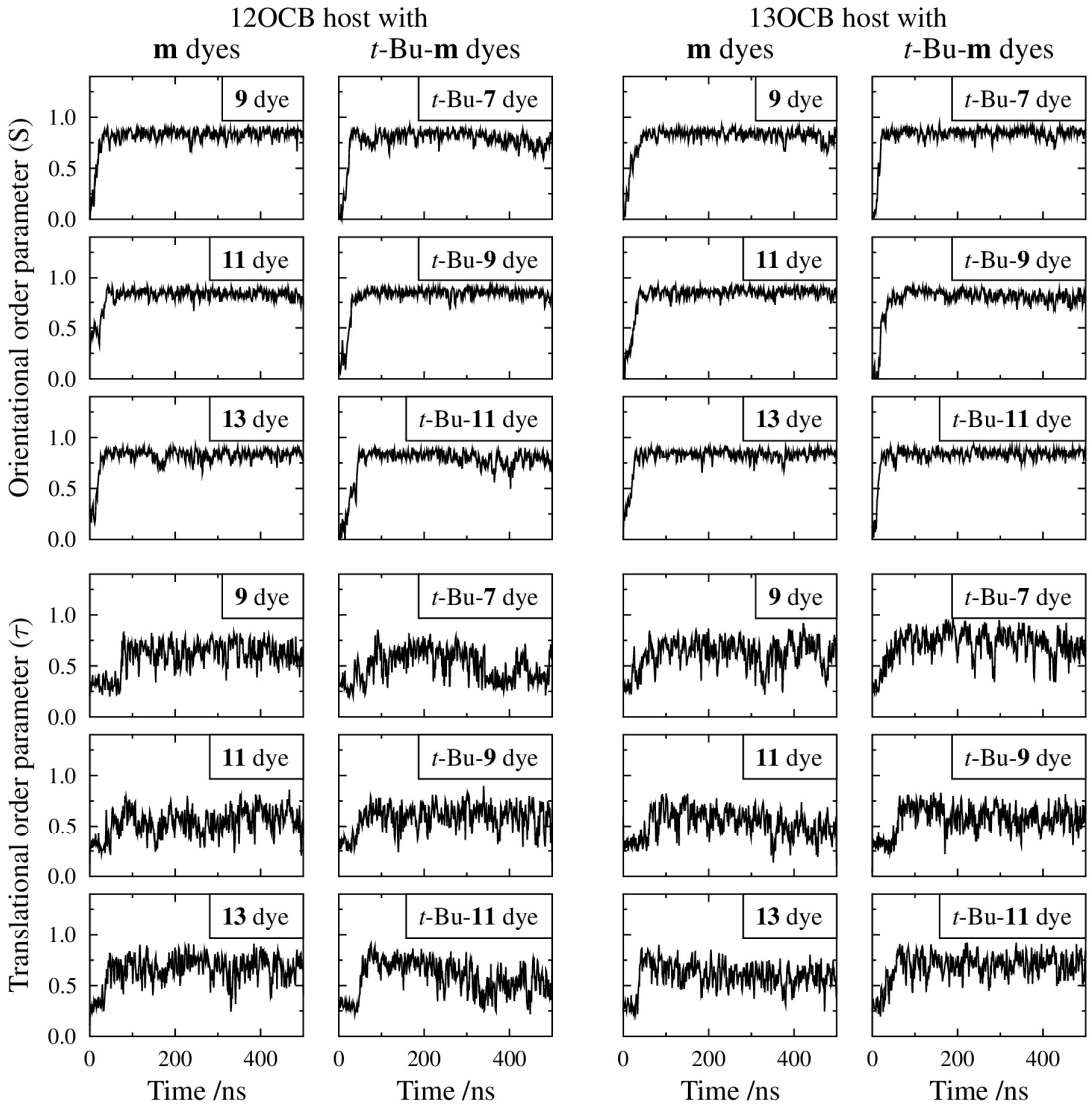

Figure 4.16: Orientational order parameter (S) and translational order parameter (τ) of the dye molecules, as a function of time during the guest-host simulations with 12OCB and 13OCB as the host, at a reduced temperature of 0.95.

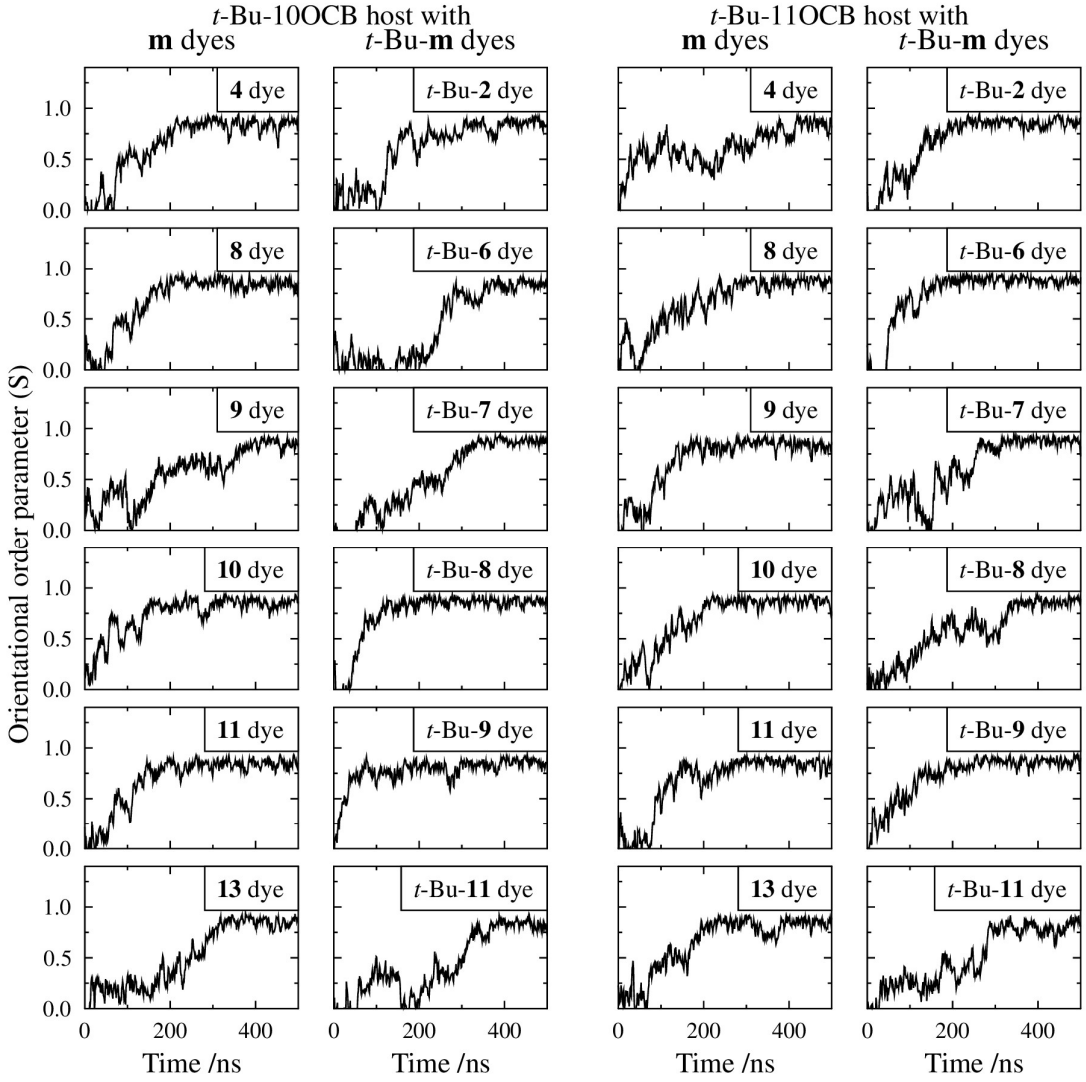

Figure 4.17: Orientational order parameter (S) of the dye molecules as a function of time during the guest-host simulations with *t*-Bu-10OCB and *t*-Bu-11OCB as the host, at a reduced temperature of 0.95.

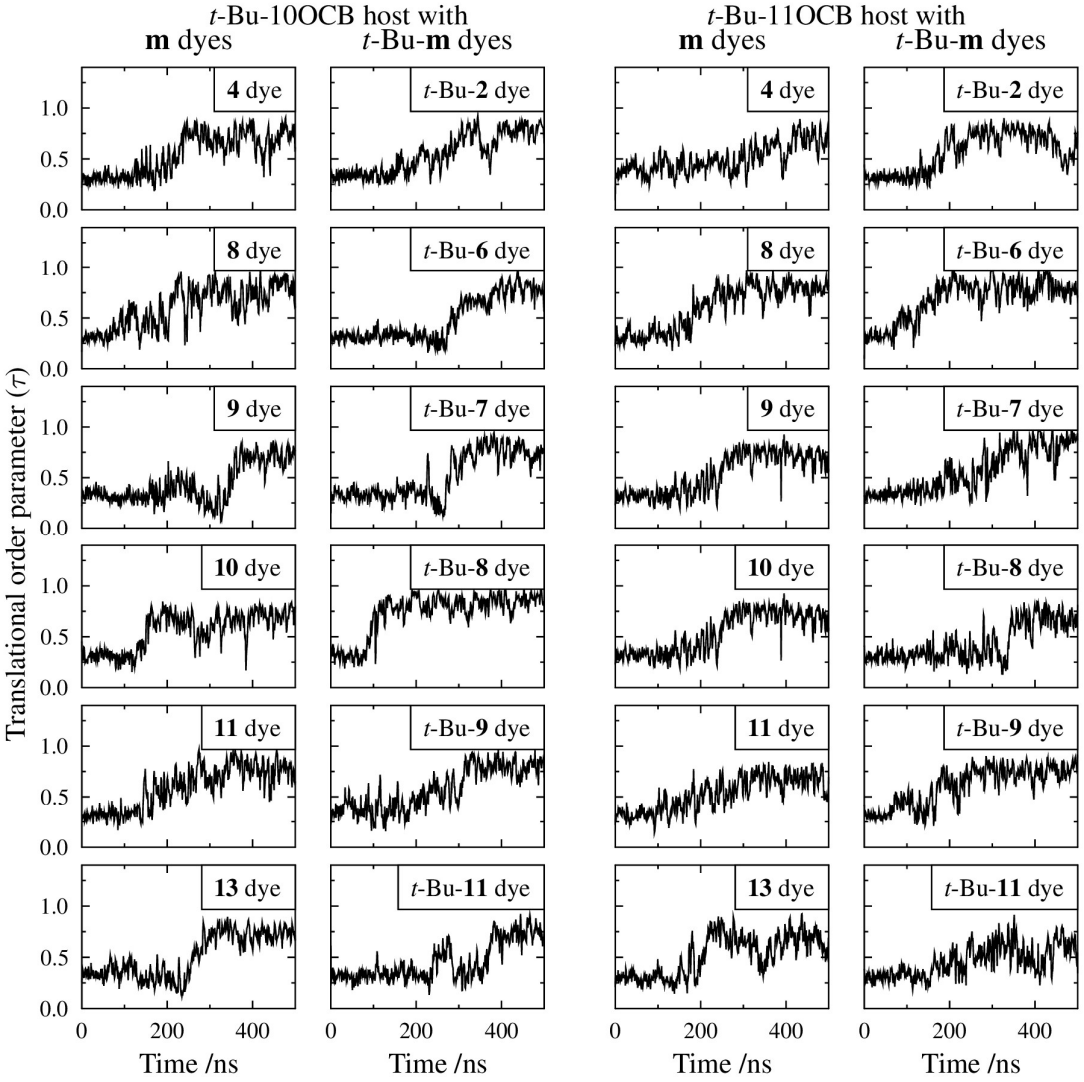

Figure 4.18: Translational order parameter (τ) of the dye molecules as a function of time during the guest-host simulations with *t*-Bu-10OCB and *t*-Bu-11OCB as the host, at a reduced temperature of 0.95.

Table 4.9: Average orientational order parameter (S) and translational order parameter (τ) of the dye molecules, averaged over plateau area for the guest-host mixtures with 12OCB and 13OCB as the hosts.

Host	Guest	S	τ	Guest	S	τ
12OCB	**9** dye	0.82	0.62	*t*-Bu-**7** dye	0.77	0.44
	11 dye	0.83	0.56	*t*-Bu-**9** dye	0.84	0.59
	13 dye	0.83	0.66	*t*-Bu-**11** dye	0.78	0.53
13OCB	**9** dye	0.82	0.63	*t*-Bu-**7** dye	0.82	0.72
	11 dye	0.85	0.46	*t*-Bu-**9** dye	0.80	0.58
	13 dye	0.81	0.61	*t*-Bu-**11** dye	0.84	0.71

Table 4.10: Average orientational order parameter (S) and translational order parameter (τ) of the dye molecules, averaged over plateau area for the guest-host mixtures with *t*-Bu-10OCB and *t*-Bu-11OCB as the hosts.

Host	Guest	S	τ	Guest	S	τ
t-Bu-10OCB	**4** dye	0.83	0.68	*t*-Bu-**2** dye	0.86	0.79
	8 dye	0.85	0.56	*t*-Bu-**6** dye	0.84	0.79
	9 dye	0.84	0.65	*t*-Bu-**7** dye	0.87	0.76
	10 dye	0.86	0.51	*t*-Bu-**8** dye	0.87	0.81
	11 dye	0.83	0.76	*t*-Bu-**9** dye	0.85	0.80
	13 dye	0.84	0.72	*t*-Bu-**11** dye	0.83	0.73
t-Bu-11OCB	**4** dye	0.82	0.66	*t*-Bu-**2** dye	0.86	0.69
	8 dye	0.86	0.79	*t*-Bu-**6** dye	0.88	0.77
	9 dye	0.83	0.72	*t*-Bu-**7** dye	0.88	0.86
	10 dye	0.85	0.79	*t*-Bu-**8** dye	0.86	0.68
	11 dye	0.85	0.66	*t*-Bu-**9** dye	0.86	0.74
	13 dye	0.83	0.68	*t*-Bu-**11** dye	0.79	0.64

4.3 Experimental studies

In this section, there is a brief report of the POM and DSC studies of the dyes alone. Then the guest-host mixture results are reported, from the POM, DSC and XRD studies. The final section contains details on the cell screening and home-built cells, followed by the polarised UV-visible absorption spectroscopy results.

4.3.1 Polarised optical microscopy and differential scanning calorimetry studies

4.3.1.1 Dyes alone

Some of the studies of the dyes alone had been undertaken as part of the dye synthesis project, as indicated,[22] and they are reported here for completion alongside studies completed during this project.

The dyes studied in this section were characterised by POM, as shown in Figure 4.19, and DSC, with the transition temperatures and enthalpies of transition given in Table 4.11, and the related DSC traces shown in Figure 4.20. On cooling from the isotropic, the *t*-Bu-**7** dye showed the presence of a fan-like focal conic texture accompanied by homeotropic regions, indicating the presence of a smectic A (SmA) phase. On further cooling, a transition occurred to give a broken focal conic texture and in the homeotropic regions a schlieren texture

appears, indicating the presence of a smectic C (SmC) phase. In the case of the *t*-Bu-**9** dye, there was a broken focal conic texture and accompanied by regions of schlieren texture and for the *t*-Bu-**11** dye only the broken focal conic and schlieren texture was observed, indicating a direct transition to a smectic C (SmC) phase.

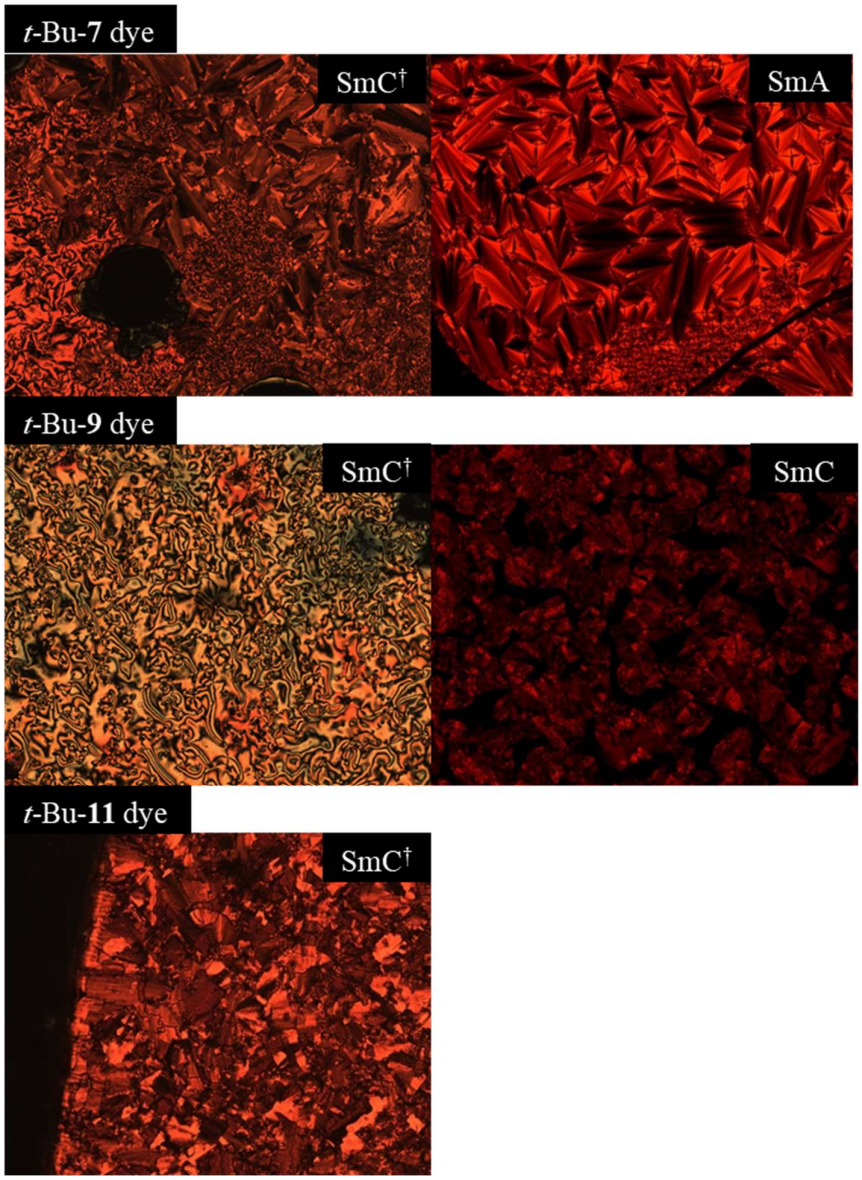

Figure 4.19: Photomicrographs showing the smectic C (SmC) and smectic A (SmA) phases of the *t*-Bu-**7** dye, and SmC only for *t*-Bu-**9** dye and *t*-Bu-**11** dye as observed between crossed polarisers. Images were taken on cooling from the isotropic liquid, captured at: (top L to R) 193 °C, 300 °C, (middle L to R) 155 °C, 283 °C, (bottom) 268 °C. The † symbol indicates images taken by S.J. Cowling.[22]

For the *t*-Bu-**7** dye, the largest peak in each heating cycle represents the melting point of the crystal into the smectic C phase, which was identified by microscopy. There is no peak observed for transition between the smectic C and smectic A phase for the *t*-Bu-**7** dye, as the peaks are close together and the peak for the smectic C transition cannot be resolved. The smaller peak around 30 ^{o}C for this dye represents the clearing point transition from the smectic A phase into the isotropic liquid.

For the other two dyes, the largest peak in each heating cycle represents the melting point of the crystal into the smectic C phase and there is a smaller peak for the clearing point, with no other transitions occurring. The clearing point peak for the *t*-Bu-**9** dye is broad in the second, which may signify a slight degradation of the sample. For these dyes, there is a decrease in both the melting point and clearing point with increasing chain length.

The calculated transition entropies are given in Table 4.12 for the *t*-Bu-**m** dyes. The magnitude of the melting point transition enthalpies and entropies are similar for the *t*-Bu-**7** and *t*-Bu-**9** dyes, and slightly higher than that for the *t*-Bu-**11** dye. For the clearing point transition enthalpies and entropies, the values are similar for the *t*-Bu-**9** and *t*-Bu-**11** dyes and smaller for the *t*-Bu-**7** dye. In this case the transition values are lower for the smectic A to isotropic transitions, and higher for the smectic C to isotropic transition.

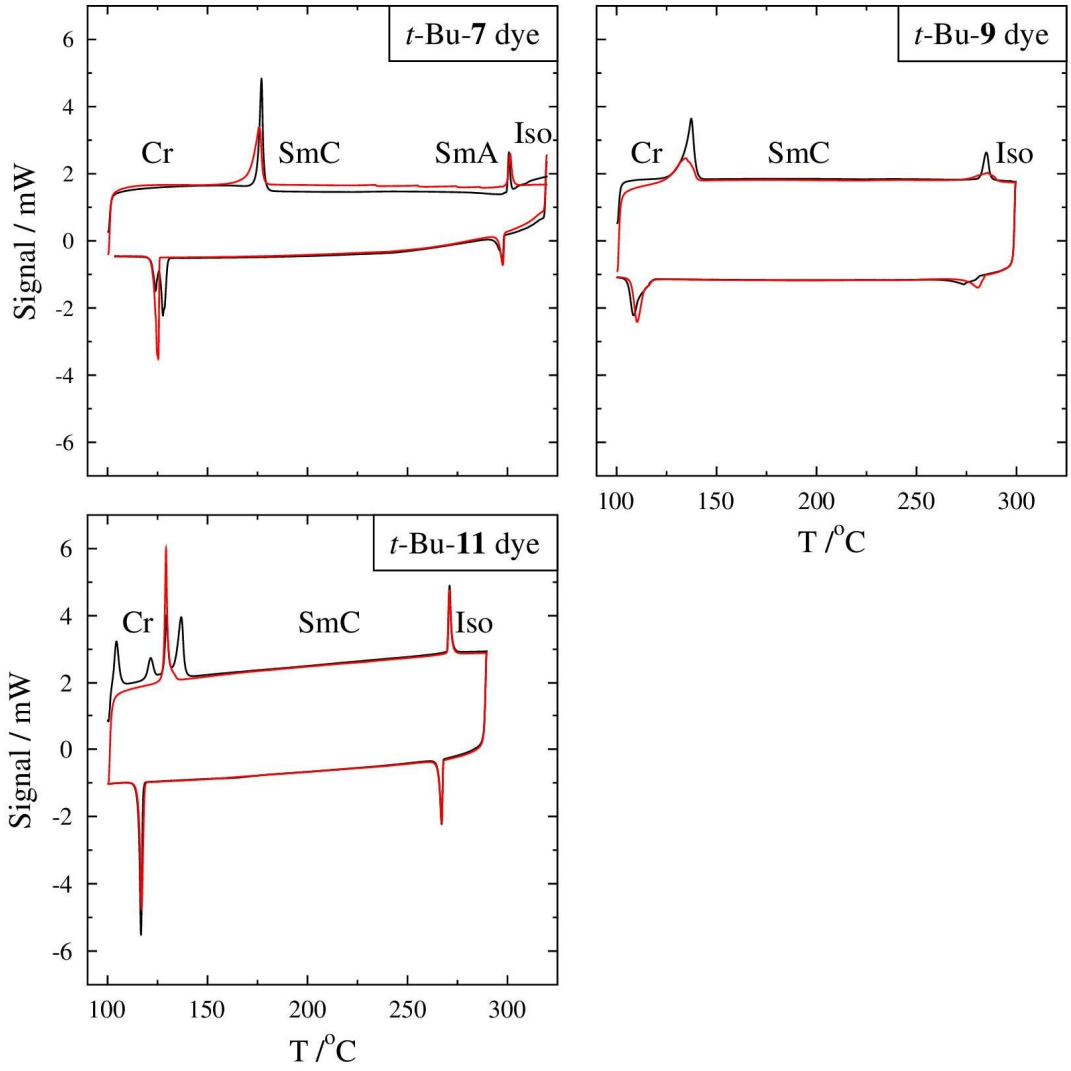

Figure 4.20: Differential scanning calorimetry traces for the *t*-Bu-**m** dyes, where m = 7, 9, 11. The two cycles are coloured black and red for the first and second cycles, respectively.

Table 4.11: Transition temperatures, in °C, for the *t*-Bu-**m** dyes, where **m** = 7, 9, 11. Transition enthalpies, in kJ mol^{-1}, for each transition are given in square brackets. † SmA to SmC transition obscured by SmA to Iso transition.

Molecule	Cr	T [ΔH]	SmC	T [ΔH]	SmA	T [ΔH]	Iso
t-Bu-**7** dye	●	176.6 [34.91]	●	†	●	300.5 [5.94]	●
t-Bu-**9** dye	●	137.9 [34.13]	●	-	-	284.7 [9.33]	●
t-Bu-**11** dye	●	129.2 [22.21]	●	-	-	270.7 [9.74]	●

Table 4.12: Transition entropies, given in J K^{-1} mol^{-1} and ΔS/R values, for the *t*-Bu-**m** dyes, where **m** = 7, 9, 11. † SmA to SmC transition obscured by SmA to Iso transition.

Molecule	Cr	ΔS	$\frac{\Delta S}{R}$	SmC	ΔS	SmA	ΔS	$\frac{\Delta S}{R}$	Iso
t-Bu-**7** dye	●	77.6	9.33	●	†	●	10.4	1.25	●
t-Bu-**9** dye	●	83.0	9.99	●	-	-	16.7	2.01	●
t-Bu-**11** dye	●	55.2	6.64	●	-	-	17.9	2.15	●

4.3.1.2 Guest-host mixtures

The guest-host mixtures studied in this section were initially characterised using POM, as shown in Figure 4.21 for the guest-host mixtures with nOCB hosts, and Figure 4.22 for the guest-host mixtures with *t*-Bu-nOCB hosts. The transition temperatures and enthalpies of transition given in Table 4.13 and Table 4.14, and DSC traces shown in Figure 4.23 and Figure 4.24. On cooling from the isotropic liquid, all the mixtures exhibited fan-like focal conic textures which were accompanied by homeotropic regions, indicating the presence of the smectic A (SmA) phase. The small wt% of dye did not seem to have any visible impact on the liquid crystal phase formed and there were no injected phases from the dye into the host phases.

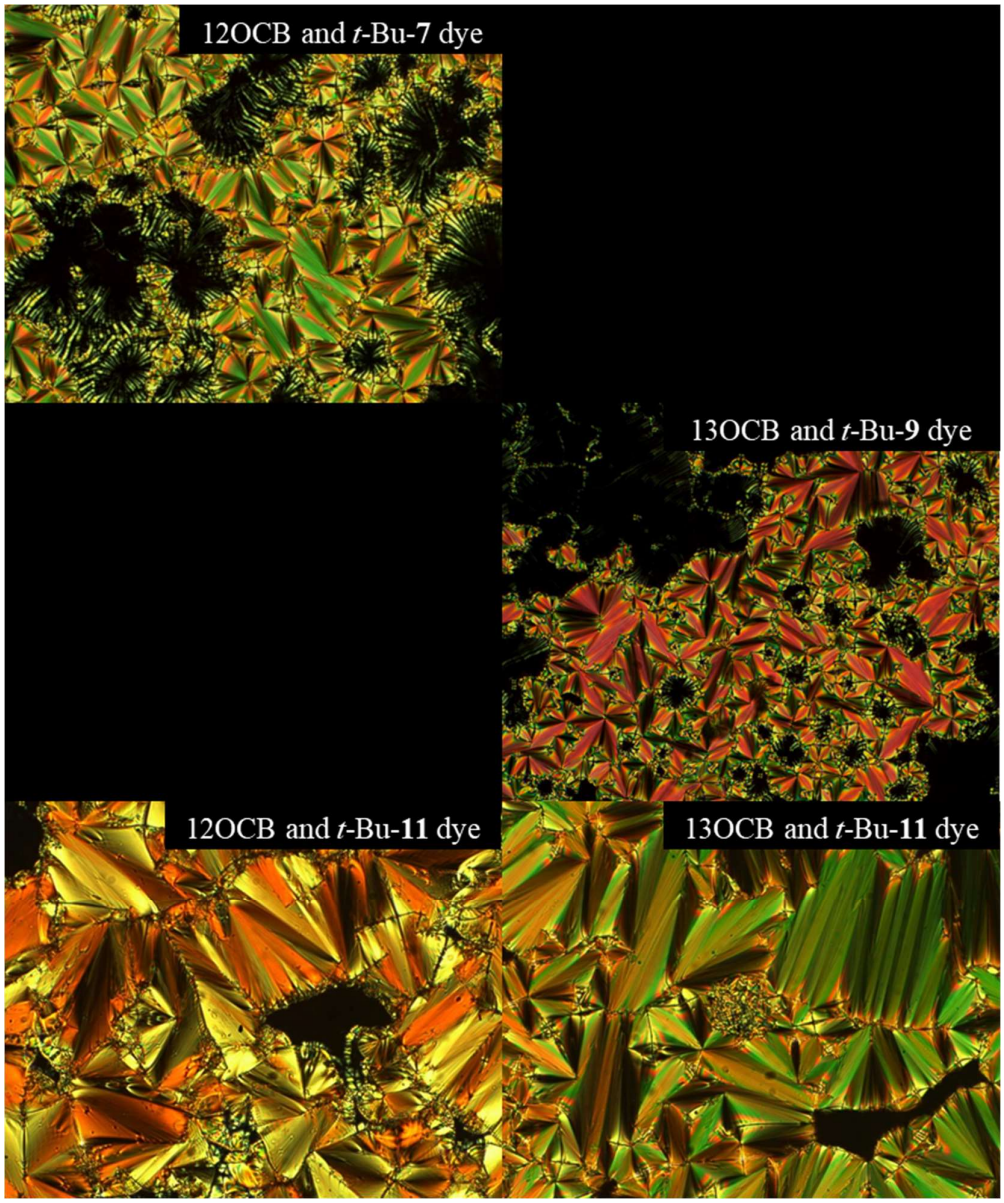

Figure 4.21: Photomicrographs showing the smectic A phase of the guest-host mixtures with 12OCB and 13OCB as hosts. Images were taken on cooling from the isotropic liquid, captured at: (top) 80.2 ºC, (middle) 90.9 ºC, (bottom L to R) 85.2 ºC and 90.8 ºC.

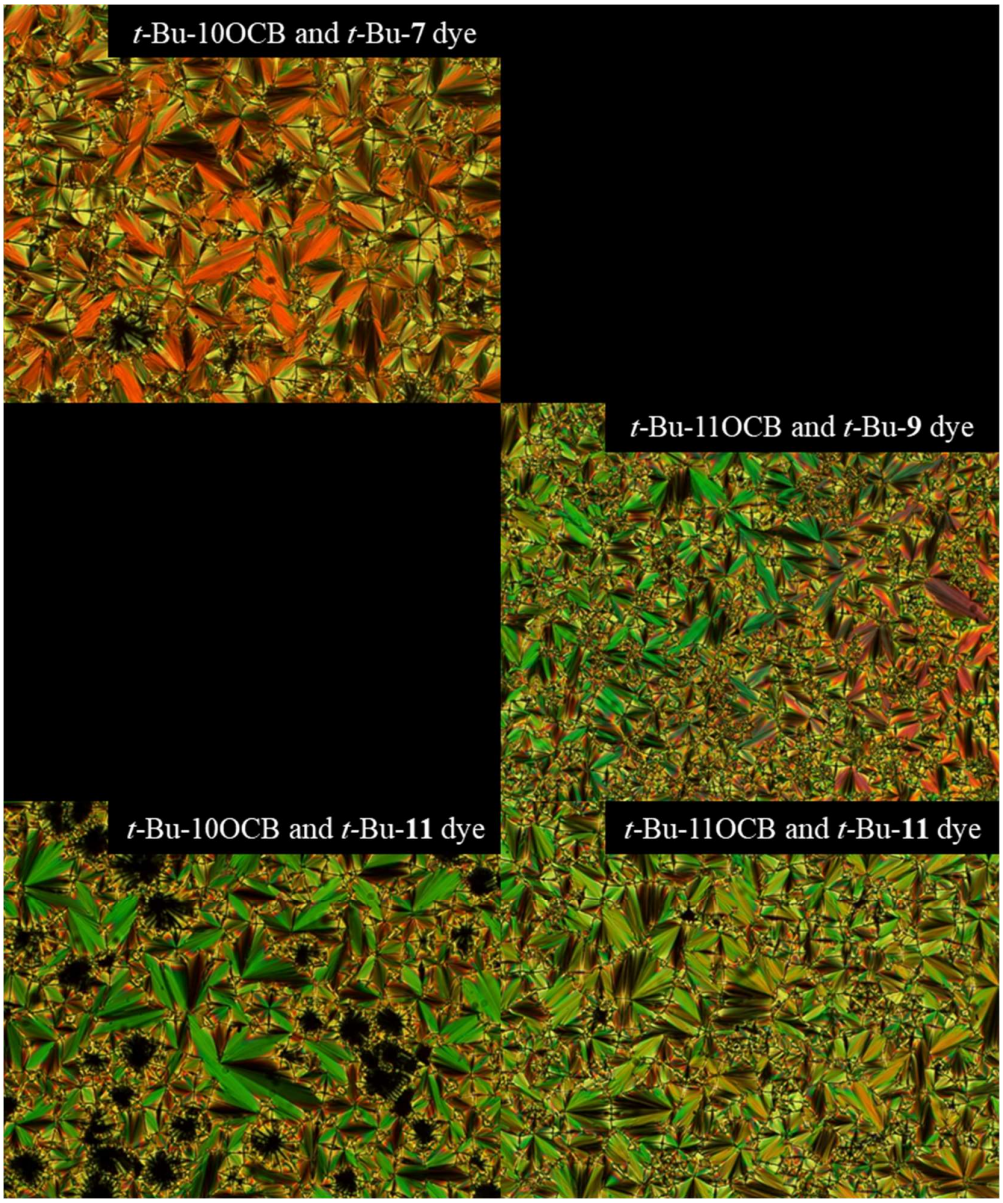

Figure 4.22: Photomicrographs showing the smectic A phase of the guest-host mixtures with *t*-Bu-10OCB and *t*-Bu-11OCB as hosts. Images were taken on cooling from the isotropic liquid, captured at: (top) 82.6 ºC, (middle) 81.9 ºC, (bottom L to R) 82.4 ºC and 86.4 ºC.

For the guest-host mixtures with nOCB hosts, the melting point temperatures are similar between the two guest-host mixtures for each host, and the same is observed for the clearing point temperatures. For the guest-host mixtures with *t*-Bu-nOCB hosts, the melting point temperatures are similar between the two guest-host mixtures for each host, and the same is observed for the clearing point temperatures.

The three DSC cycles show good reproducibility of both melting point and cooling point peaks on heating and cooling, and the phases are the same as for the host alone samples, as observed by POM. The reproducibility in the heating cycles may also indicate that the dye is well mixed, as there is no variation in the cycles caused by the dye. The transition enthalpies for the melting points show the largest magnitude for all the guest-host mixtures, and the clearing point also shows an approximate 10 times lower magnitude than the melting point transition enthalpy, as was observed for the host alone samples. The melting point transition enthalpy was generally higher for the guest-host mixtures with *t*-Bu-nOCB hosts than for the guest-host mixtures with nOCB hosts, and the clearing point transition enthalpy was higher for the guest-host mixtures with *t*-Bu-nOCB hosts.

Table 4.13: Transition temperatures, in °C, for the guest host mixtures with 12OCB and 13OCB as hosts. Transition enthalpies, in kJ mol^{-1}, for each transition are given in square brackets.

Host	Guest	Cr	T [ΔH]	SmA	T [ΔH]	Iso
12OCB	*t*-Bu-**7** dye	●	68.9 [32.63]	●	91.3 [4.68]	●
	t-Bu-**11** dye	●	69.0 [40.18]	●	90.8 [4.99]	●
13OCB	*t*-Bu-**9** dye	●	76.4 [44.70]	●	91.9 [4.98]	●
	t-Bu-**11** dye	●	76.3 [42.68]	●	92.1 [5.39]	●

Table 4.14: Transition temperatures, in °C, for the guest host mixtures with *t*-Bu-10OCB and *t*-Bu-11OCB as hosts. Transition enthalpies, in kJ mol^{-1}, for each transition are given in square brackets.

Host	Guest	Cr	T [ΔH]	SmA	T [ΔH]	Iso
t-Bu-10OCB	*t*-Bu-**7** dye	●	62.9 [28.71]	●	84.3 [5.27]	●
	t-Bu-**11** dye	●	62.7 [24.83]	●	84.5 [5.67]	●
t-Bu-11OCB	*t*-Bu-**9** dye	●	62.3 [27.33]	●	88.3 [6.66]	●
	t-Bu-**11** dye	●	62.5 [28.44]	●	88.4 [6.89]	●

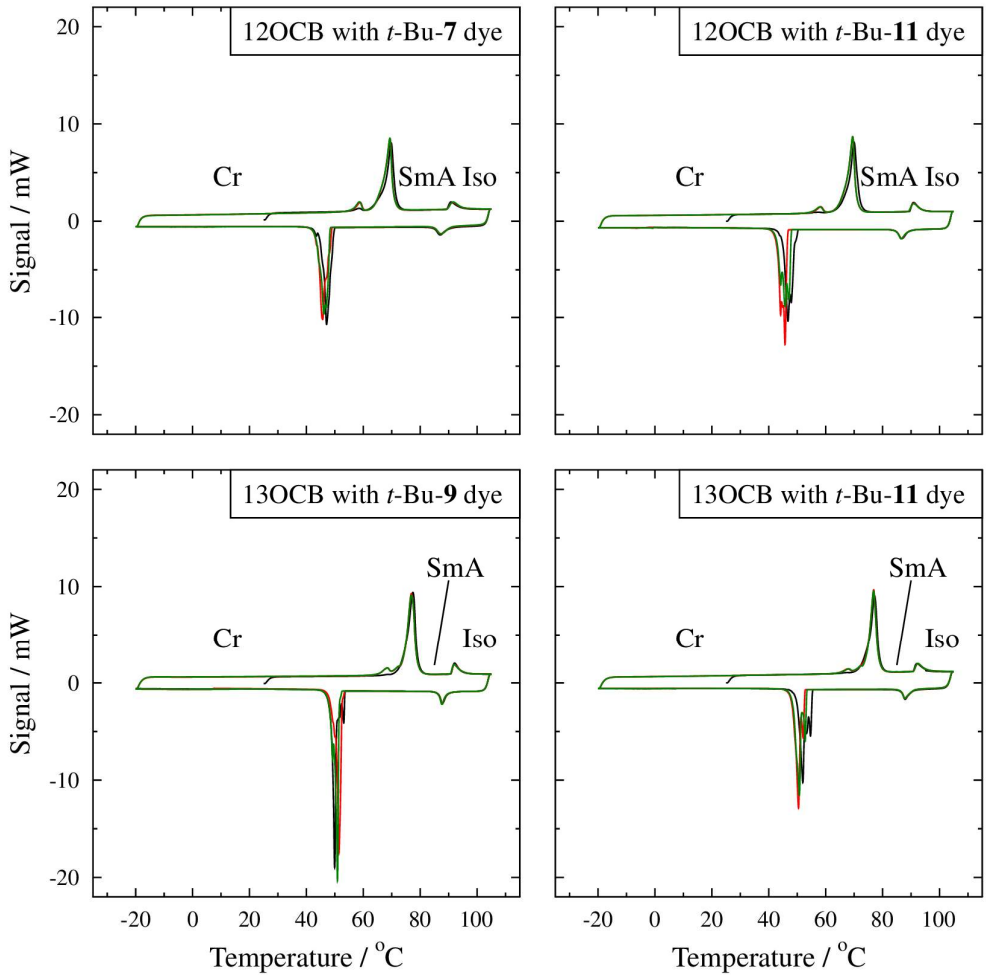

Figure 4.23: Differential scanning calorimetry traces for the guest-host mixtures with 12OCB and 13OCB as the hosts. The three cycles are coloured black, red and green for the first, second and third cycles, respectively.

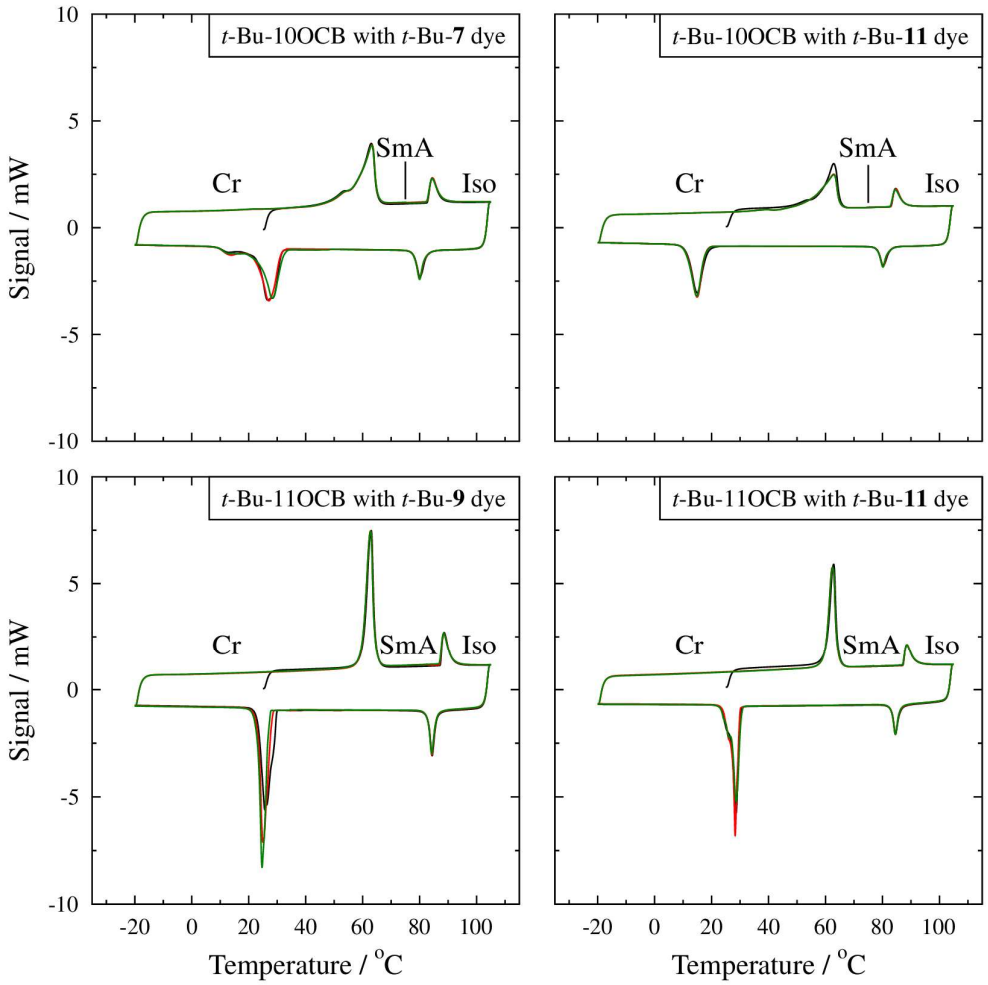

Figure 4.24: Differential scanning calorimetry traces for the guest-host mixtures with *t*-Bu-10OCB and *t*-Bu-11OCB as the hosts. The three cycles are coloured black, red and green for the first, second and third cycles, respectively.

The transition entropies were calculated using the transition temperatures and transition enthalpies from the DSC experiments. The calculated transition entropies are given in Table 4.15 for the guest-host mixtures with 12OCB and 13OCB as hosts, and Table 4.16 for guest-host mixtures with *t*-Bu-10OCB and *t*-Bu-11OCB as the hosts. The transition entropy values are also given as ΔS/R, which are normalised unitless values obtained on division by the universal gas constant (R).

For the guest-host mixtures with nOCB hosts, the melting point transition entropies are similar between the different guest-host mixtures, with no clear trend observed with the different dyes. The clearing point transition entropies are similar between the different guest-host mixtures, although the two guest-host mixtures with *t*-Bu-**11** dye both have a higher clearing point transition entropy than the guest-host mixture with the respective shorter chain dyes. For the guest-host mixtures with *t*-Bu-nOCB hosts, the melting point transition entropies are similar between the different guest-host mixtures, with no clear trend observed with the different dyes. The clearing point transition entropies are similar between the different guest-host mixtures, although the two guest-host mixtures with *t*-Bu-**11** dye both have a higher clearing point transition entropy than the guest-host mixture with the respective shorter chain dyes.

Table 4.15: Transition entropies, given in J K^{-1} mol^{-1} for the guest-host mixtures with 12OCB and 13OCB as the hosts.

Host	Guest	Cr	ΔS	$\frac{\Delta S}{R}$	SmA	ΔS	$\frac{\Delta S}{R}$	Iso
12OCB	*t*-Bu-**7** dye	●	95.4	11.47	●	12.8	1.54	●
	t-Bu-**11** dye	●	117.4	14.12	●	13.7	1.65	●
13OCB	*t*-Bu-**9** dye	●	127.7	15.38	●	13.6	1.64	●
	t-Bu-**11** dye	●	122.1	14.69	●	14.7	1.77	●

Table 4.16: Transition entropies, given in J K^{-1} mol^{-1} for the guest-host mixtures with *t*-Bu-10OCB and *t*-Bu-11OCB as the hosts.

Host	Guest	Cr	ΔS	$\frac{\Delta S}{R}$	SmA	ΔS	$\frac{\Delta S}{R}$	Iso
t-Bu-10OCB	*t*-Bu-**7** dye	●	85.4	10.27	●	13.6	1.77	●
	t-Bu-**11** dye	●	73.9	8.89	●	14.7	1.91	●
t-Bu-11OCB	*t*-Bu-**9** dye	●	81.5	9.80	●	18.4	2.22	●
	t-Bu-**11** dye	●	84.7	10.19	●	19.1	2.29	●

4.3.2 X-ray diffraction studies

4.3.2.1 Diffraction patterns

X-ray diffraction (XRD) experiments were undertaken for each of the guest-host mixtures. At selected temperature intervals starting from the isotropic liquid the sample was irradiated and diffraction images collected. The 2D diffraction pattern from the XRD measurements were integrated at each temperature to produce a 1D plot of signal intensity against diffraction angle (2θ), as shown in Figure 4.25 for the guest-host mixtures with 12OCB and

13OCB as hosts, and Figure 4.26 for the guest-host mixtures with *t*-Bu-10OCB and *t*-Bu-11OCB as the hosts. For these samples, sharp small angle peaks, related to the smectic layer, showed an increase in intensity with decreasing temperature, and also a slight shift to smaller angle in the 2θ values. There is also a broad, low-intensity wide angle peak related to the lateral packing, which shows little change with cooling. Only diffraction patterns relating to a smectic phase that was not aligned with the magnetic field were observed for all the different guest-host mixtures and this is in agreement with the results obtained from POM and DSC.

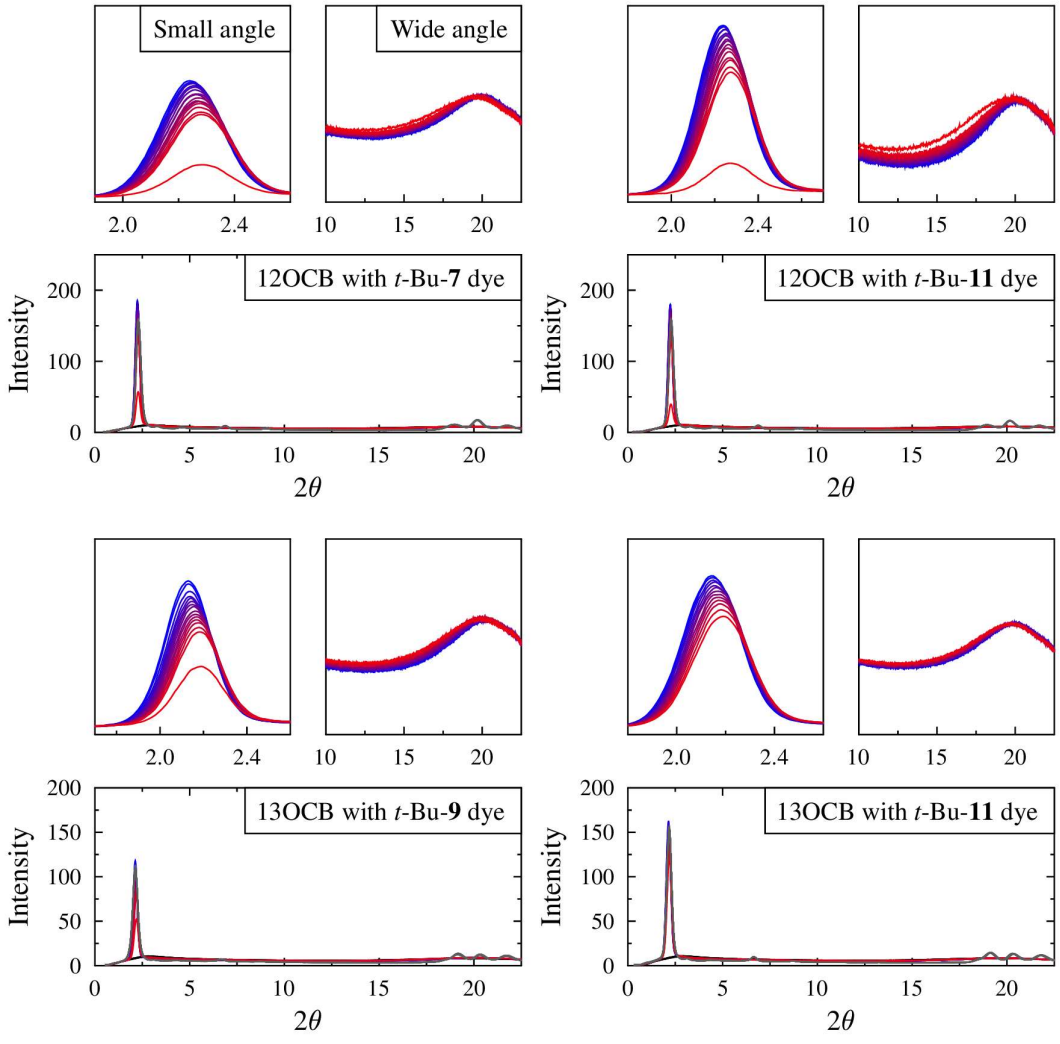

Figure 4.25: X-ray diffraction traces for the guest-host mixtures, with 12OCB and 13OCB as the hosts. The isotropic liquid and crystal phases are coloured grey and the red to blue colouring of the liquid crystal peaks illustrates the change with decreasing temperature in the range 100.0 to 29.0 °C.

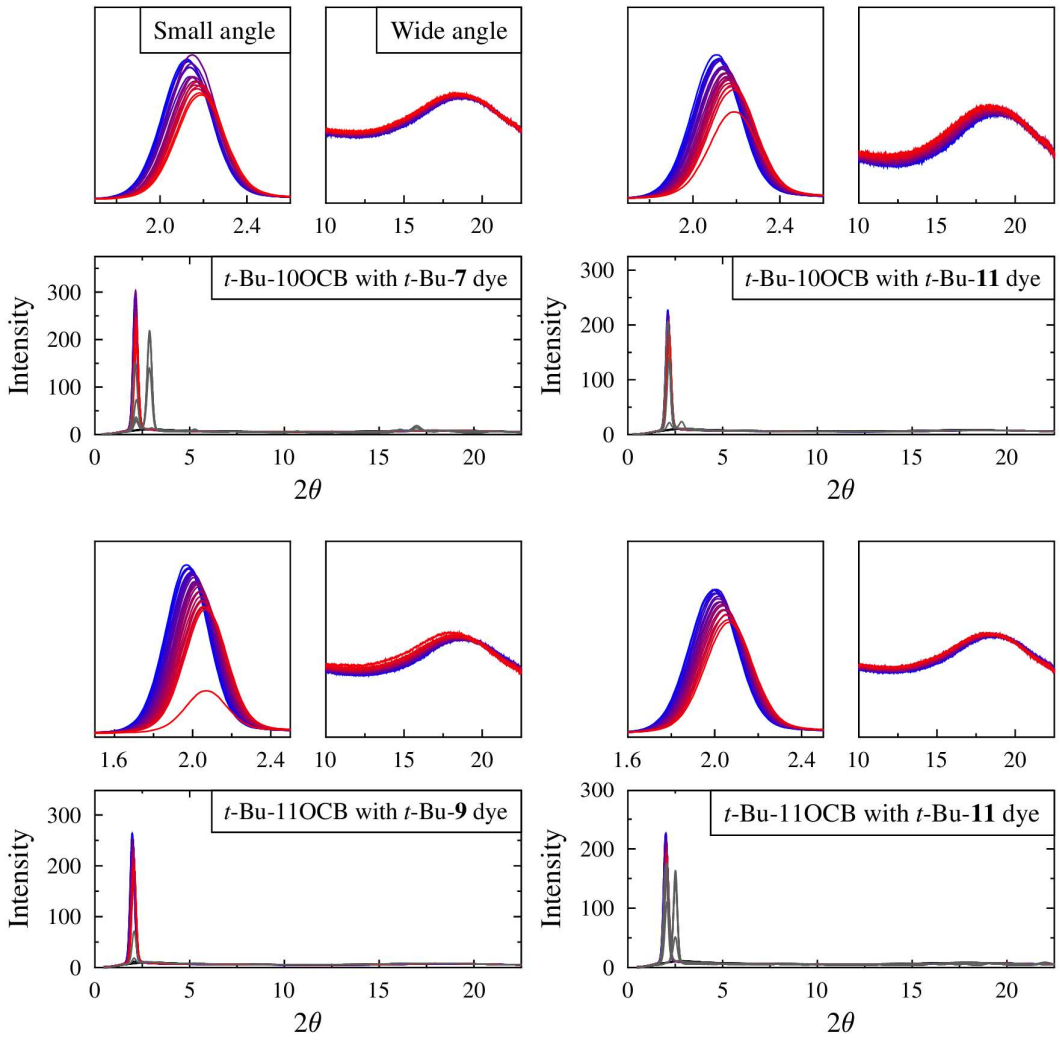

Figure 4.26: X-ray diffraction traces for the guest-host mixtures, with *t*-Bu-10OCB and *t*-Bu-11OCB as the hosts. The isotropic liquid and crystal phases are coloured grey and the red to blue colouring of the liquid crystal peaks illustrates the change with decreasing temperature in the range 100.0 to 29.0 ºC.

4.3.2.2 Layer spacing

The structure of the guest-host mixtures was investigated by converting the diffraction angle peaks to layer spacings, d. For the guest-host mixtures with 12OCB and 13OCB as the hosts, the small angle layer spacing is given in Table 4.17 and for the guest-host mixtures with *t*-Bu-10OCB and *t*-Bu-11OCB as the hosts, the small angle layer spacing is given in Table 4.18. For the guest-host mixtures with 12OCB, there is an increase in the layer spacing as the temperature decreases. The increase in layer spacing for 12OCB with *t*-Bu-**7** dye and with *t*-Bu-**11** dye is 0.08 nm and 0.07 nm, respectively. For the guest-host mixtures with

13OCB, there is also an increase in the layer spacing as the temperature decreases. The increase in layer spacing for 13OCB with *t*-Bu-**9** dye and with *t*-Bu-**11** dye is 0.11 nm and 0.08 nm, respectively.

Table 4.17: Layer spacing determined from small angle XRD peaks for the guest-host mixtures with 12OCB and 13OCB as the hosts.

Guest-host mixture	12OCB with *t*-Bu-**7** dye	12OCB with *t*-Bu-**11** dye	13OCB with *t*-Bu-**9** dye	13OCB with *t*-Bu-**11** dye
T /ºC	d /nm			
29.0				
31.4				
33.7				
36.1				
38.5				
40.8				
43.2				
45.6				
47.9				
50.3		3.95		
52.7	3.94	3.95		
55.0	3.93	3.94	4.15	
57.4	3.93	3.94	4.14	
59.8	3.92	3.93	4.13	
62.1	3.92	3.92	4.12	4.12
64.5	3.91	3.92	4.11	4.11
66.9	3.90	3.92	4.11	4.10
69.2	3.90	3.91	4.10	4.09
71.6	3.90	3.91	4.09	4.09
74.0	3.89	3.90	4.09	4.08
76.3	3.88	3.90	4.08	4.07
78.7	3.88	3.89	4.07	4.07
81.1	3.88	3.89	4.07	4.06
83.4	3.87	3.89	4.06	4.06
85.8	3.87	3.88	4.06	4.05
88.2	3.86	3.88	4.05	4.04
90.5	3.86	3.88	4.04	4.04
92.9				
95.3				
97.6				
100.0				

For the guest-host mixtures with *t*-Bu-10OCB, there is an increase in the layer spacing as the temperature decreases. The increase in layer spacing for *t*-Bu-10OCB with *t*-Bu-**7** dye and with *t*-Bu-**11** dye is 0.12 nm and 0.17 nm, respectively. For the guest-host mixtures with *t*-Bu-11OCB, there is also an increase in the layer spacing as the temperature decreases. The increase in layer spacing for *t*-Bu-11OCB with *t*-Bu-**9** dye and with *t*-Bu-**7** dye is 0.22 nm and 0.17 nm, respectively.

Table 4.18: Layer spacing determined from small angle XRD peaks for the guest-host mixtures with *t*-Bu-10OCB and *t*-Bu-11OCB as the hosts. † denotes the co-existence of the smectic A phase and crystal phase.

Guest-host mixture	*t*-Bu10OCB with *t*-Bu-**7** dye	*t*-Bu10OCB with *t*-Bu-**11** dye	*t*-Bu11OCB with *t*-Bu-**9** dye	*t*-Bu10OCB with *t*-Bu-**11** dye
T /°C	d /nm			
29.0				
31.4				
33.7		4.20†	4.48	
36.1		4.19	4.47	
38.5		4.18	4.46	
40.8	4.15†	4.18	4.45	
43.2	4.16	4.17	4.44	
45.6	4.15	4.16	4.43	4.44†
47.9	4.14	4.15	4.42	4.43
50.3	4.14	4.14	4.41	4.42
52.7	4.13	4.14	4.41	4.41
55.0	4.12	4.13	4.39	4.40
57.4	4.11	4.12	4.39	4.39
59.8	4.10	4.11	4.38	4.38
62.1	4.10	4.10	4.37	4.37
64.5	4.09	4.10	4.36	4.37
66.9	4.08	4.09	4.35	4.35
69.2	4.07	4.08	4.34	4.34
71.6	4.07	4.07	4.33	4.33
74.0	4.06	4.07	4.32	4.32
76.3	4.05	4.06	4.31	4.31
78.7	4.04	4.05	4.30	4.31
81.1	4.04	4.04	4.29	4.29
83.4	4.03	4.03	4.28	4.28
85.8	4.03	4.03	4.27	4.27
88.2			4.26	4.27
90.5			4.26	
92.9				
95.3				
97.6				
100.0				

The wide angle peaks for both series are observed to be broad, as shown in the insert regions in Figure 4.25 and Figure 4.26. The peak positions were approximated using a Gaussian fit to the relevant region in the plots, using $2\theta = 17\text{-}22^{o}$ for the guest-host mixtures with nOCB host and $2\theta = 15\text{-}20^{o}$ for the guest-host mixtures with *t*-Bu-nOCB hosts. This approach gives a 2θ value for the diffraction peak correlating to adjacent molecules within the layers, which was converted into a distance as given in Table 4.19 and Table 4.20 for the respective guest-host mixtures. The wide angle distances were only calculated for the start and end of the phases to give the overall changes occurring in each case.

For both sets of guest-host mixtures there is no significant change in the distance between adjacent molecules with changing temperature. It can be observed that the distance between the adjacent cyanobiphenyl cores is in the range 0.440-0.451 nm for the guest-host mixtures with nOCB hosts and 0.481-0.491 nm for the guest-host mixtures with *t*-Bu-nOCB hosts.

Table 4.19: Distance between adjacent molecules determined from wide angle XRD peaks for the guest-host mixtures with nOCB hosts.

Guest-host mixture	12OCB with *t*-Bu-**7** dye	12OCB with *t*-Bu-**11** dye	13OCB with *t*-Bu-**9** dye	13OCB with *t*-Bu-**11** dye
T /°C	d /nm			
29.0				
31.4				
33.7				
36.1				
38.5				
40.8				
43.2				
45.6				
47.9				
50.3		0.440		
52.7	0.444			
55.0			0.440	
57.4				
59.8				
62.1				0.445
64.5				
66.9				
69.2				
71.6				
74.0				
76.3				
78.7				
81.1				
83.4				
85.8				
88.2				
90.5	0.453	0.451	0.448	0.450
92.9				
95.3				
97.6				
100.0				

Table 4.20: Distance between adjacent molecules determined from wide angle XRD peaks for the guest-host mixtures with *t*-Bu-nOCB hosts. † denotes the co-existence of the smectic A phase and crystal phase.

Guest-host mixture	*t*-Bu10OCB with *t*-Bu-**7** dye	*t*-Bu10OCB with *t*-Bu-**11** dye	*t*-Bu11OCB with *t*-Bu-**9** dye	*t*-Bu10OCB with *t*-Bu-**11** dye
T /°C	d /nm			
29.0				
31.4				
33.7		†	0.482	
36.1		0.485		
38.5				
40.8	†			
43.2	0.481			
45.6				†
47.9				0.485
50.3				
52.7				
55.0				
57.4				
59.8				
62.1				
64.5				
66.9				
69.2				
71.6				
74.0				
76.3				
78.7				
81.1				
83.4				
85.8	0.487	0.489		
88.2				0.488
90.5			0.491	
92.9				
95.3				
97.6				
100.0				

4.3.3 UV-visible absorption studies

In order to perform UV-visible absorption studies on the guest-host mixtures, cells which were able to produce high quality alignment of the guest-host mixtures had to be selected. This section will report the preliminary cell testing, then will cover the home-built cell preparation and the resulting POM images of the cells. Following this, the UV-visible absorption measurements of the guest-host mixtures are reported.

4.3.3.1 Cell testing and development

Commercial cells of 20 μm path length

The first cells tested were commercial, parallel rubbed, 20 μm path length cells (Instec). Example POM images of 8OCB with a 1,5-thio substituted anthraquinone dye (15SB3, Figure 2.1) and of *t*-Bu-11OCB with the *t*-Bu-**9** dye are shown in Figure 4.27 with both these mixtures being at a temperature that is within the smectic A temperature range of the respective host.

It was observed that the POM image from the guest-host mixture with 8OCB had a well-oriented planar texture with very few defects, indicating good bulk alignment of the phase within the cell. By contrast, the image from the guest-host mixture with *t*-Bu-11OCB as the host shows some regions of planar orientation but primarily shows the characteristic focal conic smectic A texture, indicating that the host did not align well within the cell.

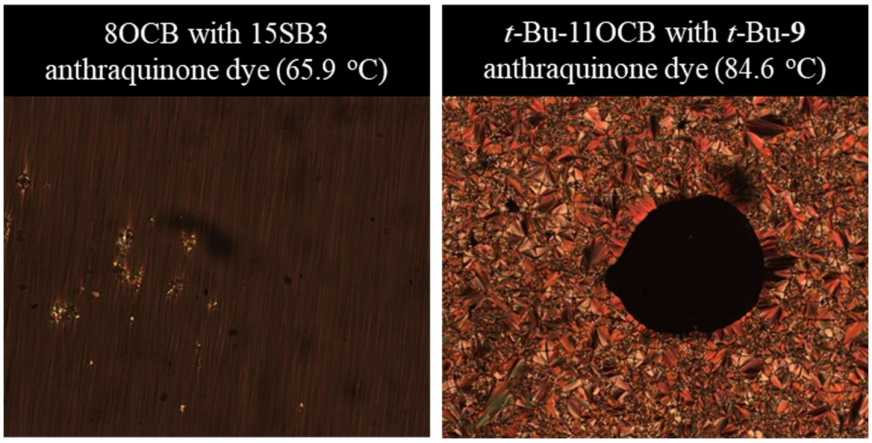

Figure 4.27: Example photomicrographs of the sample textures of the guest-host mixtures, with 8OCB with 15SB3 dye (left) and *t*-Bu-11OCB with *t*-Bu-**9** dye (right). Both mixtures are in the smectic A phase temperature range for the respective liquid crystal hosts.

Bulk alignment of the guest-host mixture with 8OCB as the host was achieved because the mixture exhibited a nematic phase as well as a smectic A phase. The nematic phase aligned easily to give a planar alignment which was preserved upon cooling into the smectic A phase. In the case of the guest-host mixture with *t*-Bu-11OCB as the host, the smectic A phase is the only phase present on cooling from the isotropic liquid. The smectic A phase evidently does not align and the characteristic focal conic textures are observed. This same lack of bulk alignment was also observed for *t*-Bu-11OCB host without any guest dye in the same cell type. The absence of bulk alignment means that such samples are not suitable for polarised UV-visible measurements, and so further cells were tested to obtain a planar, aligned texture indicative of bulk alignment, as seen for the guest-host mixture with 8OCB as the host in Figure 4.27.

Commercial cells of ≤ 5 μm path length

For screening with commercial cells of shorter path lengths, 11OCB was used as the sample because it exhibits only a smectic A phase. The 11OCB host was flow filled into cells of 5 μm (Instec), 4 μm (Planar System Inc.) and 3.2 μm (Instec) path length, and the POM images of the samples in the cells are given in Figure 4.28. It was observed that the characteristic smectic A texture was not present in any of these smaller path length cells, but there was domains of bulk alignment that were broken up by defect walls. The 3.2 μm sample showed some small areas of focal conic texture and some homeotropic domains. Overall, this suggested that using the smaller cell path lengths resulted in an improvement in the bulk alignment of the liquid crystal phase, due to a smaller volume within the cells that was not experiencing the effect of the alignment layer; in the thinner cells, there is an increase in the proportion of the sample interacting with the alignment layer and a decrease in the bulk sample in the centre of the cell. Despite this, there was still an obvious texture of defects present, particularly in comparison to the smooth texture observed for the mixture of 8OCB with 15SB3 dye, as shown in Figure 4.27. Although decreasing the cell path length had improved the bulk alignment, it also brought about further issues as the shorter path lengths would lead to a lower absorbance in the polarised UV-visible measurements.

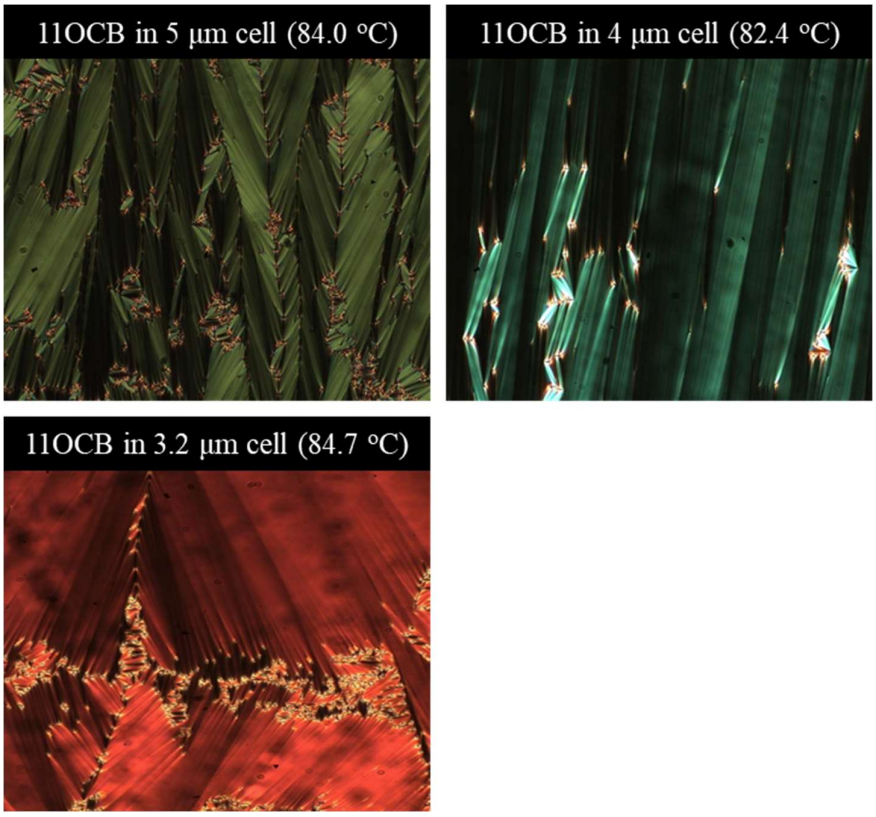

Figure 4.28: Example photomicrographs showing the sample textures of 11OCB, in the smectic A phase temperature range, in a range of different cells with different path lengths.

Further tests were undertaken with these commercial cells, including cooling the samples from the isotropic liquid within the cells at 0.1 °C min^{-1}, heating and cooling of the cells multiple times around the clearing point temperature to try to zone refine the alignment on each cycle, and also applying a voltage with varying frequencies during cooling, to try to induce alignment using the electric field. These studies did not yield any significant improvements in the bulk alignment of the samples within these cells.

Home-built cells

The use of the polyimide coated commercial cells did not yield positive results in terms of alignment so the next step was to produce homemade cells, which followed literature procedure designed to align smectic phases specifically.

The first home-built cells were made following a procedure by Patel et al.,[121] which used nylon 6,6 in a mixture of *m*-cresol and methanol. Samples of guest-host mixtures, with *t*-Bu-10OCB as the host and *t*-Bu-**7** dye and *t*-Bu-**11** dyes as the guests, were flow filled in to these cells of 15 μm path length and the POM images of the textures are shown in Figure 4.29. These images were taken at a temperature within the smectic A phase range of the host. The guest-host mixture with *t*-Bu-**11** dye gave a smooth texture indicating bulk alignment, whereas the guest-host mixture with *t*-Bu-**7** dye showed areas of smectic A texture.

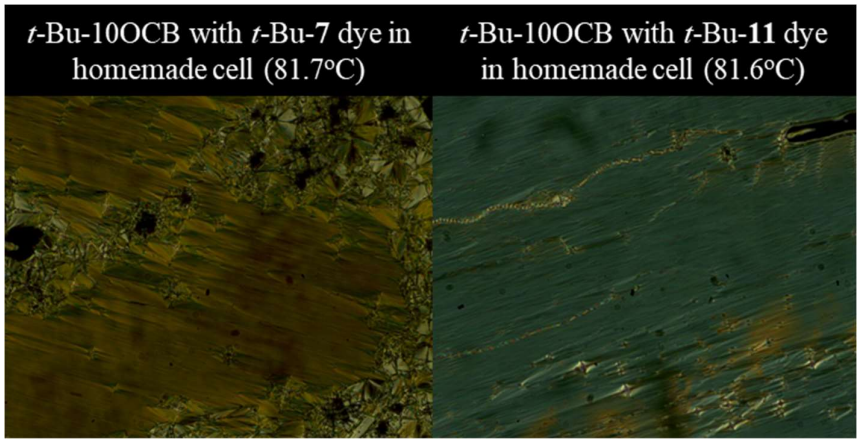

Figure 4.29: Example photomicrographs showing the sample textures of guest-host mixtures of *t*-Bu-10OCB with *t*-Bu-**7** dye (left) and *t*-Bu-**11** dye (right) in the first batch of home-built cells.

Overall, these cells were found to align the liquid crystal phase but the bulk alignment was not consistent across all samples. These cells were not consistent enough and would not give good quality results for UV-visible measurements. A second batch of home-built cells were prepared using methanoic acid as the solvent, as described in the procedure in the experimental chapter. The textures of the samples in the cells are shown in Figure 4.30. These liquid crystal hosts within the cells were found to give well aligned, planar textures and so these cells were used for the guest-host mixtures with the *t*-Bu-**m** dyes.

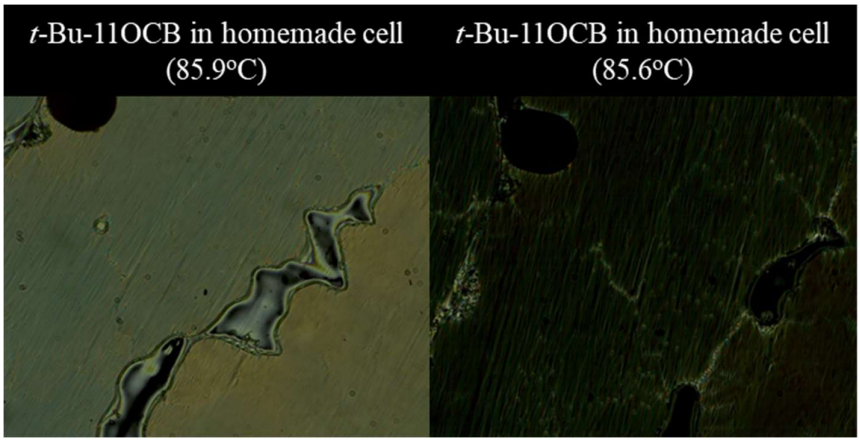

Figure 4.30: Example photomicrographs showing the sample texture of *t*-Bu-11OCB in the second batch of homemade cells.

4.3.3.2 Sample preparation

Photographs of the guest-host samples within a vial and in the home-built cells are shown in Figure 4.31 for the guest-host mixtures with nOCB hosts, and Figure 4.32 for guest-host mixtures with *t*-Bu-nOCB hosts. The vials show no visual difference between the different guest-host mixtures. The guest-host samples were heated to the isotropic liquid and the home-built cells were filled using capillary action. There is a slight difference observed in colour between the different cells, which may be a result of these images being taken at room temperature and the samples being crystallised in these images.

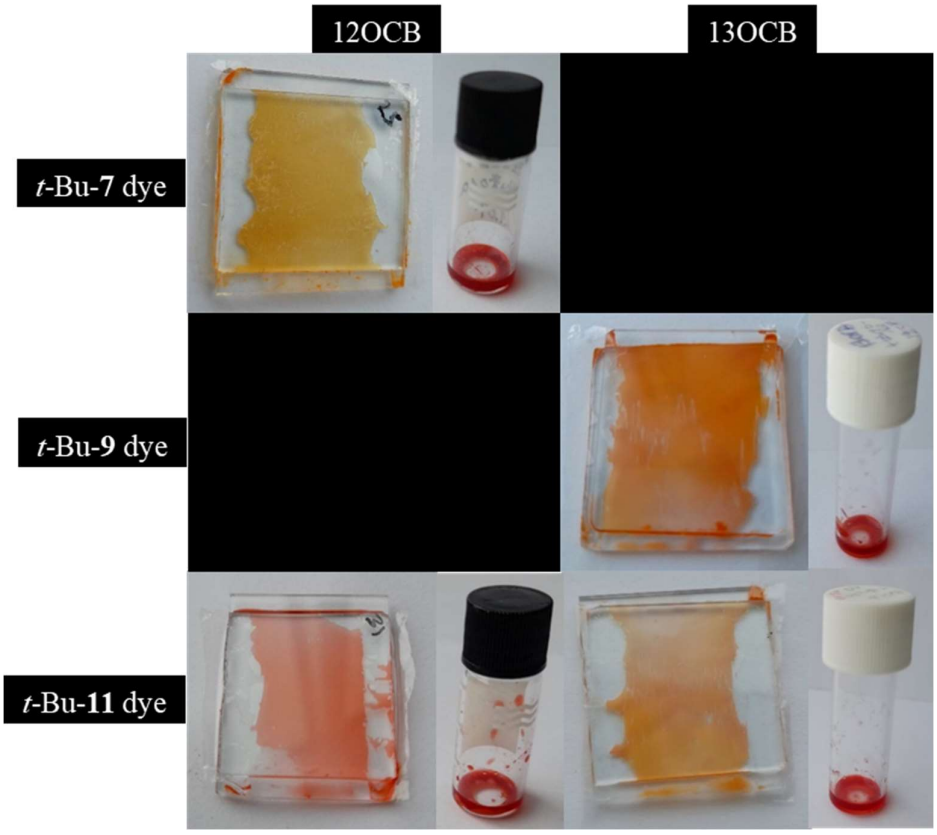

Figure 4.31: Images of the guest-host mixtures in vials and in cells, at room temperature. The images are: (Top) 12OCB with *t*-Bu-**7** dye, (Middle) 13OCB with *t*-Bu-**9** dye, (Bottom left to right) 12OCB and 13OCB with t-Bu-**11** dye.

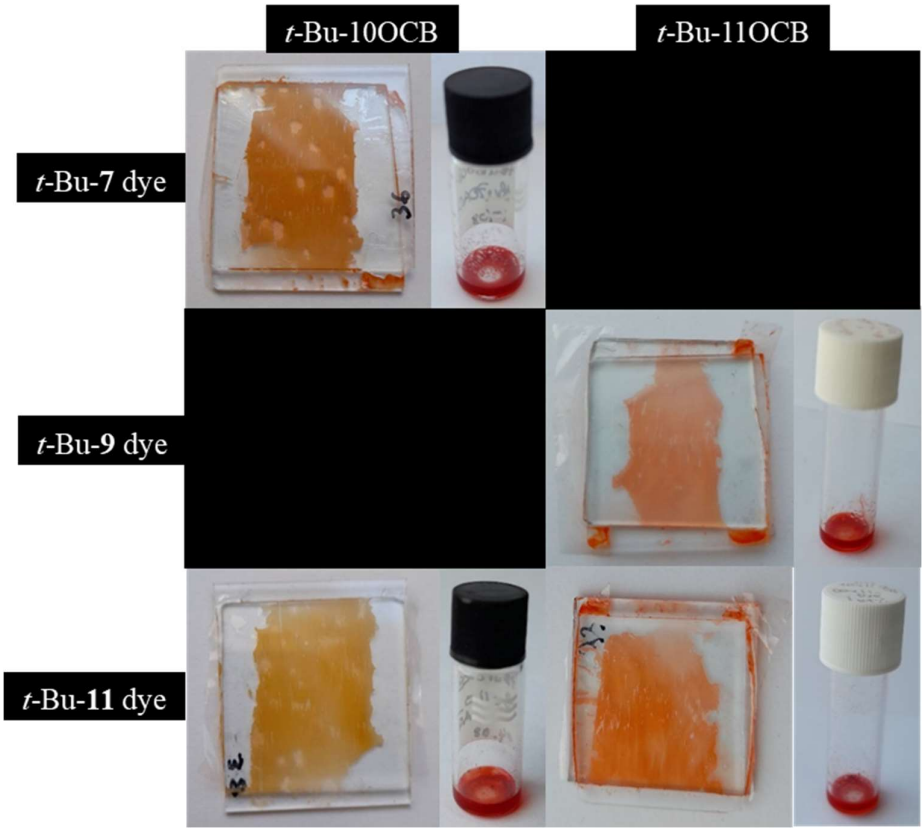

Figure 4.32: Images of the guest-host mixtures in vials and in cells, at room temperature. The images are: (Top) *t*-Bu-10OCB with t-Bu-**7** dye, (Middle) *t*-Bu-11OCB with *t*-Bu-**9** dye, (Bottom left to right) *t*-Bu-10OCB and *t*-Bu-11OCB with *t*-Bu-**11** dye.

4.3.3.3 Polarised optical microscopy

The uniformity of the sample alignment in the filled cells waschecked using POM, by cooling the samples from the isotropic liquid and observing the formation of the smectic A phase within the cell. The photomicrographs in Figure 4.33, Figure 4.34 and Figure 4.35 show the samples of guest-host mixtures with nOCB hosts and the nOCB hosts alone in the cells, and Figure 4.36, Figure 4.37 and Figure 4.38 show the samples of guest-host mixtures with *t*-Bu-nOCB hosts and the *t*-Bu-nOCB hosts alone in the cells. These photomicrographs show planar, aligned textures of the guest-host mixtures, with the dye fully dissolved and no sign of precipitation of dye in the guest-host mixtures. The two images in each case show an area of the cell with the alignment parallel to a polariser, forming a dark image, and the same area at approximately 45° to one of the polarisers resulting in a bright image. These photomicrographs showed no characteristic liquid crystal phase textures, such as focal conic textures, and all samples produced a well-formed planar orientation. There were a few domain walls observed, which can be seen most clearly in the dark images. These were not significant enough to impact the bulk alignment, and hence the overall UV-visible studies. The host alone cells also showed a uniform planar alignment, with the presence of some domain walls.

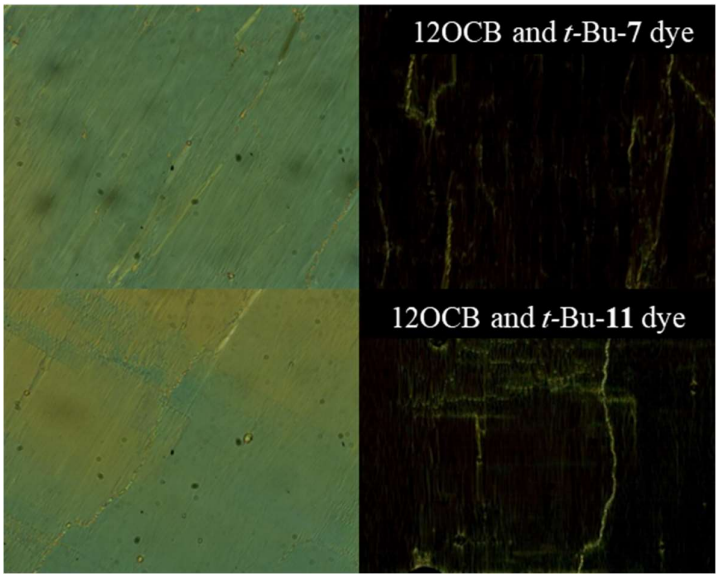

Figure 4.33: Photomicrographs showing aligned textures of the guest-host mixtures with 12OCB as the host and *t*-Bu-**7** dye and *t*-Bu-**11** dye, as the guests, at 85.5 °C and 87.0 °C respectively. The two images show the alignment at approximately 45° to the crossed polarisers (left) and parallel to one of the crossed polarisers (right).

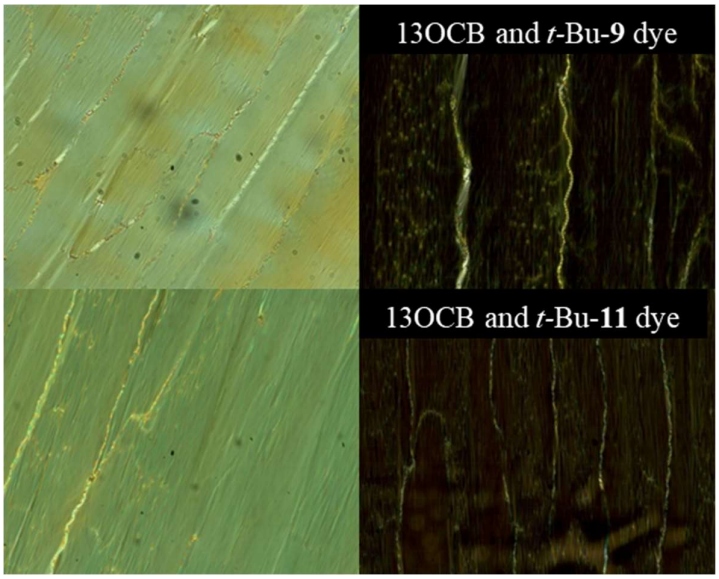

Figure 4.34: Photomicrographs showing aligned textures of the guest-host mixtures with 13OCB as the host and *t*-Bu-**9** dye and *t*-Bu-**11** dye, as the guests, at 88.9 °C and 88.0 °C respectively. The two images show the alignment at approximately 45° to a crossed polarisers (left) and parallel to one of the crossed polarisers (right).

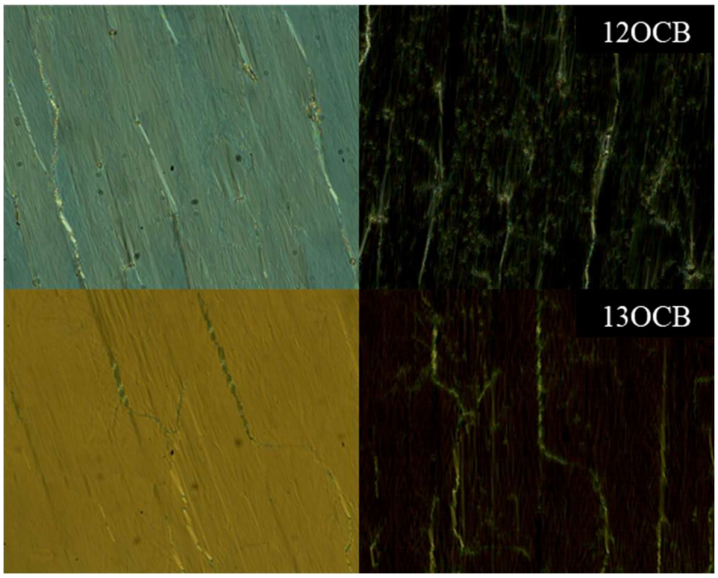

Figure 4.35: Photomicrographs showing aligned textures of the host-alone cells with 12OCB and 13OCB as the host, at 86.8 °C and 89.0 °C respectively. The two images show the alignment at approximately 45° to the crossed polarisers (left) and parallel to one of the crossed polarisers (right).

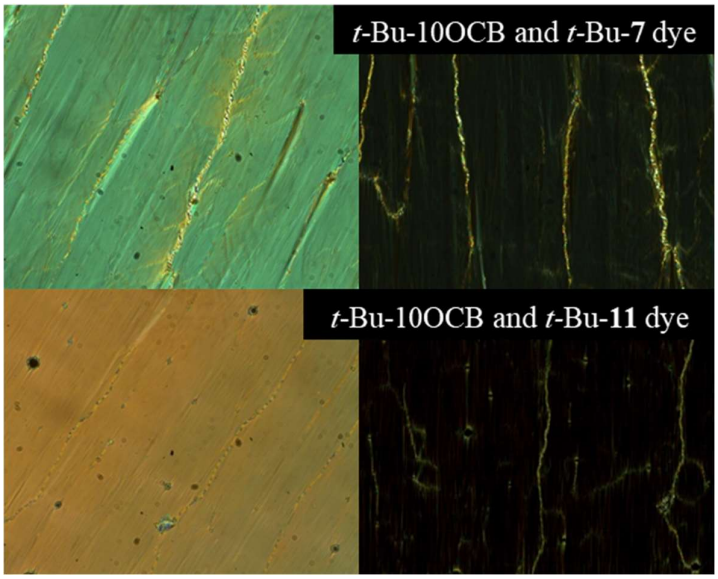

Figure 4.36: Photomicrographs showing aligned textures of the guest-host mixtures with *t*-Bu-10OCB as the host and *t*-Bu-**7** dye and *t*-Bu-**11** dye, as the guests, at 78.0 ºC and 81.5 ºC respectively. The two images show the alignment at approximately 45º to the crossed polarisers (left) and parallel to one of the crossed polarisers (right).

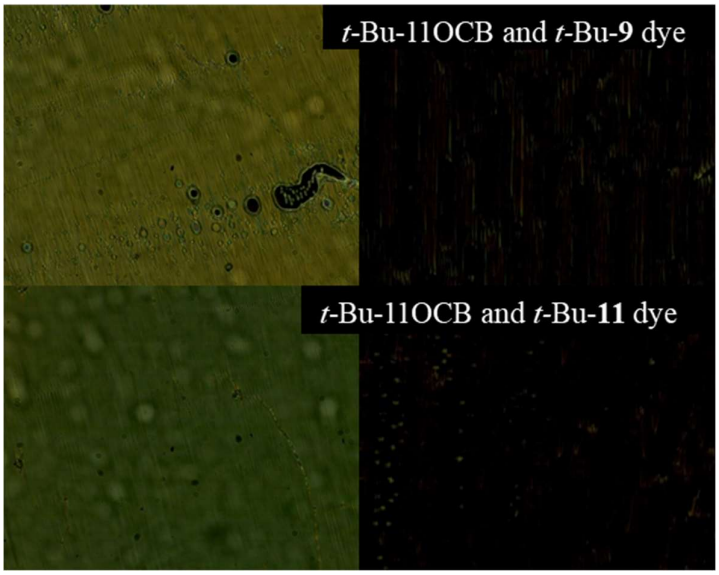

Figure 4.37: Photomicrographs showing aligned textures of the guest-host mixtures with *t*-Bu-11OCB as the host and *t*-Bu-**9** dye and *t*-Bu-**11** dye, as the guests, at 87.0 ºC and 85.0 ºC respectively. The two images show the alignment at approximately 45º to the crossed polarisers (left) and parallel to one of the crossed polarisers (right).Photomicrographs showing aligned textures of the guest-host mixtures with *t*-Bu-11OCB as the host and *t*-Bu-**9** dye and *t*-Bu-**11** dye, as the guests, at 87.0 ºC and

85.0 ºC respectively. The two images show the alignment at approximately 45º to the crossed polarisers (left) and parallel to one of the crossed polarisers (right).

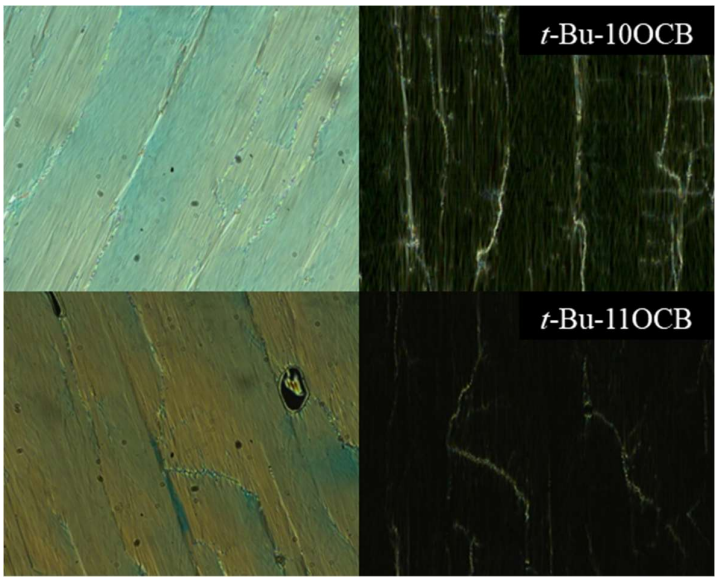

Figure 4.38: Photomicrographs showing aligned textures of the host-alone cells with *t*-Bu-10OCB and *t*-Bu-11OCB as the host, at 75.1 ºC and 85.6 ºC respectively. The two images show the alignment at approximately 45º to the crossed polarisers (left) and parallel to one of the crossed polarisers (right).

4.3.3.4 Polarised UV-visible absorption measurements

Polarised UV-visible absorption measurements were carried out across the full temperature range of the guest-host mixtures and separately of the host alone samples, as the reference, by cooling the samples from the isotropic liquid to room temperature or the crystallisation point. At each temperature, a set of measurements were taken of the guest-host mixture (sample) and the host alone (reference), and these using these two measurements at each temperature the subtracted plot was calculated, as shown in Figure 4.39. The host alone spectra were subtracted from the guest-host mixture spectra, leaving the subtracted plot for the parallel and perpendicular measurements. The host alone samples were measured to give a background measurement of the absorbance from the host, alignment layer and the glass so that the final spectra arise only from the contribution of the dye in the guest-host mixture.

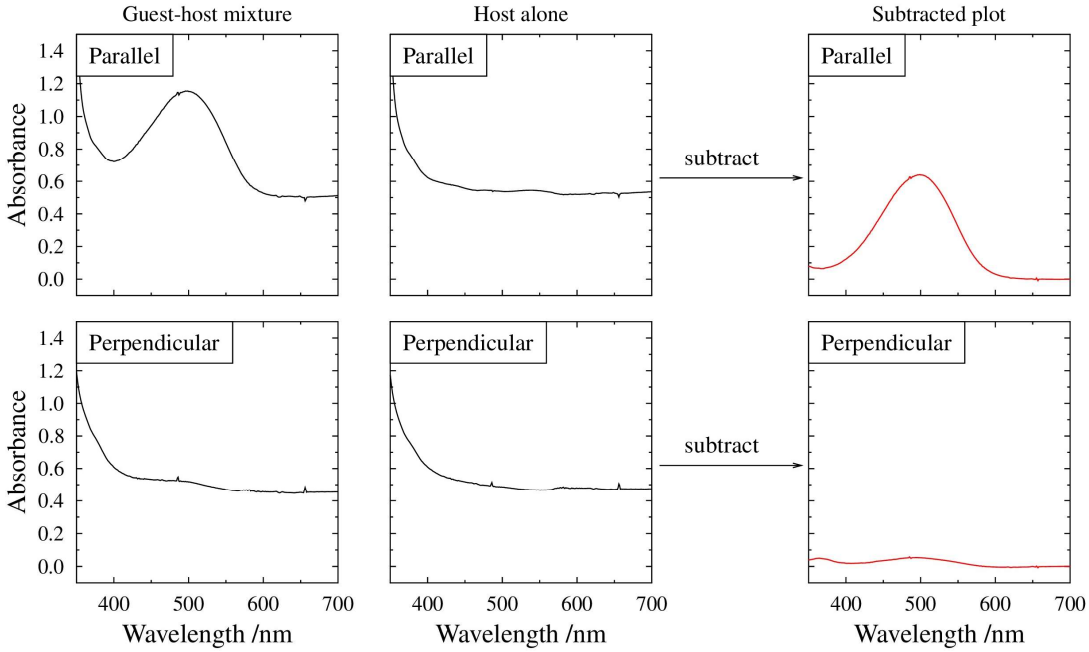

Figure 4.39: Example of the absorbance measurements taken for 12OCB with the *t*-Bu-**7** dye and of 12OCB alone at 75 °C.

At each temperature, the absorbance measurement was taken for the cell orientated with the rub direction parallel and perpendicular to the polarised UV light source to observe the maximum and minimum absorbance respectively. For each guest-host mixture, three sets of measurements of the sample were done for the guest-host mixtures with nOCB hosts and two sets of measurements of the sample were done for the guest-host mixtures with *t*-Bu-nOCB hosts. Examples of the subtracted absorption spectra for each of the guest-host mixtures are shown in Figure 4.40 and Figure 4.41, and the subtracted absorption spectra for all runs are given in appendix 6.2.

In each case, at the highest temperatures the guest-host mixture was in the isotropic phase so the peak absorbance was the same in the parallel and perpendicular orientation as the molecules in the system are isotropically oriented. As the temperature decreases, the guest-host mixtures formed a smectic A phase and the planar alignment of the molecules gave rise to a maximum absorbance when the rub direction was aligned parallel to the plane of the polarised light, and the minimum absorbance when the rub direction was perpendicular to

the plane of the polarised light. The samples were cooled until the crystallisation point and spectra past this point are not shown, as the crystal phase exhibited light scattering.

Across all samples, the wavelength at the highest absorbance (λ_{max}) and shape of each absorption peak were similar across all the different guest-host mixtures, consistent with the observed band being the same for each mixture. It can be observed that the isotropic peaks, which were the same size in both the parallel and perpendicular measurement for each guest-host mixture, were different magnitudes between different guest-host mixtures. For each dye it would be expected that the absorption coefficient (ε) will stay constant, and hence that the absorbance in the isotropic liquid is dependent on the path length of the cell (l) and the concentration of the dye (c), following the Beer-Lambert law. In these cells the path lengths were selected to be as similar between the guest-host mixtures and the respective host alone cell, and so the concentration is likely to be the source of the variation in the absorbance seen in the UV-vis results from the isotropic samples.

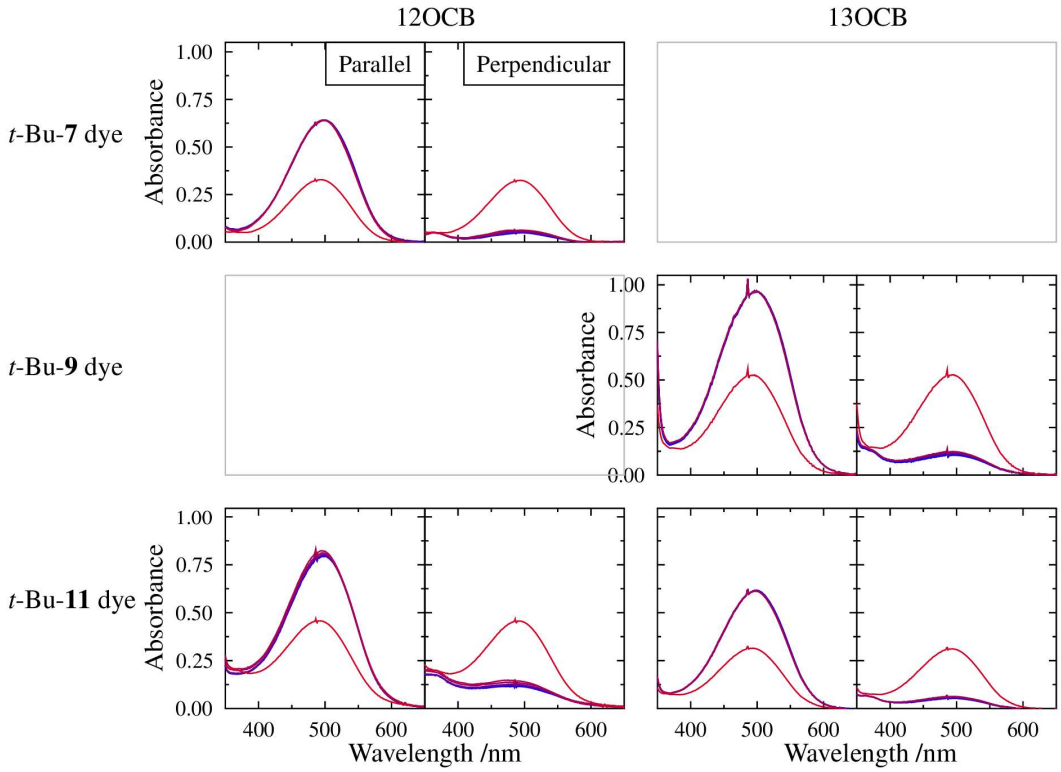

Figure 4.40: Examples of the polarised UV-vis spectra for guest-host mixtures with 12OCB and 13OCB as the hosts, showing the parallel and perpendicular absorbance with decreasing temperature, from red to blue.

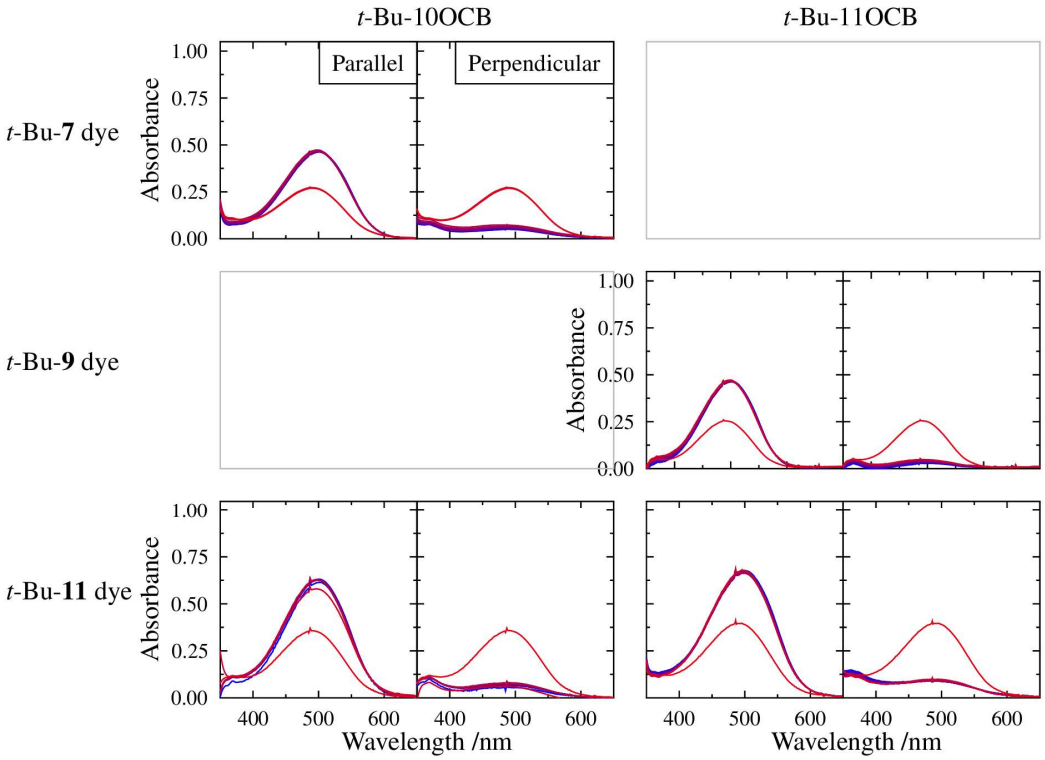

Figure 4.41: Examples of the polarised UV-vis spectra for guest-host mixtures with *t*-Bu-10OCB and *t*-Bu-11OCB as the hosts, showing the parallel and perpendicular absorbance with decreasing temperature, from red to blue.

The parallel and perpendicular absorption measurements were used to calculate the dichroic ratio (DR), using equation 4.2, which gives the ratio between the absorbance of light polarised parallel ($A_{\parallel}$) and perpendicular ($A_{\perp}$) to the alignment direction of the cell.

Equation 4.2 $$DR = \frac{A_{\parallel}}{A_{\perp}}$$

The dichroic ratio at each temperature was calculated and plotted as a function of wavelength as shown in Figure 4.42. This example shows 12OCB with *t*-Bu-**7** dye, and shows that in the region of the peak absorbance the dichroic ratio reaches a plateau. At longer wavelengths than the peak absorbance, in the region longer 600 nm, there are very low values of absorbance in both parallel and perpendicular directions, which results in large fluctuations in the dichroic ratio values. At shorter wavelengths, in the region shorter than 400 nm, there is the presence of another UV-vis band, due to a transition which is not the focus of this study, which results in the slight increase in the dichroic ratio observed at approximately 350

nm. The line in Figure 4.42 at 500 nm shows wavelength at which the peak absorbance in the parallel direction occurs, which can be denoted as the λ_{max}.

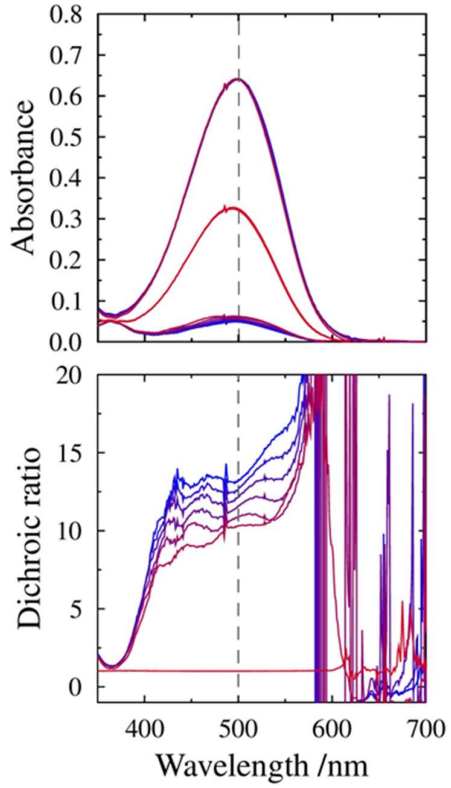

Figure 4.42: Example of the absorbance measurements taken, for 12OCB with the *t*-Bu-**7** dye across the smectic A phase temperature range. The dichroic ratio is calculated at each temperature and the marking shows the dichroic ratio at a wavelength of 500 nm

For each of the guest-host mixtures studied, the calculated dichroic ratios are given in Table 4.21 and Table 4.22 for the three runs of the guest-host mixtures with nOCB hosts, and in Table 4.23 and Table 4.24 for the two runs of the guest-host mixtures with *t*-Bu-nOCB hosts, with the respective plots of dichroic ratio with temperature given in Figure 4.43 and Figure 4.44. Each dataset shows multiple measurements of the same guest-host mixture within the same cell, unless specified otherwise. For each sample, there was some variation in the dichroic ratio profiles observed between different runs of the same sample, and some variety in the dichroic ratio values obtained, as discussed below.

For the guest-host mixtures with 12OCB as the host, shown in the top two rows of Figure 4.43, the mixture with the *t*-Bu-**7** dye shows good reproducibility across the three runs, but the mixture with the *t*-Bu-**11** dye showed more variance across the three runs. This may be due slight changes in the alignment of the samples with the repeated heating and cooling of the cell over the runs, but the overall range of the dichroic ratio across the temperature range of the phase is of a similar magnitude across the three runs and in comparison with the guest-host mixture with the *t*-Bu-**7** dye. For the guest-host mixtures with 13OCB as the host, shown in the bottom to rows of Figure 4.43, the mixture with the *t*-Bu-**9** dye showed good reproducibility in the three runs, but the mixture with the *t*-Bu-**11** dye has two runs which are similar in the dichroic ratio values but the first run is much lower. This may be due to the guest-host being less well aligned in the cell during the first run. As the sample is slowly cooled during the measurement, this may have allowed the sample to align better with the alignment layers within the cell and so lead to a larger ratio between the parallel and perpendicular states in the subsequent runs.

For the guest-host mixtures with *t*-Bu-10OCB as the host, shown in the top two rows of Figure 4.44, both of the guest-host mixtures show good reproducibility over the two runs. The mixture with the *t*-Bu-**7** dye shows a wider range of dichroic ratios with decreasing temperature on the first run, but overall the magnitude of the two runs is similar. For the guest-host mixture with *t*-Bu-11OCB with the *t*-Bu-**11** dye, shown in the bottom row of Figure 4.44, there is also good reproducibility between the two runs. For the guest-host mixture with *t*-Bu-11OCB with the *t*-Bu-**9** dye, shown in the second from bottom row of Figure 4.44, the values of the dichroic ratio were found to be much larger than seen for any of the other guest-host mixtures. This was observed over three runs, rather than two.

Table 4.21: Average calculated dichroic ratio determined from UV-visible measurements, over 475-525 nm for the guest-host mixtures with 12OCB as the host.

Guest-host mixture	12OCB with *t*-Bu-**7** dye			12OCB with *t*-Bu-**11** dye		
	Dichroic ratio at λ = 475-525 nm					
T /ºC	Run 1	Run 2	Run 3	Run 1	Run 2	Run 3
65	13.62	12.35	12.68	10.15	13.69	10.41
70	12.99	11.75	11.97	9.82	13.28	9.86
75	12.33	11.05	11.01	9.44	12.82	9.27
80	11.55	10.47	10.49	9.16	12.00	8.93
85	10.73	9.73	9.79	8.76	11.28	8.67
90	10.18	10.98	11.06	6.84	9.47	8.21

Table 4.22: Average calculated dichroic ratio determined from UV-visible measurements, over 475-525 nm for the guest-host mixtures with 13OCB as the host.

Guest-host mixture	13OCB with *t*-Bu-**9** dye			13OCB with *t*-Bu-**11** dye		
	Dichroic ratio at λ = 475-525 nm					
T /ºC	Run 1	Run 2	Run 3	Run 1	Run 2	Run 3
70	8.18	9.33	10.35	4.96	11.75	9.62
75	7.93	8.96	9.97	4.91	11.29	9.21
80	7.66	8.57	9.64	4.89	10.81	8.97
85	7.34	8.28	9.38	4.86	10.29	8.68
90	7.08	7.90	9.02	4.81	9.81	8.38

Table 4.23: Average calculated dichroic ratio determined from UV-visible measurements, over 475-525 nm for the guest-host mixtures with *t*-Bu-10OCB as the host.

Guest-host mixture	*t*-Bu-10OCB with *t*-Bu-7 dye		*t*-Bu-10OCB with *t*-Bu-11 dye	
	Dichroic ratio at λ = 475-525 nm			
T /ºC	Run 1	Run 2	Run 1	Run 2
35			11.28	9.15
40	9.38		9.52	9.02
45	9.14	8.42	9.36	8.87
50	8.84	8.17	9.12	8.69
55	8.55	7.90	8.95	8.54
60	8.24	7.60	8.77	8.40
65	7.89	7.37	8.49	8.26
70	7.47	7.11	8.28	8.12
75	7.09	6.78	8.13	7.92
80	6.55	6.57	7.85	7.77

Table 4.24: Average calculated dichroic ratio determined from UV-visible measurements, over 475-525 nm for the guest-host mixtures with *t*-Bu-11OCB as the host.

Guest-host mixture	*t*-Bu-11OCB with *t*-Bu-**9** dye			*t*-Bu-11OCB with *t*-Bu-**11** dye	
	Dichroic ratio at λ = 475-525 nm				
T /°C	Run 1	Run 2	Run 3	Run 1	Run 2
40	26.54	27.94	21.73	7.59	8.45
45	23.24	26.58	20.24	7.48	8.23
50	21.10	25.21	19.36	7.45	8.07
55	19.01	23.90	18.36	7.44	7.89
60	17.54	22.94	16.28	7.29	7.72
65	15.92	21.86	16.31	7.43	7.53
70	14.48	20.51	15.10	7.33	7.35
75	13.57	19.32	14.52	7.22	7.19
80	12.96	18.30	13.43	7.07	6.99
85	12.12	16.88	12.39	6.83	6.74

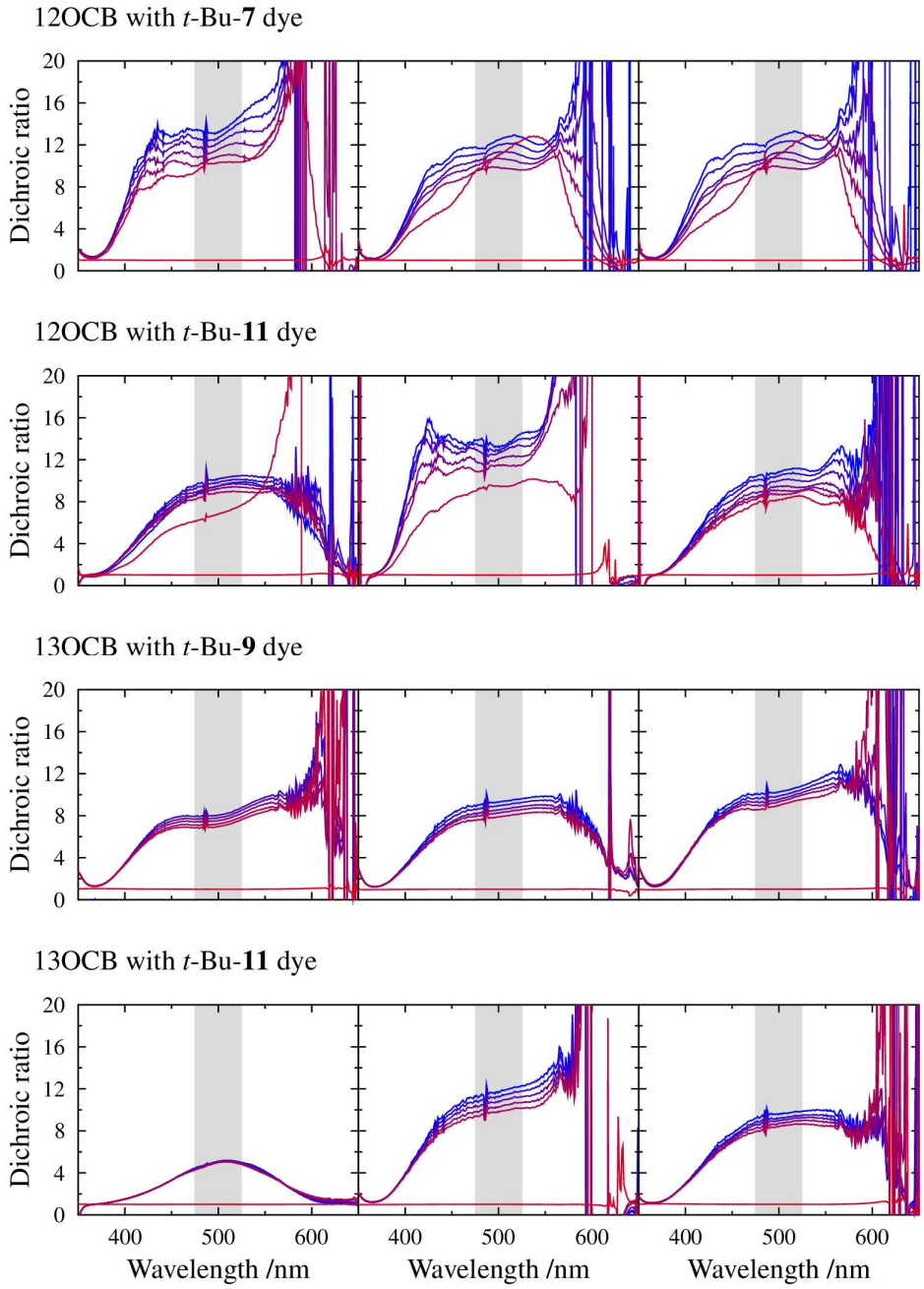

Figure 4.43: Dichroic ratio plots for each of the runs of the guest-host mixtures with 12OCB and 13OCB as the hosts. The grey band shows the region of 475-525 nm used for averaging.

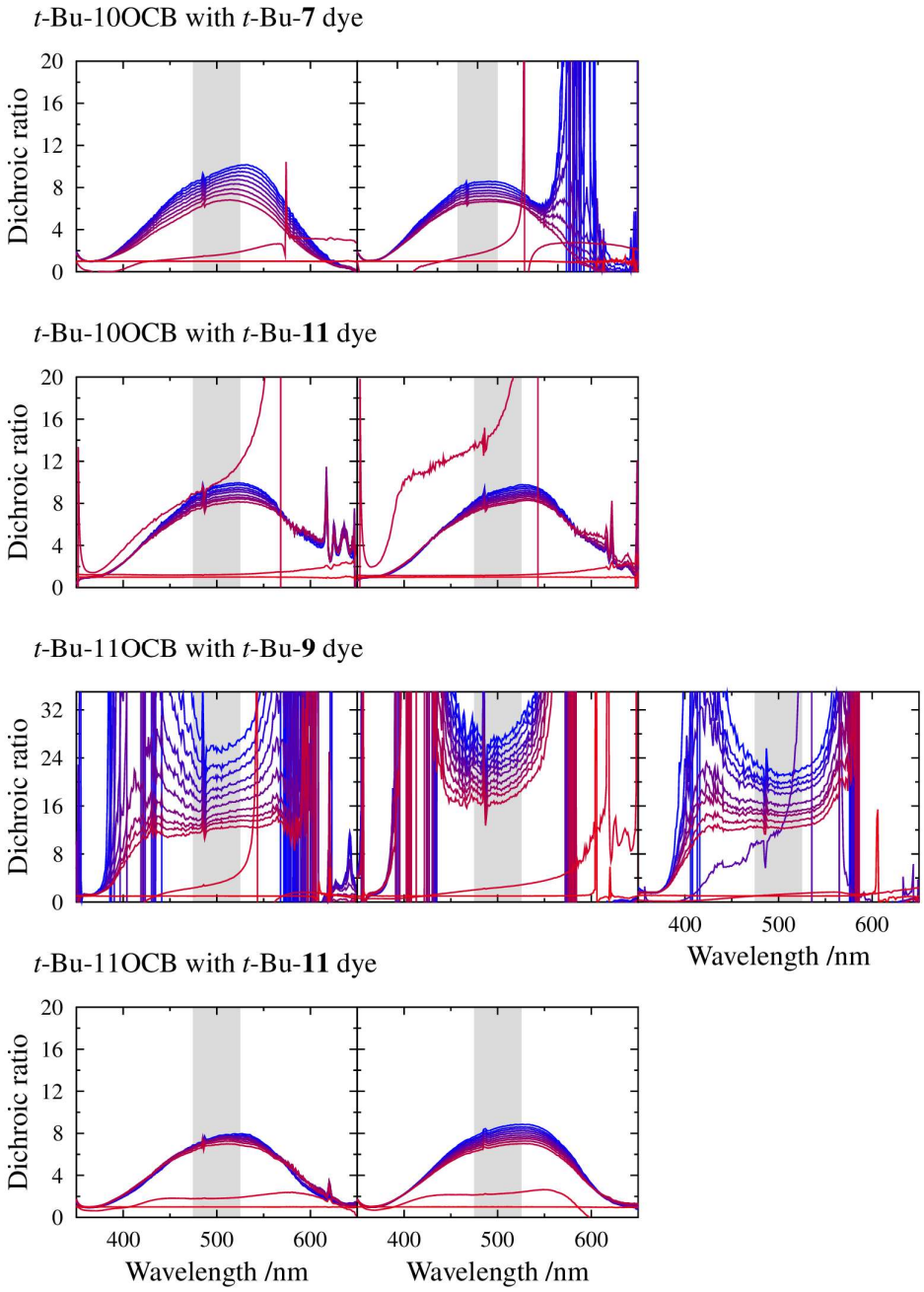

Figure 4.44: Dichroic ratio plots for each of the runs of the guest-host mixtures with *t*-Bu-10OCB and *t*-Bu-11OCB as the hosts. The grey band shows the region of 475-525 nm used for averaging.

As a result of the higher dichroic ratio observed for *t*-Bu-11OCB with the *t*-Bu-**9** dye, three more cells were tested, with the cell path lengths summarised in Table 4.25. For these tests, cell A was filled with the same guest-host mixture as the original cell and cell B and C were filled with a newly made mixture of 1.01 wt% *t*-Bu-**9** dye in *t*-Bu-11OCB host.

Table 4.25: Summary of cells used for additional tests with guest-host mixtures of *t*-Bu-11OCB with the *t*-Bu-**9** dye.

	Guest-host mixture	Cell path length /μm
Original cell	0.97 wt% mixture	15.8
Original cell		15.8
Original cell		15.8
cell A		18.0
cell B	1.01 wt% mixture	21.0
cell C		18.8

The calculated dichroic ratio spectra from the additional cells, shown in Figure 4.45, give a similar profile to the guest-host mixtures with *t*-Bu-10OCB and the guest-host mixture of *t*-Bu-11OCB and *t*-Bu-**11** dye. The guest-host mixtures in the new cells have lower dichroic ratio values than for the previous cells with *t*-Bu-11OCB and *t*-Bu-**9** dye, which may suggest that the guest-host mixture is less well aligned in these new cells.

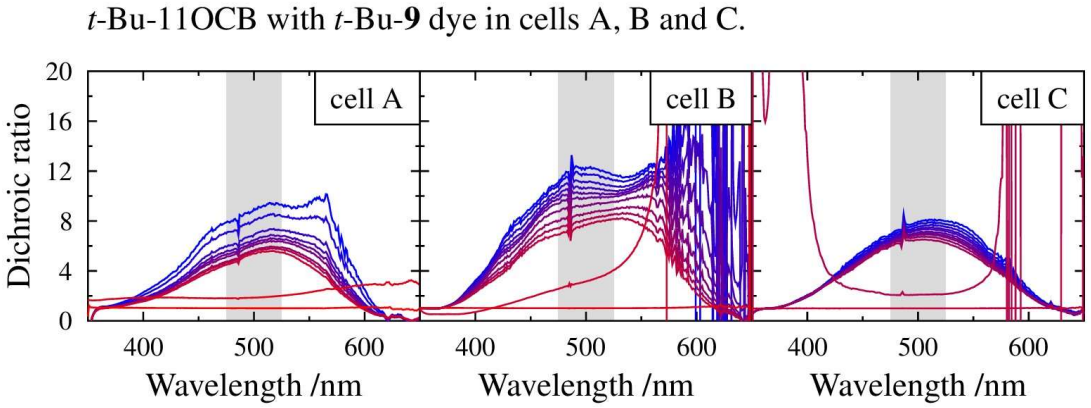

Figure 4.45: Dichroic ratio plots for each of the extra runs of the guest-host mixtures with *t*-Bu-11OCB as the host and the *t*-Bu-**9** dye, in a new cell A, and with a new mixture in two new cells B and C. The grey band shows the region of 475-525 nm used for averaging.

The calculated dichroic ratio at each temperature was averaged over the range of 475-525 nm, which was selected as the approximate region that there was a plateau in the calculated dichroic ratio, and the value in this region is summarised in Table 4.21 and Table 4.22 for the guest-host mixtures with nOCB hosts, in Table 4.23 and Table 4.24 for the guest-host mixtures with *t*-Bu-nOCB hosts, and given in Table 4.26 for cells A, B and C. These average calculated dichroic ratio values are plotted for all the guest-host mixtures in Figure 4.46, and it is observed that all guest-host mixtures show an increase in the calculated dichroic ratio with decreasing temperature.

The guest host mixtures with the 12OCB as the host have calculated dichroic ratios of a similar magnitude for both dyes and the runs with *t*-Bu-**7** dye have good reproducibility. The guest-host mixtures with 13OCB as the host also show a similar magnitude to the mixtures with 12OCB, not including the first run which have lower calculated dichroic ratios as seen in the plots in Figure 4.43. The guest-host mixtures with *t*-Bu-10OCB as the host show good reproducibility and have a lower calculated dichroic ratio over the respective temperature ranges than the guest-host mixtures with nOCB hosts. The guest-host mixtures with *t*-Bu-11OCB and *t*-Bu-**11** dye have good reproducibility and similar magnitude of calculated dichroic ratios to the guest-host mixtures with *t*-Bu-10OCB as the host. In Figure 4.46, the calculated dichroic ratios for all six runs of the guest-host mixture with *t*-Bu-11OCB with *t*-Bu-**9** dye are shown, with dark green dots for the first three runs and lighter green dots for cell A, B and C. This shows that there is a large variance in the calculated dichroic ratios across these six runs, but that the first three runs show a much higher dichroic ratio. In cell A the dichroic ratio value at 50 ^{o}C was 0.17, which was lower than the other values. This value was omitted from the plot as it was an anomalous result in the run of cell A.

Table 4.26: Additional average calculated dichroic ratio determined from UV-visible measurements, over 475-525 nm for the guest-host mixtures with *t*-Bu-11OCB as the host in cell A, B and C. *Anomalous value omitted.

Guest-host mixture	*t*-Bu-11OCB with *t*-Bu-**9** dye		
	Dichroic ratio at λ = 475-525 nm		
T /°C	cell A	cell B	cell C
40	8.77	12.01	7.79
45	7.92	11.57	7.59
50	*	11.00	7.40
55	6.79	10.54	7.23
60	6.36	10.15	7.12
65	6.11	9.80	6.93
70	5.92	9.24	6.83
75	5.51	8.56	6.75
80	5.40	8.06	6.59
85	5.22	7.63	6.38

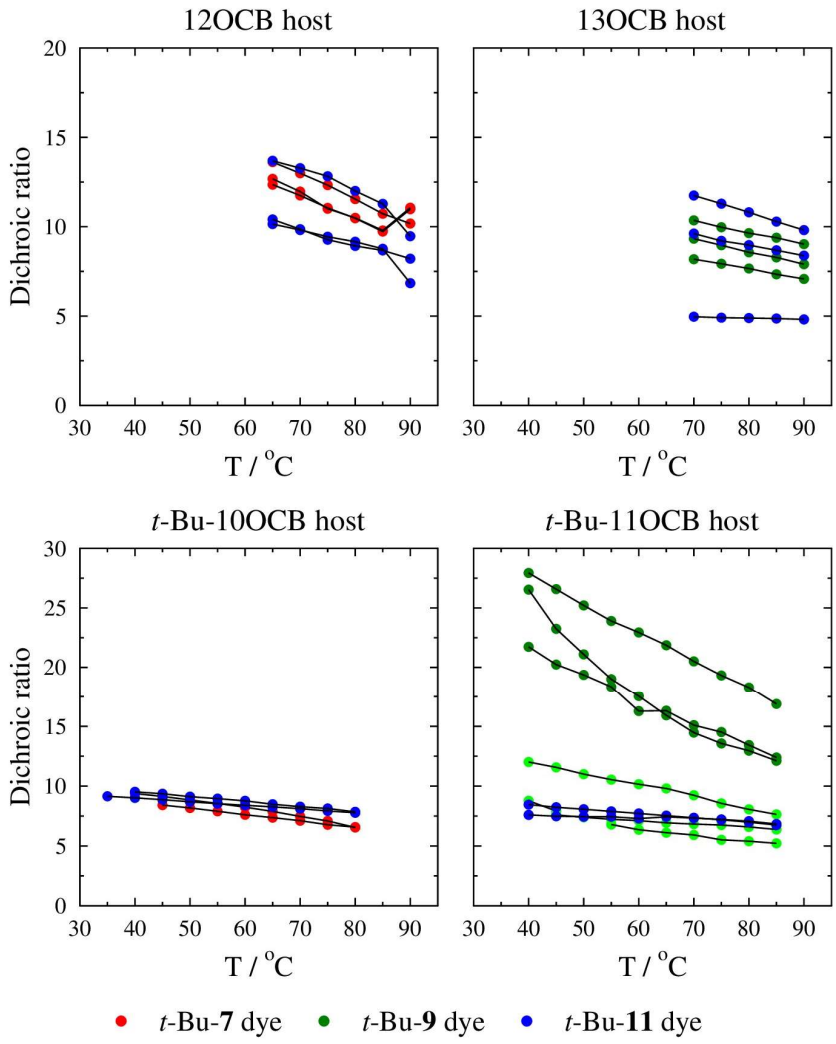

Figure 4.46: Calculated dichroic ratio with temperature for all guest-host mixtures, where red dots represent the guest host mixture with *t*-Bu-**7** dye, green dots represent the guest host mixture with *t*-Bu-**9** dye and blue dots represent the guest host mixture with *t*-Bu-**11** dye. The lighter green dots show the samples in cell A, B and C.

4.4 Discussion

4.4.1 DFT and TD-DFT results

The DFT results gave molecular lengths and widths from the all-*trans* structure of the dye molecules, which showed an odd-even effect as seen in the liquid crystal host series. For the **m** dye and *t*-Bu-**m** dye series, there is an overall trend of decreasing width until **m** = 12 for the **m** dyes and **m** = 9 for the *t*-Bu-**m** dyes, as shown in Figure 4.3. After these **m** values, the widths show a general increase, with the odd-even effect continuing. The odd-even effect in

the widths arises from the position of the terminal groups with respect to the moment of inertia axis and is observed to be more pronounced for the *t*-Bu-**m** dyes than the **m** dyes, The odd-even effect was also more pronounced for the hosts containing *t*-Bu terminal groups, and this shows that the molecular shape effect is emphasising the odd-even effect seen with increasing chain length.

This odd-even effect is also observed in the β values, for the angle between the long axis proxy and the transition dipole moment (TDM), as shown in Figure 4.47. At the shorter chain lengths in both series, there is a pronounced odd-even effect, particularly for the *t*-Bu-**m** dyes. This was also seen for the widths from the host alone and dye alone DFT studies. At the longer chain lengths, the odd-even effect is dampened and there is little change in the angle β.

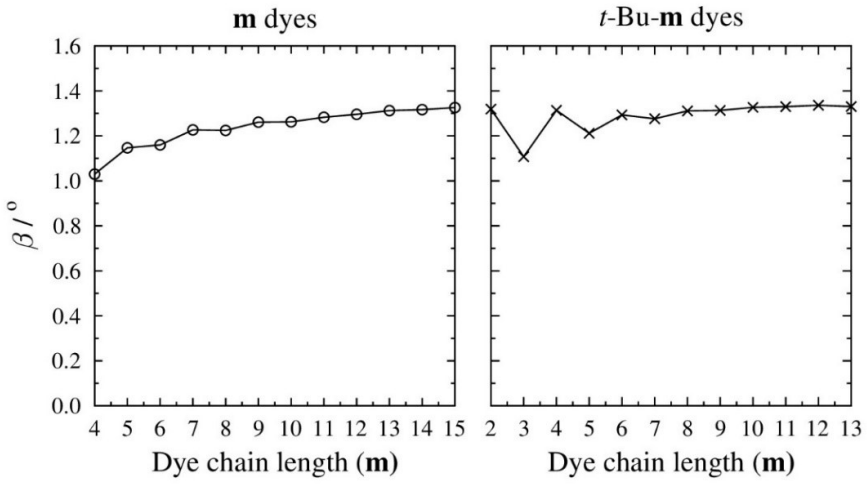

Figure 4.47: Angle between the long axis proxy, between the two phenyl rings of the dye, and the transition dipole moment (TDM) for the **m** dyes and the *t*-Bu-**m** dyes.

4.4.2 MD simulation results

4.4.2.1 Host parameters

For the guest-host mixtures, simulations of 1000 liquid crystal molecules with 9 guest dyes were undertaken for 4 different hosts and a range of dyes. A comparison can be made of the host orientational and translational order parameters at each dye chain length (**m**), which is given in Figure 4.48. The layer spacing determined for the host in each of these simulations is given in Figure 4.49.

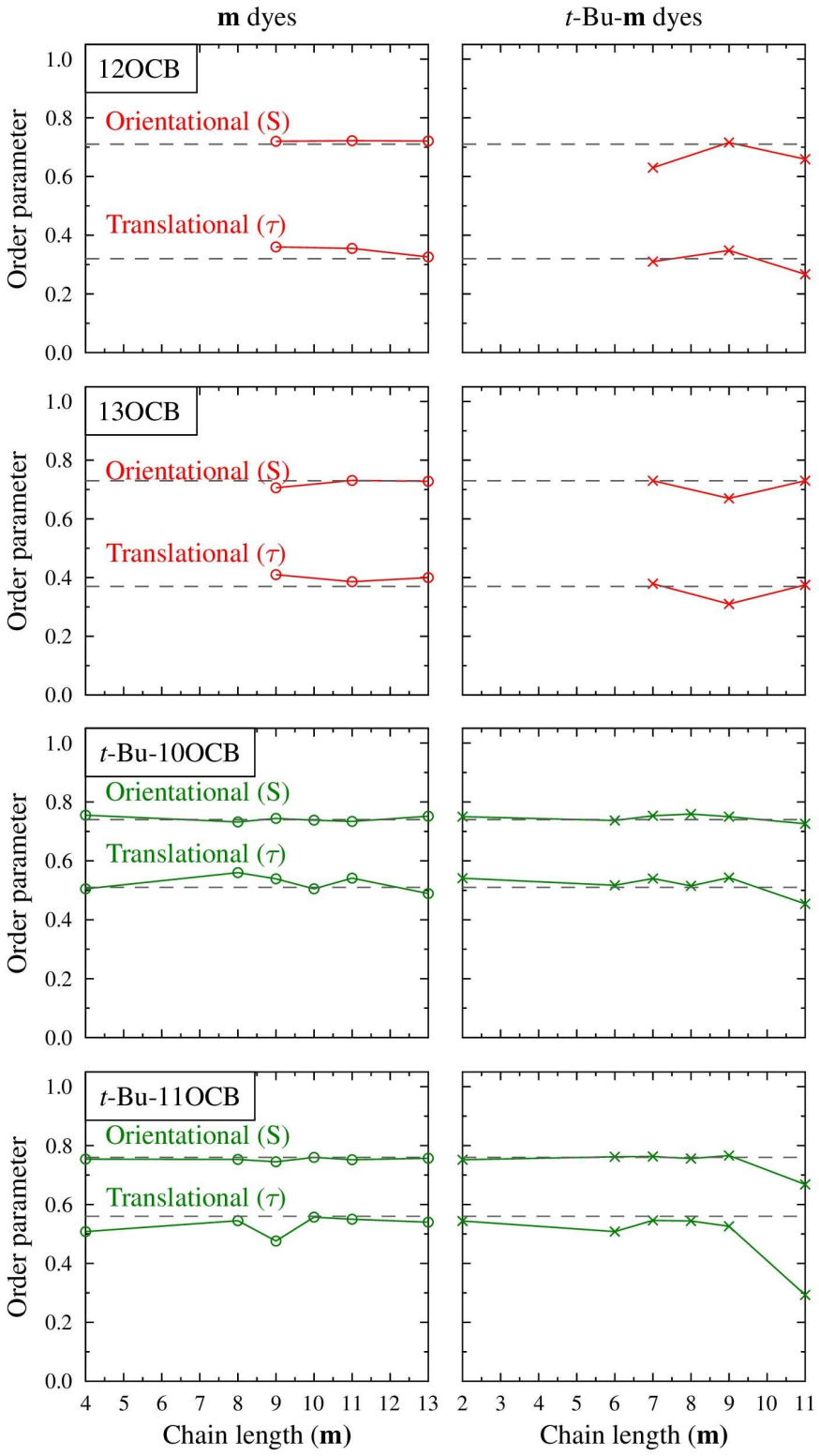

Figure 4.48: Orientational and translational order parameters with dye chain length (**m**), averaged over the stable plateau of the simulations, for nOCB and *t*-Bu-nOCB hosts. The dashed line gives the values for the host alone orientational and translational order parameters.

It can be seen that the orientational order parameter of the 12OCB host was similar for the guest-host mixtures with both the **m** dyes and *t*-Bu-**m** dyes. These values are also similar to the value of 0.71 from the simulations of the host alone. This was also observed for the orientational order parameter of the 13OCB host, which has similar orientational order parameters for all the guest-host mixtures with the **m** dyes and *t*-Bu-**m** dyes, and was also similar to the value of 0.73 from the simulations of the host alone. This shows that the addition of the dye to these hosts did not change the orientational order of the phase significantly. All the host translational order parameters for the guest-host mixtures with nOCB hosts all have a similar value to the host alone values of 0.32 and 0.37 for 12OCB and 13OCB respectively. This suggests that the addition of the dye is not disrupting the layering of the host liquid crystal phase. For these guest-host mixtures, there is no clear trends observed with the different hosts and guests which suggests that the small wt% of the dye in the simulations is not changing the overall packing of the phase.

The orientational order parameter of the *t*-Bu-10OCB host was similar for the guest-host mixtures with both the **m** dyes and *t*-Bu-**m** dyes. These values are also similar to the value of 0.74 from the simulations of the host alone. This was also observed for most of the orientational order parameters of the *t*-Bu-11OCB host, which has similar orientational order parameters for all the guest-host mixtures with the **m** dyes and *t*-Bu-**m** dyes, and was also similar to the value of 0.76 from the simulations of the host alone. The similar values indicate that the small wt% of the dye is not affecting the orientational order parameter of the host. The exception is the guest-host mixture with *t*-Bu-11OCB with the *t*-Bu-**11** dye, which shows a lower orientational order parameter than the host alone value from the simulations. The lower orientational order parameter suggests that the longest chain length of the *t*-Bu-**11** dye is disrupting the orientation of the host molecules relative to the host director. For the host translational order parameters, the values for the guest-host mixtures are similar to the host alone value of 0.51 and 0.56 for *t*-Bu-10OCB and *t*-Bu-11OCB respectively, except for *t*-Bu-11OCB with the *t*-Bu-**11** dye as the guest. This suggests that the longer dye chain length are causing a disruption of the diffuse layers in the liquid crystal phase in this guest-host mixture, whereas in the other mixtures the small wt% is not affecting the diffuse layers of the host.

In terms of the host layer spacing for the guest-host mixtures, shown in Figure 4.49, the mixtures with nOCB hosts only show a small variation from the layer spacing of the host alone, whereas the guest-host mixtures with the *t*-Bu-nOCB hosts show greater variability in the host layer spacing depending on the guest dye added. For the mixtures with *t*-Bu-10OCB, the values are similar to the host alone value of 4.27 nm but there is no clear trend in these lengths with host chain length (**m**). For the guest-host mixtures with *t*-Bu-11OCB as the host, all the layer spacings are lower than the host alone value of 4.65 nm, with the exception of *t*-Bu-**7** dye which is slightly higher than the host alone value. This observation could suggest that the *t*-Bu-11OCB host is the most sensitive to the addition of the guest dye, as the layer spacing is reduced for both types of dye. These observations suggest that the dye molecules are generally well incorporated into the diffuse layer structure of the host, and that the combination of host with bulky terminal groups and any dye causing disruption in the layer spacing of the host.

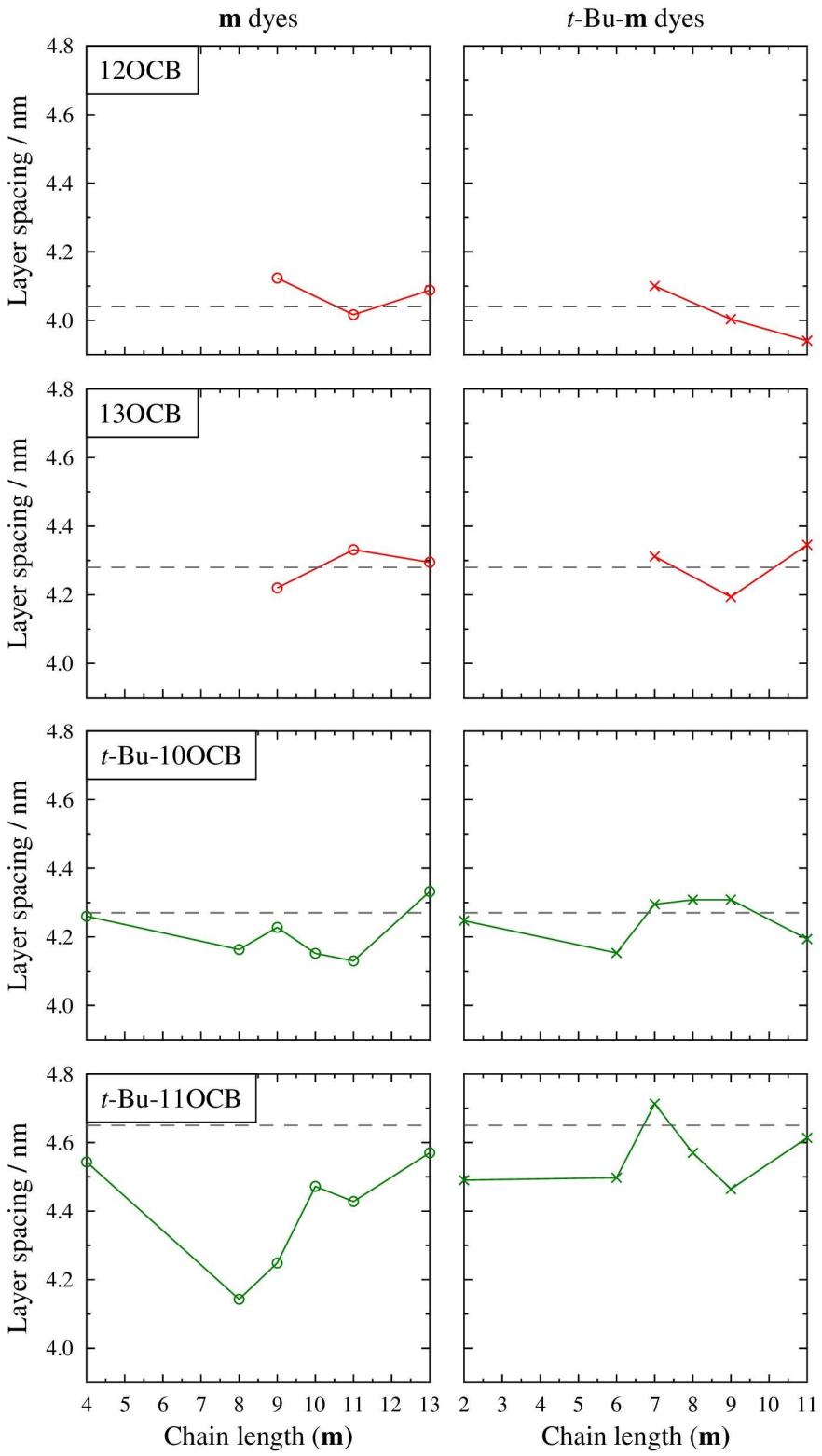

Figure 4.49: Host layer spacing with dye chain length (**m**), averaged over the stable plateau of the simulations, for nOCB and *t*-Bu-nOCB hosts. The dashed line gives the values for the host alone orientational and translational order parameters.

4.4.2.2 Guest parameters

For these guest-host simulations, the orientational order parameter of the transition dipole moment of the dye (S_ϕ) will be impacted by the alignment of the transition dipole moment of the dye with the long axis of the dye (β). This is illustrated by Figure 4.50, which shows that the angle β will have an impact on the overall order parameter determined for the transition dipole moment of the dye. The impact of the angle can be determined using equation 4.3,[79] which scales the guest orientational parameter taken from θ_{guest} with that from β.

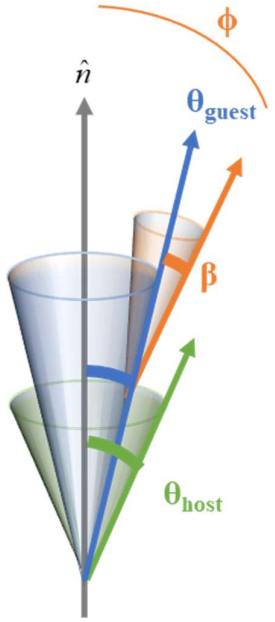

Figure 4.50: Schematic representation of the host director (n̂), with the alignment of the host molecule given by θ_{host}, the alignment of the guest molecule is given by θ_{guest}, and the alignment of the transition dipole moment (TDM) with the long axis of the dye molecule shown by the angle β. Adapted from Sims et al.[90]

Equation 4.3 $$S_\phi = S_\theta S_\beta = \left\langle \frac{1}{2}\left(3\cos^2\theta - 1\right)\right\rangle \left(\frac{1}{2}\left(3\cos^2\beta - 1\right)\right)$$

The values of S_θ, S_β and the overall parameter S_ϕ are shown in Table 4.27 and Table 4.28, and because the angle β is very small it results in a value of S_β that is close to 1. As a result of this, it can be seen that the value of the orientational order parameter of the transition dipole is effectively the same as that of the vector chosen to represent the long axis of the dye.

Table 4.27: Average orientational order parameter (S_θ) averaged over plateau area for the simulated guest-host mixtures with 12OCB and 13OCB as the hosts, the transition dipole moment (TDM) orientational order parameter relative to the long axis (S_β) and the overall orientational order parameter (S_ϕ).

Host	Guest	S_θ	S_β	S_ϕ	Guest	S_θ	S_β	S_ϕ
12OCB	**9** dye	0.82	0.9993	0.82	*t*-Bu-**7** dye	0.77	0.9993	0.77
	11 dye	0.83	0.9992	0.83	*t*-Bu-**9** dye	0.84	0.9992	0.84
	13 dye	0.83	0.9992	0.82	*t*-Bu-**11** dye	0.78	0.9992	0.77
13OCB	**9** dye	0.82	0.9993	0.82	*t*-Bu-**7** dye	0.82	0.9993	0.82
	11 dye	0.85	0.9992	0.85	*t*-Bu-**9** dye	0.80	0.9992	0.80
	13 dye	0.81	0.9992	0.81	*t*-Bu-**11** dye	0.84	0.9992	0.84

Table 4.28: Average orientational order parameter (S_θ) averaged over plateau area for the simulated guest-host mixtures with *t*-Bu-10OCB and *t*-Bu-11OCB as the hosts, the transition dipole moment (TDM) orientational order parameter relative to the long axis (S_β) and the overall orientational order parameter (S_ϕ).

Host	Guest	S_θ	S_β	S_ϕ	Guest	S_θ	S_β	S_ϕ
t-Bu-10OCB	**4** dye	0.83	0.9995	0.83	*t*-Bu-**2** dye	0.86	0.9992	0.86
	8 dye	0.85	0.9993	0.84	*t*-Bu-**6** dye	0.84	0.9992	0.84
	9 dye	0.84	0.9993	0.84	*t*-Bu-**7** dye	0.87	0.9993	0.87
	10 dye	0.86	0.9993	0.86	*t*-Bu-**8** dye	0.87	0.9992	0.87
	11 dye	0.83	0.9992	0.83	*t*-Bu-**9** dye	0.85	0.9992	0.85
	13 dye	0.84	0.9992	0.84	*t*-Bu-**11** dye	0.83	0.9992	0.83
t-Bu-11OCB	**4** dye	0.82	0.9995	0.82	*t*-Bu-**2** dye	0.86	0.9992	0.86
	8 dye	0.86	0.9993	0.86	*t*-Bu-**6** dye	0.88	0.9992	0.88
	9 dye	0.83	0.9993	0.83	*t*-Bu-**7** dye	0.88	0.9993	0.88
	10 dye	0.85	0.9993	0.85	*t*-Bu-**8** dye	0.86	0.9992	0.86
	11 dye	0.85	0.9992	0.85	*t*-Bu-**9** dye	0.86	0.9992	0.86
	13 dye	0.83	0.9992	0.83	*t*-Bu-**11** dye	0.79	0.9992	0.79

A comparison can be made of the host orientational and translational order parameters of the dye at each dye chain length (**m**), which is given in Figure 4.51. For these dyes, only the order parameters were determined, as there were no layers formed specifically by the dyes as there was only a small number within the simulation. It is observed that the guest order parameters follow the trends of the host parameters, but the orientational and translation order parameters are higher than those seen for the host. This may be as a result of the host molecules orienting the dye molecules, and so driving the orientation of the dye molecules. This may cause the dye molecules to be better oriented as a result, leading to the orientational and translational order of the dye being higher than the host parameters.

For all different guests and hosts, the orientational order parameters are all a similar value of ~0.8 and there is more variation seen in the translational order parameter. Overall, neither of these parameters show a clear trend with the odd-even chain lengths of the dyes. These parameters suggest that the dyes are well oriented relative to the host director, and that this occurs similarly across all different dye chain lengths and in the different hosts. This also suggests that the dye molecules are also well accommodated in the host layers, and that the variation in these values may be as a result of the small number of molecules averaged over.

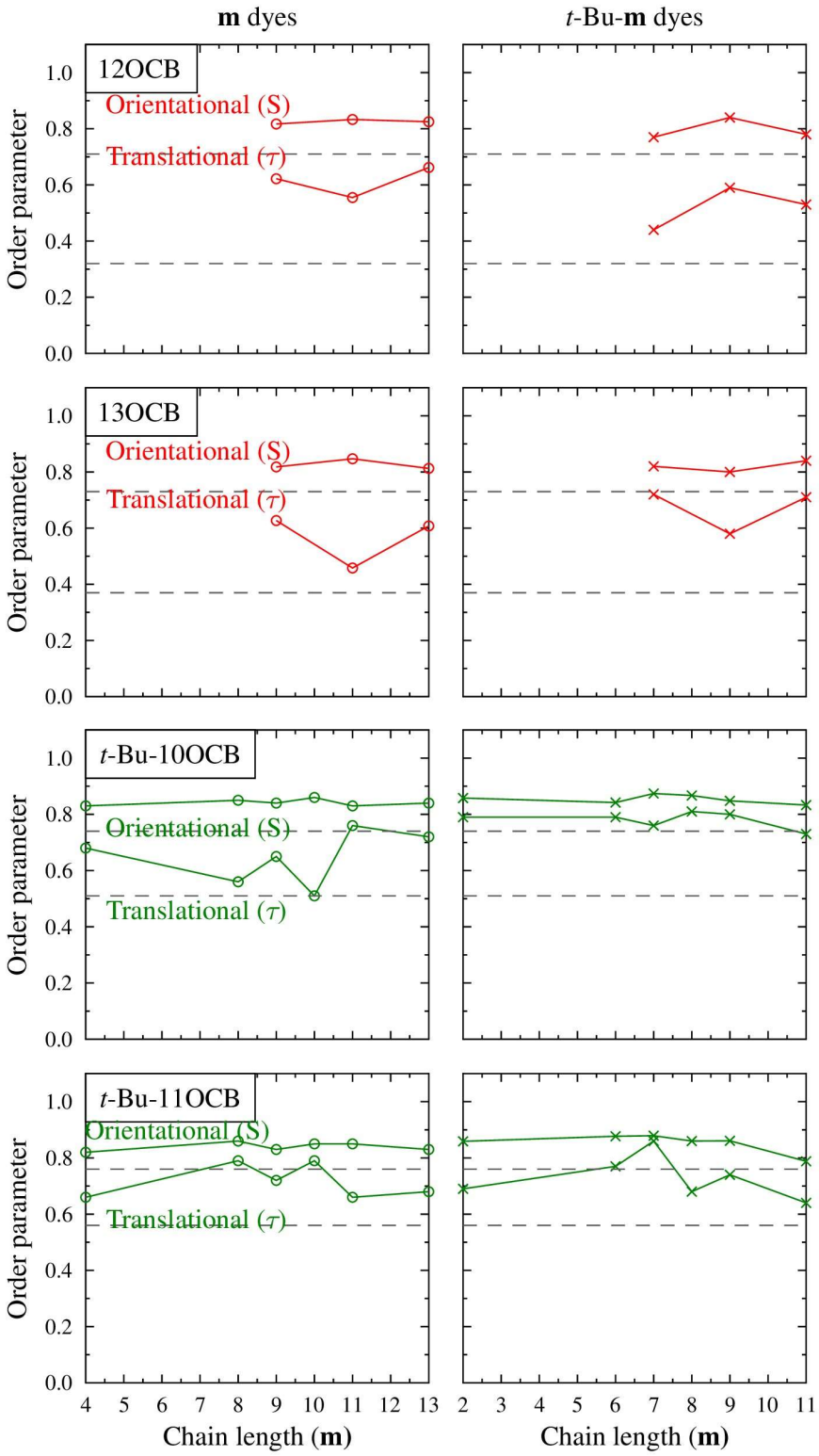

Figure 4.51: Guest layer spacing with dye chain length (**m**), averaged over the stable plateau of the simulations, for nOCB and t-Bu-nOCB hosts. The dashed line gives the values for the host alone orientational and translational order parameters.

4.4.3 Transition temperatures and thermodynamic results

4.4.3.1 Dye alone observations

Before the dyes were combined with the liquid crystal hosts in the guest-host mixtures, the three dyes were studied by POM and DSC. The melting and clearing point transitions are shown in Figure 4.52, and the transition enthalpies and entropies are shown in Figure 4.53 It was observed by POM that the *t*-Bu-**7** dye exhibited smectic C and smectic A phases, and the other two dyes only exhibited smectic C phases. The transition between the smectic C and smectic A phase for *t*-Bu-**7** dye was second order, appearing as a step in the baseline in the DSC trace. It was observed that there is a decrease in the dye melting point and clearing point with increasing chain length. In the clearing point there is a linear decrease in the transition temperature, as the dyes studied in this series are all odd numbered chain lengths so there is no even chain lengths to observed any odd-even trends in this data.

It can be seen that the transition enthalpy and entropy of the clearing point for *t*-Bu-**7** dye is lower than the other two dyes, suggesting that the difference between the smectic A phase and the isotropic phase is smaller for this dye than the difference between the smectic C phase and the isotropic liquid for the other dyes. In the transition enthalpy and entropy of the melting point, the values decrease with increasing chain length and for the clearing point the values increase with decreasing chain length. For the clearing point transition, the *t*-Bu-**7** dye has a lower transition enthalpy and entropy than the other dyes. This transition is from the smectic A to the isotropic phase, which suggests that the smectic A phase is more similar to the isotropic phase than the smectic C phase that is involved in the transition for the other dyes.

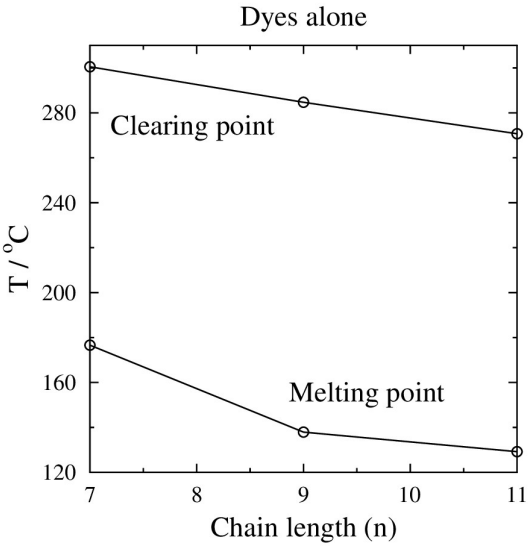

Figure 4.52: Phase transition temperatures for the *t*-Bu-**m** dyes, where **m** = 7, 9, 11.

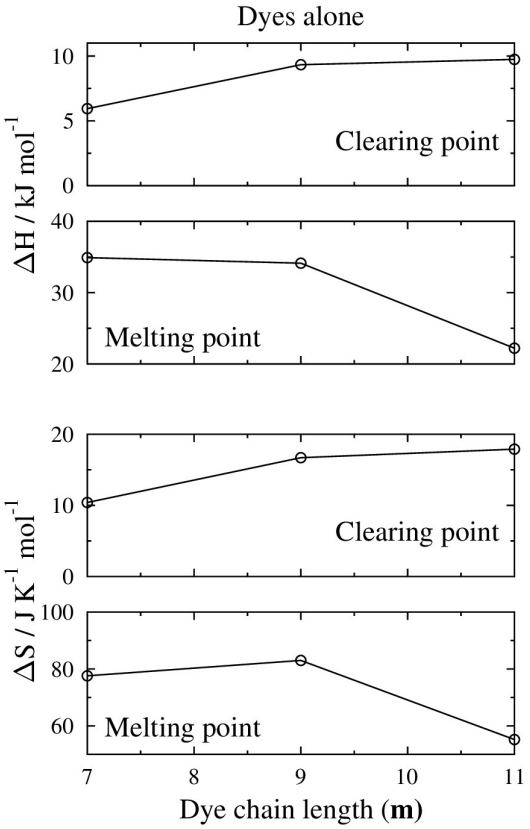

Figure 4.53: Transition enthalpies (ΔH) and transition entropies (ΔS) for the *t*-Bu-**m** dyes, where **m** = 7, 9, 11.

4.4.3.2 Guest-host mixtures

The transition temperatures of the guest-host mixtures as reported from POM and DSC can be compared across the different dye chain lengths, as shown in Figure 4.54. This figure shows the melting point and clearing point transitions for all the guest-host mixtures, and the grey bars give a predicted clearing point, which was determined by using a linear fit between the clearing points of the dye alone and the liquid crystal alone, and calculating the predicted clearing point for the exact wt% of the dye used. All the guest-host mixtures show similar values for the guest-host mixtures to the respective host alone transition temperatures, for both the melting and clearing point temperatures. For the clearing points, there is a close match between the predicted values and the guest-host mixture values. The close match of the host alone and predicted values show that the small wt% of dye added to the guest-host mixtures is not having an significant effect on the transition temperatures, and this is observed in the small increase calculated for the predicted clearing point.

The transition enthalpies and entropies of the different guest-host mixtures are illustrated in Figure 4.55 and Figure 4.56. For most of the guest-host mixtures, the transition enthalpy and entropy of the clearing point is similar to the respective host alone clearing point. This is also observed for the melting points, except for the mixture of 12OCB with the *t*-Bu-**7** dye. If the dye was either disrupting or reinforcing the layering within the smectic phase, it may be considered that there would be a change in the transition entropies. In this case there is no significant change for most of the guest-host mixtures, and so the 1 wt% of dye is not having an effect on the transition entropies. For the mixture of 12OCB with the *t*-Bu-**7** dye there is a decrease in the entropy of melting point transition, suggesting that the dye may be affecting the layering within the smectic phase.

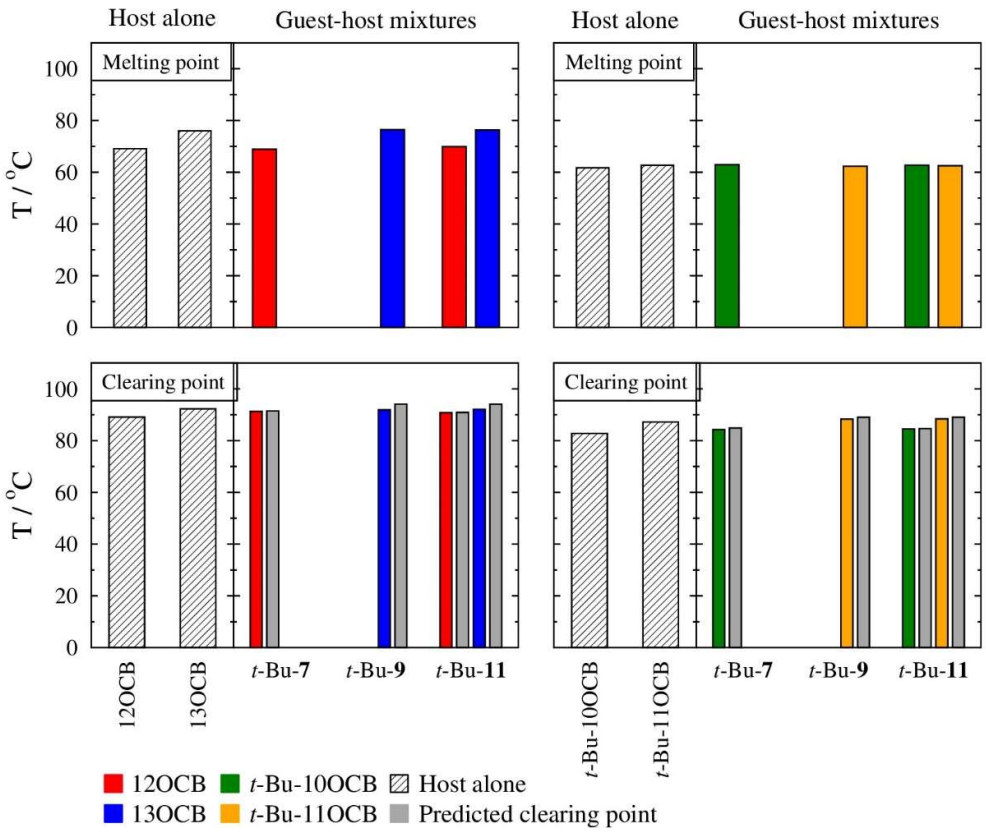

Figure 4.54: Phase transition temperatures for the guest-host mixtures with nOCB and *t*-Bu-nOCB hosts, for the *t*-Bu-**m** dyes where **m** = 7, 9, 11; the grey bars show the predicted clearing point using a linear fit of clearing point temperatures of the dyes and hosts. The striped bars at the left of each set show the transition temperatures for the respective host alone samples.

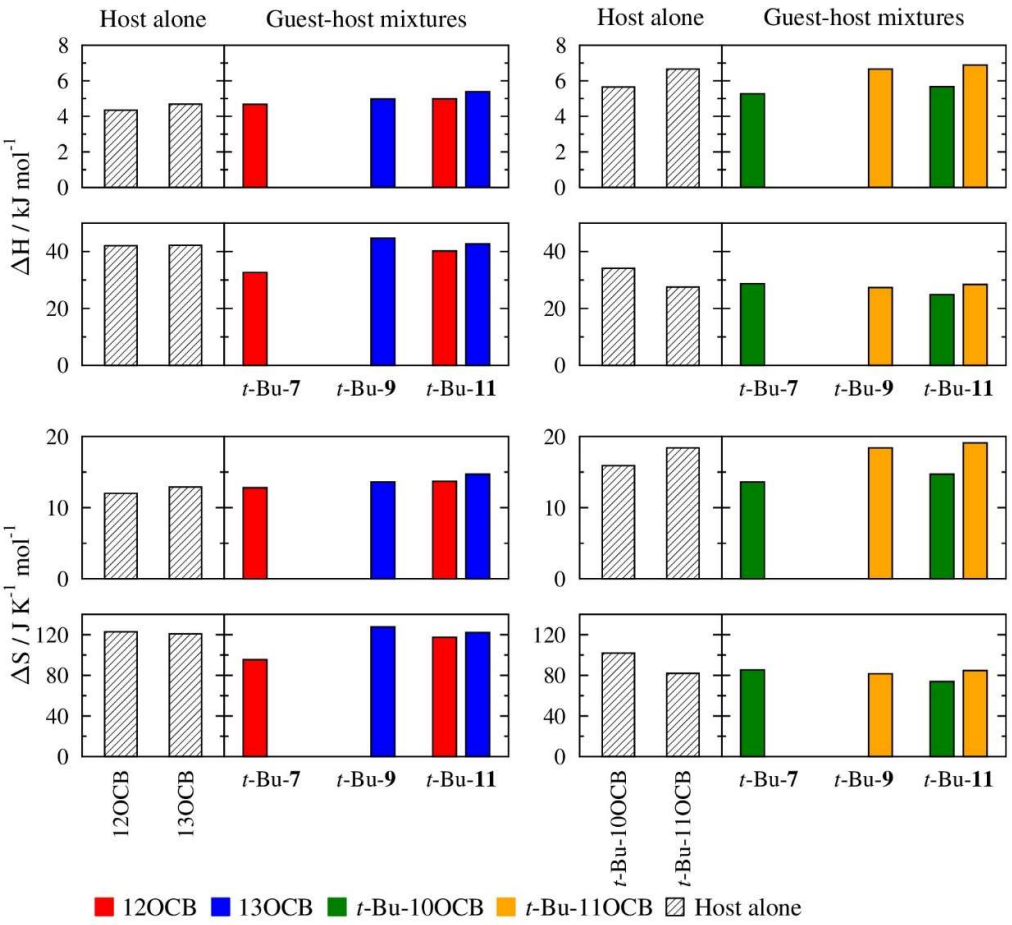

Figure 4.55: Comparison plots for the transition enthalpy and entropy values for the guest-host mixtures with nOCB and *t*-Bu-nOCB hosts. The striped bars at the left of each set show the host alone values.

4.4.4 XRD results

The XRD measurements can provide insight into the phase structure, and determine if there has been any change in the structure due to the addition of the dye into the guest-host mixture. The temperature dependent layer spacing is given in Figure 4.56, which was determined from the small angle peak in the XRD. It can be seen that the general trend observed for the host alone samples are also observed for these guest-host mixtures samples, and that the guest-host mixtures show similar layer spacings to the respective host layer spacings. For the guest-host mixtures with nOCB hosts, the guest-host layer spacing is slightly higher than the respective host layer spacing and for the *t*-Bu-nOCB hosts, the guest-host layer spacing is slightly lower than the respective layer spacing. Overall, this suggests

that the dyes are well accommodated into the hosts and are not having an impact on the layer spacing of the host.

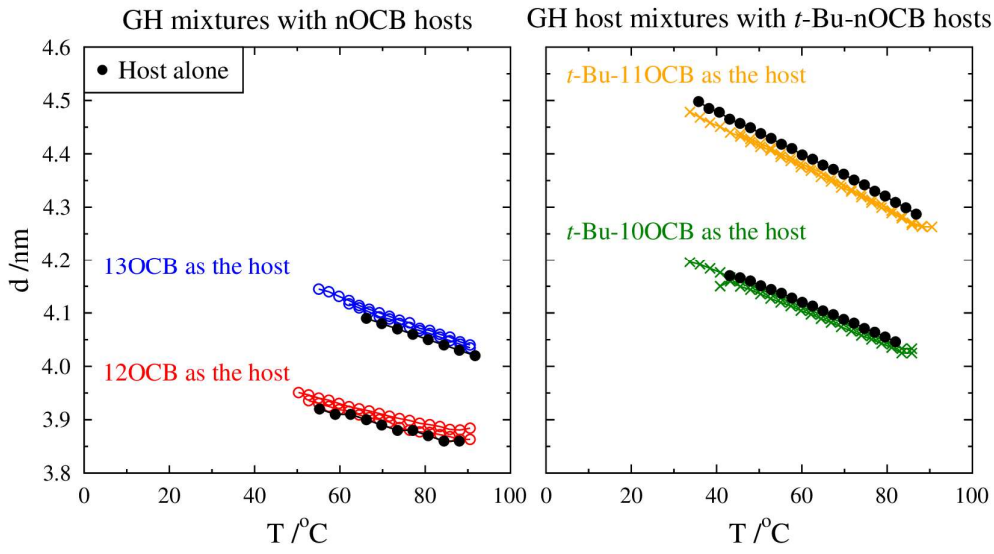

Figure 4.56: Comparison plots for the layer spacing values with temperature, for the guest-host mixtures with different dyes, and the host alone values shown in black.

The layer spacing plot was expanded to observe the individual guest-host mixtures and is shown in Figure 4.57. It can be observed that the layer spacing does not change significantly depending on the different dye added, but it can be observed that some show a larger temperature range for the smectic A phase, with the addition of the dye. Although this may be due to stabilisation of the liquid crystal phase, this was not observed from an increase in the smectic A temperature range in the POM results, so may occur as a result of greater supercooling of the phase in these measurements.

Using the DFT length measurements of the host molecules, an assessment of the structure of the phase can be made based on how the layer spacing is related to the all-*trans* molecular length. The result of this calculation is plotted against reduced temperature in Figure 4.58 and shows similar trends to the respective host alone d/l values. This shows that the overall trends of increasing d/l values with decreasing temperature are consistent with the respective host alone samples and the addition of the dye has not changed the packing of the host.

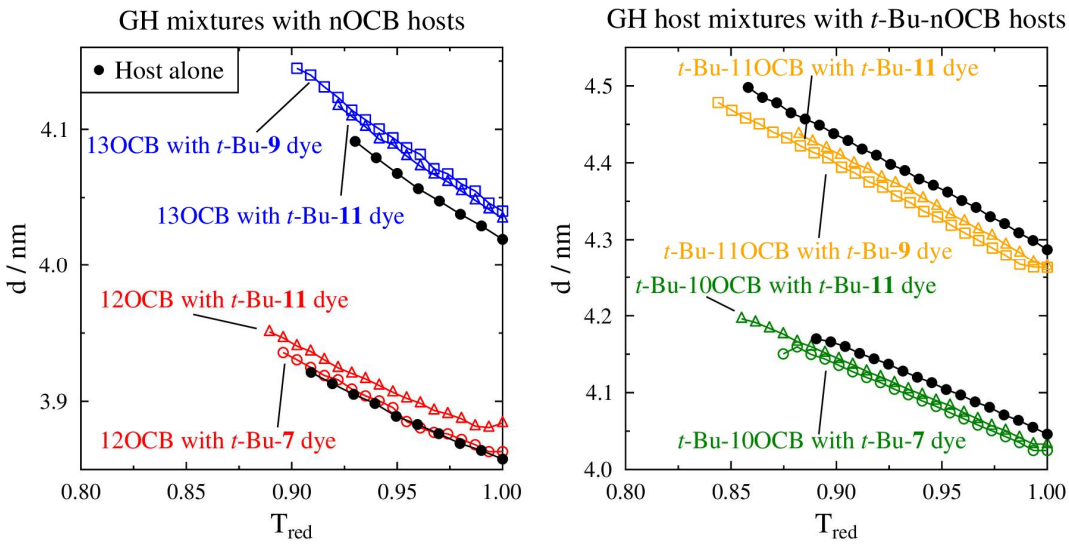

Figure 4.57: Comparison plots for the layer spacing values with reduced temperature, for the guest-host mixtures with different dyes, and the host alone values shown in black. The layer spacing scales are expanded to show both guest-host mixtures for each host (labelled).

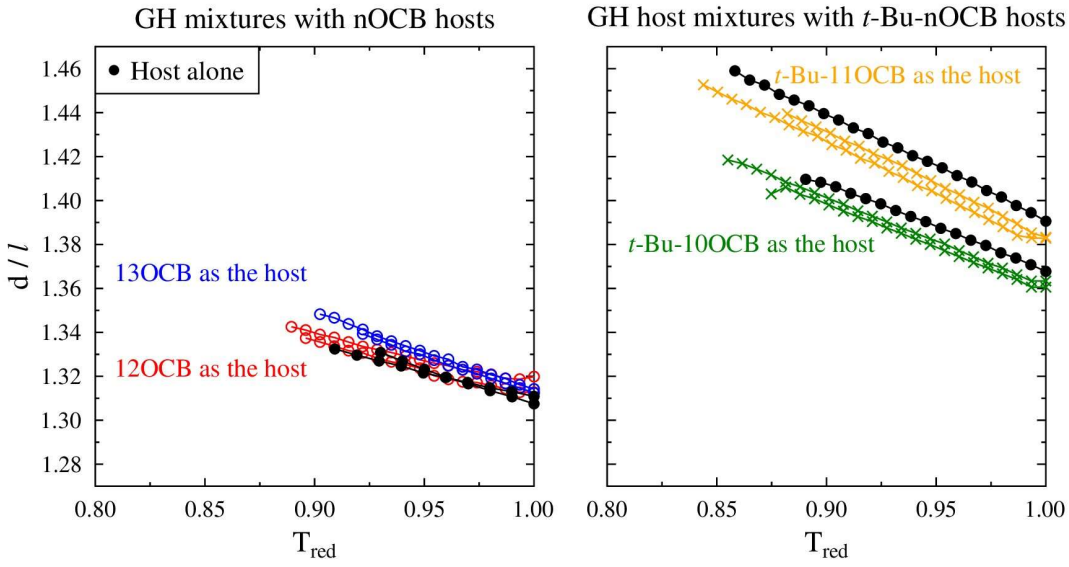

Figure 4.58: Comparison plots for the layer spacing divided by the DFT length of the molecules with reduced temperature for the guest-host mixtures with different dyes, and the host alone values shown in black.

The wide angle values from XRD can give some information about the distance between the molecules in the smectic A and nematic phases, which will relate to the distances between the cyanobiphenyl groups of the molecules. The distances for all of the guest-host mixtures are shown in Figure 4.59, with the highest and lowest values recorded and plotted against the temperature. Generally the temperature dependent change in the distance was observed to be similar to the host alone samples, with a decrease in the distance with decreasing temperature. It can be seen that the guest-host mixtures with nOCB hosts show a similar distance between adjacent molecules to the respective host alone values, although the guest-host mixtures for 13OCB have a slightly lower distance between the adjacent molecules than 13OCB alone. All the guest-host mixtures with *t*-Bu-nOCB hosts have a smaller distance between adjacent molecules than was determined for the host alone sample. This reduction in the distance may be due to a change in the packing of the molecules within the diffuse layers, and that the addition of the dye may be causing the host molecules to pack closer together. Overall, the XRD results showed smaller layer spacing and closer lateral spacing for the guest-host mixtures with the *t*-Bu-nOCB hosts, which could suggest that the addition of the dyes is causing the host molecules to pack closer together laterally.

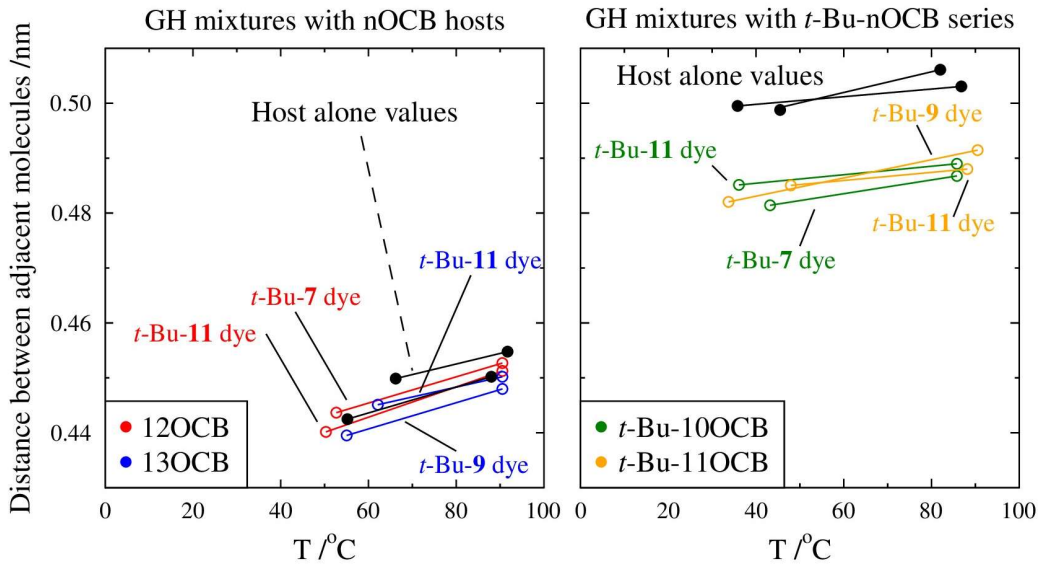

Figure 4.59: Comparison plots for the distance between adjacent molecules with temperature for the guest-host mixtures with different dyes, and the host alone values shown in black.

The layer spacing from the XRD was then compared to the simulated layer spacing determined from the MD simulations, at $T_{red} = 0.95$ for the XRD and at the same temperature as the host alone simulations for the guest-host simulations, as shown in Figure 4.60. This data was also compared to the host alone data from XRD and the MD simulations, and shows that the simulated values are all larger than the than the experimental values, which follows the trend that was observed for the host alone samples. Generally, the value obtained by the MD simulations are similar to those obtained through XRD measurements, but there does seem to be less variation in the layer spacing with the different dyes in the XRD experiments than in the simulation. This may suggest that the simulations are overestimating the layer spacing within the guest-host simulations and possibly exaggerating the impact of the different chain lengths dye with respect to the experimental variation.

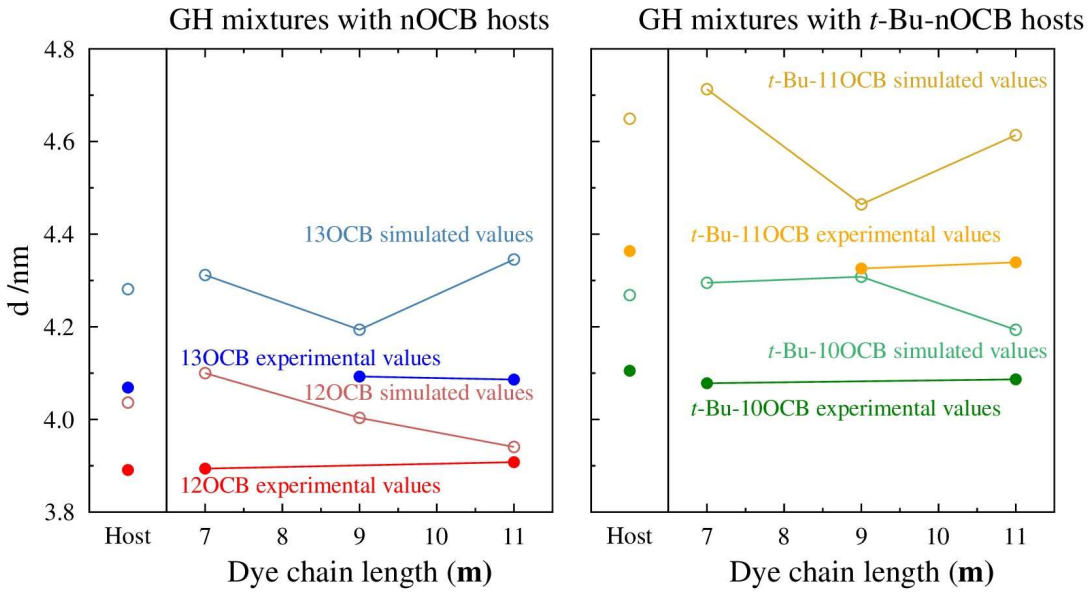

Figure 4.60: Comparison of layer spacing of the guest-host mixtures to the host alone samples, in both the experimental XRD studies (filled symbols) and the values from the MD simulations (open symbols).

4.4.5 UV-visible absorption results

4.4.5.1 Cell tests and home-built cells

The main outcome of the commercial cell tests was that the cell which contained 8OCB as host was able to align more readily as this liquid crystal host had a nematic phase and smectic A phase, so on cooling the first transition was to the nematic phase which aligned well with the polyimide alignment layer. As the phase was cooled into the smectic A phase, this alignment was preserved. In the case of the *t*-Bu-nOCB host, there was no nematic phase present so the alignment of the phase within the cell was not achieved. The tests with commercial cells with a path length of ≤ 5 μm showed that as the cell became thinner, there was easier alignment of the phase, which may be due to a reduction in the bulk sample within the centre of the cell and an increase in the proportion of the sample interacting with the alignment layer. Although using the 3.2 μm cell resulted in better alignment of the smectic A phase, this could have led to the further issue of low absorbance in the UV-visible measurements due to the small path length.

The issue with the first method of making the home-built cells was that the nylon-6,6 was difficult to dissolve in the *m*-cresol/methanol mixture. This method, reported by Patel et al., used nylon-6,9 as the polymer and did achieve good alignment of the liquid crystals being studied.[121] This may suggest that the nylon-6,9 dissolved better in the mixture of *m*-cresol/methanol. As a result of this difficulty in the dissolution, there may have been uneven deposition of the nylon-6,6 during spin-coating, resulting in a variability in the thickness of the alignment layer. In Figure 4.29, it can be observed that there is good alignment of the smectic A phase in certain areas but there is also characteristic smectic A defect texture and domain wall defects. By changing the solvent, the unaligned domain formation was reduced leading to the better aligned cells that were observed by POM, as shown in Figure 4.30. Overall, the method change led to well aligned cells and also showed how important the method of cell production is for ensuring good alignment of the liquid crystal hosts within the cell.

4.4.5.2 UV-visible results

The dichroic ratio (DR) values all show broadly similar values between the different guest-host mixtures, except from the higher dichroic ratio values seen for the *t*-Bu-11OCB and *t*-Bu-**9** dye mixture. The dichroic ratios of 7-13 for the guest-host mixtures are in the region of the values predicted by Osman et al.,[186] which was for anthraquinone dyes with a small β angle between the alignment axis and the transition dipole moment. Sims et al. also reported a dichroic ratio of 9.40 for 26B3OH dye, shown in the experimental chapter, which has a similar structure to the **m** and *t*-Bu-**m** dyes, in a nematic host (E7).[90] The dichroic ratio for the guest-host mixture with *t*-Bu-11OCB and *t*-Bu-**9** dye is much higher, which could be attributed to better alignment of the liquid crystal host within the cell.

The dichroic ratio for each guest-host mixture can be used to determine the experimental orientational order parameter of the dye in each run of the samples, with temperature. This is calculated using equation 44, using the absorbance parallel and perpendicular ($A_{\parallel}$ and $A_{\perp}$) or using the dichroic ratio (DR) values.[90]

Equation 4.4
$$S = \frac{A_{\parallel} - A_{\perp}}{A_{\parallel} + 2A_{\perp}} = \frac{DR - 1}{DR + 2}$$

The values calculated for each of the guest-host mixtures for each of the runs are given in Table 4.29 and Table 4.30 for the guest-host mixtures with 12OCB and 13OCB as the hosts respectively, and in Table 4.30 and Table 4.31 for the guest-host mixtures with *t*-Bu-10OCB and *t*-Bu-11OCB as the hosts, respectively. The temperature-dependent orientational order parameter is plotted in Figure 4.61, calculated over the range 475-525 nm from the dichroic ratio data.

The guest-host mixtures with 12OCB and 13OCB show dichroic ratios in the range of 6.84-13.69 and 7.08-11.75, respectively, and dye orientational order parameters in the range of 0.66-0.81 and 0.67-0.78, respectively. These values are similar to those reported previously by Sims et al. for a variety of dyes in a nematic liquid crystal host, in particular for 26B3OH which had a dichroic ratio of 9.40 and an orientational order parameter of 0.68.[90] For some of the guest-host mixtures the dichroic ratios were larger, but overall the average of these values across the whole temperature range is of a similar magnitude to the previously

reported mixtures. The *t*-Bu-10OCB guest-host mixtures show a dichroic ratio in the range of 6.55-11.28 and a dye orientational order parameter in the range of 0.65-0.83. Again, this is similar in magnitude to the previously reported guest-host mixtures.[90]

The guest-host mixtures with *t*-Bu-11OCB and *t*-Bu-**9** dye showed the largest dye orientational order parameters for the first three runs, but this was not reproduced for the new cells and mixture used in cell A-C. This observation of a dichroic ratio of 21-27 at the lowest temperature and the respective orientational order parameter of 0.87-0.90 suggests that this combination of guest-host was highly ordered and gave very strong contrast between the coloured and clear state. These values are much higher than those reported previously by Sims et al. for a variety of dyes in a nematic liquid crystal host, in particular for 26B3OH which had a dichroic ratio of 9.40 and an orientational order parameter of 0.68.[90] For practical applications, an orientational order parameter of ≥ 0.75 is required,[157] but having a larger one is preferable, which would make this particular guest-host mixture suitable for these applications. Another factor which may have led to these particularly high values could be the cell used, as this cell may have had the optimal alignment layer thickness and rubbing to align this sample particularly well within the cell. The POM photomicrograph of the *t*-Bu-11OCB with *t*-Bu-**9** dye cell show a very planar texture, with only a small presence of domain walls. The other cells show more of these domain walls so this may be a visual indication of this better alignment within the cell. The cell variability may also account for the lower dichroic ratio and orientational order parameter values obtained when the same mixture was added to a different cell (cell A), as there was some variation within the different cells built. This may indicate that if a more consistent method of cell building was used, such as having the cells built commercially to an appropriate design or using a rubbing machine to get consistent alignment, then these guest-host mixtures may consistently show higher dichroic ratios and differences between the guest-host mixtures with each dye may be more apparent.

Table 4.29: Average orientational order parameter (S) calculated from UV-visible measurements, over 475-525 nm for the guest-host mixtures with 12OCB as the host.

Guest-host mixture	12OCB with *t*-Bu-**7** dye			12OCB with *t*-Bu-**11** dye		
	Orientational order parameter (S) at λ = 475-525 nm					
T /°C	Run 1	Run 2	Run 3	Run 1	Run 2	Run 3
65	0.81	0.79	0.80	0.75	0.81	0.76
70	0.80	0.78	0.79	0.75	0.80	0.75
75	0.79	0.77	0.77	0.74	0.80	0.73
80	0.78	0.76	0.76	0.73	0.79	0.73
85	0.76	0.74	0.75	0.72	0.77	0.72
90	0.75	0.77	0.77	0.66	0.74	0.71

Table 4.30: Average orientational order parameter (S) calculated from UV-visible measurements, over 475-525 nm for the guest-host mixtures with 13OCB as the host.

Guest-host mixture	13OCB with *t*-Bu-**9** dye			13OCB with *t*-Bu-**11** dye		
	Orientational order parameter (S) at λ = 475-525 nm					
T /°C	Run 1	Run 2	Run 3	Run 1	Run 2	Run 3
70	0.71	0.74	0.76	0.50	0.78	0.74
75	0.70	0.73	0.75	0.57	0.77	0.73
80	0.69	0.72	0.74	0.57	0.77	0.73
85	0.68	0.71	0.74	0.56	0.76	0.72
90	0.67	0.70	0.73	0.56	0.75	0.71

Table 4.31: Average orientational order parameter (S) calculated from UV-visible measurements, over 475-525 nm for the guest-host mixtures with *t*-Bu-10OCB as the host.

Guest-host mixture	*t*-Bu-10OCB with *t*-Bu-7 dye		*t*-Bu-10OCB with *t*-Bu-11 dye	
	Orientational order parameter (S) at λ = 475-525 nm			
T /°C	Run 1	Run 2	Run 1	Run 2
35			0.77	0.73
40	0.74	0.83	0.74	0.73
45	0.73	0.71	0.74	0.72
50	0.72	0.71	0.73	0.72
55	0.72	0.70	0.73	0.72
60	0.71	0.69	0.72	0.71
65	0.70	0.68	0.71	0.71
70	0.68	0.67	0.71	0.70
75	0.67	0.66	0.70	0.70
80	0.65	0.65	0.70	0.69

Table 4.32: Average orientational order parameter (S) calculated from UV-visible measurements, over 475-525 nm for the guest-host mixtures with *t*-Bu-11OCB as the host.

Guest-host mixture	*t*-Bu-11OCB with *t*-Bu-**9** dye			*t*-Bu-11OCB with *t*-Bu-**11** dye	
	Orientational order parameter (S) at λ = 475-525 nm				
T /°C	Run 1	Run 2	Run 3	Run 1	Run 2
40	0.89	0.90	0.87	0.69	0.71
45	0.88	0.90	0.87	0.68	0.71
50	0.87	0.89	0.86	0.68	0.70
55	0.86	0.88	0.85	0.68	0.70
60	0.85	0.88	0.84	0.68	0.69
65	0.83	0.87	0.84	0.68	0.69
70	0.82	0.87	0.82	0.68	0.68
75	0.81	0.86	0.82	0.67	0.67
80	0.80	0.85	0.81	0.67	0.67
85	0.79	0.84	0.79	0.66	0.66

Table 4.33: Additional average calculated dichroic ratio determined from UV-visible measurements, over 475-525 nm for the guest-host mixtures with *t*-Bu-11OCB as the host in cell A, B and C.

Guest-host mixture	*t*-Bu-11OCB with *t*-Bu-**9** dye		
	Dichroic ratio at λ = 475-525 nm		
T /°C	cell A	cell B	cell C
40	0.72	0.79	0.69
45	0.70	0.78	0.69
50		0.77	0.68
55	0.66	0.76	0.67
60	0.64	0.75	0.67
65	0.63	0.75	0.66
70	0.62	0.73	0.66
75	0.60	0.72	0.66
80	0.59	0.70	0.65
85	0.58	0.69	0.64

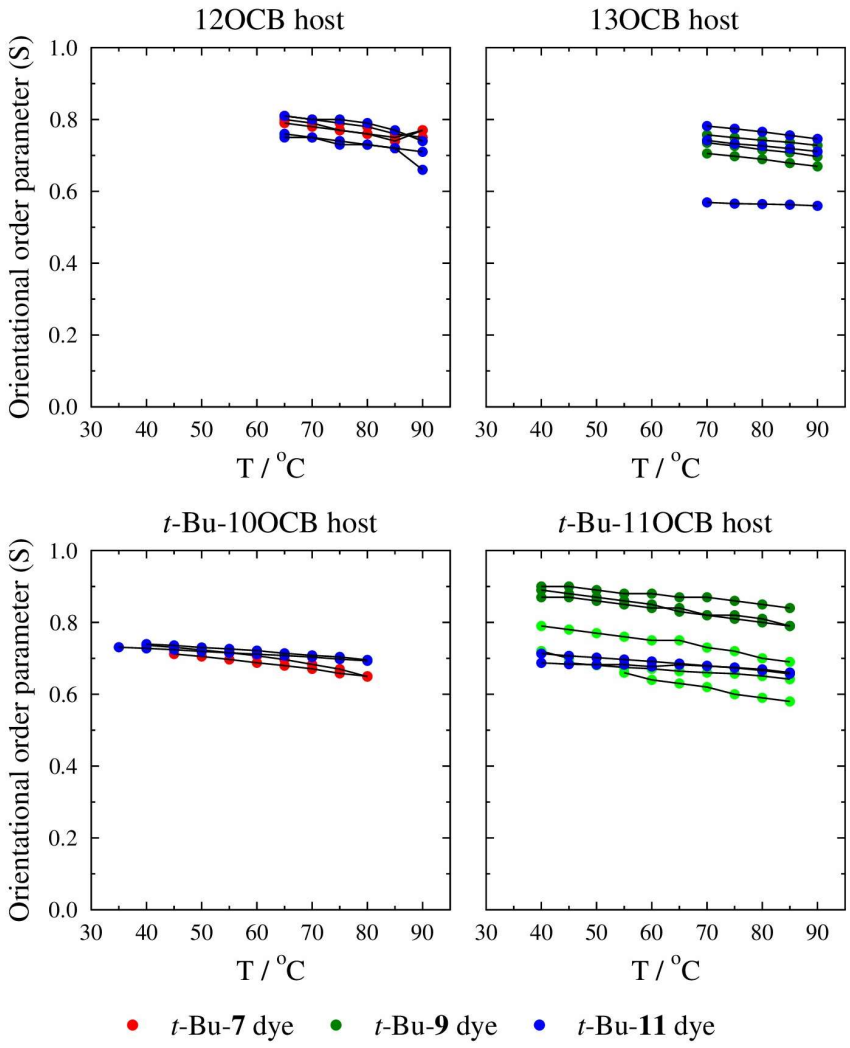

Figure 4.61: Dye orientational order parameter with temperature for guest-host mixtures with *t*-Bu-10OCB and *t*-Bu-11OCB as the hosts. The 3 extra repeats for *t*-Bu-11OCB with *t*-Bu-**9** dye are plotted in lighter green symbols.

The dye orientational order parameters determined through the UV-visible studies could then be compared to the dye and host orientational order parameters determined through the MD simulations, with all the data taken at the respective temperatures that give $T_{red} = 0.95$ in the host alone simulations, as shown in Figure 4.62. In this plot the dye orientational order parameter is compared to the experimentally determined orientational order parameter, with the host alone orientational order parameter included as comparator. The dye orientational order parameters from the simulations show higher values than the experimental orientational values, and the trends with dye chain length for the experimental results do not show a clear match between the experimental and simulation results.

For the guest-host mixtures with 12OCB as the host, the mixture with *t*-Bu-**7** dye shows a good match of the experimental orientational order parameters with the simulated values, and with *t*-Bu-**11** dye the dye orientational order parameter is lower than predicted by the simulations. For the guest-host mixtures with 13OCB as the host, both mixtures with the dyes showed lower dye orientational order parameters than predicted by the simulations. The experimental dye orientational order parameter values are similar for all the guest-host mixtures with nOCB hosts, so there is no clear trends observed with the dye chain length as seen in the simulations. It could be suggested that the effect of changing chain length may be more subtle then the simulations are showing, and so it is less obvious from the UV-visible measurements. Also, any cell alignment issues would affect the dichroic ratio and the experimental orientational order parameter calculated.

The guest-host mixtures with *t*-Bu-10OCB host show much lower experimental orientational order parameters than the simulated values, but the values show good reproducibility over the different runs. For the guest-host mixtures with *t*-Bu-11OCB as the host, the experimental orientational order parameter for the mixture with *t*-Bu-**11** dye is much lower than the simulated value. As mentioned previously, the dye orientational order parameters for the mixture with *t*-Bu-**9** dye show a large range of values with one of them matching the simulation value. This may suggest that when the sample is well aligned within the cell that it would be possible to get similar values to the high simulated orientational order parameters. Any errors in the measurements or alignment of the sample within the other cells may lead to the differences between the experimental and simulated orientational order parameters.

Overall, there is not a strong match between the dye orientational order parameters predicted from the MD simulations and those from the UV-visible measurements, although there are a few experimental limitations which may have reduced the values obtained in the experiment. Also, there are no clear trends in the dye orientational order parameters with different dye chain lengths, determined from the UV-visible measurements. Further studies with more consistent cells could lead to the results of the experiment being a better match with the simulated values and the trends simulated for the different guest-host mixtures with dye chain length.

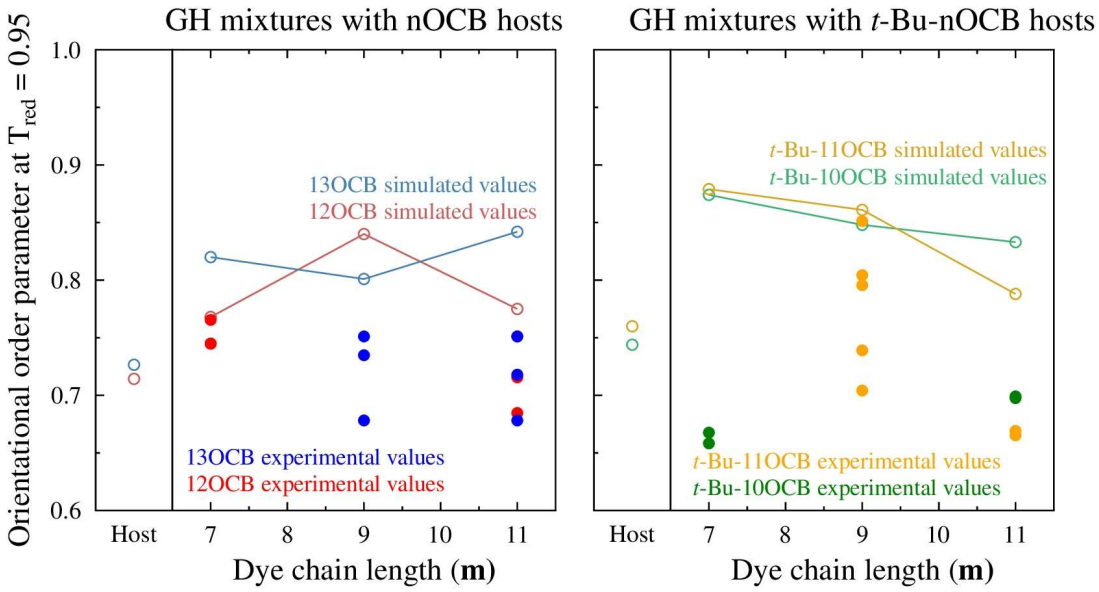

Figure 4.62: Comparison plots of dye orientational order parameter (S) for different dye chain lengths (**m**), with the simulated values taken from MD simulations of the guest-host mixtures and the host orientational order parameter from the host alone simulations, all the respective temperatures which correspond to $T_{red} = 0.95$.

4.5 Conclusions

The guest-host molecular dynamics simulations in combination with DFT studies of the dyes have provided insight into the order parameters and layer spacings of the guest-host mixtures, and allowed the selection of guest dyes and liquid crystal hosts to test. The TD-DFT calculations showed that the angle between the molecular long axis of the dye and the transition dipole moment were very close, meaning that this proxy was suitable to use for in the molecular dynamics simulations. Within the molecular dynamics simulations, the host orientational and translational order parameters in the guest-host mixtures showed similar values to those observed for the host alone samples, with the exception of the longest dye chain lengths, which had lower values. This observation may indicate that at the lengths the dyes are disrupting the packing of the host, resulting in less well aligned host molecules. The elongated chains may also disrupt the diffuse layers, and so reduce the translational order parameter in these simulations.

In terms of the experimental studies, the clearing point temperatures followed the predicted values, and showed similar values within guest-host mixtures with the same hosts. Overall the addition of the dye has only a small effect on the transition enthalpies and entropies, which can be explained by the small amount of dye in each mixture. The XRD results showed smaller layer spacing and closer lateral spacing in the guest-host mixtures than the host alone samples, which could suggest the dyes are affecting the host structure. For the UV-visible absorption spectroscopy, generally the cells were well aligned and gave good values of dichroic ratio and values of dye orientational order parameter which would be suitable for practical applications. It is important to note that although the cells did work to align the samples there were not consistent results for each run, and these results might be improved through the use of commercial cells with an appropriate nylon alignment layer and path length. The mixture of *t*-Bu-11OCB and *t*-Bu-**9** dye showed the highest dichroic ratio and dye orientational order, and would be well suited to applications.

Chapter 5

Conclusions and further work

Overall, the methods and samples used in this study have provided insight into many properties related to the use of a bulky terminal group in the design of both liquid crystal and dye molecules to promote the formation of a smectic A phase. For the host alone samples, the combination of experimental and computational studies have shown the ability of the simulations to predict experimental properties and given greater insight into the phases observed. Being able to use the MD simulations predictively gave the opportunity to study a wide range of guest-host mixtures computationally, which was able to inform the experimental aspect of the guest-host work. For the guest-host samples, the UV-vis absorption measurements had well aligned samples, with high values of dichroic ratio which would be suitable for practical applications. The mixture of *t*-Bu-11OCB and *t*-Bu-**9** dye showed the highest dichroic ratio and dye orientational order, but the results from multiple runs were not fully consistent, and could probably be improved through the use of commercial cells with an appropriate nylon alignment layer and path length.

5.1 Liquid crystal hosts

From the experimental studies, there are some clear differences observed in the behaviour of the nOCB series and the *t*-Bu-nOCB series. At the shortest chain lengths, the *t*-Bu-nOCB series shows a suppression of the nematic phase that was observed for the nOCB series, which suggests that the terminal *t*-Bu group is enhancing the nanophase segregation. The *t*-Bu terminal group is also observed to lead to a more pronounced odd-even effect in the clearing point transition temperatures. These observations showed that experimentally the terminal *t*-Bu group is having a clear impact on the phases formed by these host molecules. The DSC results give an insight into the phase transitions, showing that the clearing point transition entropy is higher for the *t*-Bu-nOCB series at all comparable chain lengths, relative to the respective nOCB series. This may indicate that the smectic A phase of the *t*-Bu-nOCB series is less liquid-like than the smectic A phase of the nOCB series, which may suggest that a more ordered smectic A phase is formed when the terminal *t*-Bu group is present. The XRD results showed larger layer spacings and distances between adjacent molecules for the *t*-Bu-nOCB series than the nOCB series. The XRD provided valuable information on the smectic A phase structure, which was not determined by other standard liquid crystal

characterisation methods. This information allowed further understanding of the differences between the smectic A phases of the nOCB series and *t*-Bu-nOCB series.

From the computational studies, the MD simulation work illustrates similar trends to those observed by the experimental work. In particular there is higher orientational and translational order observed in the MD simulations for the longer chain liquid crystal hosts, such as *t*-Bu-10OCB and *t*-Bu-11OCB, than the shorter chain liquid crystal hosts. The order parameters of the *t*-Bu-nOCB series are generally higher than those of the nOCB series, showing that generally the *t*-Bu-nOCB series are hosts which form more ordered smectic A phases and have a more defined layered structure, as a result of the addition of the bulky *t*-Bu terminal group to the chain. It is also observed that the addition of the *t*-Bu terminal group results in lower interdigitation of the alkoxy chain tail groups of the molecules, leading to the layer spacings being larger in the simulations of the *t*-Bu-nOCB series than in the nOCB series. The DFT studies gave a good understanding of the lengths of the molecules, which allowed trends in molecular shape to be considered. This technique was effective for getting a general idea of the dimensions of the molecules, but this method did not take into account the possible conformations of the alkoxy chains of the host and guest dyes. Further studies of these phases could probe the different conformations from the MD simulations, and optimise these strucutres using DFT to understand the apsect ratios, calculated from the lengths and widths of the molecules, favoured by the molecules in the phase in the MD simulations.

Overall, the simulations were shown to be a good model for the trends observed for the two series, and in particular the layer spacing measured by XRD was closely matched by the value determined from simulations. The simulations were able to provide insight into the properties of both the nOCB and the *t*-Bu-nOCB series and could suggest that this type of simulation can be used for predictively and aid in the understanding of the effects of molecular design.

5.2 Guest-host systems

The computational studies of the guest-host mixtures allowed a large range of guest-host mixtures to be studied, alongside providing insight into the order parameters and simulated layer spacing for these mixtures. The order parameters and layer spacings were observed to be similar to the host alone values in most cases, with some lower order parameters observed for the longest chain dyes with the *t*-Bu-nOCB hosts. This observation showed that the longest dye lengths may disrupt the packing of the hosts and may disrupt the layers, which would reduce the translational order. The TD-DFT calculations showed that the angle between the transition dipole moment and the molecular long axis of the dye was small for all the dyes in this study and the DFT showed that all the dyes had long, thin structures making them well suited to this guest-host application. Again, one limitation of the computational studies was the lack of conformational information from the DFT studies and MD simulations, which would give a greater understanding of the effect of the bulky terminal group on the conformation and distribution of the alkoxy chains of the dye within the MD simulations and also the effect this has on the aspect ratios observed when the dye is a guest in the liquid crystal host.

From the experimental studies for the guest-host mixtures, the UV-visible absorption measurements show generally well aligned samples which gave high dichroic ratio and dye orientational order parameter values, which were suitable values for device applications. The mixture of *t*-Bu-11OCB and *t*-Bu-**9** dye showed the highest dichroic ratio and dye orientational order, but this was not observed in all the runs. To validate this result, commercial cells could be used, with an appropriate nylon alignment layer and path length, as the cells would be consistent in their alignment and any difference between the guest-host mixtures would be easier to observe. The other experimental studies showed only a small change in enthalpies and entropies relative to the host alone samples, and no change in the phases exhibited by the liquid crystal phases of the host as a result of the small wt% of the dye added to the guest-host mixtures. The XRD results showed a decrease in the layer spacing and smaller lateral distance for the guest-host mixtures than for the host alone. This suggests that there were changes to the structure of the host phase upon the addition of the dye.

Overall, the UV-visible absorption measurements relied on the development of consistent alignment cells with a suitable alignment layer which was specific to the liquid crystal hosts studied in this report. After determining the suitable cell type, the cells were home-built to the best standard possible but there were still found to be inconsistencies in the alignment of the samples and consistency between different runs of each sample. As a result, this technique may require further work to improve the reproducibility of these results and reduce the uncertainties encountered.

Chapter 6
Appendix

6.1 Synthesis and purity data

The *t*-Bu-nOCB host liquid crystal series were prepared by Marc Holmes under the supervision of Stephen Cowling as part of a MChem research project. The compounds were purified by column chromatography on silica (DCM as eluent) and then recrystallised twice from ethanol. The tBu dyes were prepared by Charles Biddlecombe under the supervision of Stephen Cowling as part of a BSc research project. The compounds were isolated by preparative chromatography (Hexane:DCM gradient Hexane to 1:2 mixture) and recrystallised from Hexane:Toluene (4:1).

4'-((7,7-Dimethyloctyl)oxy)-[1,1'-biphenyl]-4-carbonitrile – *t*-Bu-6OCB

^{1}H NMR (400 MHz, Chloroform-d) δ 7.69 (d, J = 8.5 Hz, 2H), 7.64 (d, J = 8.5 Hz, 2H), 7.53 (d, J = 8.5 Hz, 2H), 6.99 (d, J = 8.5 Hz, 2H), 4.01 (t, 2H), 1.79 (quint, 2H), 1.53 – 1.44 (m, 2H), 1.40 – 1.13 (m, 6H), 0.87 (s, 9H).

MS (APCI$^+$, m/z): 336.2320 ($C_{23}H_{30}NO$ M+H)

4'-((8,8-Dimethylnonyl)oxy)-[1,1'-biphenyl]-4-carbonitrile – *t*-Bu-7OCB

^{1}H NMR (400 MHz, Chloroform-d) δ 7.67 (d, J = 8.5 Hz, 2H), 7.62 (d, J = 8.5 Hz, 2H), 7.51 (d, J = 8.5 Hz, 2H), 6.97 (d, J = 8.5 Hz, 2H), 3.99 (t, 2H), 1.79 (quint, 2H), 1.51 – 1.11 (m, 10H), 0.85 (s, 9H).

MS (APCI$^+$, m/z): 350.2491 ($C_{24}H_{32}NO$ M+H)

4'-((9,9-Dimethyldecyl)oxy)-[1,1'-biphenyl]-4-carbonitrile – *t*-Bu-8OCB

^{1}H NMR (400 MHz, Chloroform-d) δ 7.69 (d, J = 8.5 Hz, 2H), 7.64 (d, J = 8.5 Hz, 2H), 7.53 (d, J = 8.5 Hz, 2H), 6.99 (d, J = 8.5 Hz, 2H), 4.01 (t, 2H), 1.79 (quint, 2H), 1.53 – 1.11 (m, 12H), 0.86 (s, 9H).

MS (APCI$^+$, m/z): 364.2649 ($C_{25}H_{34}NO$ M+H)

4'-((10,10-Dimethylundecyl)oxy)-[1,1'-biphenyl]-4-carbonitrile – *t*-Bu-9OCB

^{1}H NMR (400 MHz, Chloroform-d) δ 7.67 (d, J = 8.5 Hz, 2H), 7.62 (d, J = 8.5 Hz, 2H), 7.51 (d, J = 8.5 Hz, 2H), 6.97 (d, J = 8.5 Hz, 2H), 3.99 (t, 2H), 1.78 (quint, 2H), 1.49 – 1.41 (m, 2H), 1.39 – 1.09 (m, 12H), 0.86 (s, 9H)

MS (APCI$^+$, m/z): 378.2806 ($C_{26}H_{35}NO$ M+H)

4'-((11,11-Dimethyldodecyl)oxy)-[1,1'-biphenyl]-4-carbonitrile – *t*-Bu-10OCB

^{1}H NMR (400 MHz, Chloroform-d) δ 7.69 (d, *J* = 8.5 Hz, 2H), 7.64 (d, *J* = 8.5 Hz, 2H), 7.53 (d, *J* = 8.5 Hz, 2H), 6.99 (d, *J* = 8.5 Hz, 2H), 4.00 (t, 2H), 1.79 (quint, 2H), 1.52 – 1.10 (m, 16H), 0.86 (s, 9H).

MS (APCI$^+$, m/z): 392.2967 ($C_{27}H_{38}NO$ M+H)

4'-((12,12-Dimethyltridecyl)oxy)-[1,1'-biphenyl]-4-carbonitrile – *t*-Bu-11OCB

^{1}H NMR (400 MHz, Chloroform-*d*) δ 7.69 (d, *J* = 8.5 Hz, 2H), 7.64 (d, *J* = 8.5 Hz, 2H), 7.53 (d, *J* = 8.5 Hz, 2H), 6.99 (d, *J* = 8.5 Hz, 2H), 4.00 (t, 2H), 1.79 (quint, 2H), 1.50 – 1.10 (m, 18H), 0.86 (s, 9H).

MS (APCI$^+$, m/z): 406.3121 ($C_{28}H_{40}NO$ M+H)

2,6-bis(4-((8,8-dimethylnonyl)oxy)phenyl)-1,5-dihydroxyanthraquinone – *t*-Bu-7 dye

^{1}H NMR (400 MHz, Chloroform-*d*) δ 7.92 (d**,** *J* = 7.8 Hz, 2H), 7.73 (d, *J* = 7.8 Hz, 2H), 7.64 (d, 4H), 7.00 (d, 4H), 4.02 (t, 4H), 1.80-1.70 (m, 4H) 1.50-1.10 (m, 20H), 0.86 (s, 18H). OH not observed.

MS (APCI$^+$, m/z): 733.4463 ($C_{48}H_{60}O_6$ M+H)

2,6-bis(4-((10,10-dimethylundecyl)oxy)phenyl)-1,5-dihydroxyanthraquinone – *t*-Bu-9 dye

^{1}H NMR (400 MHz, Chloroform-*d*) δ 7.92 (d, *J* = 7.8 Hz, 2H), 7.73 (d, *J* = 7.8 Hz, 2H), 7.64 (d, 4H), 7.00 (d, 4H), 4.01 (t, 4H), 1.87 – 1.77 (m, 4H), 1.50-1.10 (m, 28H), 0.85 (s, 18H). OH not observed.

MS (APCI$^+$, m/z): 789.5076 ($C_{52}H_{68}O_6$ M+H)

2,6-bis(4-((12,12-dimethyltridecyl)oxy)phenyl)-1,5-dihydroxyanthraquinone – *t*-Bu-11 dye

^{1}H NMR (400 MHz, Chloroform-*d*) δ 7.92 (d, *J* = 7.8 Hz, 2H), 7.74 (d, *J* = 7.8 Hz, 2H), 7.64 (d, 4H), 7.00 (d, 4H), 4.01 (t, 4H), 1.87-1.77 (m, 4H), 1.50-1.10 (m, 36H), 0.85 (s, 18H). OH not observed.

MS (APCI$^+$, m/z): 845.5688 ($C_{56}H_{76}O_6$ M+H)

6.2 UV-visible absorption data

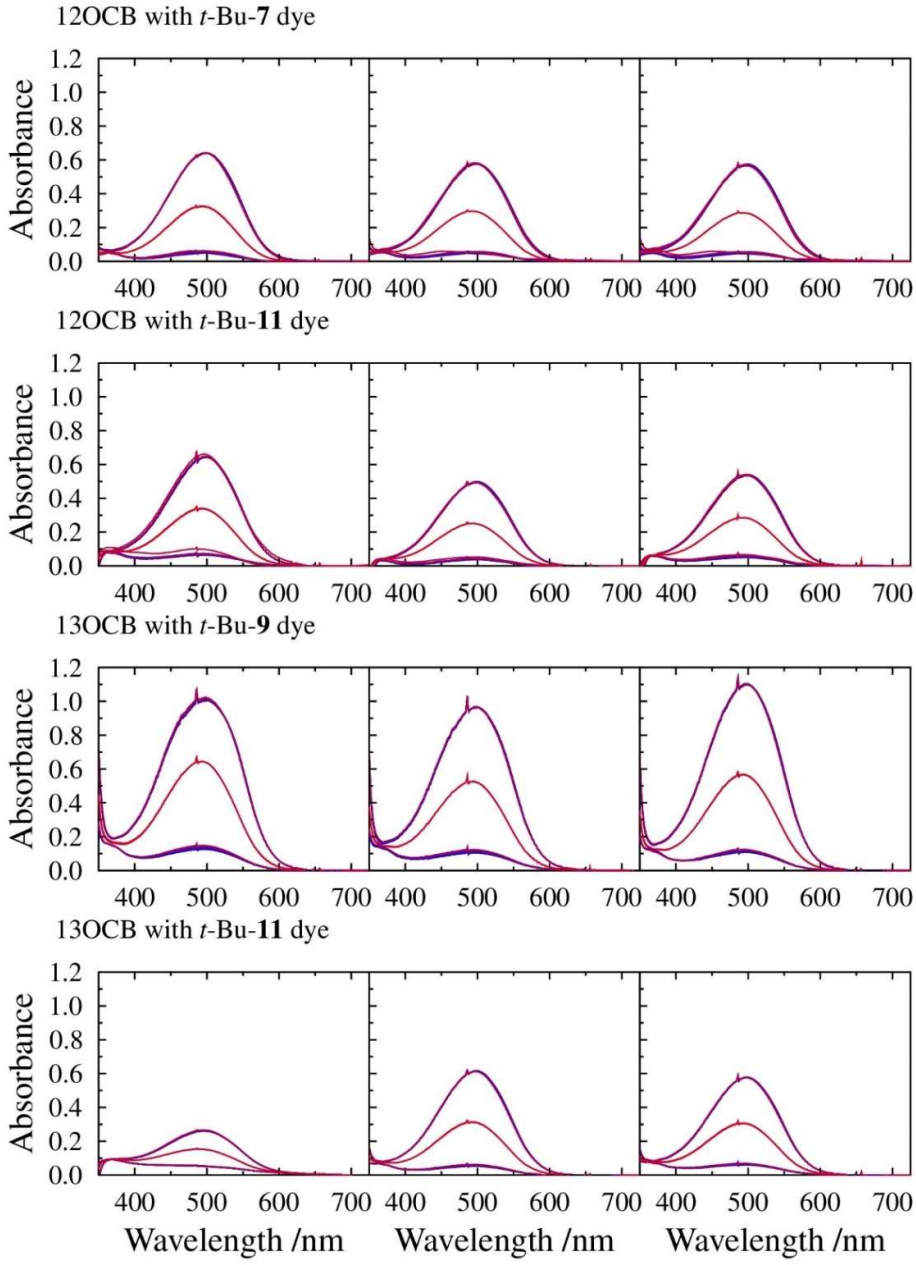

Figure 6.1: Polarised UV-vis spectra for all the runs with the guest-host mixtures using12OCB and 13OCB as the hosts, showing the parallel and perpendicular absorbance with decreasing temperature, from red to blue.

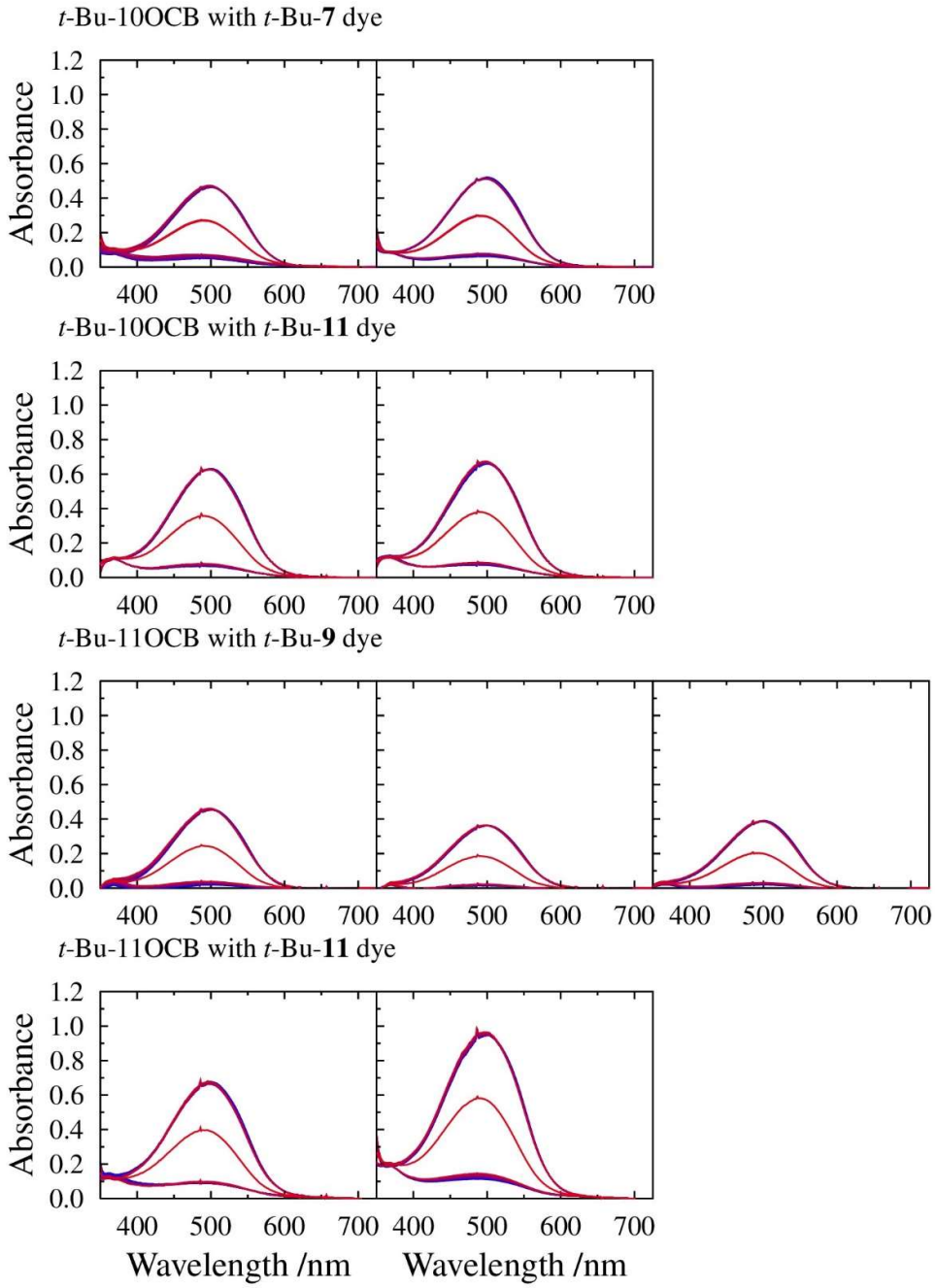

Figure 6.2: Polarised UV-vis spectra for all the runs with the guest-host mixtures using *t*-Bu-10OCB and *t*-Bu-11OCB as the hosts, showing the parallel and perpendicular absorbance with decreasing temperature, from red to blue.

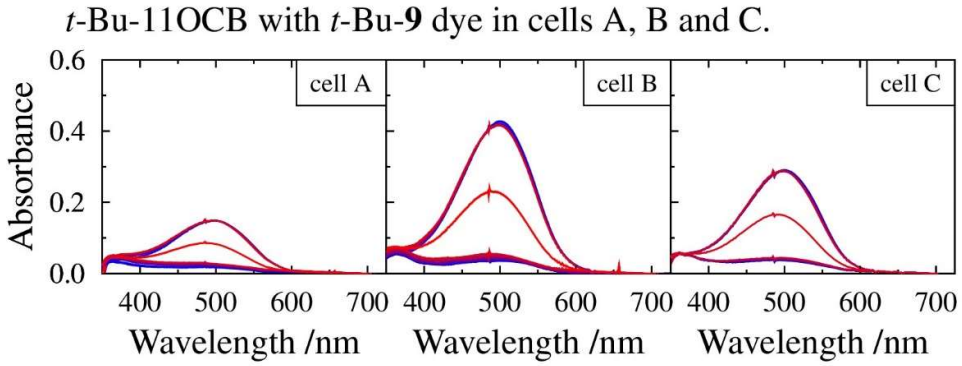

Figure 6.3: Polarised UV-vis spectra for the extra runs with the guest-host mixtures using *t*-Bu-**9** dye as the guest and *t*-Bu-11OCB as the hosts, showing the parallel and perpendicular absorbance with decreasing temperature, from red to blue.

6.3 Abbreviations

β	Angle between the transition dipole moment and the molecular long axis
COM	Centre of mass
Cr	Crystal
DFT	Density functional theory
DR	Dichroic ratio
DSC	Differential scanning calorimetry
HOMO	Highest occupied molecular orbital
Iso	Isotropic liquid
k	Layer normal vector
LUMO	Lowest unoccupied molecular orbital
m dye	26B(**m**)OH anthraquinone dye
MOI	Moment of inertia
N	Nematic
$\hat{n}$	Liquid crystal director
nOCB	n-alkoxycyanobiphenyl
POM	Polarised optical microscopy
S/S_θ	Orientational order parameter of the molecular long axis against the director
SmA	Smectic A
SmC	Smectic C
S_β	Orientational order parameter of the TDM against the long axis of the dye
S_φ	Overall orientational order parameter, combining S_θ and S_β
t-Bu-**m** dye	26B(*t*-Bu-**m**)OH anthraquinone dye
t-Bu-nOCB	*t*-Bu terminated n-alkoxycyanobiphenyl
TD-DFT	Time-dependent density functional theory
TDM	Transition dipole moment
T_{red}	Reduced temperature
τ	Translational order parameter
UV	Ultraviolet
vis	Visible
wt%	Weight percentage
XRD	X-ray diffraction
ΔH	Transition enthalpy
ΔS	Transition entropy

Chapter 7
References

1. H. Kawamoto, *Proceedings of the IEEE*, 2002, **90**, 460-500.
2. F. Reinitzer, *Liquid Crystals*, 1989, **5**, 7-18.
3. P. J. Collings and J. W. Goodby, *Introduction to Liquid Crystals : Chemistry and Physics*, CRC Press, Boca Raton, 2nd edn., 2019.
4. S. T. Lagerwall, *Liquid Crystals*, 2013, **40**, 1698-1729.
5. G. A. DiLisi, *An Introduction to Liquid Crystals*, Morgan & Claypool Publishers, USA, 2019.
6. L. Schmidt-Mende, A. Fechtenkötter, K. Müllen, R. H. Friend and J. D. MacKenzie, *Physica E: Low-dimensional Systems and Nanostructures*, 2002, **14**, 263-267.
7. G. Pelzl, I. Wirth and W. Weissflog, *Liquid Crystals*, 2001, **28**, 969-972.
8. J. Stöhr and M. G. Samant, *Journal of Electron Spectroscopy and Related Phenomena*, 1999, **98-99**, 189-207.
9. B. Broughton, in *Handbook of Liquid Crystals*, eds. J. W. Goodby, C. Tschierske, P. Raynes, H. F. Gleeson, T. Kato and P. J. Collings, Wiley-VCH, Weinheim 2nd edn., 2014, vol. 1.3, ch. 2.9 Surface Alignment of Liquid Crystals, pp. 1-22.
10. A. Takeda, S. Kataoka, T. Sasaki, H. Chida, H. Tsuda, K. Ohmuro, T. Sasabayashi, Y. Koike and K. Okamoto, *SID Symposium Digest of Technical Papers*, 1998, **29**, 1077-1080.
11. K. Hanaoka, Y. Nakanishi, Y. Inoue, S. Tanuma, Y. Koike and K. Okamoto, *SID Symposium Digest of Technical Papers*, 2004, **35**, 1200-1203.
12. D. L. White and G. N. Taylor, *Journal of Applied Physics*, 1974, **45**, 4718-4723.
13. F. J. Kahn, G. N. Taylor and H. Schonhorn, *Proceedings of the IEEE*, 1973, **61**, 823-828.
14. M. R. de la Fuente and D. Dunmur, in *Handbook of Liquid Crystals*, eds. J. W. Goodby, C. Tschierske, P. Raynes, H. F. Gleeson, T. Kato and P. J. Collings, Wiley-VCH, Weinheim, 2nd edn., 2014, vol. 1.3, ch. 2.4, pp. 8-14.
15. R. J. Mandle, E. Bevis and J. W. Goodby, in *Handbook of Liquid Crystals*, eds. J. W. Goodby, C. Tschierske, P. Raynes, H. F. Gleeson, T. Kato and P. J. Collings, Wiley-VCH, Weinheim, 2nd edn., 2014, vol. 1.3, ch. 3.1 Phase Structures of Nematic Liquid Crystals, pp. 1-17.
16. J. P. Lagerwall and F. Giesselmann, *ChemPhysChem*, 2006, **7**, 20-45.
17. D. Bauman, H. Moryson and E. Wolarz, *Acta Physica Polonica A*, 1992, **4**, 559-570.
18. G. R. Luckhurst, in *Physical Properties of Liquid Crystals: Nematics -(EMIS Datareviews series; no.25)*, INSPEC, London, 2001, ch. 1.1, pp. 57-61.
19. M. van Gurp, *Colloid and Polymer Science* 1995, **273**, 607-625.
20. D. Demus and L. Richter, *Textures of Liquid Crystals*, Verlag Chemie, Weinheim, 1978.
21. S. Chandrasekhar, *Liquid Crystals*, Cambridge University Press, Cambridge, 1980.
22. S. J. Cowling, personal communication.
23. User:Kebes~commonswiki/WikimediaCommons/CC-BY-SA-3.0, https://commons.wikimedia.org/wiki/File:LiquidCrystal-MesogenOrder-ChiralPhases.jpg, accessed: August 2023).
24. H. T. Srinivasa, *Molecular Crystals and Liquid Crystals*, 2019, **680**, 10-19.
25. M. Yoneya and H. J. C. Berendsen, *Journal of the Physical Society of Japan*, 1994, **63**, 1025-1030.
26. P. J. Collings, *Liquid Crystals: Nature's delicate phase of matter*, Princeton University Press, Princeton/Oxford, 2nd edn., 2002.

27. J. W. Goodby, in *Handbook of Liquid Crystals*, eds. J. W. Goodby, C. Tschierske, P. Raynes, H. F. Gleeson, T. Kato and P. J. Collings, Wiley-VCH, Weinheim, 2014, vol. 1.3, ch. 4.2 Structures and Properties of Smectic Liquid Crystals, pp. 4-15.
28. J. Benattar, J. Doucet, M. Lambert and A. Levelut, *Physical review A*, 1979, **20**, 2505.
29. P. A. C. Gane, A. J. Leadbetter and P. G. Wrighton, *Molecular Crystals and Liquid Crystals*, 1981, **66**, 247-266.
30. R. Pindak, D. Moncton, S. Davey and J. Goodby, *Physical Review Letters*, 1981, **46**, 1135.
31. J. W. Goodby, E. J. Davis, R. J. Mandle and S. J. Cowling, in *Handbook of Liquid Crystals*, eds. J. W. Goodby, C. Tschierske, P. Raynes, H. F. Gleeson, T. Kato and P. J. Collings, Wiley-VCH, Weinhiem, 2nd edn., 2014, vol. 1.3, ch. 1.8, pp. 4-10.
32. J. W. Goodby, in *Handbook of Liquid Crystals*, eds. J. W. Goodby, C. Tschierske, P. Raynes, H. F. Gleeson, T. Kato and P. J. Collings, Wiley-VCH, Weinheim, 2nd edn., 2014, vol. 1.3, ch. 4.1 Design and Synthesis of Smectic Liquid Crystals, pp. 6-19.
33. G. W. Gray and J. W. Goodby, *Smectic Liquid Crystals: Textures and Structures*, Leonard Hill, London, 1984.
34. C. Tschierske, *Journal of Materials Chemistry*, 1998, **8**, 1485-1508.
35. J. M. Steim, M. E. Tourtellotte, J. C. Reinert, R. N. McElhaney and R. L. Rader, *Proceedings of the National Academy of Sciences, USA*, 1969, **63**, 104-109.
36. J. A. Schröter, C. Tschierske, M. Wittenberg and J. H. Wendorff, *Journal of the American Chemical Society*, 1998, **120**, 10669-10675.
37. Y.-H. Hung, C.-Y. Liu, W.-C. Chen and J.-H. Liu, *Liquid Crystals*, 2021, **48**, 542-554.
38. M. Schadt, *Japanese Journal of Applied Physics*, 2009, **48**, 03B001.
39. R. Steinsträsser and L. Pohl, *Angewandte Chemie International Edition in English*, 1973, **12**, 617-630.
40. R. Williams, *Nature*, 1963, **199**, 273-274.
41. G. H. Heilmeier, L. A. Zanoni and L. A. Barton, *Applied Physics Letters* 1968, **13**, 46-47.
42. G. H. Heilmeier and L. A. Zanoni, *Applied Physics Letters* 1968, **13**, 91-92.
43. M. Schadt and W. Helfrich, *Applied Physics Letters*, 1971, **18**, 127-128.
44. P. Raynes, in *Handbook of Liquid Crystals*, eds. J. W. Goodby, C. Tschierske, P. Raynes, H. F. Gleeson, T. Kato and P. J. Collings, Wiley-VCH, Weinhiem, 2nd edn., 2014, vol. 1.3, ch. 8.1 TN, STN, and Guest–Host Liquid Crystal Display Devices, pp. 1-18.
45. T. J. Scheffer, *Philosophical Transactions of the Royal Society of London. Series A, Mathematical and Physical Sciences*, 1983, **309**, 189-201.
46. H. Ki Hong and H. Ho Shin, *Liquid Crystals*, 2008, **35**, 173-177.
47. D. J. Gardiner and H. J. Coles, *Journal of Physics D: Applied Physics*, 2006, **39**, 4948-4955.
48. W. A. Crossland, A. B. Davey, D. P. Chu and T. V. Clapp, in *Handbook of Liquid Crystals*, eds. J. W. Goodby, C. Tschierske, P. Raynes, H. F. Gleeson, T. Kato and P. J. Collings, Wiley-VCH, Weinhiem, 2014, vol. 1.3, ch. 8.6 Smectic A Memory Displays (SAM Displays), pp. 1-38.
49. G. H. Heilmeier and J. E. Goldmacher, *Proceedings of the IEEE*, 1969, **57**, 34-38.
50. D. J. Gardiner, S. M. Morris, F. Castles, M. M. Qasim, W. S. Kim, S. S. Choi, H. J. Park, I. J. Chung and H. J. Coles, *Applied Physics Letters*, 2011, **98**, 263508.
51. S. Sato, *Japanese Journal of Applied Physics*, 1979, **18**, 1679.

52. Y.-H. Lin, Y.-J. Wang and V. Reshetnyak, *Liquid Crystals Reviews*, 2017, **5**, 111-143.
53. M. Kawamura, M. Ye and S. Sato, *Optics Express*, 2008, **16**, 10059-10065.
54. Y. S. Tsou, Y. H. Lin and A. C. Wei, *IEEE Photonics Technology Letters*, 2012, **24**, 2239-2242.
55. K. Dolgaleva, S. K. H. Wei, S. G. Lukishova, S. H. Chen, K. Schwertz and R. W. Boyd, *Journal of the Optical Society of America B*, 2008, **25**, 1496-1504.
56. J. M. Brake, M. K. Daschner, Y.-Y. Luk and N. L. Abbott, *Science*, 2003, **302**, 2094-2097.
57. Y.-Y. Luk, M. L. Tingey, K. A. Dickson, R. T. Raines and N. L. Abbott, *Journal of the American Chemical Society*, 2004, **126**, 9024-9032.
58. I. Abdulhalim, *Liquid Crystals Today*, 2011, **20**, 44-60.
59. M. G. Tomilin, S. A. Povzun, E. V. Gribanova and T. A. Efimova, *Molecular Crystals and Liquid Crystals Science and Technology. Section A.* , 2001, **367**, 133-141.
60. M. Shlens, M. R. Stoltz and A. Benjamin, *Western Journal of Medicine*, 1975, **122**, 367.
61. R. Williams, *Journal of Chemical Physics*, 1963, **39**, 384-388.
62. I. Sage, in *Critical Reports on Applied Chemistry: Thermotropic Liquid Crystals*, ed. G. W. Gray, Wiley, UK, 1987, vol. 22, ch. 3 pp. 87-94.
63. D. J. Gardiner, C. J. Davenport, J. Newton and H. J. Coles, *Journal of Applied Physics*, 2006, **99**, 113517.
64. D. Coates, W. A. Crossland, J. H. Morrisy and B. Needham, *Journal of Physics D: Applied Physics*, 1978, **11**, 2025-2034.
65. M. V. Mitrokhin and B. Holter, *SID Symposium Digest of Technical Papers*, 2005, **36**, 1774-1777.
66. Y. Lu, J. Guo, H. Wang and J. Wei, *Advances in Condensed Matter Physics*, 2012, **2012**, 843264.
67. H. Y. Chen and J. S. Wu, *Journal of the Society for Information Display*, 2010, **18**, 415-420.
68. L. Fritsch, R. J. Mandle, S. J. Cowling and J. W. Goodby, *Journal of Materials Chemistry C*, 2021, **9**, 714-718.
69. B. Bahadur, *Liquid Crystal-Applications And Uses (Volume 1)*, World scientific, 1990.
70. S. J. Cowling, C. Ellis and J. W. Goodby, *Liquid Crystals*, 2011, **38**, 1683-1698.
71. S. J. Cowling, in *Handbook of Liquid Crystals*, eds. J. W. Goodby, C. Tschierske, P. Raynes, H. F. Gleeson, T. Kato and P. J. Collings, Wiley-VCH, Weinhiem 2nd edn., 2014, vol. 8.2 Liquid crystal dyes, ch. 8.2, pp. 1-45.
72. M. T. Sims, *Liquid Crystals*, 2016, **43**, 2363-2374.
73. G. W. Gray, *Dyes and Pigments*, 1982, **3**, 203-209.
74. H. Seki, C. Shishido, S. Yasui and T. Uchida, *Japanese Journal of Applied Physics Part 1*, 1982, **21**, 191-192.
75. H. Iwanaga, *Materials*, 2009, **2**, 1636.
76. F. Jones and T. Reeve, *Molecular Crystals and Liquid Crystals*, 1981, **78**, 201-209.
77. J. Foitzik and W. Haase, *Molecular Crystals and Liquid Crystals*, 1987, **149**, 401-416.
78. E. Wolarz, H. Moryson and D. Bauman, *Displays*, 1992, **13**, 171-178.
79. M. T. Sims, L. C. Abbott, S. J. Cowling, J. W. Goodby and J. N. Moore, *Chemistry: A European Journal*, 2015, **21**, 10123-10130.
80. N. Yasarawan and J. S. van Duijneveldt, *Langmuir*, 2008, **24**, 7184-7192.

81. M. Schadt, *The Journal of Chemical Physics*, 1979, **71**, 2336-2344.
82. Z. Chen and T. M. Swager, *Organic Letters*, 2007, **9**, 997-1000.
83. D. Bauman and H. Moryson, *Journal of Molecular Structure*, 1997, **404**, 113-120.
84. M. Matsui, S. Okada, M. Kadowaki and M. Yamada, *Liquid Crystals*, 2002, **29**, 707-712.
85. R. M. Christie, *Colour Chemistry*, Royal Society of Chemistry, Cambridge, 2001.
86. H. Iwanaga and K. Naito, *Japanese Journal of Applied Physics*, 1998, **37**, L356-L358.
87. F. C. Saunders, K. J. Harrison, E. P. Raynes and D. J. Thompson, *IEEE Transactions on Electron Devices*, 1983, **30**, 499-503.
88. M. T. Sims, R. J. Mandle, J. W. Goodby and J. N. Moore, *Liquid Crystals*, 2017, **44**, 2029-2045.
89. M. T. Sims, L. C. Abbott, S. J. Cowling, J. W. Goodby and J. N. Moore, *Journal of Physical Chemistry C*, 2016, **120**, 11151-11162.
90. M. T. Sims, L. C. Abbott, S. J. Cowling, J. W. Goodby and J. N. Moore, *Physical Chemistry Chemical Physics*, 2016, **18**, 20651-20663.
91. D. Bauman and E. Wolarz, *Zeitschrift für Naturforschung A*, 1996, **51**, 1192.
92. R. Stolarski and K. J. Fiksinski, *Dyes and Pigments*, 1994, **24**, 295-303.
93. X.-H. Zhang, C. Li, W.-B. Wang, X.-X. Cheng, X.-S. Wang and B.-W. Zhang, *Journal of Materials Chemistry*, 2007, **17**, 642-649.
94. L. Dinescu, A. Mezo, L. G. Luyt and R. P. Lemieux, *Tetrahedron Letters*, 1994, **35**, 7549-7552.
95. L. Li, C. D. Jones, J. Magolan and R. P. Lemieux, *Journal of Materials Chemistry*, 2007, **17**, 2313-2318.
96. J. Newton, H. Coles, P. Hodge and J. Hannington, *Journal of Materials Chemistry*, 1994, **4**, 869-874.
97. J. W. Goodby, I. M. Saez, S. J. Cowling, J. S. Gasowska, R. A. MacDonald, S. Sia, P. Watson, K. J. Toyne, M. Hird, R. A. Lewis, S.-E. Lee and V. Vaschenko, *Liquid Crystals*, 2009, **36**, 567-605.
98. D. J. Gardiner and H. J. Coles, *Journal of Applied Physics*, 2006, **100**, 124903.
99. S. Khosla, K. K. Raina and H. J. Coles, *Current Applied Physics*, 2003, **3**, 135-140.
100. C. Carboni, R. Mehdi, A. K. George, S. H. Al-Harthi and J. Naciri, *Molecular Crystals and Liquid Crystals*, 2004, **410**, 61-69.
101. M. Ibn-Elhaj, H. J. Coles, D. Guillon and A. Skoulios, *Journal de Physique II*, 1993, **3**, 1807-1817.
102. J. W. Goodby, R. J. Mandle, E. J. Davis, T. Zhong and S. J. Cowling, *Liquid Crystals*, 2015, **42**, 593-622.
103. R. Dabrowski and E. Żytyński, *Molecular Crystals and Liquid Crystals*, 1982, **87**, 109-135.
104. M. Petrzilka and K. Schleich, *Helvetica Chimica Acta*, 1982, **65**, 1242-1257.
105. M. Hird, in *Physical Properties of Liquid Crystals: Nematics -(EMIS Datareviews series; no.25)*, INSPEC, London, 2001, ch. 1.1, pp. 3-15.
106. M. T. Sims, L. C. Abbott, J. W. Goodby and J. N. Moore, *Soft Matter*, 2019, **15**, 7722-7732.
107. J. W. Goodby, G. H. Mehl, I. M. Saez, R. P. Tuffin, G. Mackenzie, R. Auzély-Velty, T. Benvegnu and D. Plusquellec, *Chemical Communications*, 1998, 2057-2070.
108. R. J. Mandle, E. J. Davis, C. C. A. Voll, D. J. Lewis, S. J. Cowling and J. W. Goodby, *Journal of Materials Chemistry C*, 2015, **3**, 2380-2388.
109. G. Tiberio, L. Muccioli, R. Berardi and C. Zannoni, *ChemPhysChem*, 2009, **10**, 125-136.

110. Y. Queneau, J. Gagnaire, J. J. West, G. Mackenzie and J. W. Goodby, *Journal of Materials Chemistry*, 2001, **11**, 2839-2844.
111. R. J. Mandle, L. C. Abbott, L. Fritsch, R. R. Parker, S. Hart, A. C. Whitwood, S. J. Cowling, J. N. Moore and J. W. Goodby, *Journal of Materials Chemistry C*, 2022, **10**, 5934-5943.
112. R. J. Mandle, S. J. Cowling and J. W. Goodby, *RSC Advances*, 2017, **7**, 40480-40485.
113. S. Marčelja, *Journal of Chemical Physics*, 1974, **60**, 3599-3604.
114. R. Berardi, L. Muccioli and C. Zannoni, *ChemPhysChem*, 2004, **5**, 104-111.
115. D. Bauman, A. Zięba and E. Mykowska, *Opto-Electronics Review*, 2008, **16**, 244-250.
116. N. Bielejewska, E. Chrzumnicka, E. Mykowska, R. Przybylski, M. Szybowicz, K. Wladysiak and D. Bauman, *Acta Physica Polonica A*, 2006, **110**, 777-793.
117. C. J. Gibb, J. M. Storey and C. T. Imrie, *Liquid Crystals*, 2022, **49**, 1706-1716.
118. M. Cifelli, L. De Gaetani, G. Prampolini and A. Tani, *Journal of Physical Chemistry B*, 2008, **112**, 9777-9786.
119. D. Gardiner and H. Coles, *Journal of Physics D: Applied Physics*, 2007, **40**, 977.
120. I. Dierking, L. Komitov and S. Lagerwall, *Ferroelectrics*, 1998, **211**, 165-175.
121. J. S. Patel, T. M. Leslie and J. W. Goodby, *Ferroelectrics*, 1984, **59**, 137-144.
122. D. W. Berreman, *Physical Review Letters*, 1972, **28**, 1683-1686.
123. K. Kondo, F. Kobayashi, A. Fukuda and E. Kuze, *Japanese Journal of Applied Physics*, 1981, **20**, 1773.
124. K. Kondo, H. Takezoe, A. Fukuda and E. Kuze, *Japanese Journal of Applied Physics*, 1983, **22**, L85.
125. K. Ichimura, Y. Suzuki, T. Seki, A. Hosoki and K. Aoki, *Langmuir*, 1988, **4**, 1214-1216.
126. H. Iwanaga, K. Naito and F. Aiga, *Journal of Molecular Structure*, 2010, **975**, 110-114.
127. J. Constant, J. Kirton, E. P. Raynes, I. A. Shanks, D. Coates, G. W. Gray and D. G. Mcdonnell, *Electronics Letters*, 1976, **12**, 514-515.
128. G. N. Taylor and F. J. Kahn, *Journal of Applied Physics*, 1974, **45**, 4330-4338.
129. H. Iwanaga, K. Naito and F. Effenberger, *Liquid Crystals*, 2000, **27**, 115-123.
130. H. S. Cole and R. A. Kashnow, *Applied Physics Letters*, 2008, **30**, 619-621.
131. W. Shen, H. Zhang, Z. Miao and Z. Ye, *Advanced Functional Materials*, 2023, **33**, 2210664.
132. W. Wu, G. Sun, L. Wu and C. Fan, *SID Symposium Digest of Technical Papers*, 2021, **52**, 991-994.
133. S. Baburaj, J. Parthiban, S. A. Rakhimov, R. Johnson, L. Sukhomlinova, P. Luchette, S. Jockusch, M. D. Forbes and J. Sivaguru, *Photochemistry and Photobiology*, 2023.
134. K. Goda, H. Miyauchi, R. Hattori, Y. Fujinaga and S. Yoshidome, *Molecular Crystals and Liquid Crystals*, 2022, 1-8.
135. C.-H. An, J.-H. Lee, C.-H. Han and S.-W. Oh, *Dyes and Pigments*, 2023, **212**, 111124.
136. M. Czajkowski, Ł. Duda, S. J. Czarnocki, A. B. Szukalska, M. Guzik, J. Myśliwiec, M. Skoreński, B. Potaniec and J. Cybińska, *Journal of Materials Chemistry C*, 2023, **11**, 4426-4438.
137. E. Peeters, J. Lub, J. A. Steenbakkers and D. J. Broer, *Advanced Materials*, 2006, **18**, 2412-2417.
138. M. Sheng, L. Zhang, D. Wang, M. Li, L. Li, J. L. West and S. Fu, *Dyes and Pigments*, 2018, **158**, 1-11.

139. J. W. Goodby, in *Handbook of Liquid Crystals*, eds. J. W. Goodby, C. Tschierske, P. Raynes, H. F. Gleeson, T. Kato and P. J. Collings, Wiley-VCH, Weinheim, 2nd edn., 2014, vol. 1.3, ch. 1.3 Phase Transitions: General and Fundamental Aspects, pp. 1-18.
140. D. M. Agra-Kooijman and S. Kumar, in *Handbook of Liquid Crystals*, eds. J. W. Goodby, C. Tschierske, P. Raynes, H. F. Gleeson, T. Kato and P. J. Collings, Wiley-VCH, Weinheim, 2014, vol. 1.3, ch. 1.10 X-Ray Scattering Investigations of Liquid Crystals, pp. 6-9.
141. A. Gilbert and J. Baggott, *Essentials of Molecular Photochemistry*, Blackwell Scientific Publications Oxford, 1991.
142. C. J. Cramer, *Essentials of computational chemistry: theories and models*, John Wiley & Sons, Chichester, 2013.
143. R. O. Jones, *Reviews of Modern Physics*, 2015, **87**, 897.
144. M. G. Medvedev, I. S. Bushmarinov, J. Sun, J. P. Perdew and K. A. Lyssenko, *Science*, 2017, **355**, 49-52.
145. P. Hohenberg and W. Kohn, *Physical review*, 1964, **136**, B864.
146. P. J. Hasnip, K. Refson, M. I. Probert, J. R. Yates, S. J. Clark and C. J. Pickard, *Philosophical Transactions of the Royal Society A: Mathematical, Physical and Engineering Sciences*, 2014, **372**, 20130270.
147. A. Frisch and J. Foresman, *Exploring chemistry with electronic structure methods*, Gaussian Inc, Pittsburgh, 1996.
148. R. Chen, Z. An, W. Wang, X. Chen and P. Chen, *Liquid Crystals*, 2017, **44**, 1515-1524.
149. K. D. Katariya, K. J. Nakum and M. Hagar, *Liquid Crystals*, 2022, **49**, 312-326.
150. Y. Li, Y. Chen, H. Li, C. Liu, L. Li, Y. Quan and Y. Cheng, *Angewandte Chemie*, 2023, e202312159.
151. N. J. Boyd and M. R. Wilson, *Physical Chemistry Chemical Physics*, 2018, **20**, 1485-1496.
152. J. Zhang, J. Su and H. Guo, *Journal of Physical Chemistry B*, 2011, **115**, 2214-2227.
153. M. F. Palermo, A. Pizzirusso, L. Muccioli and C. Zannoni, *Journal of Chemical Physics*, 2013, **138**, 204901.
154. J. Wang, R. M. Wolf, J. W. Caldwell, P. A. Kollman and D. A. Case, *Journal of Computational Chemistry*, 2004, **25**, 1157-1174.
155. A. Pizzirusso, M. E. Di Pietro, G. De Luca, G. Celebre, M. Longeri, L. Muccioli and C. Zannoni, *ChemPhysChem*, 2014, **15**, 1356-1367.
156. L. De Gaetani and G. Prampolini, *Soft Matter*, 2009, **5**, 3517-3526.
157. M. T. Sims, L. C. Abbott, R. J. Mandle, J. W. Goodby and J. N. Moore, *Physical Chemistry Chemical Physics*, 2023, **25**, 10367-10383.
158. M. T. Sims, L. C. Abbott, S. J. Cowling, J. W. Goodby and J. N. Moore, *Physical Chemistry Chemical Physics*, 2017, **19**, 813-827.
159. D. M. Agra-Kooijman and S. Kumar, in *Handbook of Liquid Crystals*, eds. J. W. Goodby, C. Tschierske, P. Raynes, H. F. Gleeson, T. Kato and P. J. Collings, 2014, vol. 1.3, ch. 10 X-Ray Scattering Investigations of Liquid Crystals, p. 3.
160. M. J. Frisch, G. W. Trucks, H. B. Schlegel, G. E. Scuseria, M. A. Robb, J. R. Cheeseman, G. Scalmani, V. Barone, G. A. Petersson, H. Nakatsuji, X. Li, M. Caricato, A. V. Marenich, J. Bloino, B. G. Janesko, R. Gomperts, B. Mennucci, H. P. Hratchian, J. V. Ortiz, A. F. Izmaylov, J. L. Sonnenberg, Williams, F. Ding, F. Lipparini, F. Egidi, J. Goings, B. Peng, A. Petrone, T. Henderson, D. Ranasinghe, V. G. Zakrzewski, J. Gao, N. Rega, G. Zheng, W. Liang, M. Hada, M. Ehara, K. Toyota, R. Fukuda, J. Hasegawa, M. Ishida, T. Nakajima, Y. Honda, O. Kitao, H. Nakai, T.

Vreven, K. Throssell, J. A. Montgomery Jr., J. E. Peralta, F. Ogliaro, M. J. Bearpark, J. J. Heyd, E. N. Brothers, K. N. Kudin, V. N. Staroverov, T. A. Keith, R. Kobayashi, J. Normand, K. Raghavachari, A. P. Rendell, J. C. Burant, S. S. Iyengar, J. Tomasi, M. Cossi, J. M. Millam, M. Klene, C. Adamo, R. Cammi, J. W. Ochterski, R. L. Martin, K. Morokuma, O. Farkas, J. B. Foresman and D. J. Fox, in *Gaussian 16 Rev. A.03*, Gaussian Inc., Wallingford, CT, 2016.
161. A. D. Becke, *The Journal of Chemical Physics*, 1992, **96**, 2155-2160.
162. M. J. Abraham, T. Murtola, R. Schulz, S. Páll, J. C. Smith, B. Hess and E. Lindahl, *SoftwareX*, 2015, **1-2**, 19-25.
163. S. Páll, M. J. Abraham, C. Kutzner, B. Hess and E. Lindahl, *International conference on exascale applications and software: Solving Software Challenges for Exascale 8759,* , 2015, 3-27.
164. S. Pronk, S. Páll, R. Schulz, P. Larsson, P. Bjelkmar, R. Apostolov, M. R. Shirts, J. C. Smith, P. M. Kasson and D. van der Spoel, *Bioinformatics*, 2013, **29**, 845-854.
165. B. Hess, C. Kutzner, D. Van Der Spoel and E. Lindahl, *Journal of chemical theory and computation*, 2008, **4**, 435-447.
166. D. Van Der Spoel, E. Lindahl, B. Hess, G. Groenhof, A. E. Mark and H. J. Berendsen, *Journal of Computational Chemistry*, 2005, **26**, 1701-1718.
167. E. Lindahl, B. Hess and D. Van Der Spoel, *Molecular modeling annual*, 2001, **7**, 306-317.
168. H. J. Berendsen, D. van der Spoel and R. van Drunen, *Computer physics communications*, 1995, **91**, 43-56.
169. N. J. Boyd and M. R. Wilson, *Physical Chemistry Chemical Physics*, 2015, **17**, 24851-24865.
170. S. Nosé, *Molecular Physics*, 1984, **52**, 255-268.
171. W. G. Hoover, *Physical review A*, 1985, **31**, 1695-1697.
172. G. Bussi, D. Donadio and M. Parrinello, *The Journal of Chemical Physics*, 2007, **126**, 014101.
173. B. Hess, H. Bekker, H. J. Berendsen and J. G. Fraaije, *Journal of Computational Chemistry*, 1997, **18**, 1463-1472.
174. M. Parrinello and A. Rahman, *Journal of Applied Physics*, 1981, **52**, 7182-7190.
175. U. Essmann, L. Perera, M. L. Berkowitz, T. Darden, H. Lee and L. G. Pedersen, *The Journal of Chemical Physics*, 1995, **103**, 8577-8593.
176. M. F. Palermo, A. Pizzirusso, L. Muccioli and C. Zannoni, *Journal of Chemical Physics*, 2013, **138**, 204901.
177. D. Cheung, S. Clark and M. R. Wilson, *Physical Review E*, 2002, **65**, 051709.
178. N. Kapernaum and F. Giesselmann, *Physical Review E*, 2008, **78**, 062701.
179. I. Haller, *Progress in solid state chemistry*, 1975, **10**, 103-118.
180. S. Patari and A. Nath, *Advanced Materials Proceedings*, 2017, **2**, 125-127.
181. G. A. Oweimreen and M. A. Morsy, *Thermochimica Acta*, 2000, **346**, 37-47.
182. S. J. Cowling, A. W. Hall and J. W. Goodby, *Journal of Materials Chemistry*, 2011, **21**, 9031-9042.
183. A. Leadbetter, J. Frost, J. Gaughan, G. Gray and A. Mosley, *Journal de Physique*, 1979, **40**, 375-380.
184. M. Thompson, C. Carkner, A. Bailey, N. J. Mosey, N. Kapernaum and R. P. Lemieux, *Liquid Crystals*, 2014, **41**, 1246-1260.
185. A. Maleki, Z. Seidali, M. Zakerhamidi and M. M. Ara, *Optik*, 2015, **126**, 5473-5477.
186. M. Osman, L. Pietronero, T. Scheffer and H. Zeller, *The Journal of Chemical Physics*, 1981, **74**, 5377-5383.